Channel Characterisation for Molecular Communication Systems with Practical Transmitters and Receivers

Xinyu Huang

April 2023

A Thesis Submitted for the Degree of
Doctor of Philosophy
of The Australian National University

School of Engineering
College of Engineering, Computing and Cybernetics
The Australian National University

Declaration

The contents of this thesis are the results of original research and have not been submitted for a higher degree to any other university or institution.

Much of the work in this thesis has been published or has been submitted for publication as journal papers or conference proceedings.

The research work presented in this thesis has been performed jointly with Assoc. Prof. Nan Yang (The Australian National University), Dr. Yuting Fang (University of Melbourne), Assoc. Prof. Adam Noel (University of Warwick), Prof. Robert Schober (Friedrich-Alexander-University Erlangen-Nürnberg), Dr. Stuart T. Johnston (University of Melbourne), Dr. Matthew Faria (University of Melbourne), Prof. Miaowen Wen (South China University of Technology), and Dr. Yu Huang (Guangzhou University). The substantial majority of this work was my own.

Xinyu Huang
School of Engineering,
College of Engineering, Computing and Cybernetics,
The Australian National University,
Canberra, ACT 2601,
AUSTRALIA

Acknowledgments

First and foremost, I would like to express my sincere gratitude to my primary supervisor Assoc. Prof. Nan Yang for his valuable advice, continuous support, and patience during my PhD study. His immense knowledge and plentiful experiences have encouraged me in all the time of my academic research and daily life. I would also like to thank Assoc. Prof. Xiangyun Zhou and Prof. Salman Durrani for being part of my supervisory panel. I could not have undertaken this journey without the supervision and help from all members of my supervisory panel.

I would also like to show gratitude to Dr. Yuting Fang at the University of Melbourne and Assoc. Prof. Adam Noel at the University of Warwick for their deep discussions and great feedback to our collaborated works. Many thanks to my collaborators Prof. Robert Schober at the Friedrich-Alexander-University Erlangen-Nürnberg, Prof. Miaowen Wen at the South China University of Technology, Dr. Yu Huang at the Guangzhou University, and Dr. Stuart T. Johston and Dr. Matthew Faria at the University of Melbourne for their constructive comments and valuable inputs to our research works.

It has been an amazing experience working in the wireless group at the Australian National University (ANU), thanks to everyone I have worked with and from whom I have learned so much. Thanks for all your help, support and friendship, especially Dr. Jihui Zhang, Zhifeng Tang, Dr. Huiyuan Sun, Dr. Xiaohui Zhou, Dr. Zhuo Sun, Muhammed Akram Mohamed Shafie, Simin Xu, Sahar Idrees, and Amy Bastine.

I am grateful to ANU for providing me the scholarship and stipend for my PhD study, conference attendance, and overseas academic visits.

Most importantly, none of this could have happended without my family. My parents, Junping Huang and Xiaojing Xu, who cared about my health and daily life, and offered me support and encouragement through phone calls every week - despite my own limited devotion to correspondence. My grandparents, Yurong Zhang and Tinghan Xu, who taught me to be brave and patient to difficulties that I have met during the past three and a half years. My uncle and aunt, Xiaodong Xu and Hui Ya, who took care about my daily life and provided me help in place of my parents when I was in Australia.

Finally, I would also like to pass my love and thank to Jiangyue Yu, who always stands by my side, listens to my complaints, eases my anxiety, and makes me laugh. Without you, I could not make this achievement. I also would like to thank my friends, Khaing Phyu Aung, Sharidya Rahman, Chenyue Gu, Chenyu Gu, Qianwen Liu, Lu Sun, Qian Liang, Yue Li, Yiqi

Liao, and Yueming Deng, who showed their support and care over my whole PhD journey.

Abstract

Molecular communication (MC) has emerged as a promising paradigm to facilitate microscale or nanoscale communications. In MC, information is encoded into small particles that are released by a transmitter (TX) into a fluid medium and propagate until they arrive at a receiver (RX). In particular, MC possesses important characteristics, such as low energy consumption and potential for biocompatibility, which makes it suitable for many *in vivo* applications, e.g., health monitoring and targeted drug delivery.

This thesis focuses on designing practical transmission/reception mechanisms and characterising the channel between the TX and RX from the communication and signal processing perspectives. Specifically, this thesis fills the current research gaps by i) designing practical TXs, ii) designing practical RXs, iii) investigating the co-existence of multiple non-transparent RXs, iv) proposing novel parameter estimation methods, and v) designing strategies for enhancing the energy efficiency.

First, we propose a novel imperfect TX model, namely the membrane fusion (MF)-based TX, that adopts MF between a vesicle and the TX membrane to release molecules encapsulated within the vesicle in Chapter 3. Incorporating a fully absorbing RX, the channel impulse response (CIR) is derived for two scenarios: 1) Both TX and RX are static, and 2) both TX and RX are diffusion-based mobile. Moreover, simulation results show that a low MF probability or low vesicle mobility slows the release of molecules and reduces the molecule hitting probability at the RX.

Second, we propose an absorbing RX covered by multiple non-overlapping heterogeneous receptors that may have different sizes and arbitrary locations in Chapter 4. We consider two types of TX, which are a point TX and an MF-based TX. For each type of TX, we analyse the expected molecule hitting rate at the RX as a function of the sizes and locations of the receptors. Exploiting our numerical results, we show that the expected number of absorbed molecules at the RX increases with the number of receptors, when the total area on the RX surface covered by receptors is fixed.

Third, we develop a one-dimensional (1D) diffusion-based MC system to analyse CIR between a single TX and two fully absorbing RXs in Chapter 5. In particular, we derive rigorous analytical expressions for i) the fraction of molecules absorbed, ii) the corresponding hitting rate, and iii) the asymptotic fraction of absorbed molecules as time approaches infinity at each RX. Moreover, we consider constant flow and noisy molecules in this environment, and investigate the estimation of different parameters, e.g., propagation distance and flow velocity.

A novel estimation method, namely difference estimation (DE), is proposed to eliminate the effect of noise by using the difference between the received signals at two RXs. For DE, the Cramer-Rao lower bound (CRLB) on the variance of estimation is derived. Furthermore, numerical results show that DE attains the CRLB and is less sensitive to the change of noise than independent estimation at each RX.

Finally, in Chapter 6, we design a molecule harvesting TX model, where the surface of a spherical TX is covered by heterogeneous receptors with different sizes and arbitrary locations. If molecules hit any receptor, they are absorbed by the TX immediately. Within the TX, molecules are stored in vesicles that are continuously generated and released by the TX via the MF process. Considering a transparent RX and molecular degradation during the propagation from the TX to the RX, we derive the molecule release rate and the fraction of molecules absorbed by the TX as well as the received signal at the RX. Numerical results show that different vesicle generation rates result in the same number of molecules absorbed by the TX, but different peak received signals at the RX.

This thesis relaxes idealised assumptions in MC systems adopted in existing studies, shows the difference of system performance between practical and ideal MC, investigates the system with multiple non-transparent RXs, reveals the potential benefits of estimating parameters based on received signals at multiple RXs, and designs new strategies to enhance energy efficiency in nanomachines. Thus, this thesis provides great insights for realising practical MC systems in the future.

List of Publications

Journal Articles

J1. **X. Huang**, Y. Fang, A. Noel, and N. Yang, "Membrane fusion-based transmitter design for static and diffusive mobile molecular communication systems," *IEEE Trans. Commun.*, vol. 70, no. 1, pp. 132-148, Jan. 2022. (Chapter 3)

J2. **X. Huang**, Y. Fang, S. Johnson, M. Faria, N. Yang, and R. Schober, "Analysis of MC systems employing receivers covered by heterogeneous receptors," *IEEE Trans. Mol. Biol. Multi-Scale Commun.*, vol. 9, no. 1, pp. 63-78, Mar. 2023. (Chapter 4)

J3. **X. Huang**, Y. Fang, A. Noel, and N. Yang, "Channel characterisation for 1D molecular communication with two absorbing receivers," *IEEE Commun. Lett.*, vol. 24, no. 6, pp. 1150-1154, Jun. 2020. (Chapter 5)

J4. **X. Huang**, Y. Fang, and N. Yang, "A survey on estimation schemes in molecular communications," *Digital Signal Process.*, pp. 10316, Jul. 2021. (not included in the thesis)

J5. Y. Fang, **X. Huang**, S. Johnson, M. Faria, A. W. Eckford, and J. Evans, "Quorum sensing inspired cooperative drug delivery system," *IEEE Trans. Mol. Biol. Multi-Scale Commun.*, vol. 9, no. 1, pp. 100-105, Mar. 2023. (not included in the thesis)

Conference Papers

C1. **X. Huang**, Y. Fang, A. Noel, and N. Yang, "Membrane fusion-based transmitter model design for molecular communication systems," in *Proc. IEEE ICC 2021*, Montreal, Canada, Jun. 2021, pp. 1-6. (Chapter 3)

C2. **X. Huang**, Y. Fang, S. Johnston, M. Faria, N. Yang, and R. Schober, "Analysis of receiver covered by heterogeneous receptors in molecular communications," in *Proc. IEEE ICC 2022*, Seoul, South Korea, May 2022, pp. 1-6. (Chapter 4)

C3. **X. Huang**, Y. Fang, A. Noel, and N. Yang, "Parameter estimation in a noisy 1D environment via two absorbing receivers," in *Proc. IEEE Globecom 2020*, Taipei, Taiwan (ROC), Dec. 2020, pp. 1-7. (Chapter 5)

C4. **X. Huang**, Y. Huang, M. Wen, N. Yang, and R. Schober, "Analysis of molecule harvesting by heterogeneous receptors on MC transmitters," submitted to *Proc. IEEE Globecom 2023*. (Chapter 6)

C5. **X. Huang** and N. Yang, "On the block error performance for short-packet non-orthogonal multiple access," in *Proc. IEEE ICC 2019*, Shanghai, China, May 2019, pp. 1-7. (not included in the thesis)

Acronyms

MC	Molecular communication
1D	one-dimensional
3D	three-dimensional
MF	membrane fusion
CIR	channel impulse response
BER	bit error rate
ISI	inter-symbol interference
TX	Transmitter
RX	Receiver
PMF	Probability mass function
PDF	Probability density function
RV	Random variable
CDF	Cumulative distribution function
PBSs	Particle-based simulations
APs	Absorbing patches
PTFR	A point TX and a fully absorbing RX
PTAR	A point TX and an AP-based RX
MTAR	An MF-based TX and an AP-based RX
LTI	Linear time-invariant
DE	Difference estimation
ML	Maximum-likelihood
CRLB	Cramer-Rao lower bound

HCRLB	Hammersley-Chapman-Robinson lower bound
MSE	Mean squared error
MVU	Minimum-variance unbiased
PPP	Poisson point process
SISO	Single-input-single-output
SIMO	Single-input-multiple-output
MIMO	Multiple-input-multiple-output
CTC	Circulating tumor cells
MPs	Micropollutants
ACF	Autocorrelation function
ATP	Adenosine triphosphate

Notations

$\Pr(\cdot)$	Probability
$\delta(\cdot)$	Dirac delta function
$j_0(\cdot)$	Zeroth order spherical Bessel function of the first type
$I_{\frac{1}{2}}(\cdot)$	Modified Bessel function of the first kind
$\operatorname{erfc}(\cdot)$	Complementary error function
$\operatorname{erf}(\cdot)$	Error function
$\text{Poisson}(\cdot)$	Poisson distribution
∇^2	3D spherical Laplacian
$\mathcal{O}(\cdot)$	Infinitesimal of higher order
$\mathbb{E}[\cdot]$	Expectation
$f_{\text{c}}^{-1}(\cdot)$	Inverse function of $f_{\text{c}}(t)$
R^2	Coefficient of determination

Contents

List of Figures

List of Tables

Chapter 1

Introduction

1.1 Background & Motivation

1.1.1 Limitations in Traditional Wireless Communication

The development of wireless communication with electromagnetic signals from the first generation (1G) to the fifth-generation (5G) has changed our life dramatically over the past few decades. During the decade from 2020 to 2030, significant efforts have been and will be spent to characterise and understand wireless systems beyond 5G, which is referred to as the sixth generation (6G) wireless systems [2]. One of the use cases expected for 6G is connectivity for everything, which includes real-time monitoring of buildings, transportation, water, power, and connecting with the nanoscale network. In particular, the Internet of Nano-Things (IoNT) that interconnects nanoscale devices with classical networks and the Internet has huge potential applications in human healthcare, e.g., intrabody communication, and agricultural industry [3]. Despite this prospect, due to constraints such as the ratio of the antenna size to the wavelength of the electromagnetic signal [4], it is extremely difficult to implement traditional wireless communication in IoNT. Moreover, the use of electromagnetic wireless communication inside networks of tunnels, pipelines, or salt water environment can be very inefficient due to the rapid attenuation of electromagnetic signals [5]. Inspired by nature, one possible solution to filling these gaps is to use chemical signals as information carriers, which is named as molecular communication (MC).

In MC, a transmitter (TX) releases small particles such as molecules or lipid vesicles into an aqueous or gaseous medium, where particles propagate until they arrive at a receiver (RX). The RX then detects and decodes information encoded in these particles. Specifically, the TX or the RX can be cells, molecules, e.g., DNA and RNA, or organisms, and the propagation mechanisms include the free diffusion, the flow assisted propagation, the active transportation, e.g., using motor proteins or bacteria, and the chemical reaction-based propagation.

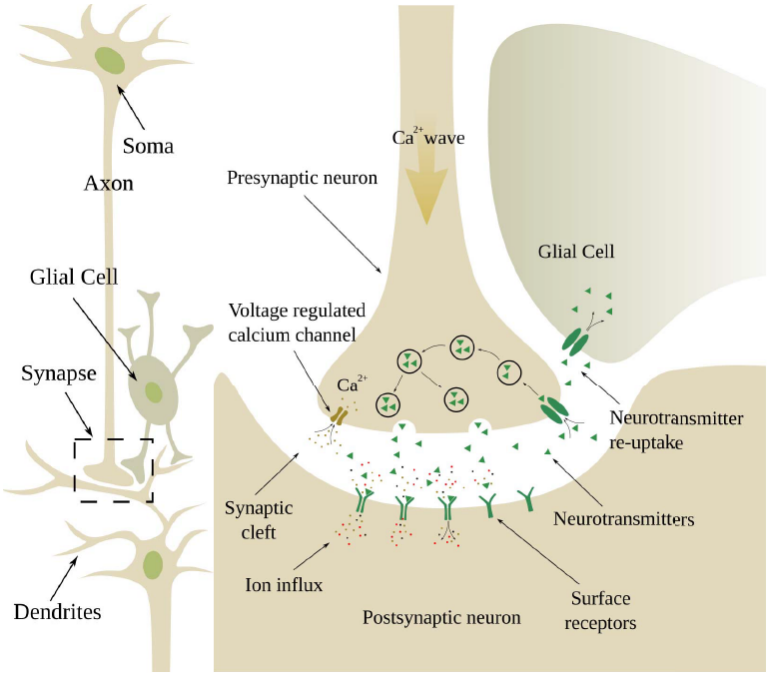

Figure 1.1: Illustration of the synaptic signalling [1].

1.1.2 MC in Biology

In nature, fully functional MC systems have already been used by living organisms, plants, and animals over billions of years. Microscale MC systems refer to as the system operating within the distances ranging from several nanometers to micrometers, and macroscale MC refers to as the system operating within the distances ranging from several centimeters to meters.

1.1.2.1 Microscale MC

Cells typically communicate using chemical signals, namely ligands, which are proteins or other molecules produced by a sending cell. In order to detect a signal, a target cell must have the right receptor. When a ligand binds to its receptor, it alters the shape or activity of the receptor, which triggers a change inside the target cell, such as alteration in the activity of a gene or cell division. Accordingly, an original intercellular signal is converted into an intracellular signal.

One typical example of cell signalling is synaptic signalling [6], in which the presynaptic neuron transmits signals to the postsynaptic neuron as shown in Fig. 1.1. When the presynaptic neuron fires an action potential, the voltage-regulated calcium ion channels are opened such that Ca^{2+} rapidly enters the presynaptic cell. These calcium ions then enable the vesicles in the presynaptic neuron to fuse with the terminal membrane and release neurotransmitters that are encapsulated within the vesicles. After neurotransmitters are released from the presynaptic

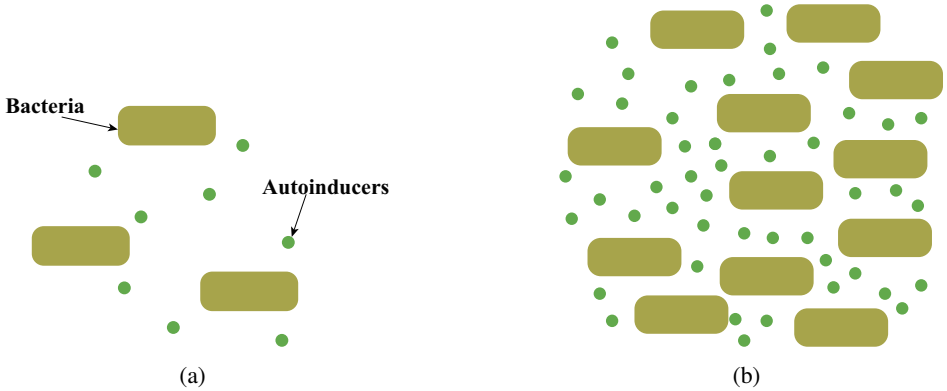

Figure 1.2: Illustration of quorum sensing in bacteria. (a) Low cell density and low autoinducer concentration. (b) High cell density causes an accumulation of autoinducers.

neuron, they diffuse rapidly across the synaptic cleft and bind to receptors on the postsynaptic neuron. The binding of neurotransmitters instigates opening and closing of ion channels, which alters the membrane potential of the postsynaptic cell and enables it to fire an action potential. Moreover, to end the synaptic signalling, neurotransmitters in the synapse are degraded by enzymes, reabsorbed by the presynaptic neuron, diffused away, and cleared by glial cells [7].

Another example for microscale MC is quorum sensing in bacteria as shown in Fig. 1.2, which is a process that enables bacterial communication and regulates bacterial gene expression [8]. In particular, bacterial communication relies on versatile chemical signalling molecules named autoinducers. During the bacterial reproductive cycle, an individual bacterium synthesize autoinducers and move autoinducers out of cells passively or actively. With the increase in the extracellular concentration of autoinducers, it becomes energetically unfavorable for intracellular autoinducers to leave the cell, which results in an increase in bacterial intracellular concentration. Once intracellular concentration increases, autoinducers bind to their receptors, triggering signalling cascades that alter transcription factor activity and gene expression. The functions carried out by bacteria within colonies due to quorum sensing include sporulation, bioluminescence, virulence, conjugation, competence, and biofilm formation [9].

1.1.2.2 Macroscale MC

Molecules play a vital role in communication at both the microscale, facilitating interactions between cells, and the macroscale, enabling communication between plants and animals. In nature, plants have developed a communication system to transmit information based on volatile organic compounds (VOCs) [10]. For example, flowers use VOCs to attract pollinators and ensure reproduction [11]. In a damaged plant, VOCs are emitted and diffuse via air to reach

undamaged plants nearby, giving them the chance to strength their own defence system. Besides the plant to plant or insect communication, plants can also communicate with rhizosphere microbes by using molecules [12]. Specifically, the plants can release isoflavones to attract bacteria and form root nodules such that the plants provide nutrients required by bacteria and bacteria offer nitrogen to plants [13]. This mutualism improves plant's health and productivity. Moreover, microbes can protect plants from pathogens and pests by emitting VOCs to stop pathogens' growth or pests' attack, and producing molecules to strength plants' defence systems [14]. Also, microbes can help plants survive in difficult areas, e.g., the places with low water availability and high level of salts [15, 16]. In addition, social insects, e.g., ants and bees, use pheromone as chemical trails for navigation and tracking [17].

1.2 Applications of MC

MC signals own special characteristics of biocompatibility and low energy consumption for generation and propagation, which makes MC suitable for many applications, such as human healthcare, water pollution control, and manufacturing.

1.2.1 Human Healthcare

We divide the applications of MC to human healthcare into two categories. The first category is the diagnosis of diseases. In particular, the identification of tumors is well suited to be achieved through MC [18]. Specifically, tumors can be detected by sensing abnormal concentration of circulating tumor cells (CTCs) in the blood stream, which contribute to the spread of tumors through the body. The monitoring of the CTC concentration allows both an early detection of a disease in its initial phase and at any relapse after an apparently successful treatment. By using implanted devices, e.g., bio-nanomachines, MC can achieve the detection of CTCs through monitoring the concentration of specific biomarkers produced by CTCs in the cardiocirculatory system [19] and delivering the collected information to the external by means of different communication techniques.

The second category is treatment of diseases. One of the most prominent areas in nanomedicine is targeted drug delivery, which aims to deliver medication locally to the specific region requiring treatment, thereby minimizing side effects on other healthy parts of the body. [20]. For drug delivery, bio-nanomachines can be embedded with drug molecules and either injected directly into the target sites or intravenously to propagate to target sites. Bio-nanomachines can use MC collaborately to search for target sites, aggregate at the target sites, and release embedded drug molecules. We note that the bio-nanomachines can be either natural, e.g., pathogens, blood cells, macrophsges, and stem cells [21, 22], or synthetic, e.g., metallic nanoparticles, carbon structures, and inorganic particles [23].

1.2.2 Water Pollution Control

A water environment can be easily polluted by micropollutants (MPs) that are synthetic or natural compounds [24], e.g., pharmaceuticals and industrial chemicals. As MPs are often at low concentration in the environment, they are not commonly monitored and measured. However, MPs have acute and chronic effects on the ecosystem, where bioaccumulation, toxicity, and resistance to elimination are potential risks of MPs. By adopting MC systems, nanomachines can be applied to identify the presence of MPs in a timely manner. Moreover, when some nanomachines locate the MPs, they can move to them and send molecular signals that can guide other nanomachines or larger-scale devices to the location of MPs and transform or degrade them [25].

1.2.3 Manufacturing - Pattern and Structure Formation

As MC can control the transport of molecules, it can be used to produce novel patterns of molecules [26]. In particular, a specific pattern of molecules can be formed by linking each location of the system with an address, and then bio-nanomachines or specific types of molecules are transported to each address. After this transportation, chemical processes can be activated to complete the structure. If the patterning processes can be programmed in sequences of molecules, it may be possible to produce a large variety of shapes and structures by using the same manufacturing machinery.

1.3 Thesis Outline and Contributions

This thesis focuses on proposing practical TXs and RXs based on the existing biological mechanisms and analysing the channel impulse response (CIR) between them. In addition, this thesis investigates the co-existence of multiple non-transparent RXs, proposes novel parameter estimation methods, and designs strategies to improve the energy efficiency of the MC system. The specific contributions of each chapter are detailed as follows:

Chapter 3 – Membrane Fusion - Based Transmitter Design

In Chapter 3, we propose a novel TX model in a three-dimensional (3D) environment, namely the membrane fusion (MF)-based TX, which uses fusion between a vesicle generated within the TX and the TX membrane to release molecules encapsulated within the vesicle. By considering a fully absorbing RX, we investigate the end-to-end CIR between the MF-based TX and the RX in two scenarios: 1) A static TX and a static RX, and 2) a diffusion-based mobile TX and a diffusion-based mobile RX. In summary, our major contributions are as follows.

- We derive the time-varying molecule release rate and the fraction of molecules released from the TX by a given time.
- For the static scenario, we derive the end-to-end i) molecule hitting rate, ii) the fraction of molecules absorbed, and iii) the asymptotic fraction of molecules absorbed at the RX due to the MF-based TX as time approaches infinity. For the mobile scenario, we derive the expected end-to-end molecule hitting rate at the mobile RX.
- By considering a sequence of bits transmitted from the TX and a threshold detector at the RX, we calculate the average bit error rate (BER) for the static and mobile scenarios. To derive the average BER in the mobile scenario, we also derive the probability mass function (PMF) for the number of molecules absorbed at the mobile RX.

The results in this chapter have been presented in [27, 28], which are listed as follows:
[27] **X. Huang**, Y. Fang, A. Noel, and N. Yang, "Membrane fusion-based transmitter model design for molecular communication systems," in *Proc. IEEE ICC 2021*, Montreal, Canada, Jun. 2021, pp. 1-6.
[28] **X. Huang**, Y. Fang, A. Noel, and N. Yang, "Membrane fusion-based transmitter design for static and diffusive mobile molecular communication systems," *IEEE Trans. Commun.*, vol. 70, no. 1, pp. 132-148, Jan. 2022.

Chapter 4 – Analysis of Receivers Covered by Heterogeneous Receptors

In Chapter 4, we consider an RX covered by heterogeneous receptors. Specifically, we model the receptors as absorbing patches (APs) and assume that there are multiple non-overlapping APs on the RX surface, where the APs can have different sizes and arbitrary but fixed locations. When molecules hit an AP, they are absorbed by the RX. Moreover, we consider two different TX models, namely, the point TX and the MF-based TX. In summary, our major contributions are as follows.

- We derive the expected molecule hitting rate, the expected fraction of absorbed molecules, and the expected asymptotic fraction of absorbed molecules as time approaches infinity at an RX with heterogeneous APs, which we refer to as AP-based RX. All expressions are functions of the sizes and locations of all APs.
- Aided by particle-based simulations (PBSs), we verify the accuracy of the derived analytical results. We also show that, for a given total area of the RX surface covered by APs, the expected number of absorbed molecules increases with the number of APs, but this increase becomes slower for larger numbers of APs.
- We compare three spatial distributions of the APs by examining the number of absorbed molecules at the RX. Specifically, we consider APs that are respectively evenly and

randomly distributed across the entire RX surface, and APs that are evenly distributed within a region of the RX surface. Our results show that evenly distributed APs across the entire RX surface result in a larger number of absorbed molecules than the other two distributions.

The results in this chapter have been presented in [29, 30], which are listed as
[29] **X. Huang**, Y. Fang, S. Johnston, M. Faria, N. Yang, and R. Schober, "Analysis of receiver covered by heterogeneous receptors in molecular communications," in *Proc. IEEE ICC 2022*, Seoul, South Korea, May 2022, pp. 1-6.
[30] **X. Huang**, Y. Fang, S. Johnson, M. Faria, N. Yang, and R. Schober, "Analysis of MC systems employing receivers covered by heterogeneous receptors," *IEEE Trans. Mol. Biol. Multi-Scale Commun.*, vol. 9, no. 1, pp. 63-78, Mar. 2023.

Chapter 5 – 1D Molecular Communication with Two Absorbing Receivers

In Chapter 5, we consider a one-dimensional (1D) environment where one TX communicates between two fully-absorbing RXs. Specifically, we consider two models. The first model considers that the TX impulsively releases molecules into the environment. The second model is built on the first model, where we perform parameter estimation in a noisy MC environment with the flow and molecular degradation. In this model, the TX continuously releases molecules and the parameter estimation is performed by using analytically derived expressions of CIR at two fully absorbing RXs. To reduce the impact of noisy molecules on the estimation, we propose a novel estimation method, namely, difference estimation (DE). In summary, our major contributions are as follows.

- We derive the exact closed-form expressions for the fraction of molecules absorbed at each RX in both models. In the first model, we also derive the molecule hitting rate and the asymptotic fraction of molecules absorbed as time approaches infinity at each RX with an impulse emission at the TX. In the second model, we derive the asymptotic expression for the number of absorbed molecules within a time interval at each RX after sufficient time has passed, when the TX emits molecules continuously.

- In the second model, we derive the Cramer-Rao lower bound (CRLB) on the variance of different parameters.

- Aided by PBSs, we verify our analytical results and show that DE attains the CRLB. In the second model, our numerical results show that the impact of noise on the performance of DE is much less than that on independent estimation of each RX, which demonstrates the superiority of DE in reducing the impact of noise.

The results in this chapter have been presented in [31, 32], which are listed as follows:

[31] **X. Huang**, Y. Fang, A. Noel, and N. Yang, "Channel characterisation for 1D molecular communication with two absorbing receivers," *IEEE Commun. Lett.*, vol. 24, no. 6, pp. 1150-1154, Jun. 2020.
[32] **X. Huang**, Y. Fang, A. Noel, and N. Yang, "Parameter estimation in a noisy 1D environment via two absorbing receivers," in *Proc. IEEE Globecom 2020*, Taipei, Taiwan (ROC), Dec. 2020, pp. 1-7.

Chapter 6 – Molecule Harvesting by Heterogeneous Receptors on Transmitters

In Chapter 6, we consider a spherical TX, whose membrane is covered by heterogeneous receptors that may have different sizes and arbitrary locations, and assume each receptor to be fully absorbing. Moreover, we model the transportation of molecules within the TX based on Chapter 3, where molecules are encapsulated within vesicles and later released from the TX through the fusion of the vesicle and the TX membrane. Instead of assuming an impulse of vesicles being released from the center of the TX as in Chapter 3, we consider the continuous generation of vesicles within the TX. Furthermore, we consider a transparent RX and investigate the CIR, where we take into account the fact that molecules may degrade when they propagate from the TX to the RX. The main contributions of this chapter can be summarised as follows.

- We derive the molecule release rate from the TX membrane for the case of a continuous generation of vesicles within the TX. We also derive the fraction of absorbed molecules at the TX and the probability that a released molecule is observed at the RX.
- PBSs are used to verify the accuracy of our expressions. Our numerical results reveal that the total number of molecules absorbed by the TX is not affected by the vesicle generation rate, while the peak received signal at the RX increases for larger vesicle generation rates.

The results in this chapter have been presented in [33], which are listed as follows:
[33] **X. Huang**, Y. Huang, M. Wen, N. Yang, and R. Schober, "Analysis of molecule harvesting by heterogeneous receptors on MC transmitters," submitted to *Proc. IEEE Globecom 2023*.

Chapter 2

Literature Review

In this chapter, we first review the very early and fundamental studies of MC. We then review some existing MC studies in the areas of TX model, RX model, co-existence of multiple RXs, mobile MC systems, parameter estimation, energy efficiency, interference in MC, synthetic biology in MC, and MC prototype. Finally, we summarise the limitations in these studies and briefly explain how we fill these gaps in the following chapters.

2.1 Early and Fundamental Studies

MC system was first proposed in [34] as a new interdisciplinary research area in nanotechnology, biotechnology, and communication technology. In [34], the authors summarised the key features of MC and compared them with traditional wireless communication. The authors also anticipated applications of MC in nanomachine communication, molecular computing, and drug/DNA delivery systems. In [35], the authors discussed the possibility of MC as a solution for nanoscale communication. According to the biological mechanisms of intracellular and intercellular communications, the authors firstly proposed the system components consisting of carrier molecules, transmitter nanomachines, receiver nanomachines, and propagation environment for carrier molecules. The authors also discussed the communication processes of MC that include encoding, sending, propagation, receiving, and decoding.

Several seminal studies, e.g., [36, 37, 38, 39], proposed MC networks based on biological mechanisms. In [36], the authors designed and empirically studied a molecular transport system that autonomously loads or unloads specified cargoes using DNA strand exchange and transports the loaded cargoes using the reverse geometry of microtubules mobility on kinesins. The authors also performed experiments to validate the cargo transported by a single microtubule. The authors in [37] focused on designing a communication interface using vesicles, where vesicles encapuslate information molecules emitted from the TX, are transported to receivers by a propagation environment, and secrete the information molecules into the receivers. In [38], the authors proposed an MC framework by using molecular motors and microtubules. Moreover, by exploiting the nature of cell-to-cell communication, the authors in [39] described

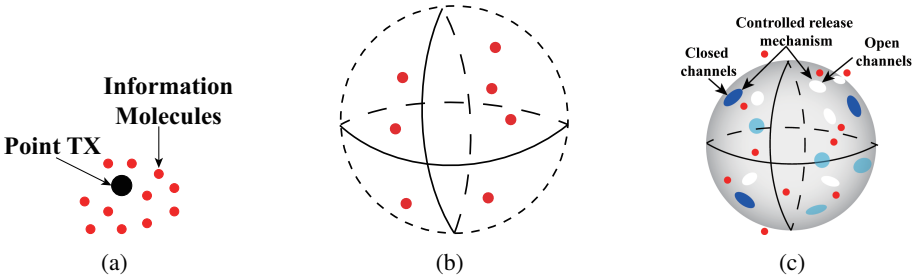

Figure 2.1: Illustration of TX models. (a) Point TX. (b) Volume TX. (c) TX with controlled release mechanism.

the design of an MC system based on intercellular calcium signalling networks and discussed possible functionalities, e.g., signal switching and aggregation, that may be achieved in the proposed network.

Other seminal studies, e.g., [40, 41, 42, 43], built the MC system from the perspective of information theory and provided theoretical analysis. [40] first investigated a 1D MC system from the perspective of information theory and derived the channel capacity. [41] extended the framework and results in [40] by considering that the information is encoded using a set of distinct molecules and derived the mutual information. In [42], the authors introduced an information theoretical approach for the MC system. By using the principle of mass action kinetics, the authors modelled the molecular delivery between two nanomachines and derived the closed-form expression for capacity of the channel. [43] designed two *in vitro* MC systems, i.e., one single-input-single-output (SISO) system and one single-input-multiple-output (SIMO). The authors investigated the probability of information molecules reaching the RX(s) and the rate of information of the systems. Several approaches, e.g., propagating information molecules, are investigated to maximise the probability and the rate.

These seminal studies are closely related to biological mechanisms and based on many assumptions, which lay the foundation for further investigation of practical TXs, practical RXs, co-existence of multiple RXs, mobile MC systems, parameter estimation, and energy efficiency in MC.

2.2 TX Models

In this section, we review some TX models that were proposed in previous studies. We divide all TX models into three categories, which are the point TXs, the volume TXs, and the TXs with controlled release mechanism, as shown in Fig. 2.1. We detail each category in the following.

2.2.1 Point TX

The point TX, as shown in Fig. 2.1(a), is the most widely applied TX model in the previous MC studies due to its simplicity [44]. It is commonly assumed that information molecules are produced from the point TX instantaneously and enter the propagation environment immediately. Compared to realistic scenarios, the point TX ignores TX properties including geometry, signalling pathways inside the TX, and the mechanism that controls the release of molecules.

2.2.2 Volume TX

Volume TX, as shown in Fig. 2.1(b), takes the TX geometry into account by assuming that the molecules are initially distributed over the TX volume. Moreover, the volume TX assumes that molecules are generated instantaneously and the TX membrane is transparent to the diffusion of molecules. According to [45], we define the CIR of an end-to-end channel as the probability of observation of one output molecule at time t at the RX when the TX is stimulated in an impulsive manner at time $t = 0$. We denote $h_{\mathrm{v}}(t)$ as the CIR for a volume TX and $h(t,r)$ as the CIR for a point TX. By assuming a uniform molecule distribution over the volume of the TX and independent movement of molecules, $h_{\mathrm{v}}(t)$ can be derived as

$$h_{\mathrm{v}}(t) = \frac{1}{V_{\mathrm{T}}} \int_{\vec{r}\in\mathcal{V}_{\mathrm{T}}} h\left(t, |\vec{r}-\vec{r}_0|\right) \mathrm{d}\vec{r}, \tag{2.1}$$

where V_{T} is the volume of the TX, $\mathcal{V}_{\mathrm{T}}$ represents the space within the TX, and $\vec{r}_0$ represents the location of the RX. In [46], the authors numerically solved (2.1) for a 3D spherical TX and both passive and fully absorbing RXs. [46] also obtained the closed-form expression of (2.1) in a 1D environment. Different from [46] that assumed a transparent TX membrane, [47] proposed a volume TX whose boundary reflects the emitted molecules and investigated the directivity gain achieved by the reflecting TX, where the directivity gain measures the degree to which the emitted molecules are concentrated in a single direction.

2.2.3 TX with Controlled Release Mechanism

Both point TX and volume TX consider a passive diffusion of molecules leaving the TX. Differently, some previous studies designed a certain release mechanism, e.g., ion channels, on the TX membrane that controls the release of molecules. The authors in [48] proposed an ion channel-based TX that takes both the TX geometry and the release mechanism into account. In particular, multiple ion channels are embedded on the TX membrane, whose opening and closing are controlled via voltage across the membrane or ligands. When ion channels open, molecules can leave the TX via passive diffusion. By assuming that the entire surface of the TX is covered by a large number of open ion channels and the signalling molecules diffuse with the same diffusion coefficient inside and outside the TX, the CIR was derived between

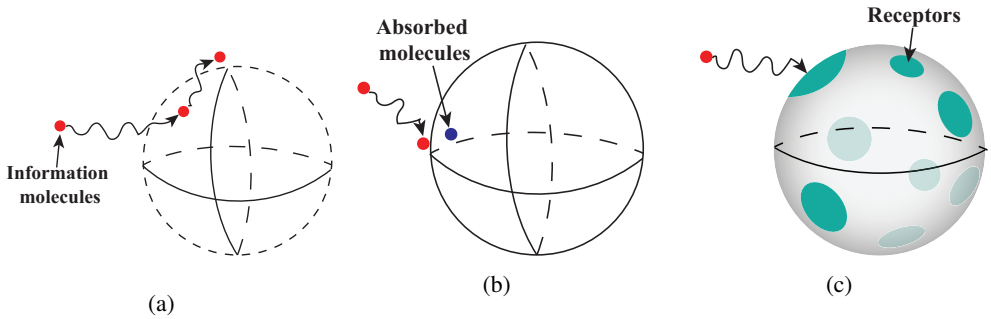

Figure 2.2: Illustration of three common RX models. (a) Transparent RX. (b) Fully absorbing RX. (c) Reactive RX.

the ion channel based TX and a transparent RX as [48, eq. (42)]

$$h(t) = \frac{r_{\mathrm{T}}}{r_0\sqrt{2D_A t}} \exp\left(-\frac{r_0^2 + r_{\mathrm{T}}^2}{4D_A t}\right) \sinh\left(\frac{r_0 r_{\mathrm{T}}}{2D_A t}\right), \tag{2.2}$$

where r_{T} is the radius of the TX, r_0 is the distance between the centres of the TX and RX, D_A is the diffusion coefficient of molecules, and $\sinh(\cdot)$ represents the hyperbolic sine function [49]. Furthermore, in [50], the authors considered using the permeability of the TX membrane to control the release of molecules. This consideration means that when molecules diffuse to the TX membrane, they can be released with a certain probability. In particular, the authors applied the transfer function approach to analyse the proposed model, where the permeability is accounted for by a feedback loop. The transfer function approach provides a much faster numerical evaluation than the PBSs.

2.3 RX Models

In this section, we review some existing RX models that were proposed in previous studies. In general, there are three common RX models, which are the transparent RX, fully absorbing RX, and reactive RX, as shown in Fig. 2.2. We detail each RX model in the following.

2.3.1 Transparent RX

The transparent RX, as shown in Fig. 2.2(a), is the most commonly considered RX model in previous studies, e.g., [51, 52, 53], which employs a passive reception mechanism. In particular, information molecules can enter and leave the RX via free diffusion. We note that the transparent RX is a good approximation when information molecules are small uncharged molecules such as ethanol, urea, and oxygen [54]. A transparent RX can also be a susceptometer as in [55], which serves as the RX that does not impede the movement of magnetic molecules. For transparent RXs, the CIR is the probability of observed molecules within the

RX. By considering an MC system with a point TX and a transparent RX, the CIR of the system is given by [56, eq. (4)]

$$h(t) = \frac{V_{\mathrm{R}}}{(4\pi D_A t)^{\frac{3}{2}}} \exp\left(-\frac{r_0^2}{4D_A t}\right), \tag{2.3}$$

where V_{R} is the volume of the RX. It is noted that (2.3) is accurate when the RX is sufficiently far away from the TX, i.e., r_0 is vary large relative to the RX radius r_{R}. Thus, it is reasonable to assume that the concentration of molecules at every point within the RX equals the concentration at the central point of the RX. If the RX is close to the TX, the uniform assumption of concentration does not hold. In this case, the authors in [52] derived an accurate expression for $h(t)$ for a transparent RX, which is given by [52, eq. (27)]

$$\begin{aligned} h(t) =& \frac{1}{2}\left[\mathrm{erf}\left(\frac{r_{\mathrm{R}}-r_0}{\sqrt{4D_A t}}\right) + \mathrm{erf}\left(\frac{r_{\mathrm{R}}+r_0}{\sqrt{4D_A t}}\right)\right] + \frac{1}{r_0}\sqrt{\frac{D_A t}{\pi}}\left[\exp\left(-\frac{(r_{\mathrm{R}}+r_0)^2}{4D_A t}\right)\right. \\ & \left. - \exp\left(-\frac{(r_{\mathrm{R}}-r_0)^2}{4D_A t}\right)\right], \end{aligned} \tag{2.4}$$

where $\mathrm{erf}(\cdot)$ denotes the error function [57]. We note that (2.3) provides an accurate approximation of (2.4) if $r_{\mathrm{R}} < 0.15 r_0$ [52].

2.3.2 Fully Absorbing RX

In biological systems, many practical RX surfaces may interact with the molecules of interest, e.g., by providing binding sites for absorption or other reactions [58]. Hence, the transparent RX model is over-simplified. One more practical RX model is fully absorbing RX [59, 60, 61], where the RX absorbs molecules as soon as they hit the RX surface. In general, we regard the number of absorbed molecules within a time interval as the received signal and the molecule hitting rate at the RX surface as the CIR for the fully absorbing RX. In [60], the authors derived CIR between a point TX and a fully absorbing RX as [60, eq. (22)]

$$h(t) = \frac{r_{\mathrm{R}}}{r_0}\frac{1}{\sqrt{4D_A t}}\frac{r_0 - r_{\mathrm{R}}}{t}\exp\left(-\frac{(r_0-r_{\mathrm{R}})^2}{4D_A t}\right). \tag{2.5}$$

Another quantity of interest is the fraction of absorbed molecules at the fully absorbing RX by time t, denoted by $H(t)$, which was derived as [60, eq. (23)]

$$H(t) = \frac{r_{\mathrm{R}}}{r_0}\mathrm{erfc}\left(\frac{r_0 - r_{\mathrm{R}}}{\sqrt{4D_A t}}\right), \tag{2.6}$$

where $\mathrm{erfc}(\cdot)$ is the complementary error function [57]. Moreover, in general, fully absorbing RX assumes that the RX surface is fully absorbing. An extension of this model was studied in

[61], where the authors considered that the RX surface is partially covered by fully absorbing receptor patches. In [59], the authors investigated the impact of molecule degradation on the absorption of molecules by the RX. Unlike previous studies focusing on a 3D environment, [62] considered a 1D environment with a uniform flow and derived a closed-form expression for the molecule hitting rate at the RX.

2.3.3 Reactive RX

Instead of being absorbed by the RX, the diffusive signalling molecules that reach the cell may reversibly react with receptors on the cell membrane and form ligand-receptor complex molecules. [63, 64] are initial studies that investigated the ligand-binding reception at the RX. In [63], the authors mathematically studied the noise at the reception when the ligand-binding is employed. The authors modelled the reception noise by using two different approaches, namely, through the ligand-reception kinetics and through the stochastic chemical kinetics. In [64], the authors showed that the ligand-binding reception can be interpreted as a low-pass filter. The authors also designed a whitening filter which is placed before the demodulator and detection blocks at the RX to suppress the noise effect of the ligand-binding reception. Unlike [63, 64] that the diffusion equation and the reaction equation are solved separately, [65] solved a coupled diffusion-reaction equation and modelled the ligand-receptor interaction as

$$A + \hat{R} \underset{k_\mathrm{b}}{\overset{k_\mathrm{f}}{\rightleftarrows}} \hat{C}, \tag{2.7}$$

where A represents information molecules of type A, $\hat{R}$ represents receptors, $\hat{C}$ represents ligand-receptor complex molecules, k_f $[\mathrm{molecule}^{-1}\mathrm{m}^3\mathrm{s}^{-1}]$ is the forward reaction rate constant, and k_b $[\mathrm{s}^{-1}]$ is the backward reaction rate constant. In [65], the authors regarded the probability of activated receptors at the RX as CIR and derived a closed-form expression for the CIR. An extension of [65] was made in [66], where the authors relaxed an assumption in [65] that the coverage area of each receptor should be small and solved an issue that the deviation between analytical results in [65] and simulation results increases with an increasing number of released molecules. To deal with these problems, the authors in [66] proposed a new boundary condition for the reversible reaction and developed an iterative approximation method to model the CIR. Furthermore, [63, 64, 65, 66, 67] did not consider the occupancy of receptors by molecules and ignored the competition of molecules when binding to the receptors. In [68], the authors proposed a determinstic model for receptor saturation in terms of a state-space description based on an eigenfunction expansion of Fick's diffusion equation. Compared to the RX of which the receptor occupancy is neglected, the authors showed that the saturation at the RX effectively reduces the peak-value of the received signal and accelerates the clearance of information molecules.

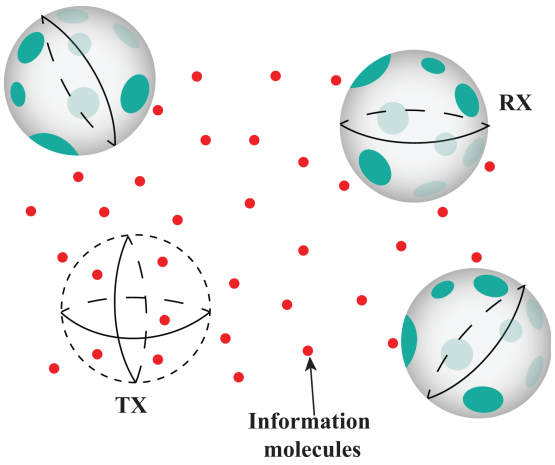

Figure 2.3: Molecular broadcast channel with one TX and three RXs.

2.4 Co-existence of Multiple RXs

By adopting concepts in the traditional wireless network, [69] first proposed the concept of molecular broadcast channel where a single TX transmits molecules to multiple RXs, as shown in Fig. 2.3. Similar to the cooperation among distributed sensors in the wireless network, the broadcast channel in MC systems can improve the reliability of transmission and enhance the cooperation between RXs. In [70], the authors applied multiple transparent RXs to cooperatively detect symbols. In particular, the RXs first make local hard decisions on the transmitted symbol and then report these decisions to a fusion centre. A suboptimal convex optimization problem is solved to determine the optimal decision thresholds that minimise the error probability of the proposed system. As the transparent RX does not impede the movement of molecules, one transparent RX does not impact received signals of other transparent RXs, and hence, the CIR between the TX and each RX can still be characterised by (2.3).

If we consider co-existence of multiple non-transparent RXs[1], molecules absorbed (reacted) by one non-transparent RX cannot be further absorbed (reacted) by other non-transparent RXs. Therefore, one non-transparent RX impacts received signals of other non-transparent RXs, and the CIR between the TX and each RX cannot be characterised by (2.5). Due to these factors, channel characterisation for multiple non-transparent RXs is quite complex. [71] is the first study that considered the co-existence of two fully absorbing RXs, where the authors determined the CIR between the TX and each RX by using PBSs. Then, the authors showed the impact of interfering RX on the target RX in terms of BER and capacity. Inspired by studies from chemical physics and biophysics, the authors in [72] proposed a novel simulation algorithm for MC system with multiple fully absorbing RXs. The proposed algorithm im-

[1]Non-transparent RXs include fully ansorbing RXs in Section 2.3.2 and reactive RXs in Section 2.3.3.

proves the accuracy of PBSs and leads to a more accurate absorption probability at each RX. In [73], the authors considered two fully absorbing RXs and utilized a trained artificial neural network to obtain the CIR between the TX and each RX. Notably, [71, 72, 73] did not provide closed-form expressions for the CIR. Instead, the authors in [74] considered a 1D environment with two fully absorbing RXs and derived the total fraction of molecules absorbed by both RXs. In [75], the authors derived the absorption probability at each RX in the form of Laplace transform by solving the partial derivative equation. In [76], the authors considered two fully absorbing RXs in a 3D environment. By quantifying the fraction of less absorbed molecules at the target RX due to the existence of the interfering RX, the authors derived the CIR at each RX.

2.5 Mobile MC Systems

Mobile TXs and RXs in MC systems have drawn considerable attention since they are required in many applications, e.g., targeted drug delivery [77], water pollution control, and human body monitoring. As the distance between the TX and the RX in such cases can be continuously changing while transmitting information, the channel is stochastic and it is challenging to perform statistical analysis of the received signal at the RX. The unknown statistical properties, e.g., mean and PMF, of the received signal bring difficulties in channel performance analysis. Motivated by this, some studies have investigated mobile MC and established a stochastic framework for channel modelling. In [78], the authors considered a mobile point TX and a mobile transparent RX, and derived closed-form expressions for the statistical properties, e.g., mean and the autocorrelation function (ACF), of the time-variant CIR. In [79], the authors considered a mobile point TX and a mobile fully absorbing RX, and derived the same statistical properties of CIR as in [78]. For bit transmission, [78] assumed that the distance between the TX and the RX is known when bits are transmitted, and [79] ignored the inter-symbol interference (ISI) when performing the error probability analysis. Moreover, in [80], the authors numerically derived the PMF of the received signal at a mobile transparent RX by using the generalised Gauss-Laguerre quadrature.

2.6 Parameter Estimation

Parameter estimation in MC systems refers to real-time monitoring or estimating pivotal environmental parameters, including the distance between the TX and the RX, the diffusion coefficient of molecules, the flow velocity in the MC environment, and others. Among these parameters, distance estimation is the most popular research area in previous studies. In particular, in the application of targeted drug delivery, distance estimation can be applied to localise the target site, e.g., a tumor, in the human body such that drugs are delivered to this site. More-

over, in biology, a cell can estimate the relative distance from an organism by producing a type of molecules to establish a chemical gradient [81]. Motivated by these applications, [82] proposed a two-way estimation method. In particular, the TX first sends molecules to the RX. When the RX detects the molecules, it immediately transmits a feedback signal. Distance can be estimated at the TX by measuring the sum of time required for this two-way transmission. In [83], the authors performed the distance estimation based on the peak number of observed molecules within the RX. This estimation scheme only needs one-way transmission and does not require synchronisation between the TX and RX. In [84], the authors considered molecule degradation and steady uniform flow in the environment. The authors derived the Cramer-Rao lower bound (CRLB) on the variance of the distance estimation error. The authors also designed a maximum likelihood (ML) distance estimator and showed that the accuracy of the estimator is very close to the CRLB.

Apart from distance estimation, estimating other parameters is also essential for MC applications. For example, the MC system can be deployed in a blood-vessel environment for human healthcare. In this application, estimating the blood flow velocity can help to measure the blood pressure. Also, estimating the diffusion coefficient of molecules can help to determine the blood composition and identify major changes in blood cell counts [85]. Motivated by these benefits, [86] investigated the joint parameter estimation and derived the Fisher information matrix such that the CRLB on the variance of each parameter estimation can be obtained. The authors also applied ML estimation and estimated the parameter numerically via either the Newton-Raphson method or an exhausive search if closed-form solutions do not exist. Moreover, [84, 86] applied CRLB to assess the performance of parameter estimation. However, for some discrete parameters, the CRLB does not exist. To overcome this limitation, [87] applied a more general Hammersley-Chapman-Robinson lower bound (HCRLB) and used this bound to evaluate the performance of estimating the number of released molecules from the TX. Unlike [82, 83, 84, 86, 87] that considered estimated parameters as constant values, [51] considered the estimated parameter, e.g., the number of released molecules from the TX, as a random variable (RV) with a given mean and variance. The authors assumed a pre-defined mean and estimated the variance by emitting multiple impulses of molecules. By asssuming that the molecule concentration is perfectly sensed over the entire environment, the variance is estimated via the ML estimation.

2.7 Energy Efficiency

One benefit of MC is that the free diffusion of molecules does not require the external energy such that the information can be transmitted from the TX to the RX with no energy cost. However, molecule generation and release from the TX is an energy consuming process in general. For example, in biology, cells produce signaling molecules by consuming adenosine

triphosphate (ATP) [54]. As nanomachines usually operate in resource-constrained environments, such as within living organisms, minimal energy consumption is crucial for prolonging their functionalities. Moreover, energy-efficient nanomachines can perform tasks effectively, as they are able to manage power consumption and distribute resources, resulting in improved overall performance. Motivated by this, some previous studies, e.g., [88, 89, 90, 91], proposed different methods to improve the energy efficiency of MC systems. In [88], the authors used bacteria as mobile relays and analyzed their information delivery energy efficiency. In [89, 90], the authors proposed a simultaneous molecular information and energy transfer technique to reduce the cost of molecule synthesis, where a relay can decode the received information as well as generate molecules for emission using absorbed molecules via chemical reactions. In [91], the authors developed a spherical molecule harvesting TX model where the membrane is equipped with receptors that can capture the information molecules. Specifically, the authors considered a homogeneous TX surface, where they assumed an infinite number of receptors cover the entire TX surface or a finite number of receptors with identical sizes are uniformly distributed over the TX surface.

2.8 Interference in MC

Molecule interference in MC is common and can directly impact the performance at the RX. Thus, it was widely investigated in previous studies. The first type of interference is noise molecules, which represents the molecules that are not released by the TX but originate from interfering natural or synthetic sources. As the RX cannot differentiate information molecules and noise molecules, the existence of noise molecules can cause significant errors in the signal detection at the RX. According to the law of rare events [92], the statistics of the observed noise molecules follows a Poisson distribution. The second type of interference in MC is inter-symbol interference (ISI), which refers to the overlap of multiple transmitted symbols caused by the late-arrival of molecules. In [93], the authors proposed an ISI-free coding scheme to increase the communication reliability while keeping a low complexity for encoding/decoding. The authors in [94] investigated ISI in synaptic channels and analyzed important parameters of the synaptic channel that are related to ISI. The third type of interference is multi-user interference, which occurs when the RX receives molecules from the TXs in other MC systems. In [95], the authors proposed Reed-Solomon (RS) error correction coding and a novel molecule modulating scheme that utilizes two types of information molecules to combat the multi-user interference. The authors in [96] introduced using the direction of releasing molecules for conveying information to mitigate the multi-user interference. The authors also proposed the binary direction shift keying modulation where the TX pumps molecules in two different directions.

2.9 Synthetic Biology in MC

The synthetic biology is an interdisciplinary field of engineering, which can program cell's genetic code, and thus provides a viable path to the practical realization of MC - enabled systems [97]. In particular, one of the latest frontiers in synthetic biology is the programming of DNA biological circuits, which modifies the predefined parts of DNA into functional genes that regulate the form of proteins. Given this, the cells can be programmed as TXs and RXs with specific functions. The authors in [98] focused on theoretically modelling a minimal subset of biological circuits necessary to an MC system. In particular, the system model was presented based on transfer functions, and the analytical expressions for signal attenuation and delay were derived. Inspired by the analog information processing in biochemical reactions, the authors in [99] developed an analog soft decoder for MC based biological circuits and discussed the most widely recognised noise models applied to this system. The authors also compared the biochemical simulation results with the performance of the system in different noise scenarios. In [100], the authors applied the concept of MC to study the potential of cell metabolism and its regulation to control the engineered cells from the external environment. The authors also used the metabolic simulation technique to derive an upper bound of the information theoretic mutual information.

2.10 MC Prototype/Testbed

In addition to theoretical studies that focus on analysis in MC systems, some studies developed MC prototypes to demonstrate the feasibility of applying chemical signals in reality. In [101], the authors proposed a tabletop MC system that is capable of transmitting short text messages over the free air. In particular, an electronically controlled spray was used as the TX, an alcohol metal-oxide sensor acts as the RX, and the open platform Arduino microcontrollers were used to control the TX and RX. We note that [101] only built a SISO MC platform. In [102], the authors developed a multiple-input-multiple-output (MIMO) MC platform, where the TX and the RX are equipped with multiple sprays and sensors to increase the data rate. Unlike [101, 102] with an open propagation environment of chemical signals, the authors in [103] designed an MC platform with a bounded propagation environment and showed that the propagation can be explained by using the advection-diffusion equation. [101, 102, 103] conducted the experiment of MC in a macroscale environment. In [104], the authors presented a biological platform that focuses on the microscale MC. Specifically, the authors used bacteria as TXs that export protons, i.e., signalling molecules, into the channel based on an external light stimulus. The protons can change the pH level of the environment, which can be detected with a pH sensor, i.e., the RX.

2.11 Limitations in Previous Studies

In this section, we list all limitations of previous studies in Sections 2.2-2.7 and briefly explained how the gaps will be filled in the following chapters.

In Section 2.2, for the mechanisms that control the release of molecules, [48, 50] only considered using ion-channels or permeability of the membrane, and none of them considered a chemical reaction-driven process for molecule release. In Chapter 3, we propose a novel TX model that uses fusion between a vesicle generated within the TX and the TX membrane to release molecules encapsulated within the vesicle.

In Section 2.3, for fully absorbing RXs and reactive RXs, previous studies, e.g., [61, 65], assumed an infinite number of receptors covering the entire RX surface or finite receptors with identical sizes that are uniformly distributed over the RX surface. In general, receptors on the RX surface may have different sizes and arbitrary locations. For example, in nature, receptors tend to form clusters on the RX surface at specific locations [105]. Since a given ligand can activate all receptors within a cluster, the cluster can be regarded as a single larger receptor. To fill this gap, in Chapter 4, we consider a RX covered by multiple non-overlapping heterogeneous receptors that can have different sizes and arbitrary but fixed locations.

In Section 2.4, for the co-existence of multiple non-transparent RXs, most previous studies, e.g., [71, 72, 73], did not provide closed-form expressions for the CIR. [74] only derived the total number of absorbed molecules by two RXs. [75] derived the absorption probability at each RX in a 1D environment, but its expression is in the form of Laplace transform, while the authors did not provide the expression in the time domain. Also, [75] did not consider molecular degradation in the environment. [76] derived the fraction of molecules absorbed at each RX in a 3D environment with two fully absorbing RXs. However, this derivation is not applicable in a 1D environment, as we will show in Section 5.6.1. We note that a 1D environment is a good approximation for many practical biological channels such as capillaries, blood vessels, active transportation channels, and communication on bio-chips [106, 107]. Therefore, the 1D environment is worth of investigation and an exact closed-form expression for the fraction of molecules absorbed over time at each RX with the consideration of molecular degradation has not been derived yet for a 1D environment. In Chapter 5, we consider a 1D environment where one TX communicates between two fully absorbing RXs. We also consider molecular degradation in the environment and derive the exact closed-form expressions for the fraction of molecules absorbed at each RX. Notably, as shown in Appendix C.1, the mathematical complexity of our method in obtaining the Laplace transform expression is much lower than that in [75] by solving the partial derivative equation.

In Section 2.5, previous studies only considered a mobile ideal point TX, and none of them have considered stochastic channel modelling between a mobile non-ideal TX and a mobile non-transparent RX. Moreover, for the statistical analysis of received signal at the mobile RX,

previous studies only considered that molecules are impulsively released from the TX such that the distance between the RX and all molecules are the same when they are released. However, if we consider a continuous release of molecules from the mobile TX, the distance between the RX and each molecule when it is released is different, which brings difficulties for the statistical analysis of the received signal. In Chapter 3, we considered a mobile MF-based TX and a mobile fully absorbing RX, and statistically analyse the distribution of received signal when molecules are continuously released from the MF-based TX.

In Section 2.6, previous studies only performed the estimation by using a single RX, and none of them considered using the received signals at multiple RXs to estimate the environmental parameters. In Chapter 5, we, for the first time, perform parameter estimation by using analytically derived expressions of the number of absorbed molecules at two fully absorbing RXs.

In Section 2.7, [91] considered a homogeneous TX surface, where the authors assumed that an infinite number of receptors cover the entire TX surface or a finite number of receptors with identical sizes are uniformly distributed over the TX surface. However, the analysis in [91] may become inaccurate in practice as the receptors on the TX surface may have different sizes and arbitrary locations. Therefore, in Chapter 6, we consider a spherical TX, whose membrane is covered by heterogeneous receptors that may have different sizes and arbitrary locations. We also evaluate the amount of energy saved and the received signal at the RX in terms of distributions of harvesting receptors on the TX membrane.

In Section 2.9, [98] described essential functional blocks of an end-to-end MC system from molecule production at the TX to the output transcription activation, and [99] analysed this system in different noise scenarios. Both [98, 99] and our research in Chapter 3, Chapter 4, and Chapter 6 aim at realising practical TXs and RXs, whose ideas are motivated by essential characteristics of biological cells. However, [98] only used transfer functions to characterise each block and there are no closed-form analytical expressions to describe the whole process in the time domain. Also, the authors did not consider the molecule propagation within the TX, the surface distribution of receptors at the RX, and molecule harvesting at the TX. We note that molecule movement within the TX, receptor distribution on the RX, and molecule harvesting are all fundamental properties of cells, and these factors can influence the received signals at the RX. Therefore, they are worth studying. In Chapter 3, we model the process of molecules released from the TX, including the diffusion of molecules within the TX. In Chapter 4, we consider a heterogeneous distribution of receptors on the RX surface. In Chapter 6, we investigate the harvest of molecules by the TX.

Chapter 3

Membrane Fusion-Based Transmitter Design

3.1 Introduction

In nature, exocytosis is a form of active transport in which a cell transports molecules out of the cell by secreting them through an energy-dependent process [108]. Exocytosis is common for cells because many chemical substances are large molecules, e.g., neurotransmitters and proteins, and cannot pass through the cell membrane by passive means [109]. In exocytosis, vesicles are carried to the cell membrane to secrete their contents into the extracellular environment. This secretion is performed by the MF process that fuses the vesicle with the cell membrane. When the vesicle moves close to the cell membrane, the v-SNARE proteins on the vesicle membrane bind to the t-SNARE proteins on the cell membrane, which generates the *trans*-SNARE complexes that catalyze MF [110]. Unlike the ideal point TX, exocytosis is an existing biological process and constrains the perfect release of molecules. Moreover, a TX model that is designed based on the exocytosis process has many applications in both natural and synthetic MC systems. The applications of the TX model in the natural MC system include facilitating the communication between cells by releasing signalling molecules, modelling the transportation process of hormones insulin and glucagon from the pancreas to control the glucose concentration in the blood, and investigating the process of removing toxins or waste products from the cell's interior to maintain homeostasis [111]. As the TX model captures some basic functions of the cell, it can be designed by modifying biological cells [25], which improves the degree of biocompatibility for the TX model in the human body for targeted drug delivery. Specifically, drug molecules are stored within the extracellular vesicles that are released from the MF-based TX by the exocytosis process [112]. Therefore, a TX that uses MF to release molecules merits investigation.

In this chapter, we propose a novel TX model in a 3D environment, namely the MF-based TX, which uses fusion between a vesicle generated within the TX and the TX membrane to release molecules encapsulated within the vesicle. By considering a fully absorbing RX that

absorbs molecules once they hit the RX surface, we investigate the end-to-end CIR between the MF-based TX and the RX in two scenarios: 1) A static TX and a static RX, and 2) a diffusion-based mobile TX and a diffusion-based mobile RX, where the CIR is the molecule hitting rate at the RX when an impulse of vesicles are released from the TX's centre [45]. Moreover, we consider a sequence of bits transmitted from the TX to the RX and investigate the error probability at the RX for both scenarios. For the mobile scenario, the distance between the TX and RX constantly changes during the non-instantaneous molecule release process such that the statistical analysis of the received signal at the mobile RX is more challenging than that in the instantaneous molecule release process. To tackle this challenge, we propose a novel method that divides the molecule release process into multiple intervals to calculate the PMF of the number of absorbed molecules. In summary, our major contributions are as follows:

1) We derive the time-varying molecule release rate and the fraction of molecules released from the TX by a given time.

2) For the static scenario, we derive the end-to-end i) molecule hitting rate, ii) the fraction of molecules absorbed, and iii) the asymptotic fraction of molecules absorbed at the RX due to the MF-based TX as time approaches infinity. For the mobile scenario, we derive the expected end-to-end molecule hitting rate at the mobile RX.

3) By considering a sequence of bits transmitted from the TX and a threshold detector at the RX, we calculate the average BER for the static and mobile scenarios. To derive the average BER in the mobile scenario, we also derive the PMF for the number of molecules absorbed at the mobile RX.

4) We propose a simulation framework for the MF-based TX model to simulate the diffusion and fusion of vesicles within the TX. In this simulation framework, the release point on the TX membrane and the release time of each molecule are determined.

Aided by the proposed simulation framework, we demonstrate the accuracy of our analytical derivations. Our numerical results show that a low MF probability or low vesicle mobility slows the release of molecules from the TX, increases the time to reach the peak molecule release rate, and reduces the end-to-end molecule hitting rate at the RX. Moreover, numerical results show the difference between the MF-based TX and an ideal point TX from the perspective of ISI. For the ideal point TX, ISI is only caused by the diffusion of molecules in the propagation environment. For the MF-based TX, ISI can also be introduced by signalling pathways inside the TX.

The rest of this chapter is organised as follows. In Section 3.2, we introduce the system model. In Section 3.3, we derive the release rate and fraction of molecules released from the TX. We also derive the end-to-end hitting rate, fraction of molecules absorbed, and asymptotic

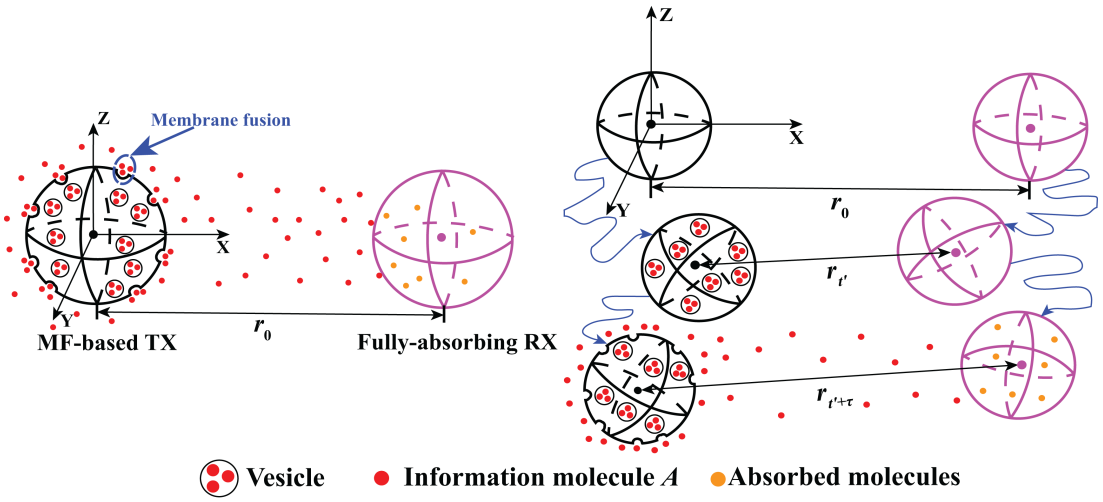

(a) Static TX and RX (b) Diffusive mobile TX and RX

Figure 3.1: Illustration of the system model where one MF-based TX communicates with one fully absorbing RX in a 3D environment. (a): Static TX and RX with fixed TX-RX distance. (b): Diffusive mobile TX and RX with the changing TX-RX distance over time.

fraction of molecules absorbed at the RX for the static scenario. In Section 3.4, we derive the expected end-to-end hitting rate for the mobile scenario. In Section 3.5, we derive the average BER for both scenarios. For the mobile scenario, we also derive and verify the PMF of absorbed molecules. In Section 3.6, we propose a simulation framework for the MF-based TX. In Section 3.7, we discuss the numerical results, and conclusions are presented in Section 3.8.

3.2 System Model

In this chapter, we consider an unbounded 3D environment where an MF-based TX communicates with a fully absorbing RX, as depicted in Fig. 3.1. We investigate two scenarios: 1) A static TX and a static RX, and 2) a diffusive mobile TX and a diffusive mobile RX, as depicted in Figs. 3.1(a) and 3.1(b), respectively. Both TX and RX are spheres with radius r_{T} and r_{R}, respectively. We assume that the propagation environment outside the spherical TX and RX is the fluid medium with uniform temperature and viscosity. Once information molecules A are released from the TX, they diffuse randomly with a constant diffusion coefficient D_A. Moreover, we consider unimolecular degradation in the propagation environment, where type A molecules can degrade into type $\hat{A}$ molecules that cannot be identified by the RX, i.e., $A \xrightarrow{k_{\mathrm{d}}} \hat{A}$ [113, Ch. 9], and k_{d} $\left[\mathrm{s}^{-1}\right]$ is the rate constant of degradation. In addition, we model the RX as a fully absorbing RX by which molecules A are absorbed once they hit the RX surface.

3.2.1 MF-based TX Model

We assume that the spherical TX releases molecules from its outer membrane after fusion between the membrane and vesicles. Each vesicle stores and transports η type A molecules. We consider that the TX is filled with the fluid medium that has uniform temperature and viscosity. Generally, vesicles can diffuse in the fluid medium based on the experiment in [114] or can be actively transported along microtubules by motor proteins [115]. In this chapter, we focus on the diffusion of vesicles. We assume that a vesicle cluster [116] exists within the TX. Vesicle clustering is a biological phenomenon observed in the presynaptic neuron, where vesicles can form clusters to sustain a high release rate of neurotransmitters. Vesicles can be released from the cluster via dephosphorylation [117]. Since we assume that the size of a vesicle [118] is relatively small compared to the size of the TX, we mathematically model the vesicle release process as an instantaneous release from a point within the TX. Once vesicles are released, they diffuse randomly with a constant diffusion coefficient D_{v}. According to [110], the natural fusion of a vesicle and the cell membrane can be considered as two steps: 1) v-SNARE proteins ($\mathrm{S_v}$) on the vesicle membrane bind to t-SNARE proteins ($\mathrm{S_t}$) on the cell membrane to generate *trans*-SNARE complexes ($\mathrm{S_c}$), and 2) $\mathrm{S_c}$ catalyzes the fusion of vesicular and cell membranes. For tractability, we apply the following main assumptions to the TX model:

A1) Vesicles are released from the TX's centre. This assumption ensures that molecules are uniformly released from the TX membrane. Considering vesicles released from any point within the TX is an interesting topic for future work.

A2) The interaction between $\mathrm{S_v}$ and $\mathrm{S_t}$ is modelled as the irreversible reaction $\mathrm{S_v} + \mathrm{S_t} \rightarrow \mathrm{S_c}$, which indicates that we only focus on the forward reaction between $\mathrm{S_v}$ and $\mathrm{S_t}$. The backward reaction for the disassembly of $\mathrm{S_c}$ occurs after MF, wherein the free $\mathrm{S_v}$ and $\mathrm{S_t}$ are used for the subsequent rounds of transport [119]. This is beyond the scope of our system model. After $\mathrm{S_c}$ is generated, it catalyzes MF, which is $\mathrm{S_c} \rightarrow$ MF [120]. Here, we assume that the reaction rate of the catalysis is much faster than the reaction between $\mathrm{S_v}$ and $\mathrm{S_t}$. Then, we can simplify this reaction network by removing the intermediate product $\mathrm{S_c}$ and combining these two reactions [121], which is given by

$$\mathrm{S_v} + \mathrm{S_t} \xrightarrow{k_{\mathrm{f}}} \mathrm{MF}, \tag{3.1}$$

where k_{f} is the forward reaction rate constant in $\mu\mathrm{m/s}$.

A3) The membrane is fully covered by an infinite number of $\mathrm{S_t}$ and the occupancy of $\mathrm{S_t}$ by $\mathrm{S_v}$ is ignored. Assuming perfect receptor coverage and ignoring occupancy are for the sake of tractability and have been widely adopted in previous studies, e.g., [65, 122].

A4) Once molecules are released, the spherical TX is assumed to not hinder the random diffusion of molecules in the propagation environment, i.e, the TX is transparent to the diffusion of released molecules. [47] analyzed the hindrance of the TX membrane to the diffusion of molecules using simulation. The joint consideration of the hindrance of the TX membrane and the absorbing RX is cumbersome for theoretical analysis. We will investigate the impact of the TX membrane on molecule diffusion in the propagation environment in future work. In Fig. 3.7(b) and Table 3.4, we relax this assumption by treating the TX membrane as a reflecting boundary for molecules in the propagation environment and perform the corresponding PBSs [123]. Results indicate that an obvious deviation is caused only when the TX and RX are very close to each other.

Based on assumptions A2 and A3, if a vesicle hits the TX membrane, it fuses to the membrane with a probability of $k_{\mathrm{f}}\sqrt{\frac{\pi\Delta t}{D_{\mathrm{v}}}}$ during a time interval Δt [124]. We define this probability as the MF probability[1]. The equation of the MF probability is accurate if $k_{\mathrm{f}} \ll \sqrt{\frac{D_{\mathrm{v}}}{\pi\Delta t}}$. The MF probability is applied in the simulation process in Section 3.6. After MF, the type A molecules stored by the vesicle are instantaneously released into the propagation environment. The location and time for the occurrence of MF are the initial location and time for molecules to start moving in the propagation environment. We note that the time scale for the MF process is ignored since it is relatively small compared to the entire transmission process [125].

3.2.2 Transceiver Mobility

We consider the following two cases for TX and RX mobility:

3.2.2.1 Static MC

We choose the centre of the TX as the origin of the environment, as depicted in Fig. 3.1(a). The centre of the RX is distance r_0 away from the centre of the TX. We consider an impulse of N_{v} vesicles released within the TX at time $t = 0$. In this case, the channel response is time-invariant.

3.2.2.2 Mobile MC

We choose the centre of the TX at time $t = 0$ as the origin of the environment, as depicted in Fig. 3.1(b). The TX and RX start to diffuse randomly with constant diffusion coefficients D_{T} and D_{R}, respectively, from time $t = 0$, and the distance between their centres at $t = 0$ is r_0. Different from the static MC case, the channel response is time-variant such that the CIR

[1]Based on this definition, the MF-based TX can be regarded as a TX with a semi-permeable boundary as in [50]. We clarify that the major difference between our work and [50] is the method of analysis. The authors in [50] applied the transfer function approach to investigate the molecule concentration within the TX, while we focus on the end-to-end communication channel and derive analytical expressions for the CIR in this channel.

depends on the release time of vesicles. To ensure generality, we consider an impulse of $N_{\rm v}$ vesicles released within the TX at time t'. We further denote $r_{t'}$ as the distance between the centres of the TX and RX at time t'. In this model, we assume that the diffusion of vesicles is relative to the TX and remains symmetric.

3.2.3 Bit Transmission

We assume for both static and mobile scenarios that information transmitted from the TX to the RX is encoded into a sequence of binary bits with length Q. The sequence of binary bits is $\mathbf{b}_{1:Q} = [b_1, b_2, ...b_Q]$ and b_q is the qth bit. We denote $T_{\rm b}$ as the bit interval length. We assume that each bit is transmitted at the beginning of the current bit interval with probabilities $\Pr(b_q = 1) = P_1$ and $\Pr(b_q = 0) = P_0 = 1 - P_1$, where $\Pr(\cdot)$ denotes the probability. For the static scenario, we consider that b_1 is transmitted at time $t = 0$. For the mobile scenario, we consider that b_1 is transmitted at time t' such that the distance between the centres of the TX and RX is a random variable (RV) when b_1 is transmitted. We adopt ON/OFF keying for the modulation, which means that $N_{\rm v}$ vesicles are released from the TX's centre at the beginning of the bit interval to transmit bit 1 while no vesicle is released to transmit bit 0. We further assume that the TX and RX are perfectly synchronised since several practical synchronisation schemes for MC have been studied and proposed in [126]. For demodulation of b_q at the RX, we adopt a widely-investigated threshold detector that compares the number of molecules absorbed during the qth bit interval with a detection threshold [79]. In this chapter, we consider the threshold of the detector is fixed for simplicity. More complex detectors, e.g., an adaptive threshold detector, are summarised in [127].

3.3 Analysis of Channel Impulse Response for Static MC

In this section, we first derive the molecule release rate and the fraction of molecules released from the TX membrane due to the impulsive emission of vesicles from the TX's centre. We define the molecule release rate as the probability of one molecule being released during the time interval $[t, t + \delta t]$ from the TX membrane, when this molecule is released from the origin at time $t = 0$. Here, δt represents a very small value of time t. We then derive the molecule hitting rate at the RX when the TX releases molecules uniformly over the TX membrane. Using the previously-derived release rate and hitting rate, we finally derive the end-to-end i) molecule hitting rate, ii) fraction of molecules absorbed, and iii) the asymptotic fraction of molecules absorbed at the RX as $t \to \infty$ due to the impulsive emission of vesicles from the TX's centre. We define the molecule hitting rate and end-to-end molecule hitting rate as the probability of one molecule hitting the RX during the time interval $[t, t + \delta t]$ when this molecule is released from the TX membrane and TX's centre at time $t = 0$, respectively.

3.3.1 Release Rate from TX Membrane

As MF guarantees the release of molecules from vesicles to the propagation environment, the probability of releasing molecules equals the vesicle fusion probability. Thus, we need to obtain the distribution of vesicle concentration within the TX to derive the release rate from the TX membrane. In the spherical coordinate system, we denote $C(r,t)$, $0 \leq r \leq r_{\mathrm{T}}$, as the distribution of vesicle concentration at time t and distance r from the TX's centre. When an impulse of vesicles is released from the TX's centre at $t = 0$, the initial condition is expressed as [128, eq. 3(c)]

$$C(r, t \to 0) = \frac{1}{4\pi r^2}\delta(r), \tag{3.2}$$

where $\delta(\cdot)$ is the Dirac delta function. We then apply Fick's second equation to describe the diffusion of vesicles within the TX. In general, Fick's second equation is a spatially 3D partial differential equation. As we consider that vesicles are released from the TX's centre, the TX model is spherically symmetric such that the diffusion of vesicles is described as [129, eq. (2.7)]

$$D_{\mathrm{v}} \frac{\partial^2 \left(rC(r,t)\right)}{\partial r^2} = \frac{\partial \left(rC(r,t)\right)}{\partial t}. \tag{3.3}$$

Based on assumption A2, the boundary condition is described by the irreversible reaction given by (3.1), which can be characterised by the radiation boundary condition [130, eq. (3.25)]

$$-D_{\mathrm{v}} \frac{\partial C(r,t)}{\partial r}\Big|_{r=r_{\mathrm{T}}} = k_{\mathrm{f}} C(r_{\mathrm{T}}, t), \tag{3.4}$$

where the left-hand side represents the diffusion flux[2] over the TX membrane. Since the flux is in the positive radial direction, the right-hand side is positive. Negative sign on the right-hand side indicates that the condition is over the inner boundary.

Based on the initial condition in (3.2), Fick's second law in (3.3), and the boundary condition in (3.4), we derive the analytical expression for the molecule release rate from the TX membrane, denoted by $f_{\mathrm{r}}(t)$, in the following theorem:

Theorem 3.1. The molecule release rate from the TX membrane at time t is given by

$$f_{\mathrm{r}}(t) = \sum_{n=1}^{\infty} \frac{4 r_{\mathrm{T}}^2 k_{\mathrm{f}} \lambda_n^3}{2\lambda_n r_{\mathrm{T}} - \sin\left(2\lambda_n r_{\mathrm{T}}\right)} j_0(\lambda_n r_{\mathrm{T}}) \exp\left(-D_{\mathrm{v}} \lambda_n^2 t\right), \tag{3.5}$$

where $j_0(\cdot)$ is the zeroth order spherical Bessel function of the first type [131] and λ_n is ob-

[2]The diffusion flux $[\text{molecule} \cdot \text{m}^{-2} \cdot \text{s}^{-1}]$ is the rate of movement of molecules across a unit area in unit time [129].

tained by solving

$$-D_{\mathrm{v}}\lambda_n j_0'(\lambda_n r_{\mathrm{T}}) = k_{\mathrm{f}} j_0(\lambda_n r_{\mathrm{T}}), \tag{3.6}$$

with $j_0'(z) = \frac{\partial j_0(z)}{\partial z}$ and $n = 1, 2, \ldots$. In particular, (3.6) is directly obtained from the radiation boundary condition in (3.4) with eigenfunction $j_0(\lambda_n r_{\mathrm{T}})$ and discrete eigenvalue λ_n.

Proof: Please see Appendix A.1. ■

Remark 3.1. We note that (3.5) becomes accurate when n increases. We also note that the number n applied in (3.5) can be determined mathematically. We denote n^* as the maximum n applied in (3.5) and $f_{\mathrm{r},n}(t) = \frac{4r_{\mathrm{T}}^2 k_{\mathrm{f}} \lambda_n^3}{2\lambda_n r_{\mathrm{T}} - \sin(2\lambda_n r_{\mathrm{T}})} j_0(\lambda_n r_{\mathrm{T}}) \exp\left(-D_{\mathrm{v}}\lambda_n^2 t\right)$. When $n \geq n^*$, $f_{\mathrm{r},n}(t) = 0$. The value of n^* increases when t decreases. In this chapter, we choose $t = \hat{t} = 0.01$ s as a criterion to obtain n^*. Therefore, n^* is obtained by numerically finding the minimum n satisfying $f_{\mathrm{r},n}(\hat{t}) = 0$.

We denote $F_{\mathrm{r}}(t)$ as the fraction of molecules released by time t and obtain it via $F_{\mathrm{r}}(t) = \int_0^t f_{\mathrm{r}}(u)\mathrm{d}u$. We present $F_{\mathrm{r}}(t)$ in the following corollary:

Corollary 3.1. The fraction of molecules released from the TX by time t is given by

$$F_{\mathrm{r}}(t) = \sum_{n=1}^{\infty} \frac{4r_{\mathrm{T}}^2 k_{\mathrm{f}} \lambda_n j_0(\lambda_n r_{\mathrm{T}})}{D_{\mathrm{v}}\left(2\lambda_n r_{\mathrm{T}} - \sin(2\lambda_n r_{\mathrm{T}})\right)} \left(1 - \exp\left(-D_{\mathrm{v}}\lambda_n^2 t\right)\right). \tag{3.7}$$

As each molecule has the same probability to be released by time t, i.e., $F_{\mathrm{r}}(t)$, the number of molecules released by time t is $N_{\mathrm{v}}\eta F_{\mathrm{r}}(t)$.

3.3.2 Hitting Rate at RX with Uniform Release of Molecules

In this subsection, we derive the hitting rate when molecules are uniformly released from the TX membrane, i.e., ignoring the internal molecules' propagation within vesicles inside the TX and the TX's MF process. This hitting rate establishes the foundation for deriving the end-to-end molecule hitting rate at the RX surface in Section 3.3.3. We consider that molecules are initially uniformly distributed over the TX membrane and released simultaneously at $t = 0$. We denote Ω_{T} as the membrane area and $h_{\mathrm{u}}(t)$ as the hitting rate at the RX due to the uniform release of molecules. We clarify that uniformly-distributed molecules means that the likelihood of a molecule released from any point on the TX membrane is the same. We denote this probability by ρ, where we have $\rho = \left(4\pi r_{\mathrm{T}}^2\right)^{-1}$. We further consider an arbitrary point $\hat{\alpha}$ on the TX membrane. Based on [59, eq. (9)], the hitting rate of a molecule at the RX at time t when the molecule is released from the point $\hat{\alpha}$ at time $t = 0$, $h_{\hat{\alpha}}(t)$, is given by

$$h_{\hat{\alpha}}(t) = \frac{r_{\mathrm{R}}(r_{\hat{\alpha}} - r_{\mathrm{R}})}{r_{\hat{\alpha}}\sqrt{4\pi D_A t^3}} \exp\left(-\frac{(r_{\hat{\alpha}} - r_{\mathrm{R}})^2}{4D_A t} - k_{\mathrm{d}} t\right), \tag{3.8}$$

where $r_{\hat{\alpha}}$ is the distance between the point $\hat{\alpha}$ and the centre of the RX.

Given that molecules are distributed uniformly over the TX membrane, $h_{\mathrm{u}}(t)$ is obtained by taking the surface integral of $h_{\alpha}(t)$ over the spherical TX membrane. Using this method, we solve $h_{\mathrm{u}}(t)$ in the following lemma:

Lemma 3.1. The molecule hitting rate at the RX at time t when the TX uniformly releases molecules over the TX membrane at time $t = 0$ is given by

$$h_{\mathrm{u}}(t) = \frac{2\rho r_{\mathrm{T}} r_{\mathrm{R}}}{r_0}\sqrt{\frac{\pi D_A}{t}}\left[\exp\left(-\frac{\beta_1}{t} - k_{\mathrm{d}}t\right) - \exp\left(-\frac{\beta_2}{t} - k_{\mathrm{d}}t\right)\right], \tag{3.9}$$

where $\beta_1 = \frac{(r_{\mathrm{T}}+r_{\mathrm{R}})(r_{\mathrm{T}}+r_{\mathrm{R}}-2r_0)+r_0^2}{4D_A}$ and $\beta_2 = \frac{(r_{\mathrm{T}}-r_{\mathrm{R}})(r_{\mathrm{T}}-r_{\mathrm{R}}+2r_0)+r_0^2}{4D_A}$.

Proof: Please see Appendix A.2. ■

We denote $H_{\mathrm{u}}(t)$ as the fraction of molecules absorbed by time t when the TX uniformly releases molecules and obtain it via $H_{\mathrm{u}}(t) = \int_0^t h_{\mathrm{u}}(u)\mathrm{d}u$. We present $H_{\mathrm{u}}(t)$ in the following corollary:

Corollary 3.2. The fraction of molecules absorbed at the RX by time t when the TX uniformly releases molecules over the TX membrane at time $t = 0$ is given by

$$\begin{aligned} H_{\mathrm{u}}(t) = \frac{\rho r_{\mathrm{T}} r_{\mathrm{R}}\pi}{r_0}\sqrt{\frac{D_A}{k_{\mathrm{d}}}}\Bigg[&\exp\left(-2\sqrt{\beta_1 k_{\mathrm{d}}}\right)\mathrm{erfc}\left(\sqrt{\frac{\beta_1}{t}} - \sqrt{k_{\mathrm{d}}t}\right) - \exp\left(2\sqrt{\beta_1 k_{\mathrm{d}}}\right) \\ &\times\mathrm{erfc}\left(\sqrt{\frac{\beta_1}{t}} + \sqrt{k_{\mathrm{d}}t}\right) - \exp\left(-2\sqrt{\beta_2 k_{\mathrm{d}}}\right)\mathrm{erfc}\left(\sqrt{\frac{\beta_2}{t}} - \sqrt{k_{\mathrm{d}}t}\right) + \exp\left(2\sqrt{\beta_2 k_{\mathrm{d}}}\right) \\ &\times\mathrm{erfc}\left(\sqrt{\frac{\beta_2}{t}} + \sqrt{k_{\mathrm{d}}t}\right)\Bigg], \end{aligned} \tag{3.10}$$

where $\mathrm{erfc}(\cdot)$ is the complementary error function [57]

3.3.3 End-to-End Hitting Rate at the RX

We denote $h_{\mathrm{e}}(t)$ as the end-to-end molecule hitting rate at the RX when an impulse of vesicles is released from the TX's centre at time $t = 0$. The molecule release rate from the TX membrane at time u, $0 \le u \le t$, is given by (3.5), which is $f_{\mathrm{r}}(u)$. For molecules released at time u, the molecule hitting rate at the RX at time t is given by (3.9), which is $h_{\mathrm{u}}(t-u)$. Based on $f_{\mathrm{r}}(u)$ and $h_{\mathrm{u}}(t-u)$, $h_{\mathrm{e}}(t)$ is given by $h_{\mathrm{e}}(t) = \int_0^t h_{\mathrm{u}}(t-u)f_{\mathrm{r}}(u)\mathrm{d}u$. Applying (3.5) and (3.9) to this equation, we derive $h_{\mathrm{e}}(t)$ in the following theorem:

Theorem 3.2. The end-to-end molecule hitting rate at the RX at time t for an impulsive emis-

sion of vesicles from the TX's centre at time $t = 0$ is given by

$$h_{\mathrm{e}}(t) = \frac{8\rho r_{\mathrm{T}}^3 r_{\mathrm{R}} k_{\mathrm{f}} \sqrt{\pi D_A} \exp\left(-k_{\mathrm{d}} t\right)}{r_0} \sum_{n=1}^{\infty} \frac{\lambda_n^3 j_0\left(\lambda_n r_{\mathrm{T}}\right)}{2\lambda_n r_{\mathrm{T}} - \sin\left(2\lambda_n r_{\mathrm{T}}\right)} \left[\varepsilon(\beta_1, t) - \varepsilon(\beta_2, t)\right], \tag{3.11}$$

where $\varepsilon(\beta,t) = \int_0^t \frac{1}{\sqrt{t-u}} \exp\left(-\frac{\beta}{t-u} - (D_{\mathrm{v}}\lambda_n^2 - k_{\mathrm{d}})u\right) \mathrm{d}u$. $\varepsilon(\beta,t)$ can be calculated numerically using MATLAB or Mathematica, e.g., using the built-in function *integral* in MATLAB or the built-in function *NIntegrate* in Mathematica.

We denote $H_{\mathrm{e}}(t)$ as the end-to-end fraction of molecules absorbed at the RX by time t and obtain it via $H_{\mathrm{e}}(t) = \int_0^t h_{\mathrm{e}}(u)\mathrm{d}u = \int_0^t H_{\mathrm{u}}(t-u) f_{\mathrm{r}}(u)\mathrm{d}u$. We present $H_{\mathrm{e}}(t)$ in the following corollary:

Corollary 3.3. The end-to-end fraction of molecules absorbed at the RX by time t for an impulsive emission of vesicles from the TX's centre at time $t = 0$ is given by

$$H_{\mathrm{e}}(t) = \frac{4r_{\mathrm{T}}^3 r_{\mathrm{R}} k_{\mathrm{f}} \rho \pi}{r_0} \sqrt{\frac{D_A}{k_{\mathrm{d}}}} \sum_{n=1}^{\infty} \frac{\lambda_n^3 j_0(\lambda_n r_{\mathrm{T}})}{2\lambda_n r_{\mathrm{T}} - \sin(2\lambda_n r_{\mathrm{T}})} \left[\varepsilon_1(\beta_1,t) - \varepsilon_2(\beta_1,t) - \varepsilon_1(\beta_2,t) + \varepsilon_2(\beta_2,t)\right], \tag{3.12}$$

where $\varepsilon_i(\beta,t)$, $i = 1,2$, is given by

$$\varepsilon_i(\beta,t) = \int_0^t \exp\left((-1)^i 2\sqrt{\beta k_{\mathrm{d}}} - D_{\mathrm{v}}\lambda_n^2 u\right) \mathrm{erfc}\left(\sqrt{\frac{\beta}{t-u}} + (-1)^i \sqrt{k_{\mathrm{d}}(t-u)}\right) \mathrm{d}u. \tag{3.13}$$

We further denote $H_{\mathrm{e},\infty}$ as the end-to-end asymptotic fraction of molecules absorbed as $t \to \infty$. We present $H_{\mathrm{e},\infty}$ in the following corollary:

Corollary 3.4. As $t \to \infty$, the end-to-end asymptotic fraction of molecules absorbed at the RX for an impulsive emission of vesicles from the TX's centre at time $t = 0$ is given by

$$H_{\mathrm{e},\infty} = \frac{2r_{\mathrm{T}} r_{\mathrm{R}} \rho \pi}{r_0} \sqrt{\frac{D_A}{k_{\mathrm{d}}}} \left[\exp\left(-2\sqrt{\beta_1 k_{\mathrm{d}}}\right) - \exp\left(-2\sqrt{\beta_2 k_{\mathrm{d}}}\right)\right]. \tag{3.14}$$

Proof: Please see Appendix A.3. ■

Remark 3.2. Eq. (3.14) indicates that the end-to-end asymptotic fraction of molecules absorbed only depends on the size of the TX and RX, the distance between centres of the TX and RX, and the diffusion coefficient and rate constant of molecule degradation in the propagation environment. $H_{\mathrm{e},\infty}$ is *independent* of other TX properties, e.g., the forward reaction rate constant in MF and the vesicle diffusion coefficient. This is because, with sufficient time, all molecules are released from the TX.

3.4 Analysis of Expected CIR for Mobile MC

In this section, we consider the scenario that both the TX and RX are mobile using diffusion. Since the distance between the centres of the TX and RX is a RV, the CIR is time-variant and modelled as a stochastic process [78]. Hence, in this section we focus on the expected CIR, i.e., the mean of the CIR over the varying distance. We first derive the expected molecule hitting rate at the RX when the TX releases molecules uniformly over the TX membrane. Using this probability, we then derive the expected end-to-end molecule hitting rate at the RX due to an impulsive emission of vesicles from the TX's centre. For the mobile scenario, we define the expected hitting rate and expected end-to-end hitting rate as the probability of one molecule hitting the RX during the time interval $[t'+\tau, t'+\tau+\delta\tau]$, $\tau \geq 0$, when this molecule is released from the TX membrane and TX's centre at time t', respectively. Here, τ is a relative time of observing absorbed molecules at the RX for a fixed t' and $\delta\tau$ represents a very small value of time τ.

3.4.1 Expected Hitting Rate at Mobile RX with Uniform Release of Molecules

We denote $\xi(r_{t'}|r_0)$ as the probability density function (PDF) of $r_{t'}$, which is the distance between centres of the TX and RX at time t', given that the initial distance between the centres of the TX and RX is r_0 at $t=0$. The coordinates of the TX's centre and RX's centre at time t' are $[x_{\mathrm{T}}(t'), y_{\mathrm{T}}(t'), z_{\mathrm{T}}(t')]$ and $[x_{\mathrm{R}}(t'), y_{\mathrm{R}}(t'), z_{\mathrm{R}}(t')]$, respectively. As both TX and RX perform Brownian motion, the displacement of each coordinate follows a Gaussian distribution. $r_{t'}$ is calculated as $r_{t'} = \sqrt{(x_{\mathrm{T}}(t')-x_{\mathrm{R}}(t'))^2 + (y_{\mathrm{T}}(t')-y_{\mathrm{R}}(t'))^2 + (z_{\mathrm{T}}(t')-z_{\mathrm{R}}(t'))^2}$, where $x_{\mathrm{T}}(t') - x_{\mathrm{R}}(t')$, $y_{\mathrm{T}}(t')-y_{\mathrm{R}}(t')$, and $z_{\mathrm{T}}(t')-z_{\mathrm{R}}(t')$ follow the Gaussian distribution. Thus, $\frac{r_{t'}}{\sqrt{2D_1 t'}}$ follows a noncentral chi-squared distribution with three degrees of freedom [132], and $\xi(r_{t'}|r_0)$ is given by [79, eq. (8)]

$$\xi(r_{t'}|r_0) = \frac{r_{t'}^{\frac{3}{2}}}{2D_1 t' \sqrt{r_0}} \exp\left(-\frac{r_{t'}^2 + r_0^2}{4D_1 t'}\right) I_{\frac{1}{2}}\left(\frac{r_{t'} r_0}{2D_1 t'}\right), \tag{3.15}$$

where $D_1 = D_{\mathrm{T}} + D_{\mathrm{R}}$ and $I_{\frac{1}{2}}(\cdot)$ is the modified Bessel function of the first kind [130]. We note that D_{T}, D_{R}, and t' should not be very large. Otherwise, $r_{t'}$ may become less than $r_{\mathrm{T}} + r_{\mathrm{R}}$ such that the TX and RX overlap with each other.

We denote $h_{\mathrm{u,m}}(\tau, t')$ as the *expected* hitting rate at the mobile RX at time $t'+\tau$ when the mobile TX releases molecules uniformly over the TX membrane at time t'. To describe the relative motion between released molecules and the RX, we define an effective diffusion coefficient D_2 as $D_2 = D_{\mathrm{R}} + D_A$ [133]. By replacing r_0, t, and D_A in (3.9) with $r_{t'}$, τ, and D_2, respectively, we obtain the hitting rate at time $t'+\tau$, i.e., $h_{\mathrm{u}}(\tau)\big|_{r_0=r_{t'}, D_A=D_2}$, for a given $r_{t'}$. We note that $r_{t'}$ is a RV with the PDF given by (3.15). Hence, we obtain $h_{\mathrm{u,m}}(\tau, t')$ as

$h_{\mathrm{u,m}}(\tau,t') = \int_0^\infty \xi(r_{t'}|r_0) h_{\mathrm{u}}(\tau)\big|_{r_0=r_{t'},D_A=D_2} \mathrm{d}r_{t'}$ and present it in the following lemma:

Lemma 3.2. The expected molecule hitting rate at the mobile RX at time $t'+\tau$ when the mobile TX uniformly releases the molecules over the TX membrane at time t is given by

$$h_{\mathrm{u,m}}(\tau,t') = \frac{\rho r_{\mathrm{T}} r_{\mathrm{R}} D_2}{r_0}\sqrt{\frac{\pi}{D_1 t' + D_2\tau}}\exp\left(-\frac{r_0^2}{4(D_1t'+D_2\tau)}\right)\left\{\exp\left(-\frac{(r_{\mathrm{T}}+r_{\mathrm{R}})^2}{4(D_1t'+D_2\tau)}\right)\right.$$
$$\times\Big[\theta(r_{\mathrm{T}},\tau,t')\theta(r_{\mathrm{R}},\tau,t')\mathrm{erfc}\left(-\vartheta(r_{\mathrm{T}},\tau,t')-\vartheta(r_{\mathrm{R}},\tau,t')-\vartheta(\tau,t')\right)-\theta(-r_{\mathrm{T}},\tau,t')\theta(-r_{\mathrm{R}},\tau,t')$$
$$\times\mathrm{erfc}(\vartheta(\tau,t')-\vartheta(r_{\mathrm{T}},\tau,t')-\vartheta(r_{\mathrm{R}},\tau,t'))\Big]-\exp\left(-\frac{(r_{\mathrm{T}}-r_{\mathrm{R}})^2}{4(D_1t'+D_2\tau)}\right)[\theta(r_{\mathrm{R}},\tau,t')\theta(-r_{\mathrm{T}},\tau,t')$$
$$\times\mathrm{erfc}(-\vartheta(r_{\mathrm{R}},\tau,t')+\vartheta(r_{\mathrm{T}},\tau,t')-\vartheta(\tau,t'))-\theta(-r_{\mathrm{R}},\tau,t')\theta(r_{\mathrm{T}},\tau,t')\mathrm{erfc}\left(\vartheta(\tau,t')-\vartheta(r_{\mathrm{R}},\tau,t')\right.$$
$$\left.\left.+\vartheta(r_{\mathrm{T}},\tau,t'))\right]\right\}, \tag{3.16}$$

where $\theta(\zeta,\tau,t') = \exp\left(\frac{r_0\zeta}{2(D_1t'+D_2\tau)}\right)$, $\vartheta(\zeta,\tau,t') = \frac{\zeta}{2}\sqrt{\frac{D_1t'}{D_2\tau(D_1t'+D_2\tau)}}$, and $\vartheta(\tau,t') = \frac{r_0}{2}\sqrt{\frac{D_2\tau}{D_1t'(D_1t'+D_2\tau)}}$.

3.4.2 Expected End-to-End Hitting Rate at the Mobile RX

We denote $h_{\mathrm{e,m}}(\tau,t')$ as the *expected* end-to-end molecule hitting rate at the mobile RX at time $t'+\tau$ when an impulse of vesicles is released from the TX's centre at time t'. The molecule release rate from the TX at time $t'+u$, $0\le u\le\tau$, is given by (3.5), which is $f_{\mathrm{r}}(u)$. For molecules released at time $t'+u$, the expected hitting rate at time $t'+\tau$ at the RX is given by (3.16), which is $h_{\mathrm{u,m}}(\tau-u,t'+u)$. Based on that, $h_{\mathrm{e,m}}(\tau,t')$ is given by $h_{\mathrm{e,m}}(\tau,t') = \int_0^\tau f_{\mathrm{r}}(u)h_{\mathrm{u,m}}(\tau-u,t'+u)\mathrm{d}u$. Applying (3.5) and (3.16) to this equation, we derive $h_{\mathrm{e,m}}(\tau,t')$ in the following theorem:

Theorem 3.3. The expected end-to-end molecule hitting rate at the mobile RX at time $t'+\tau$ for an impulsive emission of vesicles from the mobile TX's centre at time t' is given by

$$h_{\mathrm{e,m}}(\tau,t') = \sum_{n=1}^{\infty}\frac{4r_{\mathrm{T}}^3 r_{\mathrm{R}}\rho D_2 k_{\mathrm{f}}\lambda_n^3\sqrt{\pi}j_0(\lambda_n r_{\mathrm{T}})}{r_0(2\lambda_n r_{\mathrm{T}}-\sin(2\lambda_n r_{\mathrm{T}}))}\left[\kappa\left((r_{\mathrm{T}}+r_{\mathrm{R}})^2-2r_0r_{\mathrm{T}}-2r_0r_{\mathrm{R}},r_{\mathrm{T}}+r_{\mathrm{R}},-1,\tau,t'\right)\right.$$
$$-\kappa((r_{\mathrm{T}}+r_{\mathrm{R}})^2+2r_0r_{\mathrm{T}}+2r_0r_{\mathrm{R}},r_{\mathrm{T}}+r_{\mathrm{R}},1,\tau,t')-\kappa((r_{\mathrm{T}}-r_{\mathrm{R}})^2-2r_0r_{\mathrm{R}}+2l_0r_{\mathrm{T}},r_{\mathrm{R}}-r_{\mathrm{T}},-1,\tau,t')$$
$$\left.+\kappa((r_{\mathrm{T}}-r_{\mathrm{R}})^2+2r_0r_{\mathrm{R}}-2r_0r_{\mathrm{T}},r_{\mathrm{R}}-r_{\mathrm{T}},1,\tau,t')\right], \tag{3.17}$$

where $\kappa(\zeta_1,\zeta_2,\zeta_3,\tau,t')$ is given by

$$\kappa(\zeta_1,\zeta_2,\zeta_3,\tau,t') = \int_0^{\tau} \frac{1}{\sqrt{\mu(\tau,t')+\nu u}} \exp\left(-\frac{r_0^2+\zeta_1}{4(\mu(\tau,t')+\nu u)} - k_{\mathrm{d}}\tau + \left(k_{\mathrm{d}} - D_{\mathrm{v}}\lambda_n^2\right) u\right)$$
$$\times \operatorname{erfc}\left(\frac{\zeta_3 r_0}{2}\sqrt{\frac{D_2(\tau-u)}{D_1(t'+u)(\mu(\tau,t')+\nu u)}} - \frac{\zeta_2}{2}\sqrt{\frac{D_1(t'+u)}{D_2(\tau-u)(\mu(\tau,t')-\nu u)}}\right) \mathrm{d}u, \qquad (3.18)$$

with $\mu(\tau,t') = D_1 t' + D_2\tau$ and $\nu = D_1 - D_2$.

Remark 3.3. The expected end-to-end fraction of molecules absorbed by time $t'+\tau$ at the mobile RX for an impulsive emission of vesicles from the mobile TX's centre at time t' is obtained from the integral of (3.17), wherein the double integral can be calculated using MATLAB or Mathematica.

3.5 Error Probability for Static and Mobile MC

In this section, we consider the transmission of a sequence of bits from the TX to the RX. For the static scenario, we calculate the average BER, following the formulation in [78] and similar studies. For the mobile scenario, we first calculate the PMF for the number of molecules absorbed within a bit interval. Based on the derived PMF, we then calculate the average BER in the mobile scenario.

3.5.1 Average BER for Static MC

Due to the delay of molecule transport, the RX may receive molecules released from the current and all previous bit intervals. According to (3.12), the fraction of molecules absorbed during the qth bit interval when vesicles for storing those molecules released at the beginning of the gth bit interval, $0 \le g \le q$, is expressed as $H_{\mathrm{e}}((q-g+1)T_{\mathrm{b}}) - H_{\mathrm{e}}((q-g)T_{\mathrm{b}})$, where T_{b} is the bit interval length. We denote $N_{q,g}$ as the number of molecules absorbed during the qth bit interval for transmitting b_g. As the diffusion of vesicles and released molecules are independent and molecules have the same probability to be absorbed, $N_{q,g}$ can be approximated as a Poisson RV when the number of emitted vesicles is large and the success probability $H_{\mathrm{e}}(t)$ is small [134], i.e., $N_{q,g} \sim b_g \mathrm{Poiss}\left(N_{\mathrm{v}}\eta\left(H_{\mathrm{e}}((q-g+1)T_{\mathrm{b}}) - H_{\mathrm{e}}((q-g)T_{\mathrm{b}})\right)\right)$. Here, $\mathrm{Poiss}(\cdot)$ refers to a Poisson distribution. This is because sufficient diversity in the vesicle fusion points over the TX membrane is required to match the derivation of the end-to-end channel that includes integration over the entire TX membrane. As the sum of independent Poisson RVs is also a Poisson RV, we model the total number of molecules absorbed during the qth bit interval, denoted by N_q, as

$$N_q \sim \mathrm{Poiss}(\chi), \qquad (3.19)$$

Table 3.1: R^2 for the CDF of N_q, where the total number of molecules emitted is $N_{\mathrm{v}}\eta = 1000$

N_{v}, η	10, 100	20, 50	50, 20	100, 10	200, 5	500, 2	1000, 1
R^2	0.9771	0.9913	0.9969	0.9962	0.9974	0.9957	0.9974

where $\chi = N_{\mathrm{v}}\eta \sum_{g=1}^{q} b_g \left(H_{\mathrm{e}}((q-g+1)T_{\mathrm{b}}) - H_{\mathrm{e}}((q-g)T_{\mathrm{b}})\right)$. Based on (3.19), the cumulative distribution function (CDF) of the Poisson RV N_q is written as

$$\Pr\left(N_q < \Psi | \mathbf{b}_{1:q}\right) = \sum_{\psi=0}^{\Psi-1} \frac{\chi^{\psi} \exp(-\chi)}{\psi!}. \tag{3.20}$$

In Table 3.1, we calculate the coefficient of determination [71], denoted by R^2, for the CDF of N_q, where we vary N_{v} and η and keep the total number of molecules emitted as 1000. We set $q = 1$, $D_{\mathrm{v}} = 18\ \mu\mathrm{m}^2/\mathrm{s}$, $k_{\mathrm{f}} = 30\ \mu\mathrm{m}/\mathrm{s}$, and $b_q = 1$. For other parameter values, please see Table 3.3. For the simulation details, please see Section 3.6. The R^2 is used to measure the preciseness between simulation and theoretical analysis. Specifically, R^2 is given by $R^2 = 1 - SS_{\mathrm{res}}/SS_{\mathrm{tot}}$, where SS_{res} is the sum of squared differences between the theoretical analysis and simulation, and SS_{tot} is the sum of squared differences between the simulation and its mean. Since $SS_{\mathrm{res}}/SS_{\mathrm{tot}}$ represents the fraction of variance unexplained, the closer the value of R^2 is to 1, the more accurate the theoretical analysis. In this table, we observe that the R^2 increases with an increase in the number of vesicles from 10 to 50, which indicates that the accuracy of (3.20) increases when the number of vesicles emitted increases. This is due to the fact that the Poisson approximation is impacted by two sets of trials, i.e., the number of emitted vesicles and molecules, and the approximation is more sensitive to the number of emitted vesicles since it determines the initialization of the emission of molecules. When N_{v} is larger than 50, we observe a small variation of R^2 for N_{v} from 50 to 1000. We further increase the number of realisations applied in Table 3.1 by ten times for the simulation when $N_{\mathrm{v}} = 10$ and $\eta = 100$, and obtain that $R^2 = 0.9771$. This indicates that the number of realisations applied for the simulation in Table 3.1 is sufficient.

We adopt a simple threshold detector, where N_q is compared with a detection threshold to demodulate b_q. We present the threshold detector as

$$\hat{b}_q = \begin{cases} 1, & \text{if } N_q \geq \Psi \\ 0, & \text{if } N_q < \Psi, \end{cases} \tag{3.21}$$

where $\hat{b}_q$ is the demodulated bit of b_q at the RX and Ψ is the detection threshold. Based on (3.20) and (3.21), the error probability of $\hat{b}_q$ for $b_q = 1$ and $b_q = 0$ are

$$\Pr\left(\hat{b}_q = 0 | b_q = 1, \mathbf{b}_{1:q-1}\right) = \Pr\left(N_q < \Psi | b_q = 1, \mathbf{b}_{1:q-1}\right) \tag{3.22}$$

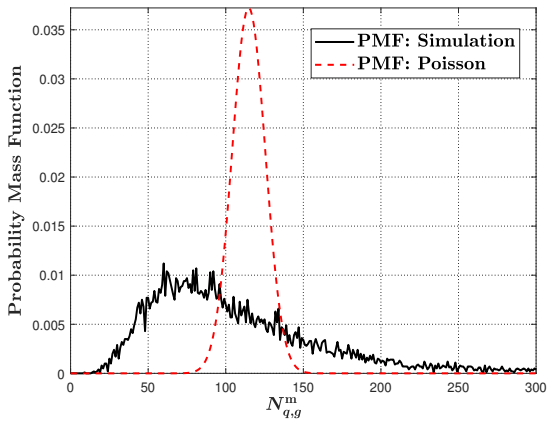

Figure 3.2: PMF of $N^{\mathrm{m}}_{q,g}$ plotted by simulation and Poisson distribution,where $q = g = 1$, $D_{\mathrm{v}} = 9\ \mu\mathrm{m}^2/\mathrm{s}$, $k_{\mathrm{f}} = 30\ \mu\mathrm{m}/\mathrm{s}$, and $D_{\mathrm{T}} = D_{\mathrm{R}} = 8\ \mu\mathrm{m}^2/\mathrm{s}$. For other parameter values, please see Table 3.3. For the simulation details, please see Section 3.6.

and

$$\Pr\left(\hat{b}_q = 1 | b_q = 0, \mathbf{b}_{1:q-1}\right) = 1 - \Pr\left(N_q < \Psi | b_q = 0, \mathbf{b}_{1:q-1}\right), \tag{3.23}$$

respectively. The BER of the qth bit, denoted by $\Phi_{\mathrm{s}}[q|\mathbf{b}_{1:q-1}]$, is given by

$$\Phi_{\mathrm{s}}[q|\mathbf{b}_{1:q-1}] = P_1 \Pr\left(\hat{b}_q = 0 | b_q = 1, \mathbf{b}_{1:q-1}\right) + P_0 \Pr\left(\hat{b}_q = 1 | b_q = 0, \mathbf{b}_{1:q-1}\right). \tag{3.24}$$

We denote $\overline{\Phi}_{\mathrm{s}}$ as the average BER over all realisations of $\mathbf{b}_{1:q-1}$ and all bits from 1 to Q for the static scenario. We present $\overline{\Phi}_{\mathrm{s}}$ as

$$\overline{\Phi}_{\mathrm{s}} = \frac{1}{Q} \sum_{q=1}^{Q} \frac{\sum_{\mathbf{b}_{1:q-1} \in \xi_q} \Phi_{\mathrm{s}}[q|\mathbf{b}_{1:q-1}]}{2^{q-1}}, \tag{3.25}$$

where ξ_q stands for all realisations of $\mathbf{b}_{1:q-1}$.

3.5.2 Average BER for Mobile MC

3.5.2.1 Statistical Analysis of Absorbed Molecules

We denote $N^{\mathrm{m}}_{q,g}$ as the number of molecules absorbed during the qth bit interval when vesicles that store these molecules are released at the beginning of the gth bit interval in the mobile scenario. Due to the distance between the centres of the TX and RX being a RV when releasing molecules, we clarify that $N^{\mathrm{m}}_{q,g}$ cannot be approximated as a Poisson RV as shown in Fig. 3.2. To obtain the accurate PMF for mobile MC, we divide the molecule release process into multiple intervals, detailed as follows.

To obtain the PMF of $N^{\mathrm{m}}_{q,g}$, we first define a release duration, denoted by $[t_g, t_{\mathrm{e},g}]$, of trans-

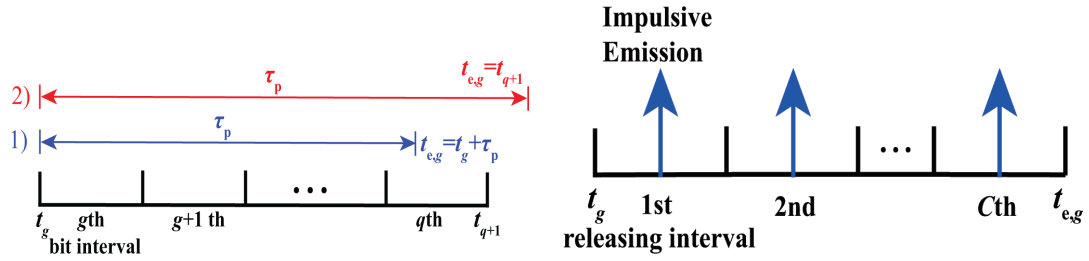

(a) Definition of the release duration (b) Division of the release duration

Figure 3.3: (a). Definition of the release duration $[t_g, t_{e,g}]$, where 1) $t_{e,g} = t_g + \tau_p$ if $t_g + \tau_p \leq t_{q+1}$ and 2) $t_{e,g} = t_{q+1}$ if $t_g + \tau_p \geq t_{q+1}$. (b). Dividing release duration $[t_g, t_{e,g}]$ into C release intervals, where the release of molecules during the cth release interval is assumed as an impulsive emission at time $\hat{\tau}_{g,c} = t_g + \frac{(2c-1)\Delta\tau}{2}$.

mitting b_g if $b_g = 1$ as shown in Fig. 3.3(a). We denote t_g as the start time of the gth bit interval, i.e., $t_g = t' + (g-1)T_b$, and $t_{e,g}$ as the end time of the release duration. We then denote τ_p as the period for all molecules released from the TX membrane, where τ_p is calculated by finding the minimum τ_p that satisfies $F_r(\tau_p) \geq 0.998$ when $n = 10000$ in (3.7). Here, we set the threshold at 0.998 such that the calculation of τ_p is sufficiently accurate. Since detection in the qth bit interval only depends on molecules released before or within the current bit interval, we have $t_{e,g} = t_g + \tau_p$ if $t_g + \tau_p \leq t_{q+1}$. Otherwise, $t_{e,g} = T_{q+1}$. We then consider the discretization of the release duration into C release intervals, as shown in Fig. 3.3(b). We denote $\Delta\tau$ as the length of each release interval, which is given by $\Delta\tau = \frac{t_{e,g}-t_g}{C}$. The expected number of molecules released within the cth interval is $N_v\eta\left(F_r(t_g + c\Delta\tau) - F_r(t_g + (c-1)\Delta\tau)\right)$. We denote $\hat{\tau}_{g,c}$ as the middle time of the cth release interval, which is obtained as $\hat{\tau}_{g,c} = t_g + \frac{(2c-1)\Delta\tau}{2}$. Since it is cumbersome to incorporate into the theoretical analysis of the precise distance between the TX and RX when each molecule is released, we assume that all molecules released within the cth release interval are combined into an impulsive emisson in the middle of the cth release interval, i.e., the number of molecules $N_v\eta\left(F_r(t_g + c\Delta\tau) - F_r(t_g + (c-1)\Delta\tau)\right)$ are impulsively released at time $\hat{\tau}_{g,c}$ from the TX membrane in the subsequent analysis.

We denote $r_{\hat{\tau}_{g,c}}$ as the distance between centres of the TX and RX at time $\hat{\tau}_{g,c}$. We further denote $\mathbf{r}_g$ as the vector that contains all $r_{\hat{\tau}_{g,c}}$ for c from 1 to C, i.e., $\mathbf{r}_g = [r_{\hat{\tau}_{g,1}}, r_{\hat{\tau}_{g,2}}, ..., r_{\hat{\tau}_{g,c}}, ..., r_{\hat{\tau}_{g,C}}]$. For a given $\mathbf{r}_g$, the expected number of molecules absorbed during the qth bit interval for transmitting b_g is

$$\psi^m_{q,g} = b_g \sum_{c=1}^{C} N_v\eta\left(F_r(t_g + c\Delta\tau) - F_r(t_g + (c-1)\Delta\tau)\right)\left(H_u(t_{q+1} - \hat{\tau}_{g,c}) - H_u(t_q - \hat{\tau}_{g,c})\right)\Big|_{r_0 = r_{\hat{\tau}_{g,c}}, D_A = D_2}. \tag{3.26}$$

For a given $\mathbf{r}_g$, we can approximate $N^{\mathrm{m}}_{q,g}$ as a Poisson RV that is given by

$$\Pr(N^{\mathrm{m}}_{q,g} = \Psi | \mathbf{r}_g) = \frac{\left(\chi^{\mathrm{m}}_{q,g}\right)^{\Psi} \exp\left(-\chi^{\mathrm{m}}_{q,g}\right)}{\Psi!}. \tag{3.27}$$

For the mobile TX and RX, each element in $\mathbf{r}_g$ is a RV, and we need to determine the joint PDF for each element in $\mathbf{r}_g$, denoted by $\xi(\mathbf{r}_g|r_0)$. By considering free diffusion as a memoryless process, i.e., the current state only depends on the previous one state, $g(\mathbf{r}_g|r_0)$ is given by [135, eq. (65)]

$$g(\mathbf{r}_g|r_0) = \prod_{c=1}^{C} g(r_{\hat{\tau}_{g,c}}|r_{\hat{\tau}_{g,c-1}}), \tag{3.28}$$

where $r_{\hat{\tau}_{g,0}} = r_0$.

Based on (3.27) and (3.28), we derive the PMF of $N^{\mathrm{m}}_{q,g}$ as

$$\Pr(N^{\mathrm{m}}_{q,g} = \Psi) = \int_0^{\infty} ... \int_0^{\infty} \Pr\left(N^{\mathrm{m}}_{q,g} = \Psi | \mathbf{l}_g\right) \xi(\mathbf{r}_g|r_0) \mathrm{d}r_{\hat{\tau}_{g,1}} ... \mathrm{d}r_{\hat{\tau}_{g,C}}. \tag{3.29}$$

We present $\Pr(N^{\mathrm{m}}_{q,g} = \Psi)$ in the following theorem:

Theorem 3.4. The PMF for the number of molecules absorbed within the qth bit interval when vesicles that store these molecules are released at the beginning of the gth bit interval, is given by

$$\Pr(N^{\mathrm{m}}_{q,g} = \Psi) = \frac{1}{\Psi!} \int_0^{\infty} ... \int_0^{\infty} \left(\chi^{\mathrm{m}}_{q,g}\right)^{\Psi} \exp\left(-\chi^{\mathrm{m}}_{q,g}\right) \prod_{c=1}^{C} \xi(r_{\hat{\tau}_{g,c}}|r_{\hat{\tau}_{g,c-1}}) \mathrm{d}r_{\hat{\tau}_{g,1}} ... \mathrm{d}r_{\hat{\tau}_{g,C}}, \tag{3.30}$$

where the multiple integral can be calculated numerically using the built-in function *NIntegrate* in Mathematica.

In Fig. 3.4, we plot the PMF of $N^{\mathrm{m}}_{q,g}$ using (3.30) and simulations to validate (3.30), where the number of intervals from 1 to 3 is adopted. We also set the length of the release duration to be equal to the bit interval T_{b}, i.e, $t_{\mathrm{e},g} - t_g = T_{\mathrm{b}}$. We further calculate the R-squared coefficient for (3.30) with varying C. The R-squared coefficient is 0.9741, 0.9709, and 0.8637 for C varying from 3 to 1. This indicates that the accuracy of (3.30) increases with an increase in the number of release intervals.

3.5.2.2 Average BER

We denote N^{m}_{q} as the number of molecules absorbed within the qth bit interval, which is given by $N^{\mathrm{m}}_{q} = \sum_{i=1}^{q} N^{\mathrm{m}}_{q,g}$. As in [136], we assume that T_{b} is sufficiently long such that elements in $\mathbf{N}^{\mathrm{m}}_{q} = [N^{\mathrm{m}}_{q,1}, N^{\mathrm{m}}_{q,2}, ..., N^{\mathrm{m}}_{q,q}]$ are independent of each other. Therefore, the PMF of N^{m}_{q} equals the

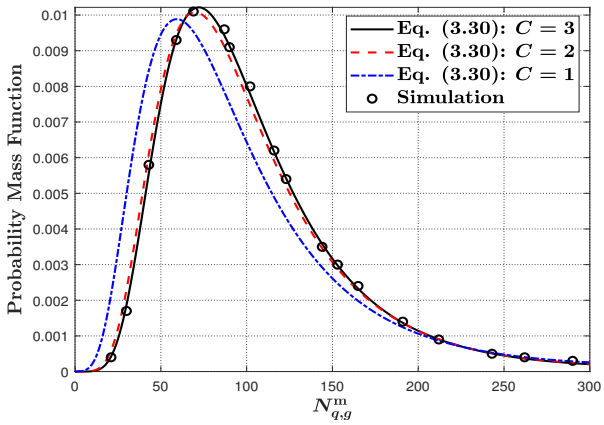

Figure 3.4: PMF of $N^{\mathrm{m}}_{q,g}$, where $D_{\mathrm{v}} = 50\ \mathrm{m}^2/\mathrm{s}$ $q = g = 1$, $k_{\mathrm{f}} = 30\ \mu\mathrm{m/s}$, and $D_{\mathrm{T}} = D_{\mathrm{R}} = 8\ \mu\mathrm{m}^2/\mathrm{s}$. For other parameter values, please see Table 3.3. For the simulation details, please see Section 3.6.

Table 3.2: R^2 for the CDF of N^{m}_q, where $N_{\mathrm{v}} = 200$

η	5	10	20	30	40	50
R^2	0.999	0.9988	0.9967	0.9965	0.9503	0.8415

convolution of the PMF of each element in $\mathbf{N}^{\mathrm{m}}_q$ [137]. We consider a vector $\hat{\mathbf{g}} = [\hat{g}_1, \hat{g}_2, ..., \hat{g}_{\Gamma}]$, where $\hat{g}_1 < \hat{g}_2 < ... < \hat{g}_{\Gamma}$, as a subset of vector $[1, 2, ..., q]$, where $\hat{\mathbf{g}}$ contains all subscripts of bit 1 for a given bit sequence $\mathbf{b}_{1:q}$, i.e., $b_{\hat{g}_1} = b_{\hat{g}_2} = ... = b_{\hat{g}_{\Gamma}} = 1$. Thus, we express the PMF of N^{m}_q as

$$\Pr\left(N^{\mathrm{m}}_q = \Psi | \mathbf{b}_{1:q}\right) = \left\{\Pr\left(N^{\mathrm{m}}_{q,\hat{g}_1} = 0 : \Psi\right) * \Pr\left(N^{\mathrm{m}}_{q,\hat{g}_2} = 0 : \Psi\right) * ... * \Pr\left(N^{\mathrm{m}}_{q,\hat{g}_{\Gamma}} = 0 : \Psi\right)\right\}[\Psi + 1], \tag{3.31}$$

where $\Pr\left(N^{\mathrm{m}}_{q,\hat{g}_\gamma} = 0 : \Psi\right) = \left[\Pr\left(N^{\mathrm{m}}_{q,\hat{g}_\gamma} = 0\right), \Pr\left(N^{\mathrm{m}}_{q,\hat{g}_\gamma} = 1\right), ..., \Pr\left(N^{\mathrm{m}}_{q,\hat{g}_\gamma} = \Psi\right)\right]$ with each element given by (3.30) and $\{\cdot\}[\Psi + 1]$ represents the $(\Psi + 1)$th element in $\{\cdot\}$. The CDF of N^{m}_q is given as $\Pr\left(N^{\mathrm{m}}_q < \Psi | \mathbf{b}_{1:q}\right) = \sum_{\psi=0}^{\Psi-1} \Pr\left(N^{\mathrm{m}}_q = \psi | \mathbf{b}_{1:q}\right)$.

In Table 3.2, we calculate the R^2 for the CDF of N^{m}_q, where we vary η and set $N_{\mathrm{v}} = 200$, $q = 1$, $D_{\mathrm{v}} = 50\ \mu\mathrm{m}^2/\mathrm{s}$, $k_{\mathrm{f}} = 30\ \mu\mathrm{m/s}$, $D_{\mathrm{T}} = D_{\mathrm{R}} = 8\ \mu\mathrm{m}^2/\mathrm{s}$, and $C = 3$. For other parameter values, please see Table 3.3. We observe that the R^2 decreases with an increase in η when N_{v} is fixed, which indicates that the accuracy of the theoretical analysis for the CDF of N^{m}_q decreases with the increase in the number of stored molecules in each vesicle. This is caused by the assumption that all molecules released within the release interval are combined into an impulsive emission. When η increases, the number of molecules in each release interval increases such that the inaccuracy of this assumption increases. One method to reduce this inaccuracy is increasing the number of release intervals, which incurs an increase in computational complexity.

By adopting the same detection criterion as in (3.21), except replacing N_q with N_q^{m}, we derive the error probability of $\hat{b}_q$ for $b_q = 1$ and $b_q = 0$ for the mobile scenario, denoted by $\Pr_{\mathrm{m}}\left(\hat{b}_q = 0 | b_q = 1, \mathbf{b}_{1:q-1}\right)$ and $\Pr_{\mathrm{m}}\left(\hat{b}_q = 1 | \hat{b}_q = 0, \mathbf{b}_{1:q-1}\right)$, as

$$\Pr_{\mathrm{m}}\left(\hat{b}_q = 0 | b_q = 1, \mathbf{b}_{1:q-1}\right) = \Pr\left(N_q^{\mathrm{m}} < \Psi | b_q = 1, \mathbf{b}_{1:q-1}\right) \tag{3.32}$$

and

$$\Pr_{\mathrm{m}}\left(\hat{b}_q = 1 | b_q = 0, \mathbf{b}_{1:q-1}\right) = 1 - \Pr\left(N_q^{\mathrm{m}} < \Psi | b_q = 0, \mathbf{b}_{1:q-1}\right), \tag{3.33}$$

respectively. The BER of the qth bit, denoted by $\Phi_{\mathrm{m}}[q|\mathbf{b}_{1:q-1}]$, is given by

$$\Phi_{\mathrm{m}}[q|\mathbf{b}_{1:q-1}] = P_1 \Pr_{\mathrm{m}}\left(\hat{b}_q = 0 | b_q = 1, \mathbf{b}_{1:q-1}\right) + P_0 \Pr_{\mathrm{m}}\left(\hat{b}_q = 1 | b_q = 0, \mathbf{b}_{1:q-1}\right). \tag{3.34}$$

We denote Φ_{m} as the average BER over all realisations of $\mathbf{b}_{1:q-1}$ and all bits from 1 to Q. $\overline{\Phi}_{\mathrm{m}}$ is obtained as

$$\overline{\Phi}_{\mathrm{m}} = \frac{1}{Q} \sum_{q=1}^{Q} \frac{\sum_{\mathbf{b}_{1:q-1} \in \xi_q} \Phi_{\mathrm{m}}[q|\mathbf{b}_{1:q-1}]}{2^{q-1}}. \tag{3.35}$$

3.6 Simulation Framework for MF-based TX

In this section, we describe the stochastic simulation framework for the MF-based TX. We use a PBS method that records the exact position of each vesicle. In particular, we determine coordinates of the release point and release time of each molecule for both scenarios.

For the static scenario, we denote the locations of a vesicle at the start and end of the $\tilde{\chi}$th simulation interval by $(x_{\tilde{\chi}-1}, y_{\tilde{\chi}-1}, z_{\tilde{\chi}-1})$ and $(x_{\tilde{\chi}}, y_{\tilde{\chi}}, z_{\tilde{\chi}})$, respectively. If the distance between a vesicle and the TX's centre is larger than r_{T} at the end of the $\tilde{\chi}$th interval, we assume that the vesicle has hit the TX membrane. As described in Section 3.2.1, this vesicle then fuses with the TX membrane with probability $k_{\mathrm{f}}\sqrt{\frac{\pi \Delta t_{\mathrm{s}}}{D_{\mathrm{v}}}}$ and is reflected with probability $1 - k_{\mathrm{f}}\sqrt{\frac{\pi \Delta t_{\mathrm{s}}}{D_{\mathrm{v}}}}$, where Δt_{s} is the simulation interval. Molecules stored in a vesicle are released at the time and location where the vesicle is fused with the TX membrane. Thus, we need to derive where and when the fusion of vesicles with the membrane occurred in the simulation. For a vesicle fusing with the TX membrane during the $\tilde{\chi}$th simulation interval, we assume that the intersection between the line that is formed by $(x_{\tilde{\chi}-1}, y_{\tilde{\chi}-1}, z_{\tilde{\chi}-1})$ and $(x_{\tilde{\chi}}, y_{\tilde{\chi}}, z_{\tilde{\chi}})$ and the membrane is the fusion point whose coordinates, denoted by $(x_{\mathrm{f},\tilde{\chi}}, y_{\mathrm{f},\tilde{\chi}}, z_{\mathrm{f},\tilde{\chi}})$, are given by [67, eqs. (38)-(40)]

$$x_{\mathrm{f},\tilde{\chi}} = \frac{-\Lambda_2 \pm \sqrt{\Lambda_2^2 - 4\Lambda_1\Lambda_3}}{2\Lambda_1}, \tag{3.36}$$

$$y_{\mathrm{f},\tilde{\chi}} = \frac{(x_{\mathrm{f},\tilde{\chi}} - x_{\tilde{\chi}-1})(y_{\tilde{\chi}} - y_{\tilde{\chi}-1})}{x_{\tilde{\chi}} - x_{\tilde{\chi}-1}} + y_{\tilde{\chi}-1}, \tag{3.37}$$

and

$$z_{\mathrm{f},\tilde{\chi}} = \frac{(x_{\mathrm{f},\tilde{\chi}} - x_{\tilde{\chi}-1})(z_{\tilde{\chi}} - z_{\tilde{\chi}-1})}{x_{\tilde{\chi}} - x_{\tilde{\chi}-1}} + z_{\tilde{\chi}-1}, \tag{3.38}$$

respectively, where $\Lambda_1 = (x_{\tilde{\chi}} - x_{\tilde{\chi}-1})^2 + (y_{\tilde{\chi}} - y_{\tilde{\chi}-1})^2 + (z_{\tilde{\chi}} - z_{\tilde{\chi}-1})^2$, $\Lambda_2 = 2(y_{\tilde{\chi}} - y_{\tilde{\chi}-1})$ $\times (x_{\tilde{\chi}} y_{\tilde{\chi}-1} - x_{\tilde{\chi}-1} y_{\tilde{\chi}}) + 2(z_{\tilde{\chi}} - z_{\tilde{\chi}-1})(x_{\tilde{\chi}} z_{\tilde{\chi}-1} - x_{\tilde{\chi}-1} z_{\tilde{\chi}})$, and $\Lambda_3 = x_{\tilde{\chi}-1}(y_{\tilde{\chi}} - y_{\tilde{\chi}-1})(x_{\tilde{\chi}-1} y_{\tilde{\chi}} - 2y_{\tilde{\chi}-1} x_{\tilde{\chi}} + y_{\tilde{\chi}-1} x_{\tilde{\chi}}) + x_{\tilde{\chi}-1}(z_{\tilde{\chi}} - z_{\tilde{\chi}-1})(x_{\tilde{\chi}-1} z_{\tilde{\chi}} - 2x_{\tilde{\chi}} z_{\tilde{\chi}-1} + x_{\tilde{\chi}-1} z_{\tilde{\chi}-1}) + (x_{\tilde{\chi}} - x_{\tilde{\chi}-1})^2 (y_{\tilde{\chi}-1}^2 + z_{\tilde{\chi}-1}^2 - r_{\mathrm{T}})$. In (3.36), $x_{\mathrm{f},\tilde{\chi}}$ is chosen by satisfying $(x_{\mathrm{f},\tilde{\chi}} - x_{\tilde{\chi}-1})(x_{\mathrm{f},\tilde{\chi}} - x_{\tilde{\chi}}) < 0$ since $x_{\mathrm{f},\tilde{\chi}}$ is between $x_{\tilde{\chi}-1}$ and $x_{\tilde{\chi}}$. We next determine the release time, which is crucial for the subsequent simulation of the molecule propagation and absorption at the RX, via interpolation. We denote $\tilde{t}_{\tilde{\chi}-1}$ as the start time of the $\tilde{\chi}$th simulation interval and $\tilde{t}_{\tilde{\chi}-1} + \Delta t_{\mathrm{f},\tilde{\chi}}$ as the fusion time of the vesicle within the χth simulation interval. Since each vesicle follows Brownian motion, the square of the displacement is proportional to the time within the same simulation interval. Therefore, we derive $\Delta t_{\mathrm{f},\tilde{\chi}}$ as

$$\Delta t_{\mathrm{f},\tilde{\chi}} = \frac{(x_{\mathrm{f},\tilde{\chi}} - x_{\tilde{\chi}-1})^2 + (y_{\mathrm{f},\tilde{\chi}} - y_{\tilde{\chi}-1})^2 + (z_{\mathrm{f},\tilde{\chi}} - z_{\tilde{\chi}-1})^2}{(x_{\tilde{\chi}} - x_{\tilde{\chi}-1})^2 + (y_{\tilde{\chi}} - y_{\tilde{\chi}-1})^2 + (z_{\tilde{\chi}} - z_{\tilde{\chi}-1})^2} \Delta t_{\mathrm{s}}. \tag{3.39}$$

For vesicles failing to fuse with the TX membrane, we assume in the reflection process that they are sent back to their positions at the start of the current simulation interval [67].

For the mobile scenario, we denote $(x_{\mathrm{f},\tilde{\chi}}^{\mathrm{m}}, y_{\mathrm{f},\tilde{\chi}}^{\mathrm{m}}, z_{\mathrm{f},\tilde{\chi}}^{\mathrm{m}})$ as coordinates of the fusion point for the mobile TX, which are given by $x_{\mathrm{f},\tilde{\chi}}^{\mathrm{m}} = x_{\mathrm{f},\tilde{\chi}} + x_{\mathrm{T}}(\tilde{t}_{\tilde{\chi}-1} + \Delta t_{\mathrm{f},\tilde{\chi}})$, $y_{\mathrm{f},\tilde{\chi}}^{\mathrm{m}} = y_{\mathrm{f},\tilde{\chi}} + y_{\mathrm{T}}(\tilde{t}_{\tilde{\chi}-1} + \Delta t_{\mathrm{f},\tilde{\chi}})$, and $z_{\mathrm{f},\tilde{\chi}}^{\mathrm{m}} = z_{\mathrm{f},\tilde{\chi}} + z_{\mathrm{T}}(\tilde{t}_{\tilde{\chi}-1} + \Delta t_{\mathrm{f},\tilde{\chi}})$. $x_{\mathrm{T}}(t)$, $y_{\mathrm{T}}(t)$, and $z_{\mathrm{T}}(t)$ are coordinates of the TX's centre at time t. The calculation of the fusion time for the mobile TX is the same as that for the static TX.

3.7 Numerical Results

In this section, we present numerical results to validate our theoretical analysis and provide insightful discussion. The simulation time interval is $\Delta t_{\mathrm{s}} = 0.001$ s and all results are averaged over 10^4 realisations. Throughout this section, we set simulation parameters as in Table 3.3, unless otherwise stated. In Figs. 3.5, 3.6, 3.7, 3.8, we vary the forward reaction rate constant and vesicle diffusion coefficient to investigate their impacts on molecule release, time to reach the peak molecule release rate, and molecule absorption for the static and mobile scenarios. Analytical results in Figs. 3.5, 3.7, 3.8, 3.9 are verified with simulations. Specifically, we observe agreement between our simulation results and analytical curves derived in Sections

Table 3.3: Simulation Parameters for Numerical Results

Parameter	Variable	Value	Reference
Number of vesicles released	N_{v}	200	
Number of molecules stored in each vesicle	η	5	
Radius of the TX/RX	$r_{\mathrm{T}}/r_{\mathrm{R}}$ $[\mu\mathrm{m}]$	10	[138]
Diffusion coefficient of the vesicle	D_{v} $[\mu\mathrm{m}^2/\mathrm{s}]$	9, 18, 50	[114]
Forward reaction rate constant	k_{f} $[\mu\mathrm{m}/\mathrm{s}]$	2, 5, 30	
Fixed distance for static MC/Initial distance for mobile MC	l/l_0 $[\mu\mathrm{m}]$	40	
Rate constant of molecule degradation	k_{d} $[\mathrm{s}^{-1}]$	0.8	[67]
Diffusion coefficient of molecule A	D_A $[\mu\mathrm{m}^2/\mathrm{s}]$	1000	[122]
Time to release vesicles/transmit b_1 for mobile MC	t' $[\mathrm{s}]$	2	
Diffusion coefficient of the TX/RX for mobile MC	$D_{\mathrm{T}}/D_{\mathrm{R}}$ $[\mu\mathrm{m}^2/\mathrm{s}]$	8, 10	[78]
Length of the transmitted binary bits	Q	5	
Bit interval	T_{b} $[\mathrm{s}]$	2	[139]
Probability to transmit bit 1/0	P_1/P_0	0.5	[78]
Number of divided release intervals	C	3	

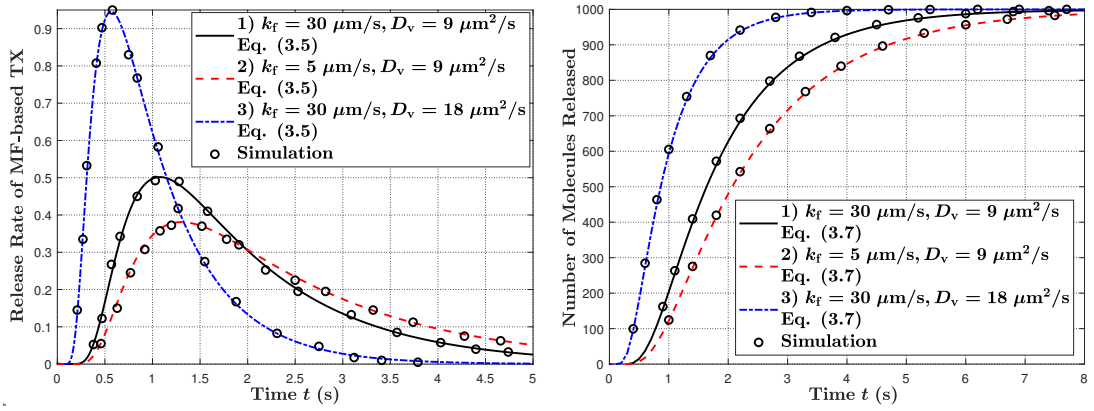

(a) Release Rate (b) Number of molecules released

Figure 3.5: Molecule release rate from the MF-based TX at time t and the number of molecules released from the MF-based TX by time t versus time t for three parameter sets.

3.3, 3.4, 3.5, which demonstrates the accuracy of our analysis.

3.7.1 MF-based TX Model Analysis

In Fig. 3.5, we plot the molecule release rate from the TX at time t versus time t in Fig. 3.5(a) and the number of molecules released from the TX by time t versus time t in Fig. 3.5(b). First, by comparing parameter sets 1) and 2) in Fig. 3.5(a), we observe that the peak release rate

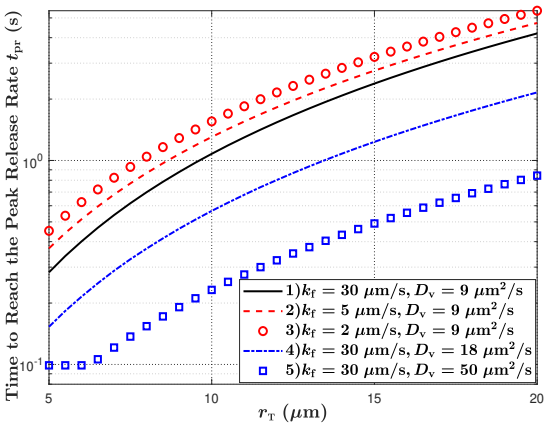

Figure 3.6: Time to reach the peak molecule release rate from the TX versus r_T for five parameter sets.

decreases and the tail of the release rate becomes longer with a decrease in k_f. This is because the decrease in k_f reduces the fusion probability between a vesicle and the TX membrane. Second, by comparing parameter sets 1) and 3) in Fig. 3.5(b), we observe that the peak release rate increases and less time is required for the TX to start releasing molecules with an increase in D_v. This is because increasing D_v accelerates the movement of vesicles. Third, in Fig. 3.5(b), we observe that all molecules can be released from the TX due to the impulsive release of vesicles if the release period is sufficiently long.

In Fig. 3.6, we plot the time to reach the peak molecule release rate from the TX, denoted by t_{pr}, versus the radius of the TX by searching for the peak value in (3.5) and recording the corresponding time. First, we observe that the time to reach the peak release rate increases with an increase in r_T. This is because a vesicle needs to diffuse for a longer time to arrive at a TX membrane with a larger radius. Second, by comparing parameter sets 1), 2), and 3), we observe that the time increases with a decrease in k_f. This is because lower k_f reduces the fusion probability, such that it takes a longer time to reach the peak probability. Third, by comparing parameter sets 1), 4), and 5), we observe that the time decreases with an increase in D_v. This is because a larger value of D_v enables vesicles to move faster, such that less time is required for the vesicle to arrive at the TX membrane.

3.7.2 CIR for Static & Mobile MC

3.7.2.1 Static MC

In Fig. 3.7, we plot the end-to-end molecule hitting rate at the RX at time t versus time t in Fig. 3.7(a) and the end-to-end number of molecules absorbed at the RX by time t versus time t in Fig. 3.7(b). We observe several similar trends between the hitting rate in Fig. 3.7(a) and the release rate in Fig. 3.5(a) for varying k_f and D_v. For example, the peak end-to-end hitting rate decreases with a decrease in k_f, as seen when comparing parameter sets 1) and 2), and the

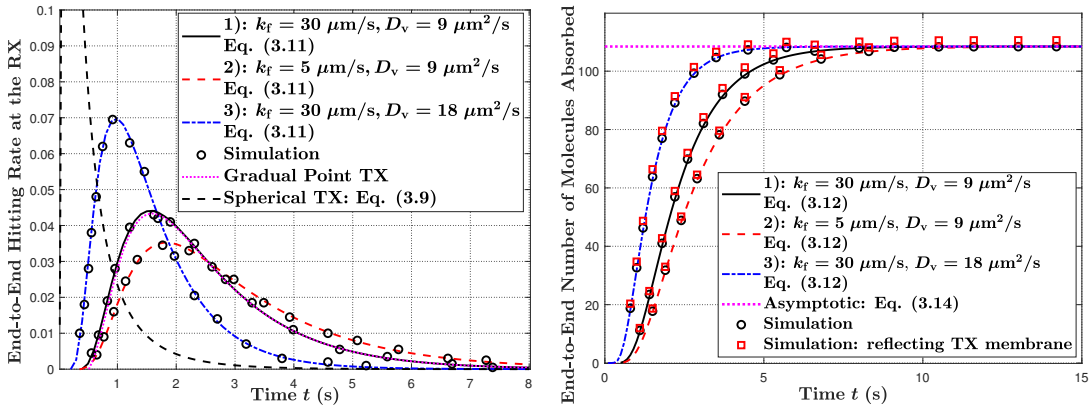

(a) Hitting Rate

(b) The number of molecules absorbed

Figure 3.7: End-to-end molecule hitting rate at the RX at time t and end-to-end number of molecules absorbed at the RX by time t versus time t for three parameter sets.

peak end-to-end hitting rate increases and less time is required for molecules to start hitting the RX with an increase in D_v, as seen when comparing parameter sets 1) and 3). These similar observations are due to the fact that absorption of molecules at the RX is directly influenced by the release of molecules at the TX.

The MF-based TX relaxes two major assumptions of the widely-applied point TX model. The first assumption is the instantaneous release of molecules, and the second assumption is molecules released from a point. To investigate the relative importance of these two assumptions to the difference between the MF-based TX and the point TX, we plot the hitting rate at the RX for a gradual point TX and a spherical TX, separately, in Fig 3.7(a) when $D_v = 9\,\mu\text{m}^2/\text{s}$ and $k_f = 30\,\mu\text{m}/\text{s}$. The gradual point TX is a point TX that releases molecules gradually with the release rate $f_r(t)$. The hitting rate of the gradual point TX is given by $f_r(t) * h_{\hat{\alpha}}(t)\big|_{r_{\hat{\alpha}}=r_0}$. The spherical TX is a TX that instantaneously releases molecules uniformly over the membrane. The hitting rate of a spherical TX is given in (3.9). From Fig. 3.7(a), we observe the deviation between curves of the MF-based TX and the gradual point TX is extremely small, while the deviation between the MF-based TX and the spherical TX is huge. Therefore, we conclude that the gradual release is the more important element to distinguish between the MF-based TX and the point TX.

In Fig. 3.7(b), we observe that the asymptotic number of molecules absorbed at the RX for the three parameter sets is the same. This is because varying k_f and D_v do not change the total number of released molecules from the TX after a sufficiently long time as shown in Fig. 3.5(b), which leads to the total number of molecules absorbed eventually being the same. This observation also complies with Remark 3.2.

In Fig. 3.7(b), we also consider the TX membrane as a reflecting boundary to the molecules

Table 3.4: R^2 of $H_e(t)$ when the TX membrane is reflecting

r_0 (μm)	40	38	36	34	32	28	26	24
R^2	0.9952	0.9962	0.9964	0.9974	0.9977	0.9995	0.999	0.993
r_0 (μm)	22	21.5	20					
R^2	0.9684	0.9457	0.9188					

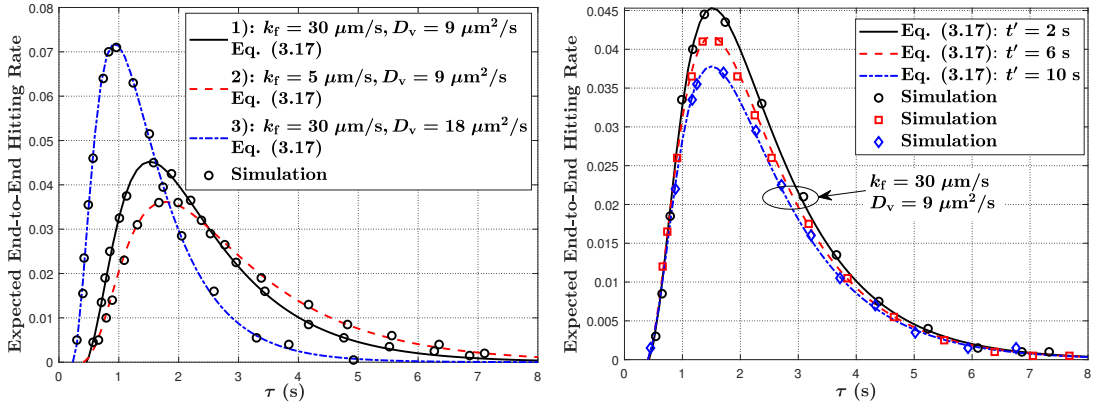

(a) Varying k_f and D_v, $t' = 2$ s

(b) Varying t'

Figure 3.8: Expected end-to-end molecule hitting rate at the mobile RX at time $t' + \tau$ versus time τ, where $D_T = D_R = 8\ \mu\text{m}^2/\text{s}$.

in the propagation environment to relax assumption A5 in Section 3.2.1, where molecules are reflected back to their positions at the start of the current simulation interval if they hit the TX membrane. We perform this simulation and plot the number of molecules absorbed. We observe that small differences exist between the simulation and analytical curves for the three parameter sets due to A5. Moreover, we calculate R^2. For parameter sets 1), 2) and 3), the R^2 is calculated as 0.9952, 0.9980, and 0.9999, respectively, which are quite close to 1. To further investigate the impact of decreasing distance between the TX and RX on R^2 for the end-to-end number of molecules absorbed, we calculate R^2 for varying r_0 in Table 3.4, where $k_f = 30\ \mu\text{m/s}$ and $D_v = 9\ \mu\text{m}^2/\text{s}$. From this Table, we observe that the R^2 first increases with the decrease in r_0, reaches the highest at $r_0 = 28\ \mu$m, and then decreases. Compared to a transparent TX membrane, the near side of the reflecting membrane (i.e., closer to the RX) impedes molecules from diffusing further away from the RX such that the RX can absorb more molecules, while the far side of the TX membrane impedes molecules released from that side from being absorbed by the RX. Hence, the highest R^2 is achieved when the effects of the near side and far side on molecular absorption are almost equal. Accordingly, the impact of considering a reflecting TX membrane on the CIR analysis is significant when r_0 is extremely small.

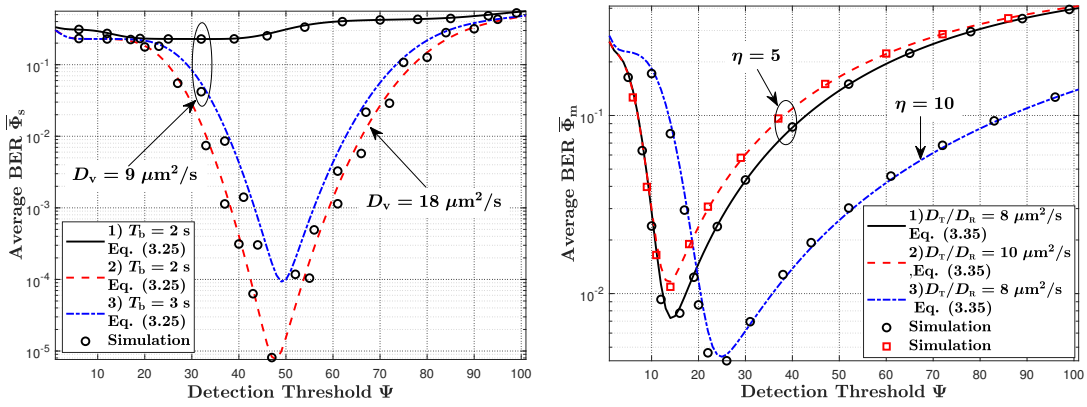

(a) Static MC (b) Mobile MC

Figure 3.9: Average BER versus the detection threshold for (a) static MC, where $k_f = 30\ \mu m/s$ and (b) mobile MC, where $D_v = 50\ \mu m^2/s$ and $k_f = 30\ \mu m/s$.

3.7.2.2 Mobile MC

In Fig. 3.8, we plot the expected end-to-end molecule hitting rate at the mobile RX at time $t' + \tau$ versus time τ, where k_f and D_v are varied in Fig. 3.8(a) and t' is varied in Fig. 3.8(b). First, the overall trend of the expected end-to-end hitting rate in Fig. 3.8(a) has identical observations as the hitting rate in Fig. 3.7(a) for varying k_f and D_v. Second, in Fig. 3.8(b), we observe that the expected end-to-end hitting rate decreases with an increase in t'. This is because larger t' means that the TX releases an impulse of vesicles after the TX and RX have been diffusing for a longer time, such that the distance between the TX and RX becomes longer on average. This observation also indicates that the communication becomes impractical when t' is sufficiently large since the hitting rate eventually tends to 0.

3.7.3 BER Analysis for Static & Mobile MC

3.7.3.1 Static MC

In Fig. 3.9(a), we plot the average BER $\overline{\Phi}_s$ versus the detection threshold Ψ for static MC, where different vesicle diffusion coefficients and bit intervals are adopted to investigate their impacts on the average BER. We first observe that the BER is much larger compared to the other parameter sets when $D_v = 9\ \mu m^2/s$ and $T_b = 2$ s. This is because the period for all molecules to be released from the TX membrane, τ_p, calculated as 9.5 s, is much larger than the bit interval. Therefore, severe ISI is expected which dominates the BER. This also illustrates the difference between the MF-based TX and an ideal point TX. For the ideal point TX, the ISI is only caused by the diffusion of molecules in the propagation environment. For the MF-based TX, the ISI is also introduced by the signalling pathways inside the TX. Second,

we introduce three methods to decrease the ISI. The first method is increasing the diffusion coefficient of the vesicle. By comparing parameter sets 1) and 2), we observe a dramatic decrease in the BER with the increase in D_{v}. This is because an increase in D_{v} reduces the period for releasing molecules, such that ISI decreases. Given that the active transport of vesicles along microtubules is much faster than free diffusion [140], the investigation of active transport of vesicles within the TX is an interesting future work for reducing the ISI. The second method is increasing the bit interval. By comparing parameter sets 1) and 3), we observe that the average BER decreases with an increase in T_{b}. This is because a larger T_{b} enables the RX to absorb more molecules in the current interval, such that fewer molecules are left to influence subsequent bit detection. One drawback of increasing the bit interval is reducing the data transmission rate. The third method is applying a sequence detector in MC to mitigate the ISI as described in [51].

3.7.3.2 Mobile MC

In Fig. 3.9(b), we plot the average BER $\overline{\Phi}_{\mathrm{m}}$ versus the fixed detection threshold Ψ as in [79] for mobile MC, where different TX and RX diffusion coefficients and the number of molecules stored within each vesicle are applied to investigate their impacts on the average BER. First, by comparing parameter sets 1) and 2), we observe that the average BER increases with an increase in D_{T} and D_{R}. This is because faster motion of the TX and RX results in a more stochastic channel such that the detection ability at the RX is reduced. Second, by comparing parameter sets 1) and 3), we observe that the minimum BER decreases with an increase in η. This is because a larger η means that more molecules are released from the TX such that more molecules are absorbed within the RX. This increases the detection accuracy at the RX.

3.8 Conclusion

In this chapter, we proposed a new TX model that is based on MF between vesicles generated within the TX and the TX membrane to release molecules. We derived the molecule release rate and the fraction of molecules released from the TX. By considering a fully-absorbing RX, we derived the CIR between the MF-based TX and RX when both TX and RX are static or diffusive mobile. By considering a sequence of bits transmitted from the TX, we calculated the average BER for two scenarios. For the mobile scenario, we derived the PMF of the number of molecules absorbed by dividing the molecule release duration into multiple release intervals. Furthermore, we proposed a simulation framework for the MF-based TX. Our numerical results showed that our analytical expressions are accurate. They also showed that a low MF probability or low vesicle mobility slows the release of molecules, extends the time to reach the peak release rate, and reduces the end-to-end molecule hitting rate at the RX. Moreover,

numerical results highlighted the difference between the MF-based TX and the ideal point TX in terms of the ISI, since the ISI of the ideal point TX is only caused by the diffusion of molecules in the propagation environment whereas the ISI of the MF-based TX is also caused by the signalling pathways within the TX.

Chapter 4

Analysis of Receivers Covered by Heterogeneous Receptors

4.1 Introduction

In this chapter, we consider an RX covered by heterogeneous receptors. Specifically, we model the receptors as APs and assume that there are multiple non-overlapping[1] APs on the RX surface, where the APs can have different sizes and arbitrary but fixed locations. When molecules hit an AP, they are absorbed by the RX. In particular, we refer to RXs with heterogeneous APs as AP-based RXs and summarize the differences between these AP-based RXs and the ligand-receptor model as follows: i) the binding of a ligand to a receptor is reversible, while the molecules are fully absorbed by the APs, ii) the ligand-receptor interaction depends on the specific types of receptors and ligands involved, while we consider generic molecules and APs in this chapter, and iii) the ligand-receptor interaction may trigger subsequent reactions within the cell, while we do not consider further reactions after molecules are absorbed by the RX. Moreover, we consider two different TX models, namely, the point TX and the MF-based TX. We assume that the point TX and the center of the MF-based TX have a fixed distance to the center of the RX, as shown in Fig. 4.1, and can be located at any point on the surface of the sphere defined by the TX-RX distance. Furthermore, we assume that the molecules may degrade while propagating in the channel. For the considered MC systems, we investigate the expected end-to-end CIR between TX and RX, averaged over all possible locations of the TX. Here, the expected CIR is defined as the expected molecule hitting rate at the RX [45]. Additionally, we consider a sequence of bits transmitted from the TX to the RX and investigate the error probability of the end-to-end MC system. In summary, our major contributions are as follows:

1) We derive the expected molecule hitting rate, the expected fraction of absorbed molecules, and the expected asymptotic fraction of absorbed molecules as time approaches infinity

[1] We assume that all APs are of the same type. If some APs overlap with each other, they would be regarded as a single AP of a larger size.

at an RX with heterogeneous APs, which we refer to as AP-based RX. All expressions are functions of the sizes and locations of all APs. The derived expressions allow us to investigate the impact of different numbers, sizes, and locations of APs on molecular absorption.

2) Aided by PBSs, we verify the accuracy of the derived analytical results. We also show that, for a given total area of the RX surface covered by APs, the expected number of absorbed molecules increases with the number of APs, but this increase becomes slower for a larger number of APs.

3) We compare three spatial distributions of the APs by examining the number of absorbed molecules at the RX. Specifically, we consider APs that are respectively evenly and randomly distributed across the entire RX surface, and APs that are evenly distributed within a region of the RX surface. Our results show that evenly distributed APs across the entire RX surface (i.e., the APs are equally spaced) result in a larger number of absorbed molecules than the other two distributions.

4) We compare three different combinations of TX and RX models in terms of their CIRs and error probabilities. In particular, we consider the combination of i) a point TX and a fully absorbing RX (PTFR), ii) a point TX and an AP-based RX (PTAR), and iii) an MF-based TX and an AP-based RX (MTAR). Our results show that compared with the ideal PTFR model, AP-based RXs cause a lower peak and shorter tail of the CIR. Furthermore, both PTAR and MTAR result in a much higher error probability compared to PTFR. This indicates the importance of our analysis of realistic TX and RX models since the existing CIR and BER analyses for ideal models are not accurate in practice.

The rest of this chapter is organised as follows. In Section 4.2, we describe the system model. In Section 4.3, we derive the CIR between a point TX and an AP-based RX. In Section 4.4, we analyze the CIR between an MF-based TX and an AP-based RX. In Section 4.5, we calculate the error probability of the MC system. In Section 4.6, we present and discuss our numerical results. In Section 4.7, we draw some conclusions.

4.2 System Model

In this chapter, we consider an unbounded 3D environment, where a TX communicates with a spherical RX, as depicted in Fig. 4.1. We choose the center of the RX as the origin of the coordinate system and denote the radius of the RX by r_{R}. We assume that the propagation environment between TX and RX is a fluid medium with uniform temperature and viscosity. Once type A molecules are released from the TX, they diffuse randomly with a constant diffusion coefficient D_A. We consider unimolecular degradation in the propagation environment, where

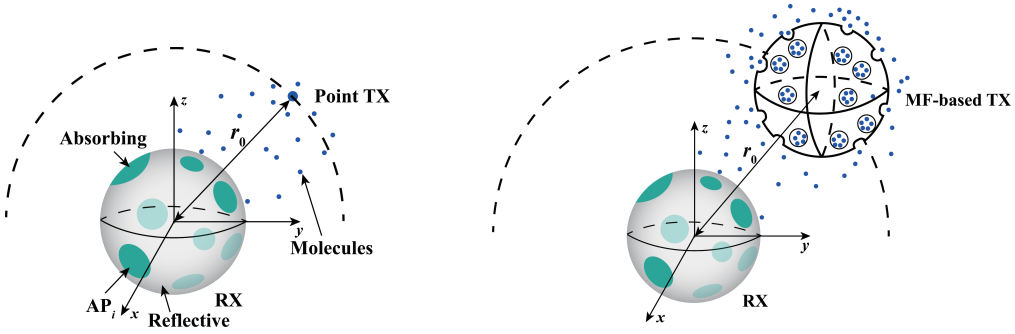

(a) Point TX (b) MF-based TX

Figure 4.1: Illustration of the considered MC system model. (a): A point TX communicates with a spherical AP-based RX. (b): A spherical MF-based TX communicates with a spherical AP-based RX.

the type A molecules can degrade to type $\hat{A}$ molecules that cannot be recognized by the RX, i.e., $A \xrightarrow{k_\mathrm{d}} \hat{A}$ [113, Ch. 9], where k_d $[\mathrm{s}^{-1}]$ is the rate constant of degradation. In the following, we first describe the novel AP-based RX model proposed in this chapter and then present the considered TX models.

4.2.1 RX Model

We assume that there are N_p non-overlapping APs on the RX surface, and denote the ith AP by AP_i. We approximate the shape of each AP as a circle[2], where the radius of AP_i is denoted by a_i. We further define $\mathcal{A}$ as the ratio of the total area of APs to the area of the RX surface, i.e., $\mathcal{A} = \sum_{i=1}^{N_\mathrm{p}} a_i^2/(4r_\mathrm{R}^2)$. In spherical coordinates, we denote $\vec{l}_i = [r_\mathrm{R}, \theta_i, \varphi_i]$ as the location of the center of AP_i, where θ_i and φ_i are the polar angle and azimuthal angle, respectively. As the APs are non-overlapping, the locations and radii of the APs satisfy $|\vec{l}_i - \vec{l}_j| \geq a_i + a_j$, $\forall i, j \in \{1, 2, ..., N_\mathrm{p}\}$, $i \neq j$. Once a molecule hits an AP, it is absorbed by the RX. As is customary in the literature [61], we ignore the occupancy of the APs by molecules such that several molecules can be concurrently absorbed by the same AP. Furthermore, we model the area of the RX surface that is not covered by APs as perfectly reflective, which means that the molecules are reflected back once they hit this part of the RX surface.

4.2.2 TX Model

In this chapter, we consider the following two TX models:

[2]Technically, the shape of the AP is not a circle when APs are located on a sphere. However, assuming circular APs is reasonable when the size of the AP is extremely small as compared to the size of the RX, e.g., when the ratio of the total area of APs to the area of the RX surface is less than 5%.

4.2.2.1 Point TX

First, we consider a point TX communicating with an AP-based RX, cf. Fig. 4.1(a). The point TX has distance r_0 to the center of the RX. For a given r_0, the TX can be located at any point on the surface of a sphere with radius r_0 around the RX and the CIR depends on the exact location of the TX. This is due to the fact that the considered RX has a heterogeneous boundary condition where the locations and sizes of the APs are determined by $\vec{l}_i$ and a_i, respectively. Thus, we focus on the expected CIR averaged over all possible locations of the TX with distance r_0 to the RX. We emphasise that the expected CIR for the given TX-RX distance is an important characteristic since, in practice, measuring the distance between two cells is much easier than determining their relative orientation. Specifically, cell A can measure its distance to cell B by detecting the nearby concentration of molecules released by cell B [141].

4.2.2.2 MF-based TX

Second, we consider a spherical TX, namely the MF-based TX, communicating with an AP-based RX, cf. Fig. 4.1(b), where the MF-based TX model was proposed in Chapter 3. Similar to Section 4.2.2.1, we assume that the center of the MF-based TX is located at a distance r_0 from the center of the RX. Thus, the center of the MF-based TX can be located on any point of the surface of a sphere with radius r_0 around the RX, and the expected CIR is averaged over all possible locations of the MF-based TX.

We emphasise that the fundamental difference between the two models in Fig. 4.1 are the different TX models, where a point TX, which releases molecules immediately into the propagation environment, is considered in Fig. 4.1(a), and an MF-based TX, which generates vesicles at its center, is considered in Fig. 4.1(b). We note that the release process of molecules in Fig. 4.1(b) is more complex and practical than that in Fig. 4.1(a). Thus, the model considered in Fig. 4.1(b) enables us to investigate a practical end-to-end MC system.

4.2.3 Bit Transmission

Similar to Section 4.2.3, we consider that information sent from the TX to the RX is encoded into $\mathbf{b}_{1:Q} = [b_1, b_2, ..., b_Q]$. At the TX side, we adopt ON/OFF keying for modulation. At the RX side, we adopt the threshold detector to demodulate b_q.

4.3 Analysis of the CIR for a Point TX

In this section, we assume a point TX and derive i) the expected molecule hitting rate, ii) the expected fraction of absorbed molecules, and iii) the expected asymptotic fraction of absorbed molecules as $t \to \infty$ at the AP-based RX by applying boundary homogenization [142]. To this

end, we first derive the expected CIR of an RX with uniform surface reaction rate. Here, a uniform surface reaction rate implies that the reactivity of the molecules is identical for all points on the RX surface. We then consider the system in steady state and derive the diffusion current of molecules across the RX surface. We note that the diffusion current $[\text{molecule} \cdot \text{s}^{-1}]$ is the rate of the molecule movement per unit time. Based on the diffusion current in steady state, we finally determine the effective reaction rate constant and apply it to derive the expected CIR of an AP-based RX.

4.3.1 Problem Formulation

In spherical coordinates, we denote the molecule concentration at time t at location $\vec{r}$ by $C(|\vec{r}|,t)$, $|\vec{r}| \geq r_{\text{R}}$. For impulsive release of molecules from the TX at time $t = 0$, the initial condition can be expressed as follows[130, Eq. (3.61)]

$$C(|\vec{r}|,t \to 0) = \frac{1}{4\pi r_0^2}\delta(|\vec{r}| - r_0). \tag{4.1}$$

After their release, the movement of the molecules by diffusion in the propagation environment is described by Fick's second law as follows [129]

$$\frac{\partial C(|\vec{r}|,t)}{\partial t} = D_A \nabla^2 C(|\vec{r}|,t) - k_{\text{d}} C(|\vec{r}|,t), \tag{4.2}$$

where ∇^2 is the 3D spherical Laplacian. For molecules hitting the RX surface, the reaction between the molecules and the RX surface is described by the radiation boundary condition [130, Eq. (3.64)], given by

$$D_A \frac{\partial C(|\vec{r}|,t)}{\partial |\vec{r}|}\bigg|_{|\vec{r}|=r_{\text{R}}} = wC(r_{\text{R}},t), \tag{4.3}$$

where w $[\mu\text{m/s}]$ denotes the surface reaction rate constant. We note that $w \to \infty$ when $\vec{r} \in \Omega_{\text{AP}}$ while $w = 0$ when $\vec{r} \in \Omega_{\text{R}}$, where Ω_{AP} and Ω_{R} denote the areas of the RX surface that are covered and not covered by APs, respectively. Due to the heterogeneous boundary condition in (4.3), it is difficult to directly solve (4.2) to obtain $C(|\vec{r}|,t)$. Hence, in this chapter, we apply boundary homogenization to derive the expected CIR. The main idea of boundary homogenization is to replace the heterogeneous boundary condition in (4.3) by a uniform boundary condition with an appropriately chosen effective surface reaction rate constant, denoted by w_{e}. This means that we replace the RX surface with heterogeneous boundary conditions shown in Fig. 4.1 with an equivalent uniform surface with reaction rate constant w_{e}. Hence, (4.3) can be re-expressed by replacing w with w_{e}. We derive the expected CIR of the RX and w_{e} in the following subsections.

4.3.2 Expected CIR of RX with Uniform Surface Reaction Rate

In this subsection, we analyze the expected CIR of an RX with uniform surface reaction rate constant w. Based on the initial condition in (4.1) and the boundary condition in (4.3), the authors of [130][3] derived $C(|\vec{r}|,t)$ by solving (4.2) when $k_{\rm d}=0$. We denote $h_{\rm u}(t,w)$ as the expected molecule hitting rate at an RX with uniform surface reaction rate. We derive $h_{\rm u}(t,w)$ including the effect of molecule degradation in the following lemma.

Lemma 4.1. The expected molecule hitting rate at an RX with uniform surface reaction rate constant w at time t when molecules are released from a point TX at time $t=0$ is given by

$$h_{\rm u}(t,w) = \frac{r_{\rm R} w}{r_0}\left[\frac{1}{\sqrt{\pi D_A t}}\exp\left(-\frac{\tilde{\varepsilon}^2}{t}-k_{\rm d}t\right) - \hat{\gamma}(w)\exp\left[\hat{\gamma}(w)(r_0-r_{\rm R})+\zeta(w)t\right] \times \operatorname{erfc}\left(\frac{\tilde{\varepsilon}}{\sqrt{t}}+\hat{\gamma}(w)\sqrt{D_A t}\right)\right], \tag{4.4}$$

where $\tilde{\varepsilon}=\frac{r_0-r_{\rm R}}{\sqrt{4D_A}}$, $\hat{\gamma}(w)=\frac{wr_{\rm R}+D_A}{D_A r_{\rm R}}$, and $\zeta(w)=\hat{\gamma}(w)^2 D_A - k_{\rm d}$.

Proof: According to [59], $h_{\rm u}(t,w)$ can be obtained as $h_{\rm u}(t,w)=h_{\rm u}(t,w)\big|_{k_{\rm d}=0}\times\exp(-k_{\rm d}t)$. We also find $h_{\rm u}(t,w)\big|_{k_{\rm d}=0}=4\pi r_{\rm R}^2 w C(r_{\rm R},t)\big|_{k_{\rm d}=0}$ based on [130, Eq. (3.107)]. Combining these two results, we obtain (4.4). ■

We now denote $H_{\rm u}(t,w)$ as the fraction of molecules captured by the RX by time t and present it in the following corollary.

Corollary 4.1. The fraction of molecules captured by an RX with uniform surface reaction rate constant w by time t, when molecules are released from a point TX, is given by

$$H_{\rm u}(t,w) = \frac{r_{\rm R} w}{r_0}\left[\alpha_1(t)-\alpha_2(t,w)\right], \tag{4.5}$$

where

$$\alpha_1(t) = \frac{1}{2\sqrt{k_{\rm d}D_A}}\left[\exp(-\hat{\beta})\operatorname{erfc}\left(\frac{\tilde{\varepsilon}}{\sqrt{t}}-\sqrt{k_{\rm d}t}\right) - \exp\left(\hat{\beta}\right)\operatorname{erfc}\left(\frac{\tilde{\varepsilon}}{\sqrt{t}}+\sqrt{k_{\rm d}t}\right)\right] \tag{4.6}$$

and

$$\alpha_2(t,w) = \frac{1}{2\zeta(w)}\left[\psi_1(t,w)-\psi_2(t,w)\right] - \frac{\hat{\gamma}(w)\exp(-\hat{\beta})}{\zeta(w)} \tag{4.7}$$

with

$$\psi_1(t,w) = 2\hat{\gamma}(w)\exp\left(\hat{\gamma}(w)(r_0-r_{\rm R})+\zeta(w)t\right)\operatorname{erfc}\left(\frac{\tilde{\varepsilon}}{\sqrt{t}}+\hat{\gamma}(w)\sqrt{D_A t}\right), \tag{4.8}$$

[3] We note that the RX in [130] is fully covered by receptors, where the forward reaction rate constant between receptors and molecules is given by w.

$$\psi_2(t,w) = \left(\hat{\gamma}(w)^2\sqrt{\frac{D_A}{k_\mathrm{d}}} - \hat{\gamma}(w)\right)\exp(-\hat{\beta})\mathrm{erf}\left(\frac{\tilde{\varepsilon}}{\sqrt{t}} - \sqrt{k_\mathrm{d}t}\right) - \left(\hat{\gamma}(w)^2\sqrt{\frac{D_A}{k_\mathrm{d}}} + \hat{\gamma}(w)\right) \times \left[\exp(-\hat{\beta}) - \exp(\hat{\beta})\mathrm{erfc}\left(\frac{\tilde{\varepsilon}}{\sqrt{t}} + \sqrt{k_\mathrm{d}t}\right)\right], \tag{4.9}$$

$\mathrm{erf}(\cdot) = 1 - \mathrm{erfc}(\cdot)$ is the error function [57], and $\hat{\beta} = (r_0 - r_\mathrm{R})\sqrt{k_\mathrm{d}/D_A}$.

Proof: We derive $H_\mathrm{u}(t,w)$ via $H_\mathrm{u}(t,w) = \int_0^t h_\mathrm{u}(u,w)\mathrm{d}u$. By substituting (4.4) into this equation, we obtain (4.5). ■

We next denote $H_{\mathrm{u},\infty}(w)$ as the asymptotic fraction of molecules captured by the RX as $t \to \infty$. We present $H_{\mathrm{u},\infty}(w)$ in the following corollary.

Corollary 4.2. When molecules are released from a point TX, as $t \to \infty$, the asymptotic fraction of molecules captured by an RX with uniform surface reaction rate constant w is given by

$$H_{\mathrm{u},\infty}(w) = \frac{r_\mathrm{R} w \exp(-\hat{\beta})}{r_0 D_A\left(\hat{\gamma}(w) + \sqrt{\frac{k_\mathrm{d}}{D_A}}\right)}\exp(-\hat{\beta}). \tag{4.10}$$

Proof: Please see Appendix B.1. ■

4.3.3 Effective Reaction Rate Constant

In this subsection, we determine the effective reaction rate constant w_e. First, we investigate the diffusion flux and diffusion current of the molecules, which lays the foundation for deriving w_e. We denote J as the diffusion flux $\left[\mathrm{molecule}\cdot\mathrm{m}^{-2}\cdot\mathrm{s}^{-1}\right]$ of the molecules, which is the rate at which the molecules move across a unit area in a unit time [129]. We note that J is given by [129, Eq. (2.6)]

$$J = -D_A\frac{\partial C(|\vec{r}|,t)}{\partial|\vec{r}|}\bigg|_{|\vec{r}|=r_\mathrm{R}}. \tag{4.11}$$

We next denote I as the diffusion current of the molecules, which represents the rate of molecule movement across the RX surface in a unit time. We note that I is given by $I = -4\pi r_\mathrm{R}^2 J$. The negative sign is due to the inward diffusion current. We next consider a steady-state diffusion. In this condition, the molecule concentration does not change with time. Thus, the partial derivative of the molecule concentration with respect to time is zero, and we have $\partial C(|\vec{r}|,t)/\partial t = 0$. If we set $k_\mathrm{d} = 0$ in (4.2), we obtain

$$\nabla^2 C(|\vec{r}|,t) = 0. \tag{4.12}$$

As explained in [143], since (4.12) is analogous to the Laplace's equation for the electro-

static potential in charge-free space, the diffusion current to an isolated absorbing RX of any size and shape can be expressed as [129, Eq. (2.24)]

$$I = 4\pi D_A G C_0, \tag{4.13}$$

where we define G as the "capacitance" of the RX and C_0 is the molecule concentration at $|\vec{r}| \to \infty$ in steady state[4]. We note that $C_0 = 1$ was adopted in some previous studies, e.g., [65, 144]. We further note that G measures the ability of the MC RX to absorb molecules, which is different from the conventional electrical capacitance of a conductor, denoted by $\hat{G}$. However, according to [129], if the MC RX and the conductor have the same size and shape, G can be obtained as $G = \hat{G}/(4\pi\varepsilon_0)$, where ε_0 is the vacuum permittivity [145]. Since expressions for $\hat{G}$ have been derived for a variety of conductors, we can obtain the corresponding G directly. For example, we have $\hat{G} = 4\pi\varepsilon_0 r_{\rm R}$ for a spherical conductor with radius $r_{\rm R}$ [146, Eq. (1)]. According to the relationship between G and $\hat{G}$, we obtain the "capacitance" of a fully absorbing RX with the same radius, denoted by $G_{\rm a}$, as $G_{\rm a} = r_{\rm R}$. Therefore, the diffusion current of a fully absorbing RX, denoted by $I_{\rm a}$, is given by $I_{\rm a} = 4\pi D_A r_{\rm R} C_0$, which aligns with the derivation in [143, Eq. (1)] based on solving (4.12). For the AP-based RX, the "capacitance" of the RX, denoted by $G_{\rm p}$, was derived in [144] by using the method of matched asymptotic expansions. In particular, the authors in [144] treated the space within the RX as an inner region and the space outside the RX as an outer region, and performed an asymptotic expansion in the limit $a_i \to 0$ on each region. The matching conditions were applied to connect the inner and outer solutions, and $G_{\rm p}$ could be obtained by combining the matched local solutions. We note that $G_{\rm p}$ is a function of the size and location of each AP, and given by [144, Eq. (3.37a)]

$$\begin{aligned}\frac{1}{G_{\rm p}} =& \frac{2}{N_{\rm p}\overline{m}\hat{\kappa}r_{\rm R}}\Bigg[1 + \frac{\hat{\kappa}}{2N_{\rm p}\overline{m}}\ln\left(\frac{\hat{\kappa}}{2}\right)\sum_{i=1}^{N_{\rm p}} m_i^2 + \frac{\hat{\kappa}}{N_{\rm p}\overline{m}} \times \left(\sum_{i=1}^{N_{\rm p}} m_i s_i + 2\sum_{i=1}^{N_{\rm p}}\sum_{j=i+1}^{N_{\rm p}} m_i m_j \mathcal{F}(\vec{l}_i', \vec{l}_j')\right) \\ &+ \left(\hat{\kappa}\ln\left(\frac{\hat{\kappa}}{2}\right)\right)^2 \frac{\hat{\vartheta}}{4N_{\rm p}\overline{m}} + \mathcal{O}\left(\hat{\kappa}^2\ln\left(\frac{\hat{\kappa}}{2}\right)\right)\Bigg],\end{aligned} \tag{4.14}$$

where $\hat{\kappa} = \frac{a_1}{r_{\rm R}}$, $m_i = \frac{2a_i}{r_{\rm R}\hat{\kappa}\pi}$, $\overline{m} = \frac{1}{N_{\rm p}}\sum_{i=1}^{N_{\rm p}} m_i$, $s_i = \frac{m_i}{2}\left(\ln\left(\frac{4a_i}{r_{\rm R}\hat{\kappa}}\right) - \frac{3}{2}\right)$, $\hat{\vartheta} = \frac{\left(\sum_{i=1}^{N_{\rm p}} m_i^2\right)^2}{N_{\rm p}\overline{m}} - \sum_{i=1}^{N_{\rm p}} m_i^3$, and

$$\mathcal{F}(\vec{l}_i', \vec{l}_j') = \frac{1}{|\vec{l}_i' - \vec{l}_j'|} + \frac{1}{2}\ln|\vec{l}_i' - \vec{l}_j'| - \frac{1}{2}\ln\left(2 + |\vec{l}_i' - \vec{l}_j'|\right) \tag{4.15}$$

with $\vec{l}_i' = \vec{l}_i/r_{\rm R}$. In (4.14), $\mathcal{O}(\cdot)$ represents the infinitesimal of higher order, which is omitted during calculation. The accuracy of (4.14) when the $\mathcal{O}(\cdot)$ term is ignored will be discussed in

[4]We note that the steady state can be achieved when considering the TX continuously releasing molecules. Therefore, different from the scenario when the TX only releases an impulse of molecules, we have $C_0 \neq 0$.

Table 4.1: Summary of expressions for Calculating $\frac{1}{G_\mathrm{p}}$:

Expression	Size and Distribution of APs
(4.14)	Any size, any distribution
(4.16)	Identical sizes, any distribution
(4.17)	Identical sizes, evenly distributed
(4.18)	Single AP

Fig. 4.2 in Section 4.6.1.

When all APs have the same size, (4.14) can be further simplied as shown in the following corollary.

Corollary 4.3. When all APs have identical sizes, i.e., $a_1 = a_2 = \cdots = a_{N_\mathrm{p}}$, G_p can be simplified as follows

$$\frac{1}{G_\mathrm{p}} = \frac{\pi}{N_\mathrm{p}\hat{\kappa} r_\mathrm{R}}\left[1 + \frac{\hat{\kappa}}{\pi}\left(\ln(2\hat{\kappa}) - \frac{3}{2} + \frac{4}{N_\mathrm{p}}\sum_{i=1}^{N_\mathrm{p}}\sum_{j=i+1}^{N_\mathrm{p}} \mathcal{F}(\vec{l}_i', \vec{l}_j')\right) + \mathcal{O}\left(\hat{\kappa}^2 \ln\left(\frac{\hat{\kappa}}{2}\right)\right)\right]. \quad (4.16)$$

Proof: When $a_1 = a_2 = \cdots = a_{N_\mathrm{p}}$, we have $m_i = \frac{2}{\pi}$ and $\hat{\vartheta} = 0$. By substituting m_i and $\hat{\vartheta}$ into (4.14), we obtain (4.16). ■

When the APs have the same size and are evenly distributed, i.e., equally spaced, on the RX surface, (4.16) can be further simplified as $N_\mathrm{p} \to \infty$ by using the mean-field approximation method [147][5], which results in [144, Eq. (4.7)]

$$\frac{1}{G_\mathrm{p}} = \frac{1}{r_\mathrm{R}}\left(1 + \frac{\pi}{N_\mathrm{p}\hat{\kappa}} + \frac{\frac{1}{2}\ln(\hat{\kappa}\sqrt{N_\mathrm{p}}) + \ln 2 - \frac{3}{2}}{N_\mathrm{p}} - 2N_\mathrm{p}^{-\frac{1}{2}} + N_\mathrm{p}^{-\frac{3}{2}}\right). \quad (4.17)$$

We note that (4.17) only depends on N_p and not on the exact locations of the APs. We will confirm the accuracy of (4.17) in Fig. 4.8 in Section 4.6.1. Our results in Fig. 4.8 show that even though (4.17) is derived as $N_\mathrm{p} \to \infty$, (4.17) is still accurate when N_p is small.

The capacitance of an RX with a single AP can be obtained by setting $N_\mathrm{p} = 1$ in (4.16). In [144], the authors applied a higher order asymptotic expansion to derive a more accurate expression, which is given by [144, Eq. (6.31)]

$$\left.\frac{1}{G_\mathrm{p}}\right|_{N_\mathrm{p}=1} = \frac{\pi}{\hat{\kappa} r_\mathrm{R}}\left[1 + \frac{\hat{\kappa}}{\pi}\left(\ln(2\hat{\kappa}) - \frac{3}{2}\right) - \frac{\hat{\kappa}^2}{\pi^2}\left(\frac{\pi^2 + 21}{36}\right) + \mathcal{O}(\hat{\kappa}^3 \ln \hat{\kappa})\right]. \quad (4.18)$$

In Table 4.1, we summarise the expressions for calculating $1/G_\mathrm{p}$ for different AP sizes and distributions. We denote $h_\mathrm{p}(t)$, $H_\mathrm{p}(t)$, and $H_{\mathrm{p},\infty}$ as the expected molecule hitting rate, the expected fraction of absorbed molecules, and the expected asymptotic fraction of absorbed

[5] We note that the ratio of the total area of APs to the RX surface is fixed and less than 1, which means as $N_\mathrm{p} \to \infty$, we have $a_i \to 0$.

molecules at an AP-based RX when the molecules are released from a point TX, respectively. We present $h_{\mathrm{p}}(t)$, $H_{\mathrm{p}}(t)$, and $H_{\mathrm{p},\infty}$ along with w_{e} in the following theorem.

Theorem 4.1. The expected molecule hitting rate, the expected fraction of absorbed molecules, and the expected asymptotic fraction of absorbed molecules as $t \to \infty$ at an AP-based RX when the molecules are released at the TX at time $t = 0$ are given by

$$h_{\mathrm{p}}(t) = h_{\mathrm{u}}(t, w_{\mathrm{e}}), H_{\mathrm{p}}(t) = H_{\mathrm{u}}(t, w_{\mathrm{e}}), H_{\mathrm{p},\infty} = H_{\mathrm{u},\infty}(w_{\mathrm{e}}), \tag{4.19}$$

respectively, where $h_{\mathrm{u}}(t,w)$, $H_{\mathrm{u}}(t,w)$, and $H_{\mathrm{u},\infty}(w)$ are given by (4.4), (4.5), and (4.10), respectively, and

$$w_{\mathrm{e}} = \frac{D_A G_{\mathrm{p}}}{r_{\mathrm{R}}(r_{\mathrm{R}} - G_{\mathrm{p}})}. \tag{4.20}$$

The expressions for G_{p} are summarised in Table 4.1.

Proof: We note that the diffusion current of molecules across an AP-based RX, denoted by I_{p}, can be obtained by replacing G with G_{p} in (4.13). The ratio between the expected asymptotic fraction of absorbed molecules at an AP-based RX and at a fully absorbing RX is equal to the ratio between the corresponding diffusion currents [65]. Thus, we have

$$\frac{H_{\mathrm{u},\infty}(w_{\mathrm{e}})|_{k_{\mathrm{d}}=0}}{H_{\mathrm{a},\infty}} = \frac{I_{\mathrm{p}}}{I_{\mathrm{a}}}, \tag{4.21}$$

where $H_{\mathrm{u},\infty}(w_{\mathrm{e}})\big|_{k_{\mathrm{d}}=0} = r_{\mathrm{R}}^2 w_{\mathrm{e}} / \left(r_0(w_{\mathrm{e}} r_{\mathrm{R}} + D_A)\right)$ based on (4.10), $H_{\mathrm{a},\infty} = r_{\mathrm{R}}/r_0$ is the asymptotic fraction of absorbed molecules as $t \to \infty$ at a fully absorbing RX [130, Eq. (3.116)], and $I_{\mathrm{a}} = 4\pi D_A r_{\mathrm{R}} C_0$. By solving (4.21), we obtain (4.20). By substituting w_{e} into (4.4), (4.5), and (4.10), we obtain (4.19). ■

4.4 Analysis of the CIR for an MF-Based TX

In this section, we consider an MF-based TX and derive the i) expected molecule hitting rate, ii) expected fraction of molecules absorbed, and iii) expected asymptotic fraction of molecules absorbed as time $t \to \infty$ at an AP-based RX. To this end, we first derive the expected molecule hitting rate at the RX when molecules are uniformly released from a spherical TX membrane with radius r_{T} at time $t = 0$. A uniform release of molecules implies that the likelihood that a molecule is released is identical for any point on the spherical TX surface. We recall that $f_{\mathrm{r}}(t)$ in (3.5) represents the molecule release rate from the MF-based TX. By using $f_{\mathrm{r}}(t)$ and the derived expected hitting rate, we derive the expected CIR between the MF-based TX and the AP-based RX.

4.4.1 Expected Hitting Rate at AP-based RX for Uniform Release of Molecules

The expected CIR analysis of the point TX in Section 4.3 lays the foundation for deriving the expected CIR of the MF-based TX. As vesicles are released from the center of the MF-based TX, molecules are uniformly released from the TX membrane. Therefore, to derive the expected end-to-end CIR between the MF-based TX and the RX, we first calculate the expected CIR when molecules are uniformly released from the TX membrane at time $t = 0$. We denote the expected hitting rate at the RX due to the uniform release of molecules as $h_{\mathrm{s}}(t)$ and present $h_{\mathrm{s}}(t)$ in the following lemma.

Lemma 4.2. The expected molecule hitting rate at an AP-based RX at time t when a spherical TX uniformly releases molecules from its surface at time $t = 0$ is given by

$$h_{\mathrm{s}}(t) = \frac{r_{\mathrm{R}} w_{\mathrm{e}}}{2 r_{\mathrm{T}} r_0} \left[\xi_1(t, r_0 - r_{\mathrm{T}} - r_{\mathrm{R}}) - \xi_1(t, r_0 + r_{\mathrm{T}} - r_{\mathrm{R}}) \right], \tag{4.22}$$

where

$$\xi_1(t,z) = \exp\left(\hat{\gamma}(w_{\mathrm{e}}) z + \zeta(w_{\mathrm{e}}) t\right) \operatorname{erfc}\left(\varpi(w_{\mathrm{e}}) \sqrt{t} + \frac{z}{\sqrt{4 D_A t}} \right) \tag{4.23}$$

with $\varpi(w_{\mathrm{e}}) = \hat{\gamma}(w_{\mathrm{e}}) \sqrt{D_A}$, and $\hat{\gamma}(w_{\mathrm{e}})$ and $\xi(w_{\mathrm{e}})$ are given in Lemma 4.1.

Proof: When molecules are released from an arbitrary point $\hat{\alpha}$ on the membrane of a spherical TX, the expected molecule hitting rate at the RX is obtained by replacing r_0 with $r_{\hat{\alpha}}$ in $h_{\mathrm{p}}(t)$ in (4.19), where $r_{\hat{\alpha}}$ is the distance between point $\hat{\alpha}$ and the center of the RX. Following Appendix A.2, we derive $h_{\mathrm{s}}(t)$ by computing the surface integral of $h_{\mathrm{p}}(t, r_{\hat{\alpha}})$ over the TX membrane, which is given by

$$h_{\mathrm{s}}(t) = \frac{1}{2 r_{\mathrm{T}}} \int_{-r_{\mathrm{T}}}^{r_{\mathrm{T}}} h_{\mathrm{p}}(t, r_{\hat{\alpha}}) \big|_{r_{\hat{\alpha}} = \sqrt{r_{\mathrm{T}}^2 + r_0^2 - 2 r_0 x}} \mathrm{d}x. \tag{4.24}$$

By substituting $h_{\mathrm{p}}(t, r_{\hat{\alpha}})$ given in (4.19) into (4.24), we obtain (4.22). ■

We denote $H_{\mathrm{s}}(t)$ as the expected fraction of absorbed molecules at the RX and present $H_{\mathrm{s}}(t)$ in the following corollary.

Corollary 4.4. The expected fraction of molecules absorbed at an AP-based RX by time t when a spherical TX uniformly releases molecules from its surface at time $t = 0$ is given by

$$H_{\mathrm{s}}(t) = \frac{r_{\mathrm{R}} w_{\mathrm{e}}}{2 r_{\mathrm{T}} r_0 \zeta(w_{\mathrm{e}})} \left[\xi_2(t, r_0 - r_{\mathrm{T}} - r_{\mathrm{R}}) - \xi_2(t, r_0 + r_{\mathrm{T}} - r_{\mathrm{R}}) \right], \tag{4.25}$$

where $\xi_2(t,z)$ is given in

$$\xi_2(t,z) = \exp\left(\hat{\gamma}(w_{\rm e})z + \zeta(w_{\rm e})t\right)\operatorname{erfc}\left(\frac{z}{\sqrt{4D_A t}} + \varpi(w_{\rm e})\sqrt{t}\right) - \frac{1}{2\sqrt{k_{\rm d}}}\exp\left(-z\sqrt{\frac{k_{\rm d}}{D_A}}\right)$$
$$\times\left[\left(\varpi(w_{\rm e}) - \sqrt{k_{\rm d}}\right)\operatorname{erf}\left(\frac{z}{\sqrt{4D_A t}} - \sqrt{k_{\rm d} t}\right) - \left(\varpi(w_{\rm e}) + \sqrt{k_{\rm d}}\right)\left(1 - \exp\left(2z\sqrt{\frac{k_{\rm d}}{D_A}}\right)\right.\right.$$
$$\left.\left.\times\operatorname{erfc}\left(\frac{z}{\sqrt{4D_A t}} + \sqrt{k_{\rm d} t}\right)\right)\right] - \exp\left(-z\sqrt{\frac{k_{\rm d}}{D_A}}\right). \tag{4.26}$$

Proof: We derive $H_{\rm s}(t)$ via $H_{\rm s}(t) = \int_0^t h_{\rm s}(u)\mathrm{d}u$. By substituting (4.22) into this equation, we obtain (4.25). ■

4.4.2 Expected CIR of AP-based RX for MF-Based TX

In this subsection, we derive the expected CIR for an AP-based RX when the molecules are released from an MF-based TX. We denote $h_{\rm MF}(t)$ as the expected molecule hitting rate at the RX at time t when vesicles are released from the center of an MF-based TX at time $t = 0$ and present $h_{\rm MF}(t)$ in the following theorem.

Theorem 4.2. The expected molecule hitting rate at an AP-based RX at time t when vesicles are released from the center of an MF-based TX at time $t = 0$ is given by

$$h_{\rm MF}(t) = \frac{2r_{\rm T}r_{\rm R}k_{\rm f}w_{\rm e}\exp(\zeta(w_{\rm e})t)}{r_0}\sum_{n=1}^{\infty}\frac{\lambda_n^3 j_0(\lambda_n r_{\rm T})}{2\lambda_n r_{\rm T} - \sin(2\lambda_n r_{\rm T})}\left[\xi_3(t, r_0 - r_{\rm T} - r_{\rm R}) - \xi_3(t, r_0 + r_{\rm T} - r_{\rm R})\right], \tag{4.27}$$

where $\xi_3(t,z) = \exp\left(\hat{\gamma}(w_{\rm e})z\right)\sigma_1(t,z)$ with

$$\sigma_1(t,z) = \int_0^t \exp\left(-(\zeta(w_{\rm e}) + D_{\rm v}\lambda_n^2)u\right)\operatorname{erfc}\left(\varpi(w_{\rm e})\sqrt{t-u} + \frac{z}{\sqrt{4D_A(t-u)}}\right)\mathrm{d}u. \tag{4.28}$$

We note that (4.28) can be numerically calculated by the built-in function in Matlab.

Proof: Please see Appendix B.2. ■

We note that (B.3) can be further rewritten as the convolution between $f_{\rm r}(t)$ and $h_{\rm s}(t)$, which indicates that the end-to-end channel between an MF-based TX and an AP-based RX can be regarded as a linear time-invariant (LTI) system with input signal $f_{\rm r}(t)$, system impulse response $h_{\rm s}(t)$, and output signal $h_{\rm MF}(t)$. We further denote $H_{\rm MF}(t)$ as the expected fraction of absorbed molecules at the RX by time t when vesicles are released from the center of the MF-based TX at time $t = 0$ and present $H_{\rm MF}(t)$ in the following corollary.

Corollary 4.5. The expected fraction of molecules absorbed at an AP-based RX by time t when vesicles are released from the center of an MF-based TX at time $t = 0$ is given by

$$H_{\mathrm{MF}}(t) = \frac{2r_{\mathrm{T}}r_{\mathrm{R}}k_{\mathrm{f}}w_{\mathrm{e}}}{r_0\zeta(w_{\mathrm{e}})}\sum_{n=1}^{\infty}\frac{\lambda_n^3 j_0(\lambda_n r_{\mathrm{T}})}{2\lambda_n r_{\mathrm{T}} - \sin(2\lambda_n r_{\mathrm{T}})}\left[\xi_4(t, r_0 - r_{\mathrm{T}} - r_{\mathrm{R}}) - \xi_4(t, r_0 + r_{\mathrm{T}} - r_{\mathrm{R}})\right], \quad (4.29)$$

where $\xi_4(t,z)$ is given by

$$\xi_4(t,z) = \exp(\hat{\gamma}(w_{\mathrm{e}})z + \zeta(w_{\mathrm{e}})t)\sigma_1(t,z) - \frac{1}{2\sqrt{k_{\mathrm{d}}}}\exp\left(-z\sqrt{\frac{k_{\mathrm{d}}}{D_A}}\right)\left[\left(\varpi(w_{\mathrm{e}}) - \sqrt{k_{\mathrm{d}}}\right)\sigma_2(t,z)\right.$$
$$\left. - \left(\varpi(w_{\mathrm{e}}) + \sqrt{k_{\mathrm{d}}}\right)\left(\frac{1}{D_{\mathrm{v}}\lambda_n^2}\left(1 - \exp(-D_{\mathrm{v}}\lambda_n^2 t)\right) - \exp\left(2z\sqrt{\frac{k_{\mathrm{d}}}{D_A}}\right)\sigma_3(t,z)\right)\right] - \frac{\exp\left(-z\sqrt{\frac{k_{\mathrm{d}}}{D_A}}\right)}{D_{\mathrm{v}}\lambda_n^2}$$
$$\times\left(1 - \exp\left(-D_{\mathrm{v}}\lambda_n^2 t\right)\right), \quad (4.30)$$

with $\sigma_2(t,z) = \int_0^t \mathrm{erf}\left(\frac{z}{\sqrt{4D_A(t-u)}} - \sqrt{k_{\mathrm{d}}(t-u)}\right)\exp(-D_{\mathrm{v}}\lambda_n^2 u)\mathrm{d}u$ and

$$\sigma_3(t,z) = \int_0^t \exp\left(-D_{\mathrm{v}}\lambda_n^2 u\right)\mathrm{erfc}\left(\frac{z}{\sqrt{4D_A(t-u)}} + \sqrt{k_{\mathrm{d}}(t-u)}\right)\mathrm{d}u. \quad (4.31)$$

We note that $\sigma_2(t,z)$ and (4.31) can be numerically calculated by the built-in function *integral* in Matlab.

Proof: We derive $H_{\mathrm{MF}}(t)$ via $H_{\mathrm{MF}}(t) = \int_0^t h_{\mathrm{MF}}(u)\mathrm{d}u = \int_0^t f_{\mathrm{r}}(u)H_{\mathrm{s}}(t-u)\mathrm{d}u$. By substituting (3.5) and (4.25) into this expression, we obtain (4.29). ■

As time $t \to \infty$, the expected fraction of absorbed molecules at the RX, denoted by $H_{\mathrm{MF},\infty}$, approaches a constant value. We present $H_{\mathrm{MF},\infty}$ in the following corollary.

Corollary 4.6. As $t \to \infty$, the expected asymptotic fraction of absorbed molecules at an AP-based RX when vesicles are released from the center of an MF-based TX at time $t = 0$ is given by

$$H_{\mathrm{MF},\infty} = \frac{r_{\mathrm{R}}w_{\mathrm{e}}}{2r_{\mathrm{T}}r_0\zeta(w_{\mathrm{e}})}\left(\frac{\varpi(w_{\mathrm{e}})}{\sqrt{k_{\mathrm{d}}}} - 1\right)\left[\exp\left(-(r_0 - r_{\mathrm{T}} - r_{\mathrm{R}})\sqrt{\frac{k_{\mathrm{d}}}{D_A}}\right) - \exp\left(-(r_0 + r_{\mathrm{T}} - r_{\mathrm{R}})\sqrt{\frac{k_{\mathrm{d}}}{D_A}}\right)\right]. \quad (4.32)$$

Proof: Please see Appendix B.3. ■

4.5 Analysis of Error Performance

In this section, we consider a sequence of bits sent from the TX to the RX as described in Section 4.2.3 and derive the resulting BER. We also calculate the optimal decision threshold that minimizes the BER at the RX. We note that all results in this section are valid for both point TXs and MF-based TXs.

For simplicity, we use $H(t)$ to represent both $H_{\mathrm{p}}(t)$ and $H_{\mathrm{MF}}(t)$, where we recall that $H_{\mathrm{p}}(t)$ and $H_{\mathrm{MF}}(t)$ represent the fraction of molecules expected to be absorbed by the RX when molecules are released from a point TX and an MF-based TX, respectively. We also use N_{T} to represent N_σ for a point TX and $N_{\mathrm{v}}\eta$ for an MF-based TX, where we recall that η is the number of molecules stored in each vesicle. Thereby, N_σ represents the total number of molecules released from the TX to transmit bit 1 in one bit interval. The fraction of molecules absorbed during the qth bit interval for the molecules released at the beginning of the gth bit interval, $1 \leq g \leq q$, is given by $H((q-g+1)T_{\mathrm{b}}) - H((q-g)T_{\mathrm{b}})$. We denote N_q as the total number of molecules absorbed during the qth bit interval. As we assume that the diffusion processes of all molecules are independent and all molecules have the same probability of being absorbed, N_q can be approximated as a Poisson random variable (RV) when the number of emitted molecules is large and the success probability of molecules being absorbed is small [134]. Therefore, we model N_q as $N_q \sim \mathrm{Poiss}(\chi)$, where $\mathrm{Poiss}(\cdot)$ denotes a Poisson distribution and χ is given by

$$\chi = N_{\mathrm{T}} b_q H(T_{\mathrm{b}}) + \underbrace{N_{\mathrm{T}} \sum_{g=1}^{q-1} b_g \left[H((q-g+1)T_{\mathrm{b}}) - H((q-g)T_{\mathrm{b}}) \right]}_{\mathrm{ISI}}. \tag{4.33}$$

Recall that b_g is the gth transmitted bit. From (4.33), we observe that the demodulation accuracy of b_q is impacted by inter-symbol interference (ISI). Furthermore, this accuracy is also affected by the random diffusion of molecules since N_q is a RV.

At the RX, we adopt a threshold detector that compares N_q with a decision threshold for demodulation of b_q. We model the threshold detector as follows

$$\hat{b}_q = \begin{cases} 1, & \text{if } N_q \geq \Psi, \\ 0, & \text{if } N_q < \Psi, \end{cases} \tag{4.34}$$

where $\hat{b}_q$ is the demodulated bit for b_q and Ψ is the decision threshold. We then denote $\Phi[q|\mathbf{b}_{1:q-1}]$ as the BER of the qth bit given the previously transmitted sequence $\mathbf{b}_{1:q-1}$. According to (4.34), $\Phi[q|\mathbf{b}_{1:q-1}]$ is given by

$$\Phi[q|\mathbf{b}_{1:q-1}] = P_1 \Pr\left(N_q < \Psi | b_q = 1, \mathbf{b}_{1:q-1}\right) + P_0 \Pr\left(N_q \geq \Psi | b_q = 0, \mathbf{b}_{1:q-1}\right). \tag{4.35}$$

We denote $\Psi^*[q|\mathbf{b}_{1:q-1}]$ as the optimal decision threshold that minimizes $\Phi[q|\mathbf{b}_{1:q-1}]$. Ac-

cording to [148, Eq. (25)], we obtain $\Psi^*[q|\mathbf{b}_{1:q-1}]$ as

$$\Psi^*[q|\mathbf{b}_{1:q-1}] = \left\lceil \frac{\ln \frac{P_0}{P_1} + N_A H(\phi)}{\ln \frac{\chi_1|\mathbf{b}_{1:q-1}}{\chi_0|\mathbf{b}_{1:q-1}}} \right\rceil, \tag{4.36}$$

where $\chi_1|\mathbf{b}_{1:q-1}$ and $\chi_0|\mathbf{b}_{1:q-1}$ are the expected total number of molecules absorbed within the qth bit interval assuming that $b_q = 1$ and $b_q = 0$ was transmitted, respectively. They are given by

$$\chi_1|\mathbf{b}_{1:q-1} = N_{\mathrm{T}} \sum_{g=1}^{q-1} b_g \left(H((q-g+1)T_{\mathrm{b}}) - H((q-g)T_{\mathrm{b}})\right) + N_A H(T_{\mathrm{b}}) \tag{4.37}$$

and

$$\chi_0|\mathbf{b}_{1:q-1} = N_{\mathrm{T}} \sum_{g=1}^{q-1} b_g \left(H((q-g+1)T_{\mathrm{b}}) - H((q-g)T_{\mathrm{b}})\right), \tag{4.38}$$

where $\lceil \cdot \rceil$ represents the ceiling function [149].

We further denote the average BER over all realisations of $\mathbf{b}_{1:q}$ and all bits $b_q, q \in \{1, ..., Q\}$, by $\overline{\Phi}$, where we recall that Q represents the number of transmitted bits. Then, $\overline{\Phi}$ is given by

$$\overline{\Phi} = \frac{1}{Q} \sum_{q=1}^{Q} \frac{\sum_{\mathbf{b}_{1:q-1}} \Phi[q|\mathbf{b}_{1:q-1}]}{2^{q-1}}. \tag{4.39}$$

Furthermore, the average optimal decision threshold that minimizes $\overline{\Phi}$ is denoted by $\overline{\Psi}^*$. Mathematically, we have

$$\overline{\Psi}^* = \arg\min_{\Psi} \overline{\Phi}. \tag{4.40}$$

We note that the optimization of $\overline{\Psi}^*$ in (4.40) can be performed numerically by a simple one-dimensional search.

4.6 Numerical Results

In this section, we present numerical results to validate our theoretical analysis and to offer insights for MC system design. Specifically, we use PBSs to simulate the random diffusion of molecules. In our simulations, if the position of a molecule at the end of the current simulation step is inside the RX volume, we assume that this molecule has hit the RX surface in this simulation step. The coordinates of the hitting points on the RX surface are calculated by (3.36), (3.37), and (3.38). If the coordinates of the hitting point of a molecule are inside an

Table 4.2: Simulation Parameters for Numerical Results

Parameter	Variable	Value	Reference
Ratio of the total area of APs to the RX surface	$\mathcal{A}$	0.05, 0.1, 0.15	[144]
Number of APs	N_{p}	1∼1000	[150]
Radius of the RX	r_{R}	10 μm	[151]
Distance between the center of RX and point TX/center of MF-based TX	r_0	20 μm	[60]
Number of emitted molecules from the point TX for bit 1	N_A	1000	[59]
Rate constant of molecule degradation	k_{d}	0.8 s^{-1}	[67]
Molecule diffusion coefficient	D_A	79.4 $\mu\mathrm{m}^2/\mathrm{s}$	[60]
Radius of the MF-based TX	r_{T}	5 μm	[151]
Number of released vesicles for bit 1	N_{v}	200	
Number of molecules stored in each vesicle	η	5	
Diffusion coefficient of vesicles	D_{v}	9 $\mu\mathrm{m}^2/\mathrm{s}$	[114]
Forward reaction rate constant of vesicles and TX membrane	k_{f}	30 $\mu\mathrm{m}/\mathrm{s}$	
Length of binary bit sequence	Q	10	
Bit interval length	T_{b}	0.8 s	
Probability of transmitting 0/1	P_0/P_1	0.5	

AP, we treat this molecule as an absorbed molecule. Otherwise, the molecule is reflected back to the position it was at the start of the current simulation step [65]. To model the location of the point TX (or the center of the MF-based TX), we fix the distance between the point TX (or the center of the MF-based TX) and the RX to r_0 and randomly generate the location of the center of the TX for each realisation. The simulation framework for modelling the molecule release for the MF-based TX is detailed in Section 3.6. We choose the simulation time step as $\Delta t_{\mathrm{s}} = 10^{-7}$ s and all results are averaged over 1000 realisations. Throughout this section, we set the simulation parameters as shown in Table 4.2, unless otherwise stated. We specify the value of N_{p} and the locations of the APs in each figure. From Figs. 4.3, 4.5, and 4.9, we observe that the simulation results (denoted by markers) match well with the derived analytical curves (denoted by solid and dashed lines) generated based on the results presented in Sections 4.3 and 4.4, which validates the accuracy of our CIR analysis. In all figures, we apply (4.16) to generate the analytical curves if the APs have identical sizes, (4.14) if the APs have different sizes, and (4.18) if there is a single AP, unless otherwise stated.

4.6.1 Point TX

In this subsection, we focus on the point TX model. We first investigate the range of $\mathcal{A}$ for which our analytical expressions are accurate. In Fig. 4.2, we plot $N_A H_{\mathrm{p},\infty}$ versus $\mathcal{A}$ for different values of N_{p}. First, when $N_{\mathrm{p}} = \{11, 81, 201\}$, we observe that the simulation results

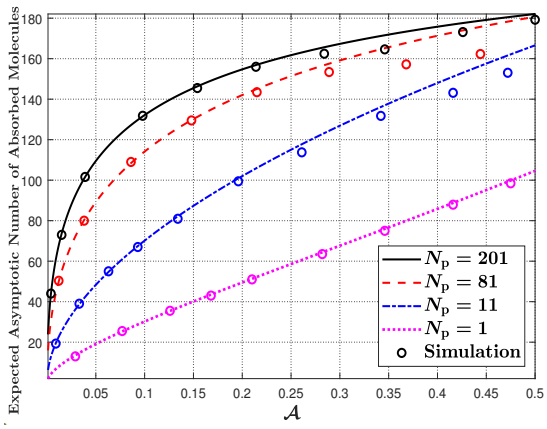

Figure 4.2: Expected asymptotic number of absorbed molecules versus $\mathcal{A}$ for different values of N_p, where APs have identical sizes and are evenly distributed.

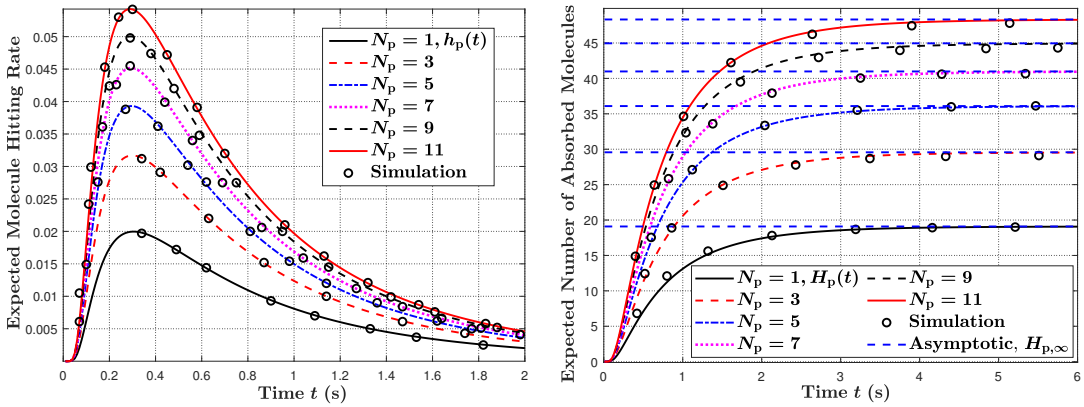

(a) Expected molecule hitting rate

(b) Expected number of absorbed molecules

Figure 4.3: Expected molecule hitting rate at time t and expected number of molecules absorbed until time t versus time t for different values of N_p and $\mathcal{A} = 0.05$.

match well with the analytical curves for $\mathcal{A} \leq 0.2$. As $\mathcal{A}$ increases, a gap between the analytical curves and simulation results emerges. This is because the range of $\mathcal{A}$, where the CIR analysis is accurate, is limited since we ignore the term $\mathcal{O}\left(\kappa^2 \ln\left(\frac{\kappa}{2}\right)\right)$ in (4.14) when calculating G_p. We note that the range of $\mathcal{A}$ for which our analytical results are accurate aligns with the typical coverage of cell membranes with receptors. For example, the ratio of the total area of a liver cell covered by insulin receptors to the total cell surface is around 0.0026 [152, 153], which is well within the range of $\mathcal{A}$ where our analytical expressions are valid. Second, we observe that the simulation results always match well with the analytical curve when $N_p = 1$. This is because $\mathcal{O}(\hat{\kappa}^3 \ln \hat{\kappa})$ in (4.18) has a higher order than $\mathcal{O}\left(\hat{\kappa}^2 \ln\left(\frac{\hat{\kappa}}{2}\right)\right)$ in (4.14) such that (4.18) is accurate even when the AP has a large size.

In Fig. 4.3(a), we show the expected molecule hitting rate at the RX at time t, and in Fig.

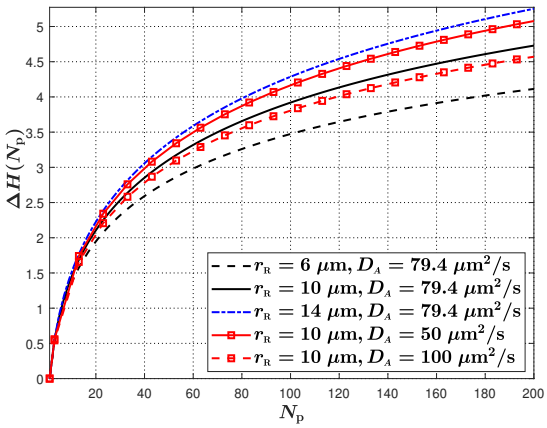

Figure 4.4: $\Delta H(N_{\mathrm{p}})$ versus N_{p} for varying r_{R} and D_A, where $\mathcal{A} = 0.05$, identical APs are evenly distributed on the RX surface.

4.3(b), we depict the expected number of molecules absorbed at the RX by time t. We set $\mathcal{A} = 0.05$ and increase the number of APs from 1 to 11. All APs have the same size and are evenly distributed on the RX surface. We observe that the expected hitting rate in Fig. 4.3(a) and the expected number of absorbed molecules in Fig. 4.3(b) increase with N_{p}. This behaviour is expected since a larger number of APs on the RX surface can absorb more molecules.

To further investigate the observation that the number of absorbed molecules increases with increasing N_{p}, we define the relative increase in the number of absorbed molecules as N_{p} increases, denoted by $\Delta H(N_{\mathrm{p}})$, as follows

$$\begin{aligned}\Delta H(N_{\mathrm{p}}) &= \frac{H_{\mathrm{p},\infty} - \tilde{H}_{\mathrm{p},\infty}}{\tilde{H}_{\mathrm{p},\infty}} \\ &= \frac{w_{\mathrm{e},N_{\mathrm{p}}}\zeta(w_{\mathrm{e},1})\left(\hat{\gamma}(w_{\mathrm{e},N_{\mathrm{p}}}) - \sqrt{\frac{k_{\mathrm{d}}}{D_A}}\right)}{w_{\mathrm{e},1}\zeta(w_{\mathrm{e},N_{\mathrm{p}}})\left(\hat{\gamma}(w_{\mathrm{e},1}) - \sqrt{\frac{k_{\mathrm{d}}}{D_A}}\right)} - 1, \end{aligned} \tag{4.41}$$

where $\tilde{H}_{\mathrm{p},\infty} = H_{\mathrm{p},\infty}|_{N_{\mathrm{p}}=1}$ represents the expected asymptotic number of absorbed molecules when $N_{\mathrm{p}} = 1$, and $w_{\mathrm{e},1}$ and $w_{\mathrm{e},N_{\mathrm{p}}}$ represent the effective reaction rate constants of RXs with a single AP and with N_{p} APs, respectively. In Fig. 4.4, we plot $\Delta H(N_{\mathrm{p}})$ versus N_{p} for different r_{R} and D_A and note that larger $\Delta H(N_{\mathrm{p}})$ imply a larger relative increase in the number of absorbed molecules. First, we observe that $\Delta H(N_{\mathrm{p}})$ increases with increasing N_{p}. This is because larger N_{p} result in more absorbed molecules. We also observe that the slope of $\Delta H(N_{\mathrm{p}})$ becomes smaller as N_{p} becomes larger, which indicates that the increase in the number of absorbed molecules becomes slower for larger N_{p}. Second, we observe that $\Delta H(N_{\mathrm{p}})$ increases if r_{R} increases and N_{p} is fixed. This is because a larger RX leads to a larger AP area such that the relative increase in the number of absorbed molecules is larger. Third, we observe that $\Delta H(N_{\mathrm{p}})$ increases if D_A decreases. This is because larger N_{p} give slowly diffusing molecules

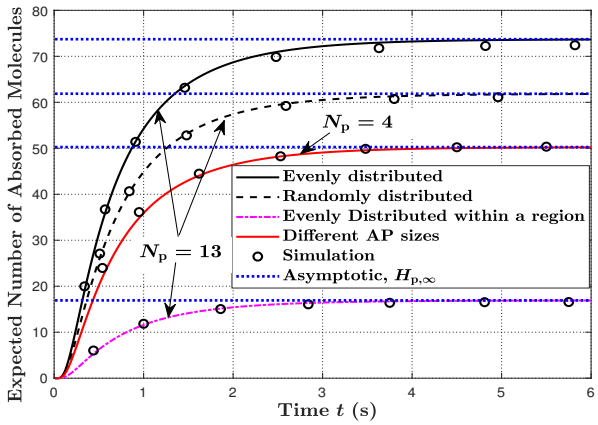

Figure 4.5: Expected number of molecules absorbed by the RX until time t versus time t for different distributions and sizes of APs, where $\mathcal{A} = 0.1$.

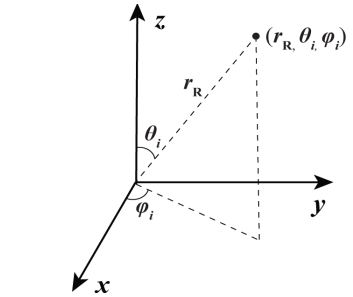

(a) Illustration of the spherical coordinates.

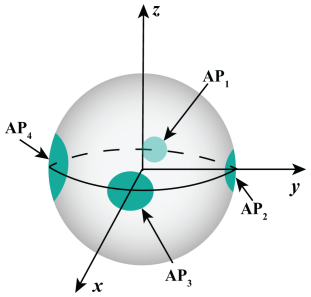

(b) Locations of the centers of the APs on the RX surface in Fig. 4.5

Figure 4.6: Illustration of the spherical coordinates and the locations of the centers of the APs on the RX surface in Fig. 4.5, where $N_{\mathrm{p}} = 4$ and the APs have different sizes.

more chances to be absorbed than fast diffusing molecules, such that the relative increase in the number of absorbed molecules for smaller D_A is larger.

In Fig. 4.5, we evaluate the impact of different AP sizes and distributions on the RX surface. First, we define $\mathcal{A}_i$ as the ratio of the area of AP_i to the area of the RX surface and set $N_{\mathrm{p}} = 4$, $\mathcal{A}_1 = 0.01$, $\mathcal{A}_2 = 0.02$, $\mathcal{A}_3 = 0.03$, and $\mathcal{A}_4 = 0.04$ to validate our analytical expressions when the APs have different sizes. Then, we set the locations of the four APs to $\vec{l}_1 = [10\,\mu\mathrm{m}, \pi/2, \pi]$, $\vec{l}_2 = [10\,\mu\mathrm{m}, \pi/2, \pi/2]$, $\vec{l}_3 = [10\,\mu\mathrm{m}, \pi/2, 0]$, and $\vec{l}_4 = [10\,\mu\mathrm{m}, \pi/2, 3\pi/2]$. In Fig. 4.6(a), we show θ_i and φ_i of the spherical coordinates, and in Fig. 4.6(b), we depict the locations of the considered four APs. We observe from Fig. 4.5 that the simulation results match well with the analytical curves, which demonstrates the accuracy of (4.19) for APs of different sizes. Second, we set $\mathcal{A} = 0.1$ and $N_{\mathrm{p}} = 13$ for different AP distributions and assume that the APs have identical size. Here, we consider three types of AP distributions: i) APs evenly distributed across the entire RX surface, ii) APs randomly distributed across the entire

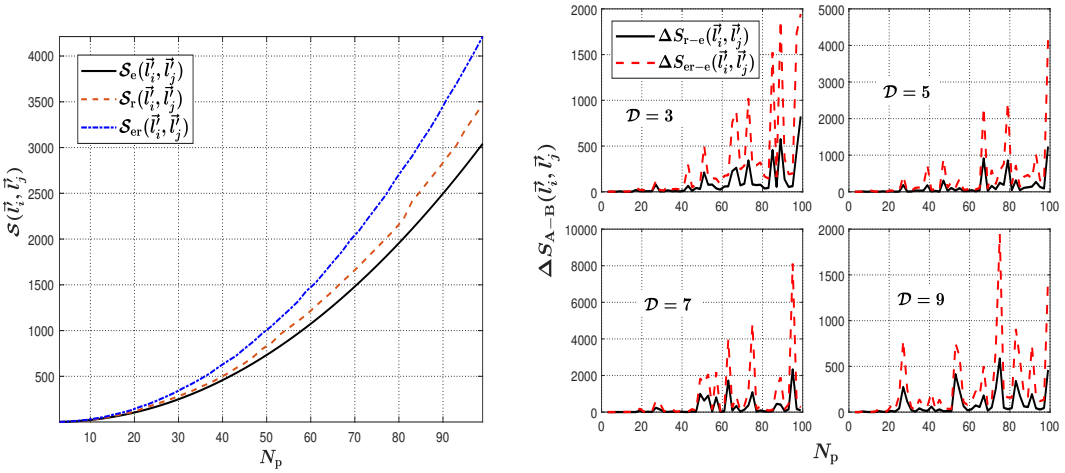

(a) APs have the identical size

(b) APs have different sizes whose variance is determined by $\mathcal{D}$.

Figure 4.7: (a): $\mathcal{S}(\vec{l}_i',\vec{l}_j')$ versus $N_{\rm p}$ for different AP distributions on the RX surface. (b): $\Delta\mathcal{S}_{\rm A-B}(\vec{l}_i',\vec{l}_j')$ versus $N_{\rm p}$. We set $\mathcal{A}=0.1$.

RX surface, and iii) APs evenly distributed within a region of the RX surface. In this chapter, we apply the Fibonacci lattice [154] to determine the locations of the evenly distributed APs across the entire RX surface. Specifically, the location of AP_i is given by

$$\theta_i = \frac{\pi}{2} - \arcsin\left(\frac{2(i-\mathcal{B}-1)}{N_{\rm p}}\right), \varphi_i = \frac{4\pi(i-\mathcal{B}-1)}{1+\sqrt{5}}, \tag{4.42}$$

where integer $\mathcal{B}$ is given by $\mathcal{B}=(N_{\rm p}-1)/2$. The locations of evenly distributed APs across the entire RX surface can also be generated by the built-in function *SpherePoints* in Mathematica. For the APs evenly distributed within a region of the RX surface, we assume that the APs are distributed within the area defined by $\theta_i \in [2.812, 3.471]$ and $\varphi_i \in [0, 2\pi]$. From Fig. 4.5, we observe that APs evenly distributed across the entire RX surface yield a larger expected number of absorbed molecules compared to the other two distributions. We next explain this observation from two perspectives:

- Theoretical perspective: According to (4.19), the expected number of absorbed molecules is directly determined by $w_{\rm e}$. In particular, a larger value of $w_{\rm e}$ results in a larger number of molecules expected to be absorbed by the RX. Moreover, based on (4.20), we observe that $w_{\rm e}$ is a monotonically increasing function with respect to $G_{\rm p}$. Furthermore, we set $\mathcal{S}(\vec{l}_i',\vec{l}_j') = \sum_{i=1}^{N_{\rm p}}\sum_{j=i+1}^{N_{\rm p}} m_i m_j \mathcal{F}(\vec{l}_i',\vec{l}_j')$, where $\mathcal{F}(\vec{l}_i',\vec{l}_j')$ is given in (4.15). In (4.14), we observe that only $\mathcal{S}(\vec{l}_i',\vec{l}_j')$ is related to the distributions of the APs, and a smaller $\mathcal{S}(\vec{l}_i',\vec{l}_j')$ leads to a larger $G_{\rm p}$. Therefore, the distribution of APs that results in a smaller

$\mathcal{S}(\vec{l}_i',\vec{l}_j')$ is expected to lead to a larger number of absorbed molecules at the RX. To compare $\mathcal{S}(\vec{l}_i',\vec{l}_j')$ for the three considered distributions, we write $\mathcal{S}(\vec{l}_i',\vec{l}_j')$ as $\mathcal{S}_{\rm e}(\vec{l}_i',\vec{l}_j')$ and $\mathcal{S}_{\rm r}(\vec{l}_i',\vec{l}_j')$ if the APs are evenly and randomly distributed across the entire RX surface, respectively, and write $\mathcal{S}(\vec{l}_i',\vec{l}_j')$ as $\mathcal{S}_{\rm er}(\vec{l}_i',\vec{l}_j')$ if the APs are evenly distributed within a region of the RX surface. Moreover, we define $\Delta\mathcal{S}_{\rm A-B}(\vec{l}_i',\vec{l}_j') = \mathcal{S}_{\rm A}(\vec{l}_i',\vec{l}_j') - \mathcal{S}_{\rm B}(\vec{l}_i',\vec{l}_j')$, $A,B \in \{\rm r,e,er\}$, to evaluate the difference between the $\mathcal{S}(\vec{l}_i',\vec{l}_j')$ for two different distributions. In Fig. 4.7(a), we plot $\mathcal{S}_{\rm e}(\vec{l}_i',\vec{l}_j')$, $\mathcal{S}_{\rm r}(\vec{l}_i',\vec{l}_j')$, and $\mathcal{S}_{\rm er}(\vec{l}_i',\vec{l}_j')$ versus $N_{\rm p}$ for APs of identical size, and in Fig. 4.7(b), we show $\Delta\mathcal{S}_{\rm A-B}(\vec{l}_i',\vec{l}_j')$ versus $N_{\rm p}$ for APs of different sizes. For APs evenly distributed within a region, we set the size of the area of this region to 40% of the entire area of the RX surface. For APs of different sizes, we randomly generate $N_{\rm p}$ integers from 1 to $\mathcal{D}$ and denote $\mathcal{G}_i$ as the ith integer. We calculate $\mathcal{A}_i$ as $\mathcal{A}_i = \mathcal{A}\mathcal{G}_i / \sum_{i=1}^{N_{\rm p}} \mathcal{G}_i$. Therefore, the variance of the size of the APs increases with $\mathcal{D}$. In Fig. 4.7(a), we observe that $\mathcal{S}_{\rm e}(\vec{l}_i',\vec{l}_j')$ is always smaller than $\mathcal{S}_{\rm r}(\vec{l}_i',\vec{l}_j')$ and $\mathcal{S}_{\rm er}(\vec{l}_i',\vec{l}_j')$. In Fig. 4.7(b), we apply different values of $\mathcal{D}$ and observe that $\mathcal{S}_{\rm r-e}(\vec{l}_i',\vec{l}_j') > 0$ and $\mathcal{S}_{\rm er-e}(\vec{l}_i',\vec{l}_j') > 0$ for all $N_{\rm p}$ and $\mathcal{D}$. These observations imply that, for evenly distributed APs, $\mathcal{S}(\vec{l}_i',\vec{l}_j')$ is always smaller than for randomly distributed APs and APs evenly distributed within a region, regardless of whether the APs have identical size or different sizes. Therefore, evenly distributed APs result in a larger number of absorbed molecules than the other two distributions.

- Physical perspective: Evenly distributed APs ensure that the APs are equally spaced covering the entire RX surface. Thus, for most locations of the TX, there are APs located in the region closest to the TX such that the probability that a molecule hits an AP is maximized. When the APs are randomly distributed or evenly distributed within a region, only those TX locations that happen to be close to a region on the RX surface with APs have a high probability of molecules hitting an AP, while other TX locations have a low probability. Therefore, the expected probability of molecules hitting an AP for randomly distributed APs and APs distributed within a region is lower than that for evenly distributed APs.

We recall that when the APs have the same size and are evenly distributed on the RX surface, $G_{\rm p}$ in (4.16) can be further simplified to (4.17). To verify (4.17), in Fig. 4.8, we plot $N_A H_{\rm p,\infty}$, i.e., the expected asymptotic number of absorbed molecules, versus $N_{\rm p}$ for different values of r_0 and $k_{\rm d}$, where $G_{\rm p}$ in $H_{\rm p,\infty}$ is given by (4.16) and (4.17), respectively. We observe that the gap between $H_{\rm p,\infty}$ calculated based on (4.16) and (4.17) is extremely small, which confirms the accuracy of (4.17).

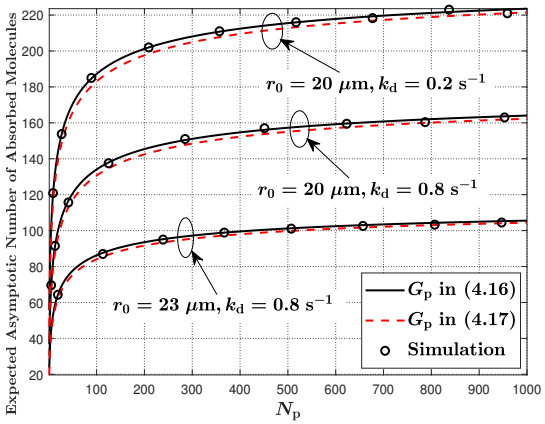

Figure 4.8: Expected asymptotic number of absorbed molecules versus N_p for different values of r_0 and k_d, where $\mathcal{A} = 0.15$ and APs of identical size are evenly distributed on the RX surface.

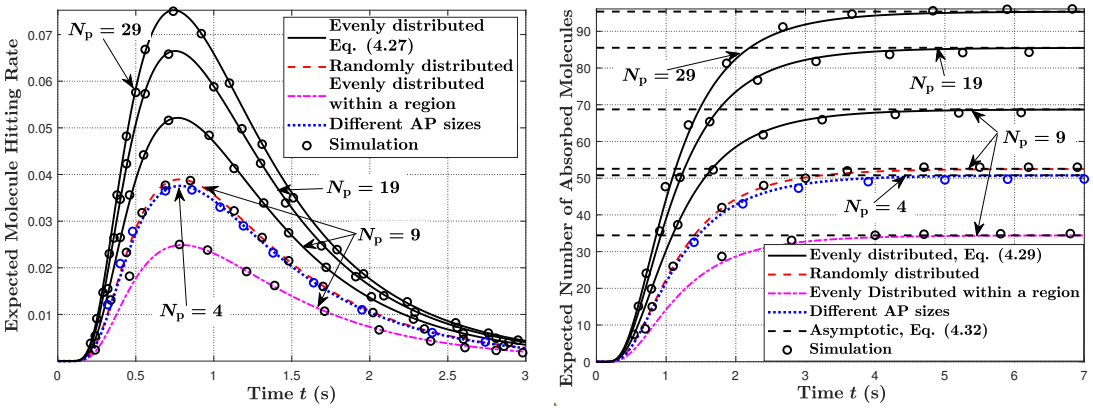

(a) Expected molecule hitting rate

(b) Expected number of absorbed molecules

Figure 4.9: Expected molecule hitting rate at time t and expected number of molecules absorbed by the RX until time t versus time t for different numbers, locations, and sizes of APs, where $\mathcal{A} = 0.1$.

4.6.2 MF-based TX

In this subsection, we consider the MF-based TX. In Fig. 4.9(a), we verify (4.27), (4.29), and (4.32) by depicting the expected molecule hitting rate versus time t, and in Fig. 4.9(b), we show the expected number of absorbed molecules versus time t for different numbers, locations, and sizes of APs. We use the same AP locations and sizes as in Fig. 4.5, considering APs evenly distributed within a region and APs having different sizes. From Fig. 4.9, we observe that the expected molecule hitting rate and the expected number of absorbed molecules increase with increasing N_p. We also observe that evenly distributed APs achieve a larger molecule hitting rate and a larger number of absorbed molecules than randomly distributed APs and APs evenly distributed within a region. These observations are consistent with the observations for point TXs.

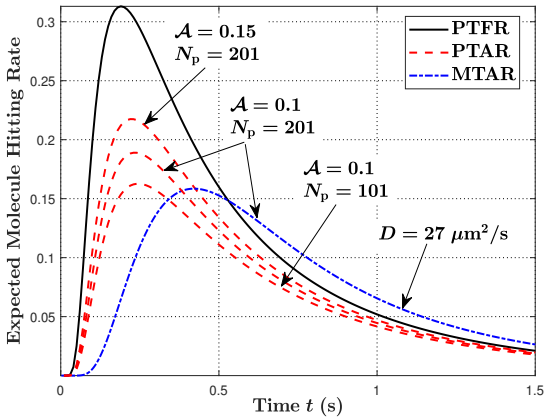

Figure 4.10: Expected molecule hitting rate versus time t for three different TX-RX models, where identical APs are evenly distributed on the RX surface.

4.6.3 Comparison of Different TX-RX Models

In this subsection, we compare three different combinations of TXs and RXs, namely i) a point TX and a fully absorbing RX (referred to as PTFR), ii) a point TX and an AP-based RX (referred to as PTAR), and iii) an MF-based TX and an AP-based RX (referred to as MTAR). We compare these three combinations with respect to the CIRs and average BERs.

In Fig. 4.10, we plot the expected molecule hitting rate versus time t for the three considered combinations of TXs and RXs, where the expected molecule hitting rate of PTFR is given by [59, Eq. (9)]. First, by comparing the molecule hitting rates of PTFR and PTAR, we observe that the peak value of the molecule hitting rate decreases and the tail becomes shorter when a fully absorbing RX is replaced by an AP-based RX. This is due to the fact that the limited coverage and the finite number of APs on the RX surface reduce the number of molecules absorbed by the RX within a time period. We also observe that, for the PTAR model, the peak value of the molecule hitting rate becomes larger and the tail is longer when $\mathcal{A}$ or the number of APs increases. Second, by comparing the molecule hitting rates of PTFR and MTAR, we observe that the peak value of the molecule hitting rate of MTAR is smaller and the tail is longer. This is because the release of molecules from the MF-based TX is slower compared to the point TX, and the absorption of molecules at the AP-based RX is limited compared to the fully absorbing RX. In summary, compared with the ideal PTFR model, the practical MFAR model results in a smaller amplitude and a longer duration of the molecule hitting rate curve.

We show the average BER in (4.39) versus the decision threshold in Fig. 4.11(a) and versus the bit interval length in Fig. 4.11(b) for the three considered TX-RX models. Due to the long PBS times, for this figure, we employ Monte Carlo simulation where the Poisson approximation is used to generate the number of absorbed molecules. We note that the derived analytical result for the CIR has been verified by PBSs and the Poisson approximation for the

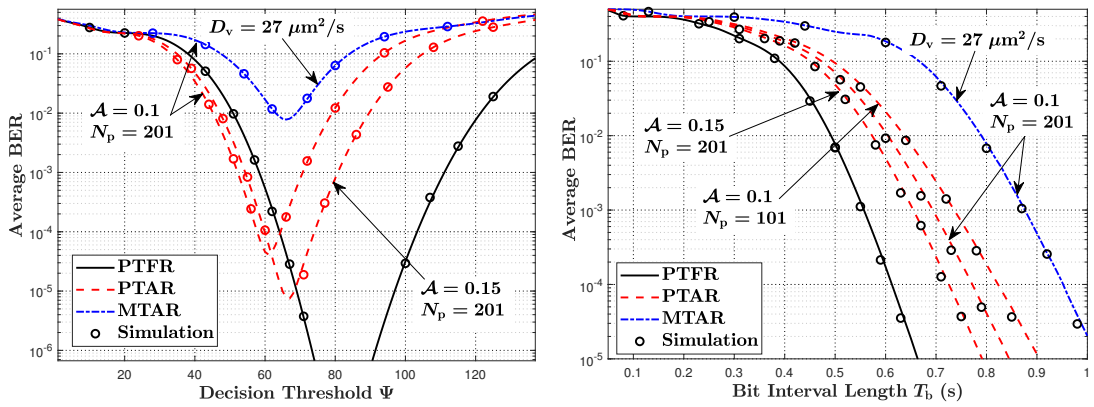

(a) Average BER versus Ψ

(b) Average BER versus T_b

Figure 4.11: (a): Average BER versus decision threshold Ψ for three TX-RX models. (b): Average BER versus bit interval length T_b for three TX-RX models, where information is demodulated at the average optimal decision threshold $\overline{\Psi}^*$. Identical APs are evenly distributed on the RX surface.

number of absorbed molecules has been widely adopted in previous studies [45]. The average BER for PTFR is plotted by replacing $H(t)$ in Section 4.5 with [59, Eq. (12)]. In Fig. 4.11(b), detection is performed based on $\overline{\Psi}^*$ obtained in (4.40). First, in Fig. 4.11(a), by comparing the average BERs for PTFR and PTAR, we observe that the BER for PTAR is slightly lower when Ψ is small and becomes much higher when Ψ is large. This is because the number of absorbed molecules is lower and the ISI is smaller for AP-based RXs. Hence, the average BER is lower when the decision threshold is small. Second, in Fig. 4.11(a), we observe that the lowest average BER of PTFR is much smaller than that of PTAR and MTAR. This is not surprising as PTFR is the simplest model with the lowest practicality. From a theoretical perspective, the low BER of PTFR is achieved because of the low proportion of interference molecules received by the fully absorbing RX. Third, in Fig. 4.11(b), we observe that the average BER of PTFR is always lower than that of PTAR when detection is performed based on the optimal decision threshold. Third, in both Fig. 4.11(a) and Fig. 4.11(b), we observe that the average BER of MTAR is much larger than that of PTFR. This is because the release of molecules from the MF-based TX is slower compared to the point TX, and the absorption of molecules at the AP-based RX is limited compared to the fully absorbing RX. The second and third observations imply that the widely-investigated BER analysis of the ideal PTFR model is not accurate when we consider a more practical combined TX-RX model.

4.7 Conclusion

In this chapter, we studied RXs that are covered by multiple heterogeneous APs with different sizes and arbitrary locations. We also considered two TXs models, namely point TXs and

MF-based TXs. We obtained closed-form expressions for the expected CIR in the presence of molecule degradation. Our simulation results confirmed the accuracy of the derived CIR expressions. Using numerical results, we showed that when the ratio of the total area of the APs to the area of the RX surface is fixed, the expected number of absorbed molecules increases with the number of APs. Moreover, we compared three spatial AP distributions and showed that evenly distributed APs result in a larger number of absorbed molecules than the other two considered distributions. In addition, we compared three combinations of TXs and RXs. Our results showed that compared to the ideal model consisting of a point TX and fully absorbing RX, the practical model with MF-based TX and AP-based RX results in a much lower CIR and a much higher average BER. This underscores the limitations of the ideal TX-RX model for application in practical MC systems.

Chapter 5

1D Molecular Communication with Two Absorbing Receivers

5.1 Introduction

In this chapter, we consider a 1D environment where one TX communicates between two fully-absorbing RXs. The 1D environment is worthy of investigation since it can approximate many practical biological channels such as capillaries, blood vessels, active transportation channels, and communication on bio-chips [106, 107]. Moreover, we emphasise that the 1D diffusion channel has been frequently applied to investigate several aspects of MC in some publications, e.g., [155, 156, 157]. Specifically, we consider two models. The first model considers that the TX impulsively releases molecules into the environment. By considering molecular degradation in the environment, we provide closed-form expressions for the fraction of molecules absorbed at each RX, by taking into account the mutual influence between RXs.

The second model is built on the first model, where we perform parameter estimation in a noisy MC environment with the flow and molecular degradation in the environment. In this model, the TX continuously releases molecules and the parameter estimation is performed by using analytically derived expressions of CIR at two fully absorbing RXs. The intended TX may not be the only source of molecules. We also consider other sources that secrete the same type of molecules as the intended TX, which interfere with the parameter estimation at RXs. In this chapter, we refer to the molecules not emitted from the intended TX as noisy molecules. To reduce the impact of noisy molecules on the estimation, we propose a novel estimation method, namely, difference estimation (DE). In this method, the difference between the number of absorbed molecules at two fully-absorbing RXs is used to estimate parameters. In addition, we consider independent maximum-likelihood (ML) estimation at each RX as a benchmark to show performance superiority of DE. Our major contributions are summarised as follows.

1) We derive the exact closed-form expressions for the fraction of molecules absorbed at each RX in both models. In the first model, we also derive the molecule hitting rate

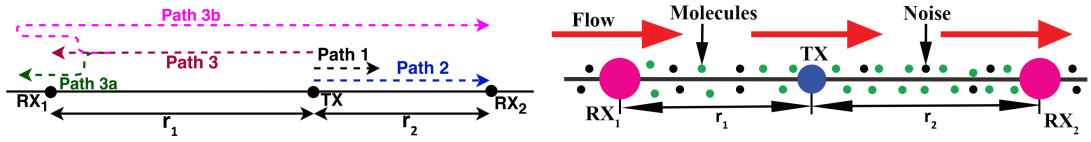

(a) System Model I (b) System Model II

Figure 5.1: Illustration of the system models, where one TX communicates with two fully absorbing RXs in a one-dimensional environment. (b): A flow exists from RX_1 towards RX_2. Green dots denote molecules emitted from the TX while black dots denote noisy molecules.

and the asymptotic fraction of molecules absorbed as time approaches infinity at each RX with an impulse emission at the TX. In the second model, we derive the asymptotic expression for the number of absorbed molecules within a time interval at each RX after sufficient time has passed, when the TX emits molecules continuously.

2) In the second model, we derive the CRLB on the variance of different parameters which include distances, emission rate, rate constant of molecule degradation, and flow velocity.

3) Aided by a PBS method, we verify our analytical results and show that DE attains the CRLB.

4) In the first model, we present the distance ranges of two RXs that do not impact molecular absorption of each other. We also show that the mutual impact between two RXs reduces with the increasing rate constant of degradation in the environment. In the second model, our numerical results show that the impact of noise on the performance of DE is much less than that on independent estimation of each RX, which demonstrates the superiority of DE in reducing the impact of noise.

The rest of this chapter is organised as follows. In Section 5.2, we introduce the system model. In Section 5.3, the closed-form expression for the fraction of absorbed molecules in the first model is derived. We also derive the corresponding hitting rate and the asymptotic fraction of absorbed molecules as time approaches infinity. In Section 5.4, we derive the expected number of absorbed molecules at each RX in the second MC model. In Section 5.5, we propose DE and derive CRLB for DE. We also apply the method of moments to estimate the unknown parameter. In Section 5.6, we discuss the numerical results, and conclusions are presented in Section 5.7.

5.2 System Model

In this chapter, we consider a 1D unbounded environment where a single TX is located between two fully absorbing RXs, i.e., RX_1 and RX_2, with distance r_1 from the RX_1 and distance r_2 from the RX_2, as depicted in Fig. 5.1. After molecules are released from the TX, they diffuse randomly with a constant diffusion coefficient D_A. We also consider the first-order chemical reaction (i.e., unimolecular degradation) in the environment, where type A molecules degrade into a new type of molecule $\hat{A}$ that cannot be identified by the RXs, i.e., $A \xrightarrow{k_\mathrm{d}} \hat{A}$ [113, Ch. 9], where k_d $[\mathrm{s}^{-1}]$ is the rate constant of degradation. We model the two RXs as point fully-absorbing RXs, which means that information molecules A are absorbed as soon as they hit the point RX_1 or RX_2.

5.2.1 System Model I

In this model, we consider the TX as a point source that can release an impulse of particles, as shown in Fig. 5.1(a). We assume that the TX transmission starts at $t = 0$ s.

5.2.2 System Model II

In this model, we consider a TX that continuously releases molecules into the environment at different times, as depicted in Fig. 5.1(b). The release time instants follow a 1D Poisson point process (PPP) with a rate μ $[\mathrm{molecules/s}]$, and a single molecule is released at each time instant. We note that μ is also the average number of molecules being released per second. We assume that the the TX starts emission at $t = 0$ s. Moreover, we consider a steady uniform flow $\vec{v}$ in the direction from RX_1 towards RX_2, where the value of the uniform flow is v $(v > 0)$. In addition, we consider that the noisy molecules released by sources in addition to the intended TX may interfere with the estimation of environmental parameters. We emphasise that this additive noise is distinct from the randomness in the number of A molecules absorbed by each RX due to diffusion, which may also interfere with the estimation. We note that one potential application of the system model in Fig. 5.1(b) is estimating parameters near a tumor in a blood-vessel environment.

In this system, estimation is based on the received signals of two RXs at time t, which is the number of absorbed molecules within the time interval $[t-\delta, t]$, where δ is the length of the time interval. We assume that each RX first performs S observations separately, and then they perform estimation jointly based on the difference between observations at two RXs. Therefore, we name this estimation method as DE. As discussed in [70], the computation of difference can be conducted with the aid of another device. For example, the two RXs may transmit their observations to a fusion centre that has easy access to computational resources. In this chapter, we assume perfect transmission between each RX and the fusion centre.

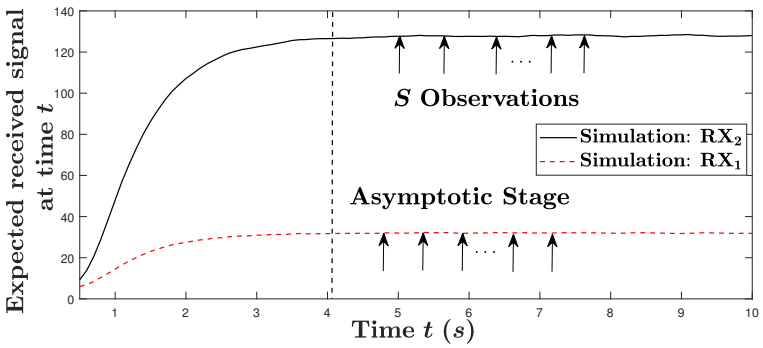

Figure 5.2: The time-varying expected received signals, where $r_1 = r_2 = 20\ \mu$m, $v = 6\ \mu$m/s, $D_A = 79.4\ \mu\text{m}^2/\text{s}$, $k_\text{d} = 0.8\ \text{s}^{-1}$, $\mu = 1000\ \text{s}^{-1}$, and $\delta = 0.5$ s. For other simulation details, please see Section 5.6.

In Fig. 5.2, we plot the expected received signals at two RXs in a noisy environment by the simulation. From this figure, we observe that the expected received signals become constant when $t > 4$ s. We refer to the stage where the expected received signal is constant as the asymptotic stage. We note that it is a short time for two RXs to reach the asymptotic stage after the TX starts releasing molecules. Therefore, we assume that RXs start to make observations at the asymptotic stage as in [158]. One advantage for using asymptotic observations is that they do not depend on time, such that time synchronisation is not required between devices, which improves the practicality of the proposed estimation method.

5.3 Derivation of CIR in System Model I

In this section, we derive closed-form expressions for the expected fraction of absorbed molecules at each RX for impulsive emission at the TX, and the asymptotic fraction of absorbed molecules at each RX as $t \to \infty$ in the basic MC model. We first derive the CIR for impulsive emission when one RX exists, which builds the foundation for deriving the CIR when two RXs exist. According to [59], the hitting rate for a single RX with molecular degradation can be obtained via the hitting rate without molecular degradation and multiplying by $\exp(-k_\text{d}t)$. Based on the existing expression for the hitting rate without molecular degradation in [74], the hitting rate at the RX at time t, denoted by $h(r_0,t)$, with molecular degradation is

$$h(r_0,t) = \frac{r_0}{\sqrt{4\pi D_A t^3}} \exp\left(-\frac{r_0^2}{4D_A t} - k_\text{d} t\right), \tag{5.1}$$

where r_0 is the distance between the TX and the RX. Using $\int_0^t h(r_0,u)\mathrm{d}u$, we obtain the fraction of molecules absorbed by time t, denoted by $H(r_0,t)$, as

$$H(r_0,t) = \frac{1}{2}\exp\left(-\sqrt{\frac{k_\mathrm{d}}{D_A}}r_0\right)\mathrm{erfc}\left(\frac{r_0}{\sqrt{4D_A t}} - \sqrt{k_\mathrm{d} t}\right) + \frac{1}{2}\exp\left(\sqrt{\frac{k_\mathrm{d}}{D_A}}r_0\right) \times \mathrm{erfc}\left(\frac{r_0}{\sqrt{4D_A t}} + \sqrt{k_\mathrm{d} t}\right). \tag{5.2}$$

As $t \to \infty$, we derive the asymptotic absorbed molecules $H(r_0, t \to \infty)$ as

$$H(r_0, t \to \infty) = \exp\left(-\sqrt{\frac{k_\mathrm{d}}{D_A}}r_0\right). \tag{5.3}$$

In the following, we derive the CIR when two RXs exist. We denote the fraction of absorbed molecules at RX_1 and RX_2 by time t for impulsive emission by $H_1(t)$ and $H_2(t)$, respectively. We also denote the corresponding hitting rates at RX_1 and RX_2 by $h_1(t)$ and $h_2(t)$, respectively.

To derive $h_1(t)$ and $h_2(t)$, we first discuss the impact of the existence of RX_1 on $h_2(t)$, based on [76]. As shown in Fig. 5.1(a), we classify all possible diffusion paths of molecules by time t in this environment into three paths, namely path 1, path 2, and path 3. Path 1 is for molecules diffusing in the environment, and path 2 and path 3 are for molecules that have hit RX_2 and RX_1, respectively. If only RX_2 exists, we can further classify path 3 into path 3a and path 3b. Path 3a represents molecules that do not hit RX_2 after firstly arriving at the location of RX_1 at time $\tau < t$, and path 3b represents molecules that hit RX_2 after firstly arriving at the location of RX_1 at time τ. Given that $h(r_2,t)$ denotes the hitting rate from the TX to RX_2 when only RX_2 exists, we find that $h_2(t)$ is less than $h(r_2,t)$, due to the existence of RX_1. Accordingly, $h_2(t)$ is obtained as [76, eq. (12)]

$$h_2(t) = h(r_2,t) - \gamma(t), \tag{5.4}$$

where $\gamma(t)$ is the reduced hitting rate impacted by the existence of RX_1. Based on the division in Fig. 5.1(a), $\gamma(t)$ is the hitting rate of path 3b and derived as

$$\gamma(t) = \int_0^t h_1(\tau)h(r_1+r_2, t-\tau)\mathrm{d}\tau, \tag{5.5}$$

where $h(r_1+r_2, t-\tau)$ is the hitting rate from RX_1 to RX_2 when RX_1 is regarded as the TX and RX_2 is the only RX. Combining (5.4) and (5.5), we derive $h_2(t)$ as [76, eq. (17)]

$$h_2(t) = h(r_2,t) - \int_0^t h_1(\tau)h(r_1+r_2, t-\tau)\mathrm{d}\tau. \tag{5.6}$$

Similarly, we obtain $h_1(t)$ as

$$h_1(t) = h(r_1,t) - \int_0^t h_2(\tau)h(r_1+r_2,t-\tau)\mathrm{d}\tau, \tag{5.7}$$

where $h(r_1,t)$ is the hitting rate from the TX to RX_1 when only RX_1 exists.

Based on (5.6) and (5.7), we solve the closed-form expressions for $H_2(t)$ and $h_2(t)$ in the following theorem:

Theorem 5.1. The fraction of absorbed molecules at RX_2 by time t for an impulsive emission of molecules is given by

$$\begin{aligned} H_2(t) = \sum_{i=0}^{\infty} \big[& R\left(2\left(i+1\right)r_1 + \left(2i+3\right)r_2, t, 2, i\right) - R\left(2\left(i+2\right)r_1 + \left(2i+3\right)r_2, t, 2, i\right) \\ & - R\left(2ir_1 + \left(2i+1\right)r_2, t, 0, i\right) + R\left(2(i+1)r_1 + \left(2i+1\right)r_2, t, 0, i\right)\big], \end{aligned} \tag{5.8}$$

where $R(x,t,a,i)$ is given by

$$\begin{aligned} R(x,t,a,i) = & \frac{\hat{\gamma}}{2}\sqrt{\frac{k_\mathrm{d}}{D_A}}\left(\alpha\beta(t) - \tilde{\alpha}\tilde{\beta}(t)\right) - \frac{i+1}{2}\left(\tilde{\alpha}\tilde{\beta}(t) + \alpha\beta(t)\right) - \frac{\hat{\gamma}}{\sqrt{\pi D_A t}} \\ & \times \exp\left(-\frac{x^2}{4D_A t} - k_\mathrm{d} t\right) + (i+1). \end{aligned} \tag{5.9}$$

In (5.9), $\hat{\gamma} = (r_1+r_2)(i+1)(i+a)$, $\alpha = \exp\left(x\sqrt{\frac{k_\mathrm{d}}{D_A}}\right)$, $\tilde{\alpha} = \exp\left(-x\sqrt{\frac{k_\mathrm{d}}{D_A}}\right)$, $\beta(t) = \mathrm{erfc}\left(\frac{x}{\sqrt{4D_A t}} + \sqrt{k_\mathrm{d} t}\right)$, and $\tilde{\beta}(t) = \mathrm{erfc}\left(\frac{x}{\sqrt{4D_A t}} - \sqrt{k_\mathrm{d} t}\right)$. The corresponding hitting rate at RX_2 by time t, $h_2(t)$, is obtained by taking the derivative of (5.8) with respect to t. By doing so, the expression for $h_2(t)$ is similar to (5.8), except for replacing $R(x,t,a,i)$ with $\mathcal{R}(x,t,a,i)$, where $\mathcal{R}(x,t,a,i) = \frac{\mathrm{d}R(x,t,a,i)}{\mathrm{d}t}$ and is given by

$$\mathcal{R}\left(x,t,a,i\right) = \frac{i+1}{\sqrt{4\pi D_A t^3}}\exp\left(-\frac{x^2}{4D_A t} - k_\mathrm{d} t\right)\left(\left(1 - \frac{x^2}{2D_A t}\right)\left(r_1+r_2\right)\left(i+a\right) - x\right). \tag{5.10}$$

Proof: Please see Appendix C.1. ■

We denote the asymptotic fraction of absorbed molecules as $t \to \infty$ at RX_1 and RX_2 by $H_{1,\mathrm{asy}}$ and $H_{2,\mathrm{asy}}$, respectively. We derive and present $H_{2,\mathrm{asy}}$ in the following theorem:

Corollary 5.1. The asymptotic fraction of absorbed molecules at RX_2 as $t \to \infty$ is given by

$$H_{2,\mathrm{asy}} = \begin{cases} \frac{\exp\left(-r_2\sqrt{\frac{k_\mathrm{d}}{D_A}}\right) - \exp\left(-(2r_1+r_2)\sqrt{\frac{k_\mathrm{d}}{D_A}}\right)}{1-\exp\left(-2(r_1+r_2)\sqrt{\frac{k_\mathrm{d}}{D_A}}\right)}, k_\mathrm{d} \neq 0 \\ \frac{r_1}{r_1+r_2}, k_\mathrm{d} = 0. \end{cases} \tag{5.11}$$

Proof: Please see Appendix C.2. ■

Remark 5.1. The closed-form expressions for $H_1(t)$, $h_1(t)$ and $H_{1,\text{asy}}$ are obtained by exchanging r_1 and r_2 therein for $H_2(t)$, $h_2(t)$ and $H_{2,\text{asy}}$, respectively.

Remark 5.2. By setting $k_\text{d} = 0$ in the expressions for $H_2(t)$ and $h_2(t)$, we can obtain the corresponding expressions without the occurrence of molecular degradation.

5.4 Derivation of CIR in System Model II

In this section, we first derive the expected number of absorbed molecules at each RX until time t due to continuous emission by the TX. We then derive the closed-form expression for the number of absorbed molecules at each RX within the time interval $[t-\delta, t]$ as $t \to \infty$, which lays the foundation for parameter estimation in Section 5.5.

We denote $N_j(t)$, $j = \{1,2\}$, as the expected number of absorbed molecules at RX_j by time t. According to the derivation of CIR in Section 5.3, we derive $N_j(t)$ in the following theorem:

Theorem 5.2. The expected number of molecules absorbed at RX_j by time t due to the continuous emission of molecules at the TX is given by

$$N_j(t) = \mu \exp\left((-1)^j \frac{r_j v}{2D_A}\right) \sum_{i=0}^{\infty} \left[R_i(2(i+1)r + r_j, t, 2) - R_i\left(2(i+2)r - r_j, t, 2\right)\right.$$
$$\left. - R_i\left(2ir + r_j, t, 0\right) + R_i(2(i+1)r - r_j, t, 0)\right], \tag{5.12}$$

where $r = r_1 + r_2$ is the distance between the two RXs and $R_i(x,t,a)$ is given by

$$R_i(x,t,a) = \frac{\hat{\gamma}\kappa}{2}\left(\alpha_1 \omega(t) - \tilde{\alpha}_1 \tilde{\omega}(t)\right) - \frac{i+1}{2}\left(\alpha_1 \omega(t) + \tilde{\alpha}_1 \tilde{\omega}(t)\right) - \frac{\hat{\gamma}}{\sqrt{D_A v^2 + 4k_\text{d} D_A}}\left(\tilde{\alpha}_1 \tilde{\beta}_1(t)\right.$$
$$\left. - \alpha_1 \beta_1(t)\right) + (i+1)t. \tag{5.13}$$

In (5.13), $\kappa = \sqrt{\frac{v^2}{4D_A^2} + \frac{k_\text{d}}{D_A}}$, $\alpha_1 = \exp(x\kappa)$, $\tilde{\alpha}_1 = \exp(-x\kappa)$, $\beta_1(t) = \text{erfc}\left(\frac{x}{\sqrt{4D_A t}} + \sqrt{(k_\text{d} + \frac{v^2}{4D_A})t}\right)$, $\tilde{\beta}_1(t) = \text{erfc}\left(\frac{x}{\sqrt{4D_A t}} - \sqrt{(k_\text{d} + \frac{v^2}{4D_A})t}\right)$, $\omega(t) = \int_0^t \beta_1(u)\text{d}u$, and $\tilde{\omega}(t) = \int_0^t \tilde{\beta}_1(u)\text{d}u$. $\omega(t)$ and $\tilde{\omega}(t)$ are calculated numerically, e.g., using the built-in function *integral* in MATLAB.

Proof: Please see Appendix C.3. ■

Since the received signal at each RX is the number of absorbed molecules within the time interval $[t-\delta, t]$, we express the received signal, denoted by $\Delta N_j(t)$, as

$$\Delta N_j(t) = N_j(t) - N_j(t-\delta). \tag{5.14}$$

As $t \to \infty$, we observe from Fig. 5.2 that $\Delta N_j(t)$ becomes constant. We derive the closed-form expression for the asymptotic value of $\Delta N_j(t)$, denoted by $\tilde{N}_j$, in the following theorem:

Theorem 5.3. The asymptotic number of molecules absorbed by RX_j within an interval $[t-\delta,t]$ as $t\to\infty$, denoted by $\tilde{N}_j$, is derived as

$$\tilde{N}_j = \mu\delta\exp\left((-1)^j\frac{r_j v}{2D_A}\right)\frac{\exp\left(-r_j\kappa\right)-\exp\left(\left(r_j-2r\right)\kappa\right)}{1-\exp\left(-2r\kappa\right)}. \tag{5.15}$$

Proof: Please see Appendix C.4. ■

5.5 DE in System Model II

In this section, we consider the system model II and assume that one environmental parameter is unknown. We apply DE to estimate this parameter. For DE, we first derive the CRLB and then apply the method of moments to estimate the parameter. To show the performance advantage of DE, we consider independent ML estimation at each RX as a benchmark.

5.5.1 Derivation of CRLB

The CRLB is a lower bound on the variance of any unbiased estimator [159, Ch. 3]. For any unbiased estimator, the mean of estimated values equals its true value, which means that its mean squared error (MSE) equals the variance. An estimator is the minimum-variance unbiased (MVU) estimator if the MSE of the estimator attains the CRLB. Therefore, the CRLB can be applied to predict the performance of the MVU estimator.

To derive the CRLB, we need the joint conditional PMF of S observations of DE, where each observation is the difference between received signals at both RXs. We first denote the vector that contains S observations of received signal at RX_j by $\mathbf{g}_j=[g_{j,1},g_{j,2},\ldots,g_{j,s},\ldots,g_{j,S}]$, where $g_{j,s}$ is the sth observation at RX_j. We then denote the vector that contains the observations of DE by $\tilde{\mathbf{g}}=[\tilde{g}_1,\tilde{g}_2,\ldots,\tilde{g}_s,\ldots,\tilde{g}_S]$ where $\tilde{g}_s=g_{2,s}-g_{1,s}$. For the unknown parameter ε, we denote the joint conditional PMF of DE by $p(\tilde{\mathbf{g}}|\varepsilon)$ that are obtained by multiplication of the conditional PMF of each observation of DE if these observations are independent. To keep the independence of each observation in $\tilde{\mathbf{g}}$, we need to first guarantee the independence of observations in $\mathbf{g}_j$. In this chapter, we assume that each observation in $\mathbf{g}_j$ is independent of other observations[1] and the time between two successive observations in $\mathbf{g}_j$ should be at least larger than δ.

As we model the release time of each molecule at the TX as a continuous random process, the time interval between releasing two successive molecules is a RV. Thus, the release time of each molecule is different, which means that the received signal follows a Poisson binomial distribution since each molecule has a different probability of being absorbed by the time the

[1] Although we cannot guarantee perfect independence between successive observations in $\mathbf{g}_j$, the dependence can become extremely rare when the time between successive observations is sufficiently long.

Table 5.1: $\tilde{\gamma}_j(\varepsilon)$ for each estimated parameter

$\tilde{\gamma}_j(r_2)$	$\frac{\mu\Delta t \exp\left((-1)^j \frac{r_j v}{2D_A}\right)}{1-\exp(-2r\kappa)} \left[\exp\left(-r_j\kappa\right)\left(\frac{v}{2D_A}-(-1)^j\kappa\right)-\exp\left(\left(r_j-2r\right)\kappa\right)\left(\frac{v}{2D_A}+(-1)^j\kappa\right)\right]$
$\tilde{\gamma}_j(\mu)$	$\tilde{N}_j/\mu$
$\tilde{\gamma}_j(v)$	$\frac{\mu\Delta t \exp\left((-1)^j \frac{r_j v}{2D_A}\right)}{\left(1-\exp(-2r\kappa)\right)^2} \Big\{ \left(\exp\left(2r\kappa\right)-1\right) \Big[\exp\left(-(2r+r_j)\kappa\right)\left(\frac{(-1)^j r_j}{2D_A}-\frac{r_j v}{\sqrt{4v^2D_A^2+16D_A^3k_\mathrm{d}}}\right)$ $-\exp\left(\left(r_j-4r\right)\kappa\right)\left(\frac{(-1)^j r_j}{2D_A}+\frac{(r_j-2r)v}{\sqrt{4D_A^2+v^2+16D_A^3k_\mathrm{d}}}\right)\Big]-\frac{vr}{\sqrt{v^2D_A^2+4k_\mathrm{d}D_A^3}}$ $\left[\exp\left(-(2r+r_j)\kappa\right)-\exp\left(\left(r_j-2r\right)\kappa\right)\right]\Big\}$
$\tilde{\gamma}_j(k_\mathrm{d})$	$\frac{\mu\Delta t \exp\left((-1)^j \frac{r_j v}{2D_A}\right)}{\left(1-\exp(-2r\kappa)\right)^2} \Big[\exp\left(-(r_j+2r)\kappa\right)\left(\frac{r_j}{\sqrt{v^2+4D_Ak_\mathrm{d}}}\left(1-\exp\left(2r\kappa\right)\right)-\frac{r}{\sqrt{\frac{v^2}{4D_A}+k_\mathrm{d}D_A}}\right)$ $-\exp\left(\left(r_j-4r\right)\kappa\right)\left(\left(\exp\left(2r\kappa\right)-1\right)\frac{r_j-2r}{\sqrt{v^2+4k_\mathrm{d}D_A}}-\frac{r}{\sqrt{\frac{v^2}{4}+k_\mathrm{d}D_A}}\right)\Big]$

observation is made. As the Poisson binomial distribution is cumbersome to work with, we approximate it by a Poisson distribution. The approximation becomes more accurate when the number of trials, i.e., emitted molecules, is larger and the success probability $\hat{H}_j(t)$ is smaller [134]. We assume that the number of absorbed noisy molecules within the time interval at each RX are identically and independently distributed Poisson RVs with constant mean ξ as in [160]. This assumption is reasonable since sources in addition to the intended TX can also be regarded as TXs. Due to the additivity of two Poisson RVs, we model each observation of the received signal as a Poisson RV with mean $\tilde{N}_j+\xi$. As $g_{2,s}$ and $g_{1,s}$ follow a Poisson distribution, the difference between observations, i.e., $\tilde{g}_s$, follows a Skellam distribution with mean $\tilde{N}_2-\tilde{N}_1$. According to the PMF of Skellam distribution in [161], the joint conditional PMF is

$$p\left(\tilde{\mathbf{g}}|\varepsilon\right)=\prod_{s=1}^{S}\exp\left(-\left(\hat{N}_1+\hat{N}_2\right)\right)\left(\frac{\hat{N}_2}{\hat{N}_1}\right)^{\frac{\tilde{g}_s}{2}} I_{\tilde{g}_s}\left(2\sqrt{\hat{N}_1\hat{N}_2}\right), \tag{5.16}$$

where $\hat{N}_j=\tilde{N}_j+\xi$ and $I_{\tilde{g}_s}(2\sqrt{\hat{N}_1\hat{N}_2})$ is the modified Bessel function of the first kind [162]. According to [159, Ch. 3], the CRLB of the variance of an unbiased estimator, denoted by $\mathrm{var}\left(\hat{\varepsilon}\right)$, is $\mathrm{var}(\hat{\varepsilon})\geq\frac{1}{L(\varepsilon)}$, where $\hat{\varepsilon}$ is the estimated value of ε, $\mathrm{var}(\hat{\varepsilon})=\mathbb{E}\left[\left(\hat{\varepsilon}-\varepsilon\right)^2\right]$ for the unbiased estimator, $\mathbb{E}[\cdot]$ represents the expectation, and $L(\varepsilon)$ is the Fisher information that is given by [159, eq. (3.6)]

$$L(\varepsilon)=-\mathbb{E}\left[\frac{\partial^2\ln p(\tilde{\mathbf{g}}|\varepsilon)}{\partial\varepsilon^2}\right], \tag{5.17}$$

where $\mathbb{E}[\cdot]$ is taken with respect to $\tilde{g}_s$. We derive $L\left(\varepsilon\right)$ in the following theorem:

Theorem 5.4. The Fisher information of DE for unknown parameter ε is derived as

$$L(\varepsilon) = S\Bigg[\frac{3\hat{N}_2-\hat{N}_1}{4\hat{N}_2^2}\tilde{\gamma}_2^2(\varepsilon)+\frac{3\hat{N}_1-\hat{N}_2}{4\hat{N}_1^2}\tilde{\gamma}_1^2(\varepsilon)-\frac{\hat{N}_1+\hat{N}_2}{2\hat{N}_1\hat{N}_2}\tilde{\gamma}_1(\varepsilon)\tilde{\gamma}_2(\varepsilon)+\left(\vartheta-\frac{4\hat{N}_2^2+3\hat{N}_2-\hat{N}_1}{4\hat{N}_1\hat{N}_2}\right)$$
$$\times\left(\sqrt{\frac{\hat{N}_2}{\hat{N}_1}}\tilde{\gamma}_1(\varepsilon)+\sqrt{\frac{\hat{N}_1}{\hat{N}_2}}\tilde{\gamma}_2(\varepsilon)\right)^2\Bigg], \tag{5.18}$$

where $\vartheta=\sum_{\tilde{g}_s=\zeta_1}^{\zeta_2}\frac{I^2_{\tilde{g}_s-1}\left(2\sqrt{\hat{N}_1\hat{N}_2}\right)}{I_{\tilde{g}_s}\left(2\sqrt{\hat{N}_1\hat{N}_2}\right)}\exp\left(-\left(\hat{N}_1+\hat{N}_2\right)\right)\left(\frac{\hat{N}_2}{\hat{N}_1}\right)^{\frac{\tilde{g}_s}{2}}$ and $\tilde{\gamma}_j(\varepsilon)=\frac{\partial\hat{N}_j}{\partial\varepsilon}$. ζ_1 and ζ_2 are found numerically as explained in the Appendix C.5. In Table 5.1, we list $\tilde{\gamma}_j(\varepsilon)$ for the distance between the TX and RX_2 r_2, flow velocity v, emission rate μ and rate constant of degradation k_d.

Proof: Please see Appendix C.5. ■

5.5.2 Method of Moments

For DE, we apply the method of moments to estimate the unknown parameter, which is finding $\hat{\varepsilon}$ that makes 1) the analytical expression for the mean of $\tilde{g}_s$, and 2) the mean of $\tilde{g}_s$ calculated by observed data, equal [159, Ch. 9]. As each item in the vector $\tilde{\mathbf{g}}$ is independent and follows the same distribution with the same mean, the mean of $\tilde{g}_s$ from observed data can be calculated by $\frac{1}{S}\sum_{s=1}^{S}\tilde{g}_s$. Since $\tilde{g}_s$ follows a Skellam distribution with mean $\tilde{N}_2-\tilde{N}_1$, we have the following estimation criteria:

$$\left(\tilde{N}_2-\tilde{N}_1\right)\Big|_{\varepsilon=\hat{\varepsilon}}=\frac{1}{S}\sum_{s=1}^{S}\tilde{g}_s, \tag{5.19}$$

where ξ is not included such that the knowledge of noise from sources in addition to the intended TX is not required to perform the estimation.

5.5.3 Benchmark

To highlight the superiority of DE in eliminating the impact of noise, we consider independent estimation at each RX as a benchmark, where each RX performs ML estimation based on their S observations in $\mathbf{g}_j$. We recall that each observation is approximated by a Poission distribution with mean $\hat{N}_j$. Therefore, the joint conditional PMF of S observations at RX_j, denoted by $p(\mathbf{g}_j|\varepsilon)$, is given by $p\left(\mathbf{g}_j|\varepsilon\right)=\prod_{s=1}^{S}\hat{N}_j^{g_{j,s}}\exp\left(-\hat{N}_j\right)/g_{j,s}!$. The principle of ML estimation is finding $\hat{\varepsilon}_j$ that maximizes $p\left(\mathbf{g}_j|\varepsilon\right)$. By solving $\frac{\partial\ln p(\mathbf{g}_j|\varepsilon)}{\partial\varepsilon}=0$, we obtain the equivalent expression $\hat{N}_j\big|_{\varepsilon=\hat{\varepsilon}_j}=\frac{1}{S}\sum_{s=1}^{S}g_{j,s}$. Since ξ is unknown in $\hat{N}_j$, one approach for independent

Table 5.2: Simulation Parameters for Numerical Results

Parameter	Variable	Value	Reference
Molecule diffusion coefficient	D_A	$79.4\ \mu\text{m}^2/\text{s}$	[60]
Number of impulsively released molecules	N_A	5000	
Rate constant of molecule degradation	k_d	$0.8\ \text{s}^{-1}$	[67]
Distance between the TX and RX_1/RX_2	r_1/r_2	$20/20\ \mu\text{m}$	
Molecule release rate	μ	$1000\ \text{s}^{-1}$	
Length of the time interval	δ	0.5 s	
Flow velocity	v	$6,10\ \mu\text{m/s}$	
Expected number of absorbed noisy molecules within the time interval	ξ	0,10	

estimation is ignoring the noise. By doing so, we obtain the following estimation criteria:

$$\tilde{N}_j\big|_{\varepsilon=\hat{\varepsilon}_j} = \frac{1}{S}\sum_{s=1}^{S} g_{j,s}. \tag{5.20}$$

We highlight that (5.20) indicates that the ML estimation at RX_j is to find $\hat{\varepsilon}_j$ that makes $\tilde{N}_j\big|_{\varepsilon=\hat{\varepsilon}_j}$ and the mean of S observations in $\mathbf{g}_j$ equal.

5.6 Numerical Results

In this section, we present numerical results to validate our theoretical analysis and provide insightful discussions. The simulation results are conducted using a PBS method [123], where all results are averaged over 2000 realisations and the simulation time step is $\Delta t_\text{s} = 0.001$ s. Throughout this section, we set the simulation parameters as shown in Table 5.2, unless othewise stated.

5.6.1 System Model I

In this subsection, we focus on validating theoretical analysis in Section 5.3 and provide insightful discussions for the system model I in Fig. 5.1(a).

In Fig. 5.3, we investigate the number of summation terms that should be applied in (5.8). In Fig. 5.3(a), we apply three data sets to investigate the impact of r_1, r_2, and k_d on the number of summation terms. First, when only applying $i = \{0,1\}$ in (5.8), we observe that the equation first reaches the highest point, i.e., $H_{2,\text{asy}}$, and then drops. Applying a larger number of terms results in $H_2(t) = H_{2,\text{asy}}$ for a longer time, but increases computional complexity. To reduce such complexity, we clarify that applying $i = \{0,1\}$ is adequate since it enables (5.8) to reveal the absorbed molecules before becoming visually indistinguishable from the asymptotic value, and increasing terms in (5.8) does not change the absorbed molecules calculated before

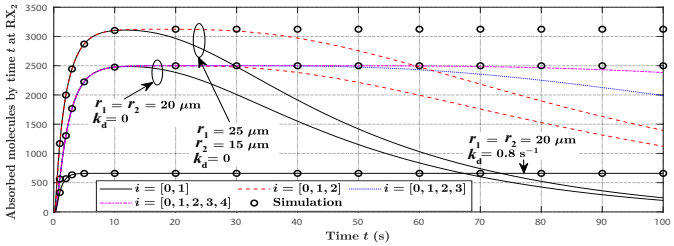

(a) Three data sets are applied: i) $r_1 = r_2 = 20\,\mu$m, $k_d = 0$, ii) $r_1 = 25\,\mu$m, $r_2 = 15\,\mu$m, $k_d = 0$, iii) $r_1 = r_2 = 20\,\mu$m, $k_d = 0.8$ s^{-1}, where $D_A = 79.4\,\mu$m^2/s is applied for three data sets.

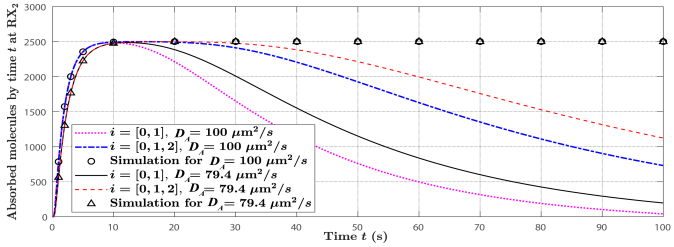

(b) Two data sets are applied: i) $r_1 = r_2 = 20\,\mu$m, $D_A = 79.4\,\mu$m^2/s, ii) $r_1 = r_2 = 20\,\mu$m, $D_A = 100\,\mu$m^2/s, where $k_d = 0$ is applied for two data sets.

Figure 5.3: Absorbed molecules by time t at RX$_2$ versus time t, where different number of terms are applied in (5.8).

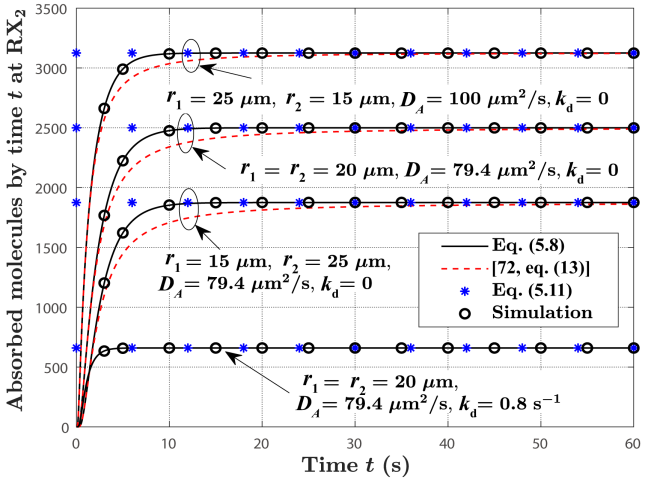

Figure 5.4: Molecules absorbed by time t at RX$_2$ versus time t, where molecular emission is impulsive at the TX.

reaching the asymptotic value. After reaching the asymptotic value, we set $H_2(t) = H_{\text{asy}}$. Second, comparing data set i) with data set ii) and data set iii), we observe that changing r_1, r_2, and k_d does not change the fact that applying $i = \{0, 1\}$ is adequate for (5.8). In Fig. 5.3(b), we apply two data sets to investigate the impact of D_A on the number of terms. We still observe that changing D_A does not impact the fact that applying $i = \{0, 1\}$ is adequate for (5.8).

In Fig. 5.4, we plot molecules absorbed at RX$_2$ by time t using (5.8) and [76, eq. (13)],

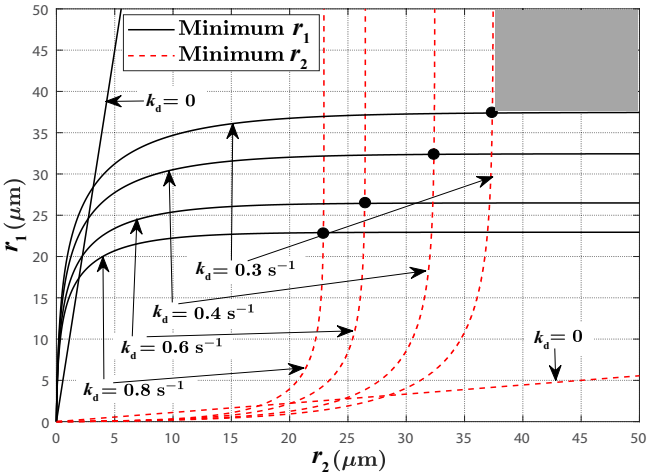

Figure 5.5: Mimimum r_1 that does not influence absorbing molecules at RX_2 versus r_2, and minimum r_2 that does not influence absorbing molecules at RX_1 versus r_1, where different k_d is applied. Constraint for calculating minimum r_1 and minimum r_2 is 0.01, and the grey area represents distances of two RXs that do not impact each other when $k_\mathrm{d} = 0.3$ s^{-1}.

respectively. We note that [76, eq. (13)] was initially applied to a 3D environment but can also be applied to a 1D environment[2]. In this figure, we first keep $k_\mathrm{d} = 0$ s^{-1} and vary r_1, r_2, and D_A to investigate the accuracy of (5.8) and [76, eq. (13)]. We also investigate the molecular degradation by setting $k_\mathrm{d} = 0.8$ s^{-1} and plot the absorbed molecules at RX_2 with (5.8). First, we clearly observe that the simulation matches well with (5.8) and a gap exists between the simulation and [76, eq. (13)] for 3 s $\leq t \leq$ 30 s, which demonstrates the accuracy advantage of (5.8) relative to [76, eq. (13)]. Second, we observe that the asymptotic value of (5.8) and [76, eq. (13)] converge as $t \to \infty$. Last, we observe that (5.11) matches with the simulation for both $k_\mathrm{d} = 0$ and $k_\mathrm{d} = 0.8$ s^{-1} when t is large, which demonstrates the correctness of (5.11).

In Fig. 5.5, we plot the minimum r_1 that does not impact molecular absorption at RX_2 versus r_2, and the minimum r_2 that does not impact molecular absorption at RX_1 versus r_1, for different k_d. We examine the impact of RX_1 on RX_2 based on the gap between the fraction of absorbed molecules at RX_2 and the fraction of absorbed molecules for the single RX as $t \to \infty$, which is expressed as $H(r_2, t \to \infty) - H_{2,\mathrm{asy}}$, where $H(r_2, t \to \infty)$ is given by (5.3) and $H_{2,\mathrm{asy}}$ is given by (5.11). We calculate the minimum r_1 which satisfies the condition $\left(H(r_2, t \to \infty) - H_{2,\mathrm{asy}}\right) / H(r_2, t \to \infty) < 0.01$ for given r_2. We also suppose that RX_1 does not impact the molecular absorption at RX_2 when this condition is satisfied. Similarly, we calculate the minimum r_2 for given r_1. From this figure, we first observe that minimum r_1 intersects minimum r_2 when $k_\mathrm{d} \neq 0$. The upper right area of the intersection for each k_d represents

[2]In the 3D environment, [76] assumed that molecules are absorbed at the same points before reaching another RX. The points on RX_1 and RX_2 are denoted by s_1' and s_2', where s_1' and s_2' are found numerically. As RX_1 and RX_2 are regarded as points in a 1D environment, s_1' and s_2' are points RX_1 and RX_2. Substituting s_1' and s_2' with RX_1 and RX_2 in [76, eq. (13)], we obtain the fraction of absorbed molecules at RX_2 in a 1D environment, based on the method in [76].

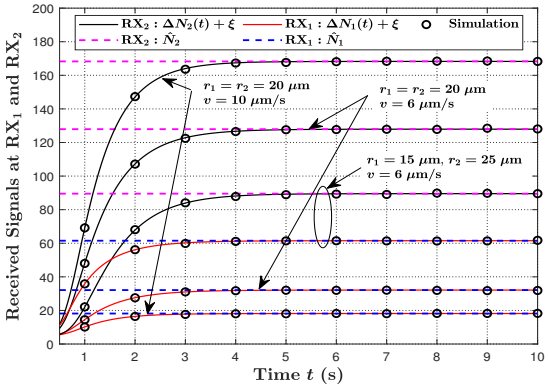

Figure 5.6: Received signals $\Delta N_j(t) + \xi$ and $\hat{N}_j$ versus time t at RX_j for three parameter sets: 1) $r_1 = r_2 = 20\ \mu$m, $v = 10\ \mu$m/s, 2) $r_1 = r_2 = 20\ \mu$m, $v = 6\ \mu$m/s, 3) $r_1 = 15\ \mu$m, $r_2 = 25\ \mu$m, $v = 6\ \mu$m/s, where $\xi = 5$ for all parameter sets.

the range for r_1 and r_2 of two RXs that do not impact each other, because the condition for two RXs not impacting each other's molecular absorption is that r_1 and r_2 are simultaneously larger than minimum r_1 and minimum r_2, respectively. For example, if r_1 and r_2 are in the grey area, then two RXs do not impact each other when $k_{\mathrm{d}} = 0.3\ \mathrm{s}^{-1}$. When $k_{\mathrm{d}} = 0$, there is no intersection such that two RXs always impact each other. Second, we observe that the range for two RXs not impacting each other decreases with decreasing k. When k decreases, there is a larger number of molecules in the environment such that the mutual influence between two RXs is higher, which results in the less range for two RXs not impacting each other. Third, we observe that minimum r_1 and minimum r_2 firstly increase when r_2 and r_1 increase, respectively, and then become constant after the intersection. This is because increasing r_2 means that the molecular absorption at RX_2 decreases. In this case, if r_1 keeps the same value, then the molecular absorption at RX_1 relatively increases, which results in a larger impact on the molecular absorption at RX_2. Therefore, the minimum r_1 increases to reduce the impact on RX_2. Beyond the intersection, two RXs will not impact each other such that increasing r_2 will not lead to increase in minimum r_1.

5.6.2 System Model II

In this subsection, we focus on validating theoretical analysis for the flow-aided noisy model in Section 5.4 and evaluating the estimation method proposed in Section 5.5.

In Fig. 5.6, we plot the received signals $\Delta N_j(t) + \xi$ and the asymptotic received signals $\hat{N}_j$ at two RXs versus time t, where different flow velocities and distances between the TX and two RXs are considered to investigate the impact of the flow and distance on the received signals[3].

[3]The Péclet number is defined as the ratio between the advection and diffusion, which is $\mathrm{Pe} = \frac{vr_2}{D_A}$. In each parameter set, $\mathrm{Pe} > 1$. Therefore, flow is the dominant transport mechanism in this environment [45].

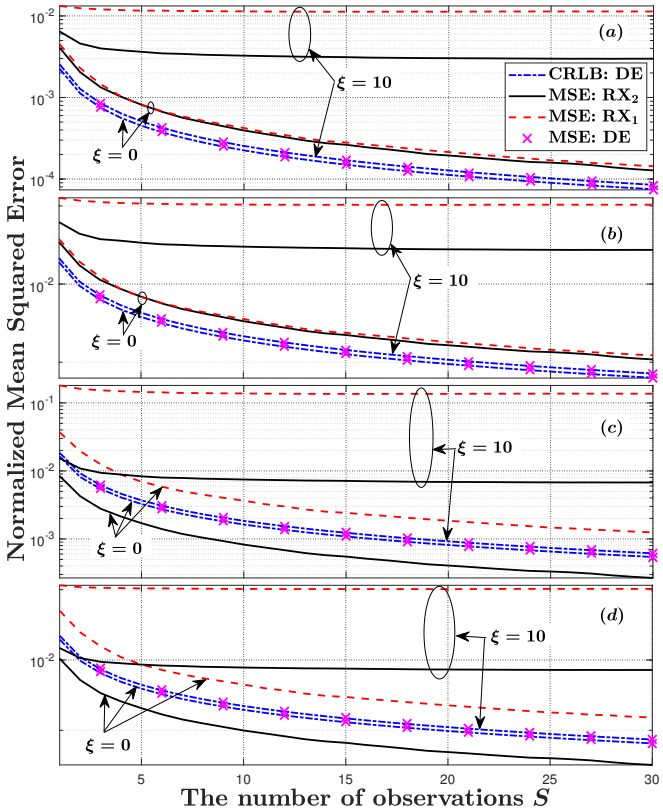

Figure 5.7: The normalized MSE versus the number of observations S, where $\xi = 0$ and $\xi = 10$ are considered. (a): Estimation of r_2. (b) : Estimation of v. (c) : Estimation of μ. (d) : Estimation of k_{d}.

We first observe that the simulation matches well with $\Delta N_j(t) + \xi$ and $\hat{N}_j$, which demonstrates the correctness of (5.12) and (5.15). Furthermore, comparing parameter sets 1) and 2), we observe that the received signals increase at RX_2 and decrease at RX_1 with an increase in the flow velocity. This is because we assume that the direction of the flow is from RX_1 towards RX_2. In addition, comparing parameter sets 2) and 3), we observe that the received signals increase with a decrease in the distance between the TX and RX.

In Fig. 5.7, we plot the normalized MSE for DE and two RXs and the CRLB for DE versus the number of observations, where $\xi = 0$ and $\xi = 10$ in this environment are considered. In this figure, we set $r_1 = r_2 = 20\ \mu$m and $v = 6\ \mu\mathrm{m/s}$. Both MSE and CRLB are normalized over ε^2. First, we observe that the normalized MSE attains the CRLB for DE, which indicates that the method of moments applied in DE achieves the minimum variance. Second, we observe that the normalized MSEs at two RXs increase with the increase in noise. Third, in Fig. 5.7(a) and Fig. 5.7(b), we observe that the normalized MSEs at two RXs are close to each other when $\xi = 0$ and the MSE of DE is always lower than that at either of the RXs. This is because r_2 and v have no impact on the number of molecules in this environment, which means that the performance of the estimation for r_2 and v is not related to the number of molecules absorbed

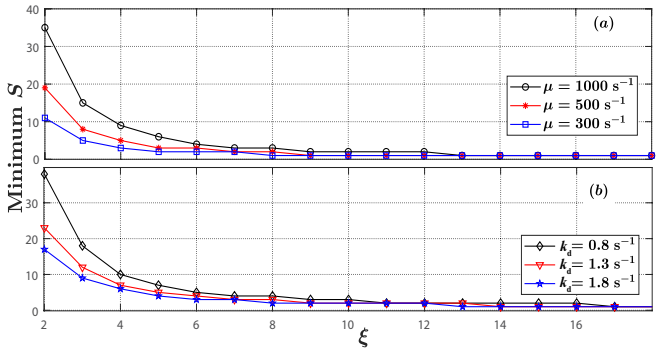

Figure 5.8: The minimum number of observations S required for MSE in DE to be less than the MSE at RX_2 versus the mean of noise ξ. (a): Estimation of μ. (b): Estimation of k_d.

at each RX. As DE combines observations of both RXs, DE achieves a better performance. When noise increases, the impact on the estimation of DE is much less than that at either RX, which indicates the superiority of DE in eliminating the impact of noise in estimation. This is because the difference of received signals in DE offsets the impact of noise. Fourth, in Fig. 5.7(c) and Fig. 5.7(d), we observe a large gap between normalized MSEs of either RX and the performance of RX_2 is better than DE when $\xi = 0$. This is because μ and k_d influence the number of molecules in the environment, which means that the number of absorbed molecules at either RX influences the performance of estimation. When $\xi = 0$, RX_2 performs estimation based on a larger number of molecules than DE and RX_1. Therefore, RX_2 achieves the best performance. It is worth noting that the performance of RX_2 becomes worse than DE for $S > 2$ when $\xi = 10$ and the increase of MSE in DE is much less than the increase at RX_2, which still proves that DE is superior than independent estimation in eliminating the impact of noise. This superiority becomes obvious with the increase in ξ and S.

In Fig. 5.8, we plot the minimum number of observations required for the MSE in DE to be less than the MSE at RX_2, where the estimation of μ and k_d are considered because of the observations of Fig. 5.7(c) and Fig. 5.7(d). From this figure, we first observe that the minimum number of observations required decreases with an increase in the noise mean, which indicates that the increase of MSE at DE is much slower than that at RX_2, demonstrating that DE is less sensitive to the increase in noise than RX_2. After $\xi > 13$ and $\xi > 17$ for the estimation of μ and k_d, respectively, the MSE in DE is always less than the MSE at RX_2 since the minimum S drops to one. Second, we observe that the minimum number of observations decreases with a decrease in μ or increase in k_d. This is because a decrease in μ or increase in k_d results in a decrease in the received signal at RX_2, which makes RX_2 more susceptible to an increase in noise than DE.

5.7 Conclusion

In this chapter, we focused on a 1D molecular communication system with two different models. In the first system model, we investigated CIR between a single TX and two fully-absorbing RXs. We derived new closed-form expressions for i) the fraction of absorbed molecules, ii) the corresponding hitting rate, and iii) the asymptotic fraction of absorbed molecules as time approaches infinity at each RX. In the second system model, we investigated parameter estimation by the cooperation of two RXs in a noisy 1D environment and derived the analytical expressions for the CIR at both RXs. Moreover, in the second model, we considered DE and derived the CRLB. To show the advantage of DE, independent estimation at each RX was also investigated. Our numerical results verified our analytical results. In the first model, we investigated distance ranges for two RXs that do not impact molecular absorption of each other, which showed that the mutual influence between two RXs decreases with the increase in the rate constant of degradation. In the second model, numerical results showed that DE is less sensitive to an increase in noise than independent estimation. For the estimation of r_2 and v, DE always achieves the better performance than independent estimation. For the estimation of μ and k_{d}, DE becomes better than independent estimation with an increase in noise or in the number of observations.

Chapter 6

Molecule Harvesting by Heterogeneous Receptors on Transmitters

6.1 Introduction

Molecule harvesting is a known biological mechanism in synaptic communication. One typical example is reuptake [163], which is the re-absorption of neurotransmitters in the synaptic cleft by neurotransmitter transporters on the pre-synaptic neuron. This mechanism is necessary for synaptic communication since it allows to recycle neurotransmitters and control the time duration of signal transmission. Motivated by this biological example, as mentioned in Section 2.7, a recent study [91] developed a spherical molecule harvesting TX model where the membrane is equipped with receptors that can react with information molecules. Specifically, the authors considered a homogeneous TX surface, where they assumed an infinite number of receptors cover the entire TX surface or a finite number of receptors with identical sizes are uniformly distributed over the TX surface. However, the analysis in [91] may become inaccurate in practice as the receptors on the TX surface may have different sizes and arbitrary locations. In particular, receptor clustering [105] is one phenomenon that leads to heterogeneous receptors on the cell membrane. Therefore, in this chapter, we consider a spherical TX, whose membrane is covered by heterogeneous receptors that may have different sizes and arbitrary locations, and assume each receptor to be fully absorbing. Moreover, we model the transportation of molecules within the TX based on Chapter 3, where molecules are encapsulated within vesicles and later released from the TX through the fusion of the vesicle and the TX membrane. Instead of assuming an impulse of vesicles being released from the centre of the TX as in Chapter 3, we consider the continuous generation of vesicles within the TX. Furthermore, we consider a transparent RX and investigate the CIR, where we take into account the fact that molecules may degrade when they propagate from the TX to the RX. We emphasise that the analysis in [91] is not applicable when considering heterogeneous boundary

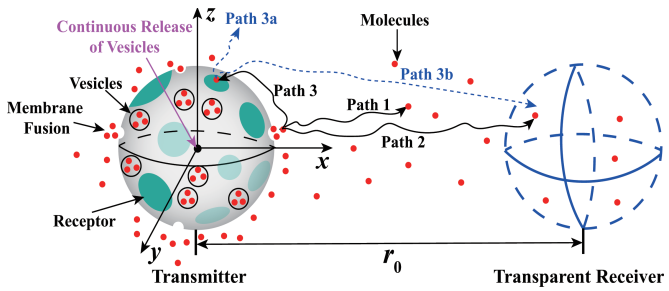

Figure 6.1: Illustration of the MC system model where a spherical TX covered by heterogeneous receptors communicates with a transparent RX.

conditions and vesicle-based release at the TX.

The main contributions of this chapter can be summarised as follows. We derive the molecule release rate from the TX membrane for the case of a continuous generation of vesicles within the TX. We also derive the fraction of absorbed molecules at the TX and the probability that a released molecule is observed at the RX, where all expressions are functions of the size and location of each receptor. PBSs are used to verify the accuracy of our expressions. Our numerical results reveal that the total number of molecules absorbed by the TX is not affected by the vesicle generation rate, while the peak received signal at the RX increases for larger vesicle generation rates.

The rest of this chapter is organised as follows. In Section 6.2, we describe the system model. In Section 6.3, we derive the molecule release rate from the TX membrane and the fraction of absorbed molecules by the TX. In Section 6.4, we derive the received signal at the RX. In Section 6.5, we present and discuss our numerical results. In Section 6.6, we draw some conclusions.

6.2 System Model

In this chapter, we consider an unbounded three-dimensional (3D) environment where a spherical TX communicates with a transparent spherical RX, as depicted in Fig. 6.1. We choose the centre of the TX as the origin of the environment and denote the radii of the TX and RX by r_{T} and r_{R}, respectively.

6.2.1 TX Model

In this subsection, we present the TX model in terms of vesicle generation, molecule propagation, and the receptors on the TX membrane.

6.2.1.1 Vesicle Generation

For the considered TX model, we assume that type-A molecules are stored within and transported by vesicles, where each vesicle stores η molecules. We assume that vesicles are continuously generated in the centre of the TX. In particular, each vesicle is generated at a random time instant, and we approximate the generation process as a 1D PPP [164]. We note that PPP has been frequently used to describe random biological processes as [165]. In particular, several previous studies, e.g., [166, 167], have modelled the generation of molecules as a 1D PPP. Furthermore, we denote N_{v} as the total number of vesicles that the TX generates for a single transmission and μ [vesicles/s] as the average number of vesicles generated per second.

6.2.1.2 Transportation of Molecules

We assume that the TX is filled with a fluid medium that has uniform temperature and viscosity. After vesicles are generated in the centre of the TX, they diffuse randomly with a constant diffusion coefficient D_{v} until reaching the TX membrane. Then, these vesicles fuse with the membrane to release the encapsulated molecules. According to [27], we model the MF process between the vesicle and the TX membrane as an irreversible reaction with forward reaction rate constant k_{f} [μm/s]. Thereby, if a vesicle hits the TX membrane, it fuses with the membrane with a probability of $k_{\mathrm{f}}\sqrt{\pi\Delta t/D_{\mathrm{v}}}$ during a time interval Δt [124]. After MF, the molecules stored by the vesicles are instantaneously released into the propagation environment.

6.2.1.3 Receptors on the TX Membrane

We assume that there are N_{r} non-overlapping heterogeneous receptors distributed on the TX membrane, which may have different sizes and arbitrary locations. We assume the shape of the ith receptor to be a circle with radius a_i. We define $\mathcal{A}$ as the ratio of the total area of the receptors to the TX surface, i.e., $\mathcal{A} = \sum_{i=1}^{N_{\mathrm{r}}} a_i^2/(4r_{\mathrm{T}}^2)$. In a spherical coordinate system, we denote $\vec{l}_i = [r_{\mathrm{T}}, \theta_i, \varphi_i]$ as the location of the centre of the ith receptor, where θ_i and φ_i represent the azimuthal and polar angles of the ith receptor, respectively. As the receptors are non-overlapping, the locations and radii of the receptors satisfy $|\vec{l}_i - \vec{l}_j| \geq a_i + a_j, \forall i, j \in \{1, 2, ..., N_{\mathrm{r}}\}$. In this model, we assume that all receptors are fully absorbing and can only absorb the released type-A molecules. With this assumption, once a released diffusing type-A molecule hits a receptor, it is absorbed by the TX immediately. Furthermore, we assume that the TX membrane area that is not covered by receptors is perfectly reflective, which means that released diffusing type-A molecules are reflected back once they hit this area. In addition, we assume that the protein which catalyses the MF between the vesicle and the TX membrane is different from the receptor which absorbs molecules. Therefore, the molecule release and absorption are treated as two independent processes.

6.2.2 Propagation Environment and RX Model

In this system, we consider a transparent spherical RX whose boundary does not impede the diffusion of molecules. The centre of the RX is distance r_0 away from the centre of the TX. We assume that the RX can perfectly count the number of molecules within its volume at time t and use this value as the received signal. We also assume that the propagation environment between TX and RX is a fluid medium with uniform temperature and viscosity. Once molecules are released from the TX, they diffuse randomly with a constant diffusion coefficient D_A. We further assume unimolecular degradation in the propagation environment, where type-A molecules can degrade to type-$\hat{A}$ molecules that can neither be absorbed by the TX nor be observed by the RX, i.e., $A \xrightarrow{k_\mathrm{d}} \hat{A}$ [113, Ch. 9], where k_d $[\mathrm{s}^{-1}]$ is the rate constant of degradation.

6.3 Analysis of Release and Harvest of Molecules at TX

In this section, we first analyze the release of molecules from the TX when jointly considering the continuous generation of vesicles and the MF process at the TX membrane, and derive the molecule release rate from the TX membrane. We define the molecule release rate as the probability of molecules being released during the time interval $[t, t+\delta t]$ from the TX membrane, when the vesicles storing these molecules were continuously generated in the origin starting at time $t = 0$. Second, we incorporate the effect of the heterogeneous receptors on the TX membrane and analyze the absorption of molecules by the TX. We further derive the fraction of molecules absorbed by the TX until time t.

6.3.1 Molecule Release Rate from TX Membrane

We define $\hat{\tau}$ as the mean time duration for generating all vesicles, which is given by $\hat{\tau} = N_\mathrm{v}/\mu$. Therefore, when $t \in [0, \hat{\tau}]$, the vesicle generation is active. When $t > \hat{\tau}$, the vesicle generation ceases. In Chapter 3, we assumed that vesicles are instantaneously generated in the centre of the TX and provided the corresponding molecule release rate $f_\mathrm{r}(t)$ in (3.5), where we took the MF process into account. In the following theorem, based on $f_\mathrm{r}(t)$, we derive the molecule release rate, denoted by $f_\mathrm{c}(t)$, when vesicles are continuously generated in the centre of the TX.

Theorem 6.1. The mean molecule release rate from the TX membrane at time t, when vesicles are continuously generated starting at time $t = 0$, is given by

$$f_\mathrm{c}(t) = \begin{cases} f_{\mathrm{c},1}(t), & \text{if } 0 < t \leq \hat{\tau}, \\ f_{\mathrm{c},2}(t), & \text{if } t > \hat{\tau}, \end{cases} \tag{6.1}$$

where

$$f_{\mathrm{c},1}(t) = \frac{4r_{\mathrm{T}}^2 k_{\mathrm{f}}\mu}{N_{\mathrm{v}}D_{\mathrm{v}}} \sum_{n=1}^{\infty} \frac{\lambda_n j_0(\lambda_n r_{\mathrm{T}})}{2\lambda_n r_{\mathrm{T}} - \sin(2\lambda_n r_{\mathrm{T}})} \left(1 - \exp\left(-D_{\mathrm{v}}\lambda_n^2 t\right)\right), \tag{6.2}$$

and

$$f_{\mathrm{c},2}(t) = \frac{4r_{\mathrm{T}}^2 k_{\mathrm{f}}\mu}{N_{\mathrm{v}}D_{\mathrm{v}}} \sum_{n=1}^{\infty} \frac{\lambda_n j_0(\lambda_n r_{\mathrm{T}})}{2\lambda_n r_{\mathrm{T}} - \sin(2\lambda_n r_{\mathrm{T}})} \left[\exp\left(-D_{\mathrm{v}}\lambda_n^2 (t-\hat{\tau})\right) - \exp\left(-D_{\mathrm{v}}\lambda_n^2 t\right)\right]. \tag{6.3}$$

Proof: Please see Appendix D.1. ■

6.3.2 Molecule Harvesting at TX

As vesicles are generated at the centre of the TX, molecules are uniformly released from the TX membrane, i.e., the probability of molecule release is identical for any point on the TX membrane. Therefore, we first need to derive the number of molecules absorbed by the TX at time t when these molecules are uniformly and simultaneously released from the TX membrane at time $t = 0$, which is denoted by $H(t)$. To this end, we consider a scenario similar to the model in Fig. 4.1(a), where molecules were uniformly released at time $t = 0$ from the surface of a virtual sphere centred at the TX's centre with a radius d, where $d \geq r_{\mathrm{T}}$. The fraction of molecules absorbed by the TX in this scenario was derived in (4.5). Based on this result, we present $H(t)$ in the following lemma.

Lemma 6.1. The fraction of molecules absorbed by the TX at time t, when the molecules are uniformly and simultaneously released from the TX membrane at time $t = 0$, is given by

$$H(t) = \frac{w\mathrm{erf}(\sqrt{k_{\mathrm{d}}t})}{\sqrt{k_{\mathrm{d}}D_A}} - \frac{w\gamma}{\hat{\xi}}\Big(\exp(\hat{\xi}t)\mathrm{erfc}\left(\gamma\sqrt{D_A t}\right) + \gamma\sqrt{\frac{D_A}{k_{\mathrm{d}}}}\mathrm{erf}\left(\sqrt{k_{\mathrm{d}}t}\right) - 1\Big), \tag{6.4}$$

where $w = D_A G_{\mathrm{T}}/(r_{\mathrm{T}}(r_{\mathrm{T}} - G_{\mathrm{T}}))$, $\gamma = 1/(r_{\mathrm{T}} - G_{\mathrm{T}})$, $\hat{\xi} = \gamma^2 D_A - k_{\mathrm{d}}$, $\mathrm{erf}(\cdot)$ is the error function. According to the definition and explanation in Section 4.3.3, G_{T} can be treated as the "capacitance" of the TX, which is determined by the locations and sizes of the receptors. The expressions of G_{T} have been calculated in [144] as shown in Table 4.1 with replacing r_{R} with r_{T} and N_{p} with N_{r}.

Proof: We recall that $H_{\mathrm{u}}(t)$ in (4.5) represents the fraction of molecules absorbed by the TX at time t, when the molecules are uniformly released from a virtual spherical surface at time $t = 0$. $H(t)$ can be obtained from $H_{\mathrm{u}}(t)$ by setting $d \to r_{\mathrm{T}}$, i.e., $H(t) = \lim_{d \to r_{\mathrm{T}}} H_{\mathrm{u}}(t)|_{r_0 = d}$. By substituting (4.5) into this expression, we obtain (6.4). ■

We then denote $H_{\mathrm{e}}(t)$ as the fraction of molecules absorbed by the TX at time t when vesicles are continuously generated in the centre of the TX starting at time $t = 0$. We present $H_{\mathrm{e}}(t)$ in the following theorem.

Theorem 6.2. The fraction of molecules absorbed at the TX by time t when vesicles are continuously generated in the centre of the TX starting at time $t = 0$ is given by

$$H_{\mathrm{e}}(t) = f_{\mathrm{c}}(t) * H(t), \tag{6.5}$$

where $f_{\mathrm{c}}(t)$ and $H(t)$ are given by (6.1) and (6.4), respectively.

Proof: When molecules are released from the TX membrane at time u, $0 \leq u \leq t$, the fraction of these molecules that can be absorbed by the TX is given by $f_{\mathrm{c}}(u)H(t-u)$. Therefore, $H_{\mathrm{e}}(t)$ can be expressed as $H_{\mathrm{e}}(t) = \int_0^t f_{\mathrm{c}}(u)H(t-u)\mathrm{d}u$, which can be further rewritten as the convolution in (6.5). ■

6.4 Analysis of Received Signal at RX

In this section, we derive expressions for the received signals at the RX in two steps. In the first step, we assume that no receptors exist on the TX surface and derive the received signal at the RX. In the second step, we determine the number of molecules that no longer arrive at the RX because they were absorbed by the receptors on the TX. Based on these derivations, we finally obtain the received signal at the RX.

6.4.1 Problem Formulation

We classify all possible diffusion paths of molecules after their release from the TX membrane into three categories, namely path 1, path 2, and path 3, as shown in Fig. 6.1. Path 1 is the path where molecules diffuse in the propagation environment at time t, path 2 is the path where molecules move into the RX at time t, and path 3 is the path where molecules hit a receptor on the TX surface at time t. If receptors are assumed to not exist, we can further divide path 3 into path 3a and path 3b. Path 3a is the path where molecules diffuse in the propagation environment at time t after having hit the TX at time u, where $u \leq t$, and path 3b is the path where molecules move into the RX at time t after having hit the TX at time u. Then, the received signal at the RX at time t includes molecules from path 2 and path 3b. The presence of receptors causes the received signal at the RX to decrease, and this decrease is caused by the molecules associated with path 3b, which will no longer arrive at the RX. In light of this, we denote $P_{\mathrm{T}}(t)$, $P_{\mathrm{r}}(t)$, and $P(t)$ as the probabilities that a released molecule is observed at the RX at time t when receptors do not exist, when molecules move along path 3b, and when receptors exist, respectively. Accordingly, $P(t)$ can be calculated as

$$P(t) = P_{\mathrm{T}}(t) - P_{\mathrm{r}}(t). \tag{6.6}$$

6.4.2 Derivation of Received Signal

We first consider no receptors on the TX membrane. Similar to the procedure in Section 6.3.2, to derive $P_{\mathrm{T}}(t)$, we need to first derive the received signal at the RX when molecules are uniformly and simultaneously released from the TX membrane at time $t = 0$, denoted by $P_{\mathrm{u}}(t)$. When a molecule is released from an arbitrary point $\hat{\alpha}$ on the membrane of a spherical TX, the probability that this molecule is observed at the RX, denoted by $P_{\hat{\alpha}}(t)$, is given by [52, Eq. (27)]

$$P_{\hat{\alpha}}(t) = \frac{1}{2}\left[\mathrm{erf}\left(\frac{r_{\mathrm{R}} - r_{\hat{\alpha}}}{\sqrt{4D_A t}}\right) + \mathrm{erf}\left(\frac{r_{\mathrm{R}} + r_{\hat{\alpha}}}{\sqrt{4D_A t}}\right)\right]\exp(-k_{\mathrm{d}} t) + \frac{1}{r_{\hat{\alpha}}}\sqrt{\frac{D_A t}{\pi}}\left[\exp\left(-\frac{(r_{\mathrm{R}} + r_{\hat{\alpha}})^2}{4D_A t} - k_{\mathrm{d}} t\right) - \exp\left(-\frac{(r_{\mathrm{R}} - r_{\hat{\alpha}})^2}{4D_A t} - k_{\mathrm{d}} t\right)\right], \tag{6.7}$$

where $r_{\hat{\alpha}}$ is the distance between point $\hat{\alpha}$ and the centre of the RX. By taking the surface integral of $P_{\hat{\alpha}}(t)$ over the TX membrane, we derive and present $P_{\mathrm{u}}(t)$ in the following lemma.

Lemma 6.2. If there are no receptors on the TX membrane, the probability that a molecule is observed at the RX at time t, when these molecules were uniformly and simultaneously released from the TX membrane at time $t = 0$, is given by

$$P_{\mathrm{u}}(t) = \frac{1}{8 r_0 r_{\mathrm{T}}}\left[\hat{\xi}_1(r_0 - r_{\mathrm{T}}, t) + \hat{\xi}_1(r_{\mathrm{T}} - r_0, t) - \hat{\xi}_1(r_0 + r_{\mathrm{T}}, t) - \hat{\xi}_1(-r_0 - r_{\mathrm{T}}, t)\right] + \frac{D_A t}{2 r_{\mathrm{T}} r_0} \times \left[\hat{\xi}_2(r_{\mathrm{T}} + r_0, t) + \hat{\xi}_2(-r_{\mathrm{T}} - r_0, t) - \hat{\xi}_2(r_0 - r_{\mathrm{T}}, t) - \hat{\xi}_2(r_{\mathrm{T}} - r_0, t)\right], \tag{6.8}$$

where

$$\hat{\xi}_1(z,t) = \exp\left(-\frac{(r_{\mathrm{R}} - z)^2}{4D_A t} - k_{\mathrm{d}} t\right)(r_{\mathrm{R}} + z)\sqrt{\frac{4D_A t}{\pi}} + \left(r_{\mathrm{R}}^2 + 2D_A t - z^2\right)\mathrm{erf}\left(\frac{r_{\mathrm{R}} - z}{\sqrt{4D_A t}}\right) \times \exp\left(-k_{\mathrm{d}} t\right), \tag{6.9}$$

and $\hat{\xi}_2(z,t) = \mathrm{erf}\left(\frac{r_{\mathrm{R}} + z}{\sqrt{4D_A t}}\right)\exp\left(-k_{\mathrm{d}} t\right)$.

Proof: Following Appendix A.2, we derive $P_{\mathrm{u}}(t)$ by computing the surface integral of $P_{\hat{\alpha}}(t)$ over the TX membrane, which is given by

$$P_{\mathrm{u}}(t) = \frac{1}{2r_{\mathrm{T}}}\int_{-r_{\mathrm{T}}}^{r_{\mathrm{T}}} P_{\hat{\alpha}}(t)\big|_{r_{\hat{\alpha}} = \sqrt{r_{\mathrm{T}}^2 + r_0^2 - 2r_0 x}}\,\mathrm{d}x. \tag{6.10}$$

By substituting (6.7) into (6.10), we obtain (6.8). ■

Based on $P_{\mathrm{u}}(t)$, we present $P_{\mathrm{T}}(t)$ in the following lemma.

Lemma 6.3. If there are no receptors on the TX membrane, the probability that a released molecule is observed at the RX at time t, when the vesicles are generated in the centre of the

TX starting from time $t = 0$, is given by

$$P_{\mathrm{T}}(t) = f_{\mathrm{c}}(t) * P_{\mathrm{u}}(t), \tag{6.11}$$

where $f_{\mathrm{c}}(t)$ and $P_{\mathrm{u}}(t)$ are given in (6.1) and (6.8), respectively.

Proof: The proof is similar to the proof of Theorem 6.2, and thus omitted here. ■

Next, we derive the probability that a released molecule is observed at the RX associated with path 3b. As we assume that $\mathcal{A}$ and a_i are extremely small compared to the distance between the TX and RX, each receptor can be regarded as a point TX which releases molecules with a release rate that equals the hitting rate of molecules on this receptor at time t. As molecules are uniformly released from the TX membrane, the probability of molecules hitting any point on the receptors is the same. We denote $h_{\mathrm{e},i}(t)$ as the hitting rate of molecules on the ith receptor at time t, and express $h_{\mathrm{e},i}(t)$ as $h_{\mathrm{e},i}(t) = \frac{\mathcal{A}_i}{\mathcal{A}} h_{\mathrm{e}}(t)$, where $\mathcal{A}_i = a_i^2/(4r_{\mathrm{T}}^2)$ is the ratio of the area of the ith receptor to the TX surface and $h_{\mathrm{e}}(t)$ is the total hitting rate of molecules on the TX membrane. We recall that $\mathcal{A}$ is the ratio of the total area of receptors to the TX surface, as mentioned in Section 6.2.1.3. Then, we are ready to derive $P_{\mathrm{r}}(t)$ and $P(t)$. We present $P_{\mathrm{r}}(t)$ and $P(t)$ in the following theorem.

Theorem 6.3. The probability that a released molecule is observed at the RX at time t, when vesicles are continuously generated in the centre of the TX starting from time $t = 0$, is given by

$$P(t) = f_{\mathrm{c}}(t) * P_{\mathrm{u}}(t) - P_{\mathrm{r}}(t), \tag{6.12}$$

where

$$P_{\mathrm{r}}(t) = \frac{f_{\mathrm{c,d}}(t) * H(t)}{\mathcal{A}} * \sum_{i=1}^{N_{\mathrm{r}}} \mathcal{A}_i P_{\hat{\alpha}}(t)\big|_{r_{\hat{\alpha}}=d_i}. \tag{6.13}$$

In (6.13), $f_{\mathrm{c,d}}(t)$ is given by

$$f_{\mathrm{c,d}}(t) = \begin{cases} \frac{4r_{\mathrm{T}}^2 k_{\mathrm{f}} \mu}{N_{\mathrm{v}}} \sum_{n=1}^{\infty} \frac{\lambda_n^3 j_0(\lambda_n r_{\mathrm{T}})}{2\lambda_n r_{\mathrm{T}} - \sin(2\lambda_n r_{\mathrm{T}})} \exp\left(-D_{\mathrm{v}} \lambda_n^2 t\right), & \text{if } 0 < t \leq \hat{\tau}, \\ \frac{4r_{\mathrm{T}}^2 k_{\mathrm{f}} \mu}{N_{\mathrm{v}}} \sum_{n=1}^{\infty} \frac{\lambda_n^3 j_0(\lambda_n r_{\mathrm{T}})}{2\lambda_n r_{\mathrm{T}} - \sin(2\lambda_n r_{\mathrm{T}})} \left[\exp\left(-D_{\mathrm{v}} \lambda_n^2 t\right) - \exp\left(-D_{\mathrm{v}} \lambda_n^2 (t-\tau)\right)\right], & \text{if } t > \hat{\tau}, \end{cases} \tag{6.14}$$

d_i represents the distance between the centre of the ith receptor and the centre of the RX, i.e., $d_i = \sqrt{r_{\mathrm{T}}^2 - 2r_0 r_{\mathrm{T}} \cos(\varphi_i) \sin(\theta_i) + r_0^2}$, and $f_{\mathrm{c}}(t)$, $P_{\mathrm{u}}(t)$, $H(t)$, and $P_{\hat{\alpha}}(t)$ are given in (6.1), (6.8), (6.4), and (6.7), respectively.

Proof: Please see Appendix D.2. ■

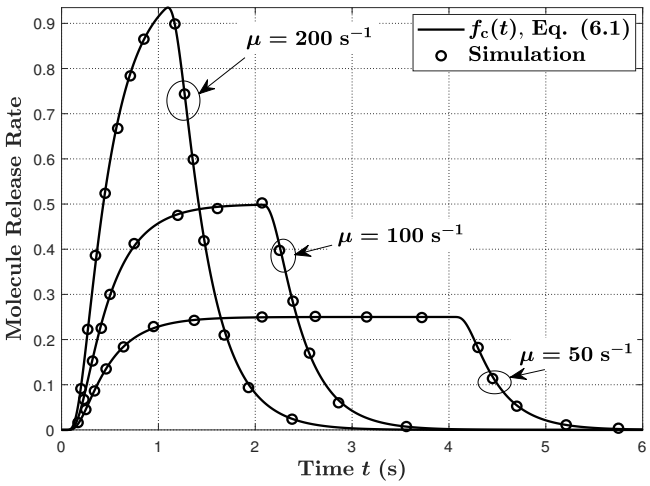

Figure 6.2: Molecule release rate from the TX versus time t for different values of μ.

6.5 Numerical Results

In this section, we present numerical results to validate our theoretical analysis and offer insightful discussions on our considered TX model. Specifically, we use PBSs to simulate the random diffusion of molecules. As we assume the generation process of vesicles as a 1D PPP, the time instant for generating the ith vesicle equals the summation of the previous $i-1$ exponentially distributed random numbers in our simulations. The simulation framework for modelling the diffusion of vesicles within the TX and the MF process at the TX membrane is detailed in Section 3.6, and the framework for modelling the absorption of molecules by heterogeneous receptors is detailed in Section 4.6. We choose the simulation time step as $\Delta t = 10^{-6}$ s and all results are averaged over 1000 independent realisations of generating $N_{\rm v}$ vesicles of the TX. Throughout this section, we set $r_{\rm T} = 5\ \mu$m, $r_{\rm R} = 10\ \mu$m, $N_{\rm v} = 200$, $\eta = 20$, $\mu = \{50, 100, 200\}$s^{-1}, $D_{\rm v} = 9\ \mu$m^2/s, $k_{\rm f} = 30\ \mu$m/s, $\mathcal{A} = 0.1$, $N_{\rm r} = \{1, 4, 11\}$, $r_0 = 20\ \mu$m, $D_A = 79.4\ \mu$m^2/s, and $k_{\rm d} = 0.8$ s^{-1} [151], unless otherwise stated. From Figs. 6.2-6.4, we observe that the simulation results match well with the derived analytical curves, which validates our theoretical analysis in Sections 6.3 and 6.4.

In Fig. 6.2, we plot the molecule release rate $f_{\rm c}(t)$ versus time t for different values of μ. We observe that when μ is small, $f_{\rm c}(t)$ maintains a constant value for a period of time. When μ is large, $f_{\rm c}(t)$ first increases and then decreases after reaching the maximum value. This is because small μ leads to long emission periods such that the concentration distribution of molecules within the TX becomes stable, which results in a stable molecule release rate.

In Fig. 6.3, we plot the number of molecules absorbed by the TX $N_{\rm v}\eta H_{\rm e}(t)$, versus time t, where we set $\mu \in \{50, 100, 200\}$ s^{-1} and employ different numbers, distributions, and sizes of receptors. For receptors that are evenly distributed over the TX membrane, we apply the Fibonacci lattice [154] to determine the locations, which are given by [29, Eq. (42)]. For

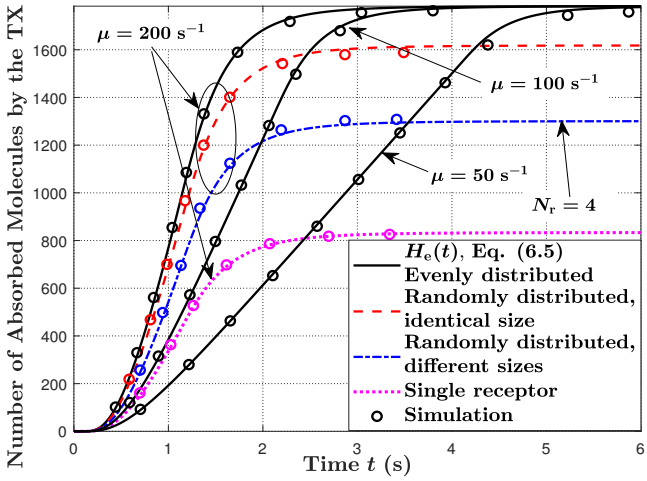

Figure 6.3: The number of molecules absorbed by the TX until time t versus time t for different distributions of receptors and different μ, where $N_r = 11$.

receptors that are randomly distributed over the TX surface, we consider receptors that either have the same size or different sizes. For receptors with different sizes, we set their areas as $\mathcal{A}_1 = 0.01$, $\mathcal{A}_2 = 0.02$, $\mathcal{A}_3 = 0.03$, and $\mathcal{A}_4 = 0.04$, and their locations as $\vec{l}_1 = [5\ \mu\text{m}, \pi/2, \pi]$, $\vec{l}_2 = [5\ \mu\text{m}, \pi/2, \pi/2]$, $\vec{l}_3 = [5\ \mu\text{m}, \pi/2, 0]$, and $\vec{l}_4 = [5\ \mu\text{m}, \pi/2, 3\pi/2]$. For the single receptor, we set the location as $\vec{l}_s = [-r_T, 0, 0]$. First, when receptors are evenly distributed over the TX membrane, we observe that the total number of molecules that the TX can absorb is independent of the value of μ, which means the fraction of molecules that can be recycled for subsequent transmissions does not depend on the generation rate of vesicles. Second, we observe that a larger μ leads to a faster increase of the number of absorbed molecules to the maximum value. This is because the absorption rate of molecules is directly determined by the release rate of molecules, and a larger μ leads to a higher molecule release rate.

In Fig. 6.4, we plot the number of observed molecules within the RX $N_v \eta P(t)$, versus time t, where the parameter setting for the locations and sizes of the receptors and the vesicle generation rate are the same as in Fig. 6.3. First, when receptors have identical sizes and are evenly distributed on the TX membrane, we observe that a larger μ leads to a higher peak received signal. This is because a larger μ leads to a faster release of molecules into the propagation environment such that more molecules can be observed within the RX at the same time. Second, by considering both Fig. 6.3 and Fig. 6.4, we observe that the received signal is weaker when the TX absorbs more molecules. This illustrates a trade-off between energy efficiency and error performance since a weaker received signal can result in a higher decoding error at the RX.

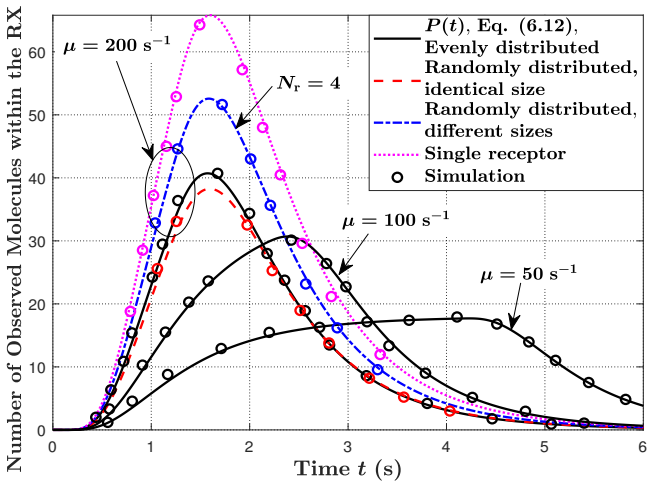

Figure 6.4: The number of observed molecules within the RX at time t versus time t for different distributions of receptors and μ, where $N_r = 11$.

6.6 Conclusion

In this chapter, we investigated molecule harvesting for a spherical TX covered by heterogeneous receptors of different sizes and at arbitrary locations. By considering a continuous generation of vesicles within the TX and a transparent RX, we derived the molecule release rate and the fraction of molecules that are absorbed by the TX. We also derived the probability that a released molecule is observed at the RX. Simulations verified our analysis. Our numerical results showed that the vesicle generation rate determines the peak value of the received signal, but does not affect the fraction of molecules that can be harvested for subsequent transmissions. Future directions of this research include determining the maximum fraction of molecules absorbed by the TX for achieving a desired error performance target.

Chapter 7

Conclusions

In this chapter, we first summarise the main contributions of this thesis, and then discuss several interesting future research directions.

7.1 Thesis Conclusion

In this thesis, we focused on addressing gaps in the current MC studies on practical TX design, practical RX design, co-existence of multiple non-transparent RXs, mobile MC systems, parameter estimation, and energy efficiency. We summarised our contributions to overcome each limitation are as follows:

- **Practical TX design**: Inspired by the biological process of exocytosis, in Chapter 3, we proposed a TX model that is based on the MF between vesicles generated within the TX and the TX membrane to release molecules. We derived the molecule release rate and the fraction of molecules released from the TX. Numerical results highlighted the difference between the MF-based TX and the ideal point TX in terms of the ISI, since ISI of the ideal point TX is only caused by the diffusion of molecules in the propagation environment whereas the ISI of the MF-based TX is also caused by the signalling pathways within the TX.

- **Practical RX design**: Motivated by the fact that receptors on the cell membrane do not have definite locations and sizes due to receptor clustering, in Chapter 4, we proposed a RX that is covered by multiple heterogeneous receptors with different sizes and arbitrary locations. We derived the received signal at the RX for various numbers, distributions, and sizes of receptors. Numerical results showed that the number of absorbed molecules at the RX increases with the number of receptors, when the total area of the receptors is fixed.

- **Co-existence of multiple non-transparent RXs**: Due to the presence of a non-transparent RX affecting the received signals at other non-transparent RXs, the process of characterising channels among multiple non-transparent RXs becomes highly intricate and chal-

lenging. In Chapter 5, we considered a 1D environment with two fully absorbing RXs and derived the closed-form expressions for i) the fraction of absorbed molecules, ii) the corresponding hitting rate, and iii) the asymptotic fraction of absorbed molecules as time approaches infinity at each RX. Numerical results showed that the mutual influence between two RXs decreases with the increase in the rate constant of degradation.

- **Mobile MC systems**: The analysis of the mobile MC system is more challenging than the static system because of the varying distance between the mobile TX and RX. In Chapter 3, we considered a mobile MF-based TX and a mobile fully absorbing RX, and derived the expected CIR between them. We also derived the PMF for the number of molecules absorbed at the mobile RX by dividing the molecule release duration into multiple release intervals.

- **Parameter estimation**: Parameter estimation within the MC system is crucial to extract information from the microscale environment and facilitate the system design. In Chapter 5, we considered a noisy 1D environment and applied the cooperation of two RXs to estimate parameters. In particular, we used DE and derived the CRLB. Numerical results showed that DE can effectively mitigate the impact of noise on estimation.

- **Energy efficiency**: Motivated by the limited methods to charge the nanomachines currently, in Chapter 6, we proposed a molecule harvesting TX model to improve the energy efficiency of the MC system. The membrane of the TX is covered by heterogeneous receptors to harvest molecules. We derived the number of molecules that are absorbed by the TX for next rounds of transmission and showed that the number of harvested molecules is not related to the vesicle generation rate within the TX.

In summary, our TX and RX designs in Chapter 3 and Chapter 4 act as a theoretical fundamental analysis for researchers to anticipate the performance of nanomachines within MC systems in the future, given that nanomachines, e.g., artificial cells, mimic one or many functions of a biological cell [168]. Moreover, our investigation of two fully absorbing RXs in Chapter 5 provides a novel and imitable method for channel characterisation when multiple fully absorbing RXs co-exist. Therefore, the work in Chapter 5 can be extended to a 3D environment with a large number of RXs co-exist. In addition, the current studies that investigate the energy efficiency in MC systems are quite limited. Our work in Chapter 6 shows the possibility of reducing the energy cost from the perspective of TX design, which acts as a fundamental study to inspire researchers taking into account energy efficiency when designing TXs and RXs.

7.2 Potential Gaps and Application Scope

7.2.1 Potential Gaps

The entire thesis focuses on investigating more practical MC systems by relaxing some idealised assumptions made for TXs and RXs in previous studies. Although our work has enabled the TXs and RXs more features from the biological cells, the real biological MC system is far more complicated, and there is still a huge gap to bridge for accurately modelling real biological MC TXs and RXs. Specifically, we describe the gaps between our TX and RX models and the real TXs and RXs in the biological system as follows.

TX Model in Chapter 3 & 6

- We simplified the molecule generation process within the TX. In biological cells, molecules are generated through a series of complex biochemical processes, which includes DNA transcription, mRNA translation, post-translational modification, enzymatic reactions, and metabolic pathways [169]. In our TX model, we only assume that molecules are generated at the centre of the TX.

- We simplified the transportation of vesicles within the TX. Vesicles move within the cell through a process that involves the cytoskeleton, motor proteins, and energy from ATP [169]. The cytoskeleton provides a network of protein filaments that act as tracks for vesicle transport, while motor proteins use energy from ATP hydrolysis to prompt the vesicle movement along these tracks. In our model, we only assume that vesicles perform free diffusion with the TX.

- Reuptake typically occurs through active transport, which requires ATP or the energy stored in electrochemical gradients. The transporter proteins use this energy to move the molecules against their concentration gradient, from an area of lower concentration outside the cell to an area of higher concentration inside the cell [7]. In our model, we assumed that molecules are absorbed by the TX as soon as they hit the receptors and did not consider the impact of energy on the molecule harvesting.

RX Model in Chapter 4

- In biological cells, cellular communication is based on the ligand-receptor binding, which is a dynamic process, and the ligand and receptor interact through non-covalent molecular interactions, such as hydrogen bonding [169]. The ligands can continuously associate with and dissociate from their receptors. Moreover, upon ligand binding, many receptors undergo a conformational change that allows them to transmit the extracellu-

lar signal to the intracellular environment. In our RX model, we did not consider these factors and assumed that molecules can be absorbed as soon as they hit the receptors.

- After ligand-receptor binding, a series of secondary chemical reactions occurs within the cell. These reactions ultimately lead to various cellular responses, such as changes in gene expression, cellular metabolism, or cell division. In our model, we did not consider these secondary reactions and regarded the number of absorbed molecules as the received signal.
- Receptors can move laterally within the plane of the plasma membrane through diffusion [170]. The lipid bilayer of the cell membrane acts as a fluid environment, allowing the receptors to move within it. In our RX model, we assumed fixed receptors on the surface.

7.2.2 Application Scope

Although there are some gaps between our current models and practical biological cells, we still emphasise the value of our work in this thesis as follows.

- Simplified models ensure the tractability of mathematical derivations. If all biological characteristics are considered in the MC system, it requires substantial computational resources and time for simulation. On the other hand, analytical expressions can be derived to describe simplified TX and RX models, which allows faster simulation and efficient parameter estimation.
- Our simplified TX and RX models serve as a starting point for developing more complex and biologically accurate models. For example, our research can provide a better understanding of the impacts of vesicular transportation and heterogeneous receptors on the MC system, and other researchers can extend our model by incrementally adding complexity and refining these assumptions.
- The simplied TX and RX models allow us to focus on the most crucial elements of the MC system, e.g., the transportation of molecules with the TX and the reception of molecules by receptors. This can help to identify key factors that drive communication efficiency and provide valuable insights into the design and optimisation of the MC system.

7.3 Future Research Directions

7.3.1 TX Design

As mentioned in Section 3.2.1, one constraint in our MF-based TX is that MF can occur at any location on the TX membrane. In reality, the MF sites are limited, and we plan to model

the heterogeneous t-SNARE proteins with varying sizes and arbitrary positions on the TX membrane. Consequently, MF can only take place at sites containing the t-SNARE proteins, and the TX membrane will exhibit a heterogeneous boundary condition for vesicles within it. We will also derive a new molecule release probability that accounts for this boundary condition.

One interesting observation in Chapter 6 is that a larger number of molecules harvested by the TX leads to a lower received signal at the RX, which motivates us to strike a balance between the energy efficiency and error performance in the future study. We will set a threshold for the acceptable error performance at the RX and maximise the number of molecules absorbed by the TX. We will also determine the corresponding distributions and sizes of receptors to provide guidelines for the TX design.

In the synaptic communication, the receptors on the pre-synaptic neuron can not only harvest neurotransmitters, but also serve as parts of a negative feedback loop in the signal transmission. In particular, this type of receptors is named as autoreceptors [171], which can inhibit further release or synthesis of the neurotransmitters from the pre-synaptic neuron. Motivated by this biological mechanism, in the future study, we will incorporate the negative feedback into our TX design, where the TX can adjust the molecule release based on the number of molecules absorbed by receptors on it. If the number of absorbed molecules is larger than a pre-defined threshold, the TX regards that it has released enough molecules such that stopping further release and synthesis of molecules. The threshold will be determined based on the received signal at the RX, and this investigation will further improve the energy efficiency and mitigate ISI at the RX.

7.3.2 RX Design

In Chapter 4, we proposed an RX covered by heterogeneous receptors and derived the received signal as a function of the sizes and distributions of receptors. In the current study, we only showed that the evenly distributed receptors on the RX surface leads to a higher received signal than randomly distributed receptors and receptors within a region. In the future study, we will optimise the sizes and distributions of receptors to maximise the received signal.

Another future research direction is modelling the mobility of receptors on the RX surface, which is motivated by the fact that cell membrane is composed of a mixture of phospholipids in a fluid phase such that receptors undergo isotropic random movement akin to Brownian motion [170]. We will consider that receptors perform Brownian motion over the RX surface and tract the movement of receptors by the algorithm in [172]. We will also analyse and observe the impact of mobile receptors on the received signal at the RX.

7.3.3 Multiple Practical TXs and RXs

We currently only investigate a SISO MC system. In the future study, we will consider a MIMO system with multiple practical TXs and RXs. For multiple TXs, we will take the molecule harvesting into account at each TX, where the molecules can only be harvested by one of the TXs. Therefore, we need to develop a new mathematical framework to evaluate the mutual influence among TXs, which makes the analysis more complex than current studies considering multiple point TXs. We will also use a similar method to characterise the mutual influence among multiple non-transparent RXs and derive the received signal and BER at each RX.

7.3.4 Development of MC Simulators

Our current studies only modelled the practical MC systems from a mathematical perspective. If we further increase the complexity of the system, the mathematical methods may become too complicated to deal with related problems. In the future research, we will develop innovative simulators to validate the modelling and analysis of practical MC systems. Specifically, the users can input the values of parameters related to the practical TXs, RXs, and environment into the simulators, and the simulators can output the received signal at each RX. The simulators will be coded with Python by using the PBSs. We will also enhance the feasibility of the simulators by designing it to support an arbitrary number of TXs and RXs, and maintain the computational complexity of the simulators at an acceptable level. Overall, such simulators will help scientists and engineers to accurately predict the behaviour of the practical MC systems.

Appendix A

A.1 Proof of Theorem 3.1

Using separation of variables [173], we express $C(r,t)$ as $C(r,t) = R(r)T(t)$, where $R(r)$ and $T(t)$ are functions of r and t, respectively. Substituting $C(r,t)$ into (3.3), we obtain

$$\frac{2D_{\mathrm{v}}R^{'}(r)}{rR(r)} + \frac{D_{\mathrm{v}}R^{''}(r)}{R(r)} = \frac{T^{'}(t)}{T(t)} \overset{(a)}{=} \hat{\varepsilon}, \tag{A.1}$$

where $R^{'}(r) = \frac{\partial R(r)}{\partial r}$, $R^{''}(r) = \frac{\partial^2 R(r)}{\partial r^2}$, and $T^{'}(t) = \frac{\partial T(t)}{\partial t}$. The left-hand side of the first equality in (A.1) is a function of r, denoted by $\hat{\varepsilon}(r)$, and the right-hand side is a function of t, denoted by $\hat{\varepsilon}(t)$. As $\hat{\varepsilon}(r) = \hat{\varepsilon}(t)$, $\hat{\varepsilon}(r)$ and $\hat{\varepsilon}(t)$ are equal to a constant $\hat{\varepsilon}$ that results in the equality (a). Based on (A.1), we obtain

$$r^2R^{''}(r) + 2rR^{'}(r) - \frac{\hat{\varepsilon}}{D_{\mathrm{v}}}r^2R(r) = 0. \tag{A.2}$$

By setting $\hat{\varepsilon} = -D_{\mathrm{v}}\lambda_n^2$, $n = 1,2,3,...$, (A.2) becomes the radial equation when solving the Helmholtz equation in spherical coordinates [174]. For each given λ_n, the solution of $R(r)$ in (A.2), denoted by[1] $R_n(r)$, is given by $R_n(r) = \mathcal{C}_n j_0(\lambda_n r)$, where $\mathcal{C}_n$ is a constant. As $R_n(r)$ needs to satisfy the boundary condition in (3.4), we substitute $R_n(r)$ into (3.4) and obtain (3.6). Based on (A.1), we then obtain

$$\frac{T_n^{'}(t)}{T_n(t)} = -D_{\mathrm{v}}\lambda_n^2. \tag{A.3}$$

By considering an obvious condition $T_n(t \to \infty) = 0$, one principle solution of $T_n(t)$ is

[1] The general solution of the Helmholtz equation is $j_{\hat{n}}(x)$, where $\hat{n} = 0,1,2,3,....$ In (A.2), $j_0(x)$ is applied since the TX model is symmetric.

$T_n(t) = B_n \exp\left(-D_{\mathrm{v}}\lambda_n^2 t\right)$. Based on the principle of superposition, $C(r,t)$ becomes

$$C(r,t) = \sum_{n=1}^{\infty} R_n(r)T_n(t) = \sum_{n=1}^{\infty} \mathcal{C}_n B_n j_0\left(\lambda_n r\right) \exp\left(-D_{\mathrm{v}}\lambda_n^2 t\right). \tag{A.4}$$

We next determine $\mathcal{C}_n B_n$ based on the initial condition in (3.2). According to the Sturm-Liouville theory [175], if $n \neq n^{'}$, $r j_0(\lambda_n r)$ and $r j_0(\lambda_{n^{'}} r)$ are orthogonal to each other, which is

$$\int_0^{r_{\mathrm{T}}} r^2 j_0(\lambda_n r) j_0(\lambda_{n^{'}} r)\mathrm{d}r = \begin{cases} \frac{2\lambda_n r_{\mathrm{T}} - \sin(2\lambda_n r_{\mathrm{T}})}{4\lambda_n^3}, n = n^{'}, \\ 0, \qquad\qquad\quad n \neq n^{'}. \end{cases} \tag{A.5}$$

We substitute (A.4) into (3.2) and then multiply $j_0\left(\lambda_n r\right)$ to both sides of the equality. With some mathematical manipulations and taking the integral of both sides with respect to r, we obtain

$$\sum_{n=1}^{\infty} \mathcal{C}_n B_n \int_0^{r_{\mathrm{T}}} r^2 j_0^2(\lambda_n r)\mathrm{d}r = \frac{1}{4\pi}\int_0^{r_{\mathrm{T}}} \delta(r) j_0(\lambda_n r)\mathrm{d}r. \tag{A.6}$$

Based on (A.5) and (A.6), we obtain $\mathcal{C}_n B_n = \frac{\lambda_n^3}{\pi(2\lambda_n r_{\mathrm{T}} - \sin(2\lambda_n r_{\mathrm{T}}))}$. By substituting $\mathcal{C}_n B_n$ into (A.4), we obtain $C(r,t)$. According to [130, eq. (3.106)], the molecule release rate is expressed as $f_{\mathrm{r}}(t) = 4\pi r_{\mathrm{T}}^2 k_{\mathrm{f}} C(r_{\mathrm{T}},t)$. By substituting $C(r_{\mathrm{T}},t)$ into $f_{\mathrm{r}}(t)$, we obtain (3.5).

A.2 Proof of Lemma 3.1

We perform the surface integral by considering a small surface element that is the lateral surface of a conical frustum, denoted by $\mathrm{d}S$, on the TX membrane. The point $\hat{\alpha}$ is on $\mathrm{d}S$ with the coordinates (x,y,z). The base and top radii of this conical frustum are y and $y+\mathrm{d}y$, respectively, and the slant height is $\sqrt{\mathrm{d}^2x + \mathrm{d}^2y}$. Based on the expression for the lateral surface area of a conical frustum, $\mathrm{d}S$ is calculated as $\mathrm{d}S = 2\pi y\sqrt{1+\left(\frac{\mathrm{d}y}{\mathrm{d}x}\right)^2}\mathrm{d}x + \pi\frac{\mathrm{d}y}{\mathrm{d}x}\sqrt{1+\left(\frac{\mathrm{d}y}{\mathrm{d}x}\right)^2}\mathrm{d}^2x$. Since $y = \sqrt{r_{\mathrm{T}}^2 - x^2}$, we have $\frac{\mathrm{d}y}{\mathrm{d}x} = -\frac{x}{\sqrt{r_{\mathrm{T}}^2-x^2}}$. By substituting $\frac{\mathrm{d}y}{\mathrm{d}x}$ into $\mathrm{d}S$, we obtain $\mathrm{d}S = 2\pi r_{\mathrm{T}}\mathrm{d}x - \frac{\pi x r_{\mathrm{T}}}{r_{\mathrm{T}}^2-x^2}\mathrm{d}^2x \approx 2\pi r_{\mathrm{T}}\mathrm{d}x$, where $\frac{\pi x r_{\mathrm{T}}}{r_{\mathrm{T}}^2-x^2}\mathrm{d}^2x$ is omitted since it is a higher order infinitesimal. As $\mathrm{d}S$ is an infinitesimal, we treat the distance between each point on $\mathrm{d}S$ and the center of the RX as $r_{\hat{\alpha}}$, where $r_{\hat{\alpha}}$ can be expressed based on x as $r_{\hat{\alpha}} = \sqrt{r_{\mathrm{T}}^2 + l^2 - 2lx}$. By substituting $r_{\hat{\alpha}}$ into (3.8), we obtain $h_{\hat{\alpha}}(t,x)$. Accordingly, the hitting rate at the RX for molecules released from $\mathrm{d}S$ is $\rho h_{\hat{\alpha}}(t,x)\mathrm{d}S$. Furthermore, $h_{\mathrm{u}}(t)$ is obtained by integrating $\rho h_{\hat{\alpha}}(t,x)\mathrm{d}S$, i.e., $h_{\mathrm{u}}(t) = \int_{\Omega_{\mathrm{t}}} \rho h_{\hat{\alpha}}(t,x)\mathrm{d}S = \int_{-r_{\mathrm{T}}}^{r_{\mathrm{T}}} 2\pi r_{\mathrm{T}}\rho h_{\hat{\alpha}}(t,x)\mathrm{d}x$. By substituting $h_{\hat{\alpha}}(t,x)$ into $h_{\mathrm{u}}(t)$ and solving the integral, we obtain (3.9).

A.3 Proof of Corollary 3.4

According to (3.12), we have $H_{\mathrm{e}}(t) = H_{\mathrm{u}}(t) * f_{\mathrm{r}}(t)$. Performing the Laplace transform of this expression, we obtain $\mathcal{H}_{\mathrm{e}}(s) = \mathcal{F}_{\mathrm{r}}(s)\mathcal{H}_{\mathrm{u}}(s)$, where $\mathcal{H}_{\mathrm{e}}(s)$, $\mathcal{F}_{\mathrm{r}}(s)$, and $\mathcal{H}_{\mathrm{u}}(s)$ are the Laplace transform of $H_{\mathrm{e}}(t)$, $f_{\mathrm{r}}(t)$, and $H_{\mathrm{u}}(t)$, respectively. According to the final value theorem [176, eq. (1)], if $H_{\mathrm{e}}(t)$ has a finite limit as $t \to \infty$, then we have $\lim_{t\to\infty} H_{\mathrm{e}}(t) = \lim_{s\to 0} s\mathcal{H}_{\mathrm{e}}(s)$. Thus, we calculate $\lim_{t\to\infty} H_{\mathrm{e}}(t)$ as

$$\lim_{t\to\infty} H_{\mathrm{e}}(t) = \frac{8r_{\mathrm{T}}^3 r_{\mathrm{R}} k_{\mathrm{f}} \rho \pi}{r_0 D_{\mathrm{v}}} \sqrt{\frac{D_A}{k_{\mathrm{d}}}} \left[\exp\left(-2\sqrt{\beta_1 k_{\mathrm{d}}}\right) - \exp\left(-2\sqrt{\beta_2 k_{\mathrm{d}}}\right)\right] \sum_{n=1}^{\infty} \frac{\lambda_n j_0(\lambda_n r_{\mathrm{T}})}{2\lambda_n r_{\mathrm{T}} - \sin(2\lambda_n r_{\mathrm{T}})}. \tag{A.7}$$

By substituting $t \to \infty$ into (3.7) and noting that $F_{\mathrm{r}}(t \to \infty) = 1$, we obtain $\sum_{n=1}^{\infty} \frac{\lambda_n j_0(\lambda_n r_{\mathrm{T}})}{2\lambda_n r_{\mathrm{T}} - \sin(2\lambda_n r_{\mathrm{T}})} = \frac{D_{\mathrm{v}}}{4r_{\mathrm{T}}^2 k_{\mathrm{f}}}$. By substituting this expression into (A.7), we obtain (3.14).

Appendix B

B.1 Proof of Corollary 4.2

According to (4.5), we have

$$H_{\mathrm{u},\infty}(w) = \frac{r_{\mathrm{R}} w}{r_0}\left[\alpha_1(\infty) - \alpha_2(\infty, w)\right]. \tag{B.1}$$

Based on (4.6), we have $\alpha_1(\infty) = \exp(-\hat{\beta})/\sqrt{k_{\mathrm{d}} D_A}$. To obtain $\alpha_2(\infty, w)$, we need to determine $\psi_1(\infty, w)$ and $\psi_2(\infty, w)$ in (4.7). In (4.8), if $\zeta(w) \leq 0$, we have $\psi_1(\infty, w) = 0$. If $\zeta(w) > 0$, we obtain

$$\begin{aligned}
\psi_1(\infty, w) &= 2\hat{\gamma}(w)\exp(\hat{\gamma}(w)(r_0 - r_{\mathrm{R}}))\lim_{t\to\infty}\frac{\operatorname{erfc}\left(\frac{\tilde{\varepsilon}}{\sqrt{t}} + \hat{\gamma}(w)\sqrt{D_A t}\right)}{\exp(-\zeta(w)t)} \\
&\overset{(a)}{=} 2\hat{\gamma}(w)\lim_{t\to\infty}\frac{\exp\left(-\left(\frac{\tilde{\varepsilon}^2}{t} + k_{\mathrm{d}} t\right)\right)}{-\zeta(w)}\left(\frac{\tilde{\varepsilon}}{\sqrt{t^3}} - \hat{\gamma}(w)\sqrt{\frac{D_A}{t}}\right) \\
&= 0,
\end{aligned} \tag{B.2}$$

where step (a) is obtained by applying L'Hôpital's rule. Therefore, we have $\psi_1(\infty, w) = 0$ for any value of $\zeta(w)$. According to (4.9), we obtain $\psi_2(\infty, w) = -2\hat{\gamma}(w)^2\sqrt{D_A/k_{\mathrm{d}}}\exp\left(-\hat{\beta}\right)$. By substituting $\psi_1(\infty, w)$ and $\psi_2(\infty, w)$ into (4.7), we obtain $\alpha_2(\infty, w)$. Then, by substituting $\alpha_1(\infty)$ and $\alpha_2(\infty, w)$ into (B.1), we obtain (4.10).

B.2 Proof of Theorem 4.2

As $f_{\mathrm{r}}(t)$ is the molecule release rate from the MF-based TX membrane at time t and $h_{\mathrm{s}}(t)$ is the expected molecule hitting rate at the AP-based RX at time t when molecules are uniformly released from the TX membrane at $t = 0$, $h_{\mathrm{MF}}(t)$ is obtained as

$$h_{\mathrm{MF}}(t) = \int_0^t f_{\mathrm{r}}(u) h_{\mathrm{s}}(t-u)\mathrm{d}u, \tag{B.3}$$

where $f_{\mathrm{r}}(t)$ is given by (3.5). By substituting (3.5) and (4.22) into (B.3), we obtain (4.27).

B.3 Proof of Corollary 4.6

We note that $H_{\mathrm{MF}}(t)$ can be represented as $H_{\mathrm{MF}}(t) = f_{\mathrm{r}}(t) * H_{\mathrm{s}}(t)$. By performing the Laplace transform of both sides, we obtain $\mathcal{H}_{\mathrm{MF}}(s) = \hat{f}_{\mathrm{r}}(s)\mathcal{H}_{\mathrm{s}}(s)$, where $\mathcal{H}_{\mathrm{MF}}(s)$, $\hat{f}_{\mathrm{r}}(s)$, and $\mathcal{H}_{\mathrm{s}}(s)$ are the Laplace transforms of $H_{\mathrm{MF}}(t)$, $f_{\mathrm{r}}(t)$, and $H_{\mathrm{s}}(t)$, respectively. According to [177, Eqs. (1.8), (5.1), (17.68)], we obtain

$$\hat{f}_{\mathrm{r}}(s) = \sum_{n=1}^{\infty} \frac{4r_{\mathrm{T}}^2 k_{\mathrm{f}} \lambda_n^3 j_0(\lambda_n r_{\mathrm{T}})}{(2\lambda_n r_{\mathrm{T}} - \sin(2\lambda_n r_{\mathrm{T}}))(s + D_{\mathrm{v}}\lambda_n^2)}, \tag{B.4}$$

and

$$\mathcal{H}_{\mathrm{s}}(s) = \frac{r_{\mathrm{R}} w_{\mathrm{e}}}{2r_{\mathrm{T}} r_0 \zeta(w_{\mathrm{e}})} \left[\hat{\xi}_2(s, r_0 - r_{\mathrm{T}} - r_{\mathrm{R}}) - \hat{\xi}_2(s, r_0 + r_{\mathrm{T}} - r_{\mathrm{R}}) \right], \tag{B.5}$$

where $\hat{\xi}_2(s,z)$ is given by

$$\begin{aligned}
\hat{\xi}_2(s,z) = {} & \exp(\hat{\gamma}(w_{\mathrm{e}})z) \frac{\exp(-\frac{z}{2D_A}(\varpi(w_{\mathrm{e}}) + \sqrt{s+k_{\mathrm{d}}}))}{\sqrt{s+k_{\mathrm{d}}}(\varpi(w_{\mathrm{e}}) + \sqrt{s+k_{\mathrm{d}}})} - \frac{1}{2\sqrt{k_{\mathrm{d}}}} \exp\left(-z\sqrt{\frac{k_{\mathrm{d}}}{D_A}}\right) [(\varpi(w_{\mathrm{e}}) \\
& - \sqrt{k_{\mathrm{d}}}) \left(\frac{1}{s} - \frac{\exp(-\frac{z}{D_A}(\sqrt{s+k_{\mathrm{d}}} - \sqrt{k_{\mathrm{d}}}))}{\sqrt{s+k_{\mathrm{d}}}(\sqrt{s+k_{\mathrm{d}}} - \sqrt{k_{\mathrm{d}}})} \right) - \left(\varpi(w_{\mathrm{e}}) + \sqrt{k_{\mathrm{d}}}\right) \left(1 - \exp\left(2z\sqrt{\frac{k_{\mathrm{d}}}{D_A}}\right) \right. \\
& \left. \times \frac{\exp(-\frac{z}{\sqrt{D}}(\sqrt{k_{\mathrm{d}}+s} + \sqrt{k_{\mathrm{d}}}))}{(\sqrt{s+k_{\mathrm{d}}} + \sqrt{k_{\mathrm{d}}})\sqrt{s+k_{\mathrm{d}}}} \right) \Bigg] - \frac{\exp\left(-z\sqrt{\frac{k_{\mathrm{d}}}{D_A}}\right)}{s}.
\end{aligned} \tag{B.6}$$

Based on the final value theorem [176, Eq. (1)], we have $\lim_{t\to\infty} H_{\mathrm{MF}}(t) = \lim_{s\to 0} s\mathcal{H}_{\mathrm{MF}}(s)$. By substituting (B.4) and (B.5) into this equation, we obtain (4.32).

Appendix C

C.1 Proof of Theorem 5.1

Taking the integral for both (5.6) and (5.7) over the interval $[0,t]$, we obtain

$$H_2(t) = H(r_2,t) - H_1(t) * h(r_1+r_2,t), \tag{C.1}$$

$$H_1(t) = H(r_1,t) - H_2(t) * h(r_1+r_2,t), \tag{C.2}$$

where $*$ is the convolution operator. Substituting $H_1(t)$ in (C.1) with (C.2) and performing the Laplace transform, we obtain

$$\mathcal{H}_2(s) = \frac{\exp\left(-r_2\sqrt{\frac{s+k_\mathrm{d}}{D_A}}\right) - \exp\left(-(2r_1+r_2)\sqrt{\frac{s+k_\mathrm{d}}{D_A}}\right)}{s\left(1-\exp\left(-2(r_1+r_2)\sqrt{\frac{s+k_\mathrm{d}}{D_A}}\right)\right)}, \tag{C.3}$$

where $\mathcal{H}_2(s)$ is the Laplace transform of $H_2(t)$. To obtain the inverse Laplace transform of (C.3), we define two new equations as

$$G_1(s) = \frac{\exp\left(-r_2\sqrt{\frac{s+k_\mathrm{d}}{D_A}}\right) - \exp\left(-(2r_1+r_2)\sqrt{\frac{s+k_\mathrm{d}}{D_A}}\right)}{(s+k_\mathrm{d})\left(1-\exp\left(-2(r_1+r_2)\sqrt{\frac{s+k_\mathrm{d}}{D_A}}\right)\right)} \tag{C.4}$$

and

$$G_2(s) = \underbrace{\frac{\exp\left(-\frac{r_2}{\sqrt{D_A}}s\right)}{s^2\left(1-\exp\left(-\frac{2(r_1+r_2)}{\sqrt{D_A}}s\right)\right)}}_{G_{2,1}(s)} - \underbrace{\frac{\exp\left(-\frac{2(r_1+r_2)}{\sqrt{D_A}}s\right)}{s^2\left(1-\exp\left(-\frac{2(r_1+r_2)}{\sqrt{D_A}}s\right)\right)}}_{G_{2,2}(s)}. \tag{C.5}$$

We note that $\mathcal{H}_2(s) = G_1(s) + \frac{k_\mathrm{d}}{s}G_1(s)$ and $G_1(s) = G_2(\sqrt{s+k_\mathrm{d}})$. Thus, we first solve

the inverse Laplace transform of $G_2(s)$. From (C.5), we observe that $G_{2,1}(s)$ and $G_{2,2}(s)$ have similar forms. Thus, we only show the process of performing the inverse Laplace transform of $G_{2,1}(s)$. We re-write $G_{2,1}(s)$ as

$$G_{2,1}(s) = \exp\left(-\frac{r_2}{\sqrt{D_A}}s\right) \times \frac{1}{s\left(1-\exp\left(-\frac{r_1+r_2}{\sqrt{D_A}}s\right)\right)} \times \frac{1}{s\left(1+\exp\left(-\frac{r_1+r_2}{\sqrt{D_A}}s\right)\right)}. \tag{C.6}$$

According to [177, eqs. (5.1), (5.34), (5.36), (1.18)], the inverse Laplace transform of $G_{2,1}(s)$, denoted by $g_{2,1}(t)$, is

$$g_{2,1}(t)=\begin{cases} 0,\ 0<t<\frac{r_2}{\sqrt{D_A}} \\ (i+1)\left(t-\frac{r_2}{\sqrt{D_A}}-\frac{r_1+r_2}{\sqrt{D_A}}i\right),\ \frac{r_2}{\sqrt{D_A}}+\frac{2i(r_1+r_2)}{\sqrt{D_A}}<t<\frac{r_2}{\sqrt{D_A}}+2(i+1)\frac{r_1+r_2}{\sqrt{D_A}}, i=0,1,2,3,... \end{cases} \tag{C.7}$$

According to [177, eq. (1.27)], the inverse Laplace transform of $G_{2,1}(\sqrt{s})$ is

$$\begin{aligned} &\mathcal{L}^{-1}\left\{G_{2,1}(\sqrt{s})\right\} = \frac{1}{2\sqrt{\pi t^3}}\int_0^\infty \hat{u}\exp\left(-\frac{\hat{u}^2}{4t}\right) g_{2,1}(\hat{u})\mathrm{d}\hat{u} \\ &=\frac{1}{\sqrt{4\pi t}}\sum_{i=0}^{\infty}(i+1)\left[2\exp\left(-\frac{\hat{u}^2}{4t}\right)\left(\frac{ir_1+(i+1)r_2}{\sqrt{D_A}}-\hat{u}\right)+\sqrt{4\pi t}\,\mathrm{erf}\left(\frac{\hat{u}}{\sqrt{4t}}\right)\right]\Bigg|_{\frac{2ir_1+(2i+1)r_2}{\sqrt{D_A}}}^{\frac{2(i+1)r_1+(2i+3)r_2}{\sqrt{D_A}}}, \end{aligned} \tag{C.8}$$

where $\hat{F}(x)\big|_a^b = \hat{F}(b)-\hat{F}(a)$. As aforementioned, $G_{2,1}(s)$ and $G_{2,2}(s)$ have similar forms. Therefore, the inverse Laplace transform of $G_{2,2}(\sqrt{s})$, denoted as $\mathcal{L}^{-1}\{G_{2,2}(\sqrt{s})\}$, can be derived analogously. Based on [177, eq. (1.3)], (C.8), and $\mathcal{L}^{-1}\{G_{2,2}(\sqrt{s})\}$, the inverse Laplace transform of $G_1(s)$, denoted by $g_1(t)$, is derived as

$$g_1(t) = \exp(-k_\mathrm{d}t)\left(\mathcal{L}^{-1}\left\{G_{2,1}(\sqrt{s})\right\} - \mathcal{L}^{-1}\left\{G_{2,2}(\sqrt{s})\right\}\right). \tag{C.9}$$

Given $\mathcal{H}_2(s) = G_1(s) + \frac{k_\mathrm{d}}{s}G_1(s)$, the inverse Laplace transform of $\mathcal{H}_2(s)$ is

$$H_2(t) = g_1(t) + k_\mathrm{d}\int_0^t g_1(\hat{u})\mathrm{d}\hat{u}. \tag{C.10}$$

Substituting (C.9) into (C.10), we obtain (5.8).

C.2 Proof of Corollary 5.1

According to the final value theorem, if $H_2(t)$ has a finite limit as $t \to \infty$, we have

$$\lim_{t\to\infty} H_2(t) = \lim_{s\to 0} s\mathcal{H}_2(s). \tag{C.11}$$

When $k_\mathrm{d} \neq 0$, substituting (C.3) into (C.11), we obtain

$$H_{2,\mathrm{asy}} = \frac{\exp\left(-r_2\sqrt{\frac{k_\mathrm{d}}{D_A}}\right) - \exp\left(-(2r_1+r_2)\sqrt{\frac{k_\mathrm{d}}{D_A}}\right)}{1-\exp\left(-2(r_1+r_2)\sqrt{\frac{k_\mathrm{d}}{D_A}}\right)}. \tag{C.12}$$

When $k_\mathrm{d} = 0$, we apply L'Hôpital's rule [178] to (C.12), and we have

$$\begin{aligned} H_{2,\mathrm{asy}} &= \lim_{k_\mathrm{d}\to 0} \frac{\frac{\partial}{\partial k_\mathrm{d}}\left(\exp\left(-r_2\sqrt{\frac{k_\mathrm{d}}{D_A}}\right) - \exp\left(-(2r_1+r_2)\sqrt{\frac{k_\mathrm{d}}{D_A}}\right)\right)}{\frac{\partial}{\partial k_\mathrm{d}}\left(1-\exp\left(-2(r_1+r_2)\sqrt{\frac{k_\mathrm{d}}{D_A}}\right)\right)} \\ &= \frac{r_1}{r_1+r_2}. \end{aligned} \tag{C.13}$$

Combining (C.12) and (C.13), we obtain (5.11).

C.3 Proof of Theorem 5.2

We denote $\hat{H}_j(t)$ as the probability that molecules can be absorbed by time t, when these molecules are released from the TX at time $t = 0$. Then, $N_j(t)$ can be computed as $N_j(t) = \mu * \hat{H}_j(t)$. As μ is constant, we can further express $N_j(t)$ as $N_j(t) = \mu \int_0^t \hat{H}_j(u)\mathrm{d}u$. We note that $\hat{H}_j(t)$ includes the effect of flow in the environment. To obtain $N_j(t)$, we first calculate $\hat{H}_j(t)$.

We denote $h_\mathrm{v}(r_0,t,k_\mathrm{d},v)$ as the molecule hitting rate with flow when only one RX exists. According to [179], $h_\mathrm{v}(r_0,t,k_\mathrm{d},v)$ is given by

$$h_\mathrm{v}(r_0,t,k_\mathrm{d},v) = \frac{r_0}{\sqrt{4\pi D_A t^3}} \exp\left(\frac{r_0 v}{2D_A} - \frac{r_0^2}{4D_A t} - \left(\frac{v^2}{4D_A} + k_\mathrm{d}\right)t\right). \tag{C.14}$$

In (C.14), we assume that the direction of the flow is from the TX toward RX. For the opposite direction, we replace v with $-v$. Then, we have

$$h_\mathrm{v}(r_0,t,k_\mathrm{d},v) = \exp\left(\frac{r_0 v}{2D_A}\right) h\left(r_0,t,k_\mathrm{d}+\frac{v^2}{4D_A}\right), \tag{C.15}$$

where $f(r_0,t,k_\mathrm{d})$ is given by (5.1). We denote $H_\mathrm{v}(r_0,t,k_\mathrm{d},v)$ as the fraction of absorbed molecules by time t with flow when only one RX exists. which is obtained by integrating

$h_{\mathrm{v}}(r_0,t,k_{\mathrm{d}},v)$ over time t. Accodring to (C.15), we have

$$H_{\mathrm{v}}(r_0,t,k_{\mathrm{d}},v)=\exp\left(\frac{r_0 v}{2D_A}\right)H\left(r_0,t,k_{\mathrm{d}}+\frac{v^2}{4D_A}\right), \tag{C.16}$$

where $H(r_0,t,k_{\mathrm{d}})$ is given by (5.2). Similar to (C.1)and (C.2), we can express $\hat{H}_1(t)$ and $\hat{H}_2(t)$ as

$$\hat{H}_2(t)=H_{\mathrm{v}}(r_2,t,k_{\mathrm{d}},v)-\hat{H}_1(t)*h_{\mathrm{v}}(r_1+r_2,t,k_{\mathrm{d}},v), \tag{C.17}$$

$$\hat{H}_1(t)=H_{\mathrm{v}}(d_1,t,k,-v)-\hat{H}_2(t)*h_{\mathrm{v}}(d_1+d_2,t,k,-v), \tag{C.18}$$

Substituting (C.15) and (C.16) into (C.18) and (C.17) and performing the Laplace transform for (C.18) and (C.17), we obtain

$$\hat{\mathcal{H}}_2(s)=\exp\left(\frac{r_2 v}{2D_A}\right)\mathcal{H}_2\left(s,\frac{v^2}{4D_A}+k_{\mathrm{d}}\right), \tag{C.19}$$

where $\hat{\mathcal{H}}_2(s)$ is the Laplace transform of $\hat{H}_2(t)$ and $\mathcal{H}_2(s,k_{\mathrm{d}})$ is given by (C.3). Performing the inverse Laplace transform of (C.19), we obtain $\hat{H}_2(t)=\exp\left(\frac{r_2 v}{2D_A}\right)H_2(t,\frac{v^2}{4D_A}+k_{\mathrm{d}})$. Substituting $\hat{H}_2(t)$ into $N_2(t)=\mu\int_0^t\hat{H}_2(u)\mathrm{d}u$, we obtain $N_2(t)$. $N_1(t)$ can be obtained by exchanging r_1 and r_2 and replacing v with $-v$ therein for $N_2(t)$. Based on the expressions for $N_1(t)$ and $N_2(t)$, a unified formula can be written as (5.12).

C.4 Proof of Theorem 5.3

According to the final value theorem, if $\hat{H}_2(t)$ has a finite limit as $t\to\infty$, we have

$$\lim_{t\to\infty}\hat{H}_2(t)=\lim_{s\to 0}s\hat{\mathcal{H}}_2(s). \tag{C.20}$$

Substituting (C.19) into (C.20), we obtain $\hat{H}_2(t)\big|_{t\to\infty}$ as

$$\begin{aligned}\hat{H}_2(t)\big|_{t\to\infty}&=\exp\left(\frac{r_2 v}{2D_A}\right)\lim_{s\to 0}s\mathcal{H}_2\left(s,\frac{v^2}{4D_A}+k_{\mathrm{d}}\right)\\&=\exp\left(\frac{r_2 v}{2D_A}\right)H_{2,\mathrm{asy}}\left(k_{\mathrm{d}}+\frac{v^2}{4D_A}\right),\end{aligned} \tag{C.21}$$

where $H_{2,\mathrm{asy}}(k_{\mathrm{d}})$ is given by (5.11). According to $N_2(t)=\mu\int_0^t\hat{H}_2(u)\mathrm{d}u$, absorbed molecules

at RX_2 within the time interval $[t-\delta, t]$ at the asymptotic stage is

$$\tilde{N}_2 = \mu \delta \hat{H}_2(t)\big|_{t\to\infty}. \tag{C.22}$$

Substituting (C.21) into (C.22), we obtain $\tilde{N}_2$. $\tilde{N}_1$ can be obtained by exchanging r_1 and r_2 and replacing v with $-v$ therein for $\tilde{N}_2$. Based on the expressions for $\tilde{N}_1$ and $\tilde{N}_2$, a unified formula can be written as (5.15).

C.5 Proof of Theorem 5.4

For the CRLB to exist, the regularity condition [159] must be satisfied, which is $\mathbb{E}\left[\frac{\partial \ln p(\tilde{\mathbf{g}}|\varepsilon)}{\partial \varepsilon}\right] = 0$. Substituting (5.16) into $\mathbb{E}\left[\frac{\partial \ln p(\tilde{\mathbf{g}}|\varepsilon)}{\partial \varepsilon}\right]$, we obtain

$$\mathbb{E}\left[\frac{\partial \ln p\left(\tilde{\mathbf{g}}|\varepsilon\right)}{\partial \varepsilon}\right] = \sum_{s=1}^{S} -\tilde{\gamma}_1(\varepsilon) - \tilde{\gamma}_2(\varepsilon) + \frac{\mathbb{E}\left[\tilde{g}_s\right]}{2}\left(\frac{\tilde{\gamma}_2(\varepsilon)}{\hat{N}_2} - \frac{\tilde{\gamma}_1(\varepsilon)}{\hat{N}_1}\right) + \left(\mathbb{E}\left[\frac{I_{\tilde{g}_s-1}\left(2\sqrt{\hat{N}_1\hat{N}_2}\right)}{I_{\tilde{g}_s}\left(2\sqrt{\hat{N}_1\hat{N}_2}\right)}\right]\right.$$
$$\left. - \frac{\tilde{g}_s}{2\sqrt{\hat{N}_1\hat{N}_2}}\right)\left(\sqrt{\frac{\hat{N}_2}{\hat{N}_1}}\tilde{\gamma}_1(\varepsilon) + \sqrt{\frac{\hat{N}_1}{\hat{N}_2}}\tilde{\gamma}_2(\varepsilon)\right). \tag{C.23}$$

Based on the definition of expectation, $\mathbb{E}\left[\frac{I_{\tilde{g}_s-1}\left(2\sqrt{\hat{N}_1\hat{N}_2}\right)}{I_{\tilde{g}_s}\left(2\sqrt{\hat{N}_1\hat{N}_2}\right)}\right]$ is calculated as

$$\mathbb{E}\left[\frac{I_{\tilde{g}_s-1}\left(2\sqrt{\hat{N}_1\hat{N}_2}\right)}{I_{\tilde{g}_s}\left(2\sqrt{\hat{N}_1\hat{N}_2}\right)}\right] = \sum_{\tilde{g}_s=-\infty}^{\infty} \frac{I_{\tilde{g}_s-1}\left(2\sqrt{\hat{N}_1\hat{N}_2}\right)}{I_{\tilde{g}_s}\left(2\sqrt{\hat{N}_1\hat{N}_2}\right)} \exp\left(-\left(\hat{N}_1+\hat{N}_2\right)\right)\left(\frac{\hat{N}_2}{\hat{N}_1}\right)^{\frac{\tilde{g}_s}{2}} I_{\tilde{g}_s}\left(2\sqrt{\hat{N}_1\hat{N}_2}\right)$$
$$= \sqrt{\frac{\hat{N}_2}{\hat{N}_1}}\hat{\eta} = \sqrt{\frac{\hat{N}_2}{\hat{N}_1}}, \tag{C.24}$$

where

$$\hat{\eta} = \sum_{\tilde{g}_s=-\infty}^{\infty} \exp\left(-\left(\hat{N}_1+\hat{N}_2\right)\right)\left(\frac{\hat{N}_2}{\hat{N}_1}\right)^{\frac{\tilde{g}_s-1}{2}} I_{\tilde{g}_s-1}\left(2\sqrt{\hat{N}_1\hat{N}_2}\right) \tag{C.25}$$

is the summation of PMF of Skellam distribution. Therefore, $\hat{\eta} = 1$. Substituting (C.24) and $\mathbb{E}\left[\tilde{g}_s\right] = \tilde{N}_2 - \tilde{N}_1$ into (C.23), we obtain $\mathbb{E}\left[\frac{\partial \ln p(\tilde{\mathbf{g}}|\varepsilon)}{\partial \varepsilon}\right] = 0$. We then calculate $L(\varepsilon)$. Substituting

(5.16) into (5.17), we obtain

$$L(\varepsilon)=\sum_{\tilde{g}_s=1}^{S}-\frac{3\hat{N}_2-\hat{N}_1}{4\hat{N}_2^2}\tilde{\gamma}_2^2(\varepsilon)+\frac{3\hat{N}_1-\hat{N}_2}{4\hat{N}_1^2}\tilde{\gamma}_1^2(\varepsilon)-\frac{\hat{N}_1+\hat{N}_2}{2\hat{N}_1\hat{N}_2}\tilde{\gamma}_1(\varepsilon)\tilde{\gamma}_2(\varepsilon)\left(\frac{\mathbb{E}\left[\frac{\tilde{g}_s I_{\tilde{g}_s-1}}{I_{\tilde{g}_s}}\right]}{\hat{N}_1\hat{N}_2}-\frac{\mathbb{E}\left[\tilde{g}_s^2\right]}{4\hat{N}_1\hat{N}_2}\right.$$
$$\left.+\frac{1}{2}+\frac{1}{4}\left(\mathbb{E}\left[\frac{I_{\tilde{g}_s-2}\left(\sqrt{2\hat{N}_1\hat{N}_2}\right)}{I_{\tilde{g}_s}\left(\sqrt{2\hat{N}_1\hat{N}_2}\right)}\right]+\mathbb{E}\left[\frac{I_{\tilde{g}_s+2}\left(\sqrt{2\hat{N}_1\hat{N}_2}\right)}{I_{\tilde{g}_s}\left(\sqrt{2\hat{N}_1\hat{N}_2}\right)}\right]\right)-\mathbb{E}\left[\frac{I_{\tilde{g}_s-1}^2\left(\sqrt{2\hat{N}_1\hat{N}_2}\right)}{I_{\tilde{g}_s}^2\left(\sqrt{2\hat{N}_1\hat{N}_2}\right)}\right]\right)$$
$$\times\left(\sqrt{\frac{\hat{N}_2}{\hat{N}_1}}\tilde{\gamma}_1(\varepsilon)+\sqrt{\frac{\hat{N}_1}{\hat{N}_2}}\tilde{\gamma}_2(\varepsilon)\right)^2. \tag{C.26}$$

Similar to the method in (C.24), we calculate $\mathbb{E}\left[\frac{\tilde{g}_s I_{\tilde{g}_s-1}}{I_{\tilde{g}_s}}\right]=\sqrt{\frac{\hat{N}_2}{\hat{N}_1}}\left(\hat{N}_2-\hat{N}_1+1\right)$, $\mathbb{E}\left[\tilde{g}_s^2\right]=\left(\hat{N}_2-\hat{N}_1\right)^2+\hat{N}_1+\hat{N}_2$, $\mathbb{E}\left[\frac{I_{\tilde{g}_s-2}\left(2\sqrt{\hat{N}_1\hat{N}_2}\right)}{I_{\tilde{g}_s}\left(2\sqrt{\hat{N}_1\hat{N}_2}\right)}\right]=\frac{\hat{N}_2}{\hat{N}_1}$, and $\mathbb{E}\left[\frac{I_{\tilde{g}_s+2}\left(2\sqrt{\hat{N}_1\hat{N}_2}\right)}{I_{\tilde{g}_s}\left(2\sqrt{\hat{N}_1\hat{N}_2}\right)}\right]=\frac{\hat{N}_1}{\hat{N}_2}$. In $L(\varepsilon)$, ϑ represents the value of $E\left[\frac{I_{\tilde{g}_s-1}^2\left(\sqrt{2\hat{N}_1\hat{N}_2}\right)}{I_{\tilde{g}_s}^2\left(\sqrt{2\hat{N}_1\hat{N}_2}\right)}\right]$ that is also calculated based on the definition of the expectation. For calculating ϑ, we do not need the summation from $\tilde{g}_s=-\infty$ to $\tilde{g}_s=\infty$, and we focus on the range of $\tilde{g}_s$ that makes the PMF of the Skellam distribution larger than a threshold that we choose to be 10^{-3} in our paper, i.e., $\exp\left(-\left(\hat{N}_1+\hat{N}_2\right)\right)\left(\frac{\hat{N}_2}{\hat{N}_1}\right)^{\frac{\tilde{g}_s}{2}} I_{\tilde{g}_s}\left(2\sqrt{\hat{N}_1\hat{N}_2}\right)\geq 10^{-3}$. The validation of this threshold is performed in our numerical tests. After solving this expression, we have $\zeta_1\leq\tilde{g}_s\leq\zeta_2$. Substituting $\mathbb{E}\left[\frac{\tilde{g}_s I_{\tilde{g}_s-1}}{I_{\tilde{g}_s}}\right]$, $\mathbb{E}\left[\tilde{g}_s^2\right]$, $\mathbb{E}\left[\frac{I_{\tilde{g}_s-2}\left(2\sqrt{\hat{N}_1\hat{N}_2}\right)}{I_{\tilde{g}_s}\left(2\sqrt{\hat{N}_1\hat{N}_2}\right)}\right]$, $\mathbb{E}\left[\frac{I_{\tilde{g}_s+2}\left(2\sqrt{\hat{N}_1\hat{N}_2}\right)}{I_{\tilde{g}_s}\left(2\sqrt{\hat{N}_1\hat{N}_2}\right)}\right]$, and ϑ into (C.26), we obtain (5.18).

Appendix D

D.1 Proof of Theorem 6.1

We first consider $0 < t \leq \hat{\tau}$. When a vesicle is generated in the center of the TX at time u, $0 \leq u \leq \hat{\tau}$, the probability that this vesicle fuses with the TX membrane at time t is given by $f_{\mathrm{r}}(t-u)$. Here, the molecule release rate equals the vesicle fusion probability since MF guarantees the release of molecules into the propagation environment. Due to the continuous generation of vesicles, the number of vesicles fusing with the TX membrane during time interval $[t, t+\delta t]$ is given by $\mu \int_0^t f_{\mathrm{r}}(t-u)\,\mathrm{d}u$. As we define $f_{\mathrm{c}}(t)$ as the probability of a vesicle fusing with the TX membrane during an infinitesimally small time interval, we obtain $f_{\mathrm{c}}(t)$ as

$$f_{\mathrm{c}}(t) = \frac{\mu}{N_{\mathrm{v}}} \int_0^t f_{\mathrm{r}}(t-u)\,\mathrm{d}u = \frac{\mu}{N_{\mathrm{v}}} \int_0^t f_{\mathrm{r}}(u)\,\mathrm{d}u. \tag{D.1}$$

By substituting (3.5) into (D.1), we obtain (6.2). Second, we consider $t > \hat{\tau}$. With this condition, all considered vesicles have already been generated by the TX. Therefore, the number of vesicles fusing with the TX membrane during time interval $[t, t+\delta t]$ is given by $\mu \int_0^{\hat{\tau}} f_{\mathrm{r}}(t-u)\,\mathrm{d}u$. Then, we obtain $f_{\mathrm{c}}(t)$ as

$$f_{\mathrm{c}}(t) = \frac{\mu}{N_{\mathrm{v}}} \int_0^{\hat{\tau}} f_{\mathrm{r}}(t-u)\,\mathrm{d}u = \frac{\mu}{N_{\mathrm{v}}} \int_{t-\hat{\tau}}^t f_{\mathrm{r}}(u)\,\mathrm{d}u. \tag{D.2}$$

By substituting (3.5) into (D.2), we obtain (6.3).

D.2 Proof of Theorem 6.3

We first derive $h_{\mathrm{e}}(t)$ by taking the derivative of $H_{\mathrm{e}}(t)$ with respect to t, given by $h_{\mathrm{e}}(t) = \frac{\partial H_{\mathrm{e}}(t)}{\partial t} = H(t) * \frac{\partial f_{\mathrm{c}}(t)}{\partial t}$. By substituting (6.1) into $\frac{\partial f_{\mathrm{c}}(t)}{\partial t}$, we obtain (6.14). We then derive $P_{\mathrm{r}}(t)$. We recall that $h_{\mathrm{e},i}(u)$ is the molecule release rate from the ith receptor at time u, and $P_{\hat{\alpha}}(t-u)\big|_{r_{\hat{\alpha}}=d_i}$ is the probability that a molecule is observed at the RX at time t assuming this molecule was released from the ith receptor at time u. We then denote $P_{\mathrm{r},i}(t)$ as the

probability that a molecule is observed at the RX at time t assuming molecules were continuously released from the ith receptor, and derive it as $P_{\mathrm{r},i}(t) = \int_0^t h_{\mathrm{e},i}(u) P_{\hat{\alpha}}(t-u)\big|_{r_{\hat{\alpha}}=d_i} \mathrm{d}u = h_{\mathrm{e},i}(t) * P_{\hat{\alpha}}(t)\big|_{r_{\hat{\alpha}}=d_i}$. Then, the probability that a molecule is observed at the RX assuming molecules were released from all receptors is given by $P_{\mathrm{r}}(t) = \sum_{i=1}^{N_{\mathrm{r}}} P_{\mathrm{r},i}(t)$. By substituting $P_{\mathrm{r},i}(t)$ into this expression, we obtain (6.13). Finally, by substituting (6.11) and (6.13) into (6.6), we obtain (6.12).

Bibliography

[1] D. Bi, A. Almpanis, A. Noel, Y. Deng, and R. Schober, "A survey of molecular communication in cell biology: Establishing a new hierarchy for interdisciplinary applications," *IEEE Commun. Surv. Tut.*, vol. 23, no. 3, pp. 1494–1545, Thirdquarter 2021. (cited on pages xxi and 2)

[2] Z. Zhang, Y. Xiao, Z. Ma, M. Xiao, Z. Ding, X. Lei, G. K. Karagiannidis, and P. Fan, "6g wireless networks: Vision, requirements, architecture, and key technologies," *IEEE Veh. Technol. Mag.*, vol. 14, no. 3, pp. 28–41, Sep. 2019. (cited on page 1)

[3] I. F. Akyildiz and J. M. Jornet, "The internet of nano-things," *IEEE Wirel. Commun.*, vol. 17, no. 6, pp. 58–63, 2010. (cited on page 1)

[4] I. F. Akyildiz, F. Brunetti, and C. Blázquez, "Nanonetworks: A new communication paradigm," *Comput. Netw.*, vol. 52, no. 12, pp. 2260–2279, Aug. 2008. (cited on page 1)

[5] T. Nakano, A. W. Eckford, and T. Haraguchi, *Molecular Communication*, 1st ed. Cambridge: Cambridge Univ. Press, 2013. (cited on page 1)

[6] L. Squire, D. Berg, F. E. Bloom, S. Du Lac, A. Ghosh, and N. C. Spitzer, *Fundamental Neuroscience*, 4th ed. Waltham, USA: Acad. Press, 2012. (cited on page 2)

[7] J. Masson, C. Sagne, M. e. Hamon, and S. El Mestikawy, "Neurotransmitter transporters in the central nervous system," *Pharmacol. Rev.*, vol. 51, no. 3, pp. 439–464, Sep. 1999. (cited on pages 3 and 109)

[8] M. B. Miller, B. L. Bassler *et al.*, "Quorum sensing in bacteria," *Year. Rev. Microbiol.*, vol. 55, no. 1, pp. 165–199, Oct. 2001. (cited on page 3)

[9] S. Mukherjee and B. L. Bassler, "Bacterial quorum sensing in complex and dynamically changing environments," *Nat. Rev. Microbiol.*, vol. 17, no. 6, pp. 371–382, June 2019. (cited on page 3)

[10] H. Ueda, Y. Kikuta, and K. Matsuda, "Plant communication: Mediated by individual or blended VOCs?" *Plant Signal. Behav.*, vol. 7, no. 2, pp. 222–226, Feb. 2012. (cited on page 3)

[11] B. B. Simpson and J. L. Neff, "Floral rewards: Alternatives to pollen and nectar," *Ann. Mo. Bot. Gard.*, pp. 301–322, 1981. (cited on page 3)

[12] N. M. v. Dam, A. Weinhold, and P. Garbeva, "Calling in the dark: The role of volatiles for communication in the rhizosphere," in *Deciphering chemical language of plant communication*, 1st ed. Berlin, Germany: Springer, 2016, pp. 175–210. (cited on page 4)

[13] J. M. Chaparro, A. M. Sheflin, D. K. Manter, and J. M. Vivanco, "Manipulating the soil microbiome to increase soil health and plant fertility," *Biol. Fertil. Soils*, vol. 48, no. 5, pp. 489–499, May 2012. (cited on page 4)

[14] S. C. Van Wees, S. Van der Ent, and C. M. Pieterse, "Plant immune responses triggered by beneficial microbes," *Curr. Opin. Plant Biol.*, vol. 11, no. 4, pp. 443–448, Aug. 2008. (cited on page 4)

[15] P. Garbeva and L. Weisskopf, "Airborne medicine: bacterial volatiles and their influence on plant health," *New Phytol.*, vol. 226, no. 1, pp. 32–43, Oct. 2020. (cited on page 4)

[16] R. Ortíz-Castro, H. A. Contreras-Cornejo, L. Macías-Rodríguez, and J. López-Bucio, "The role of microbial signals in plant growth and development," *Plant Signal. Behav.*, vol. 4, no. 8, pp. 701–712, Aug. 2009. (cited on page 4)

[17] R. K. Vander Meer, M. D. Breed, M. Winston, and K. E. Espelie, *Pheromone Communication in Social Insects: Ants, Wasps, Bees, and Termites*. New York, NY: Routledge, 2019. (cited on page 4)

[18] L. Felicetti, M. Femminella, G. Reali, and P. Liò, "A molecular communication system in blood vessels for tumor detection," in *Proc. ACM Nanocom.*, Atlanta, Georgia, USA, May 2014, pp. 1–9. (cited on page 4)

[19] J. Lin, L. Ma, D. Zhang, J. Gao, Y. Jin, Z. Han, and D. Lin, "Tumour biomarkers—tracing the molecular function and clinical implication," *Cell Prolif.*, vol. 52, no. 3, p. e12589, Mar. 2019. (cited on page 4)

[20] L. Felicetti, M. Femminella, G. Reali, and P. Liò, "Applications of molecular communications to medicine: A survey," *Nano Commun. Netw.*, vol. 7, pp. 27–45, Aug. 2016. (cited on page 4)

[21] J.-W. Yoo, D. J. Irvine, D. E. Discher, and S. Mitragotri, "Bio-inspired, bioengineered and biomimetic drug delivery carriers," *Nature Rev. Drug discovery*, vol. 10, no. 7, pp. 521–535, Jul. 2011. (cited on page 4)

[22] C. Sabu, C. Rejo, S. Kotta, and K. Pramod, "Bioinspired and biomimetic systems for advanced drug and gene delivery," *J. Controlled Release*, vol. 287, pp. 142–155, Oct. 2018. (cited on page 4)

[23] E. K.-H. Chow and D. Ho, "Cancer nanomedicine: From drug delivery to imaging," *Sci. Transl. Med.*, vol. 5, no. 216, p. 216rv4, Dec. 2013. (cited on page 4)

[24] A. Chavoshani, M. Hashemi, M. M. Amin, and S. C. Ameta, *Micropollutants and Challenges: Emerging in the Aquatic Environments and Treatment Processes*, 1st ed. Cambridge, MA: Elsevier, 2020. (cited on page 5)

[25] T. Nakano, M. J. Moore, F. Wei, A. V. Vasilakos, and J. Shuai, "Molecular communication and networking: Opportunities and challenges," *IEEE Trans. NanoBiosci.*, vol. 11, no. 2, pp. 135–148, June 2012. (cited on pages 5 and 23)

[26] T. S. Ray, "An evolutionary approach to synthetic biology: Zen and the art of creating life," *Artif. Life*, vol. 1, no. 1_2, pp. 179–209, Oct. 1993. (cited on page 5)

[27] X. Huang, Y. Fang, A. Noel, and N. Yang, "Membrane fusion-based transmitter design for molecular communication systems," in *Proc. IEEE ICC 2021*, Montreal, QC, Canada, Aug. 2021, pp. 1–6. (cited on pages 6 and 97)

[28] ——, "Membrane fusion-based transmitter design for static and diffusive mobile molecular communication systems," *IEEE Trans. Commun.*, vol. 70, no. 1, pp. 132–148, Jan. 2021. (cited on page 6)

[29] X. Huang, Y. Fang, S. T. Johnston, M. Faria, N. Yang, and R. Schober, "Analysis of receiver covered by heterogeneous receptors in molecular communications," in *Proc. IEEE ICC 2022*, Seoul, Korea, Republic of, May 2022, pp. 3703–3708. (cited on pages 7 and 103)

[30] ——, "Analysis of MC systems employing receivers covered by heterogeneous receptors," pp. 1–14, Apr. 2022. [Online]. Available: arXiv:2204.13443 (cited on page 7)

[31] X. Huang, Y. Fang, A. Noel, and N. Yang, "Channel characterization for 1-D molecular communication with two absorbing receivers," *IEEE Commun. Lett.*, vol. 24, no. 6, pp. 1150–1154, Jun. 2020. (cited on pages 7 and 8)

[32] ——, "Parameter estimation in a noisy 1D environment via two absorbing receivers," in *Ptoc. IEEE GLOBECOM 2020*, Taipei, Taiwan, Dec. 2020, pp. 1–7. (cited on pages 7 and 8)

[33] X. Huang, Y. Huang, M. Wen, N. Yang, and R. Schober, "Analysis of molecule harvesting by heterogeneous receptors on MC transmitters," submitted to *Proc. IEEE ICC 2023*. (cited on page 8)

[34] S. Hiyama, Y. Moritani, T. Suda, R. Egashira, A. Enomoto, M. Moore, and T. Nakano, "Molecular communication," in *Proc.NSTI Nanotech.*, vol. 89, no. 2, May 2005, p. 162. (cited on page 9)

[35] T. Suda, M. Moore, T. Nakano, R. Egashira, A. Enomoto, S. Hiyama, and Y. Moritani, "Exploratory research on molecular communication between nanomachines," in *Proc. GECCO 2005*, vol. 25, Washington, DC, USA, June 2005, p. 29. (cited on page 9)

[36] S. Hiyama, Y. Moritani, T. Suda, T. Shima, and K. Sutoh, "An autonomous molecular transport system using dnas and motor proteins in molecular communication," in *Proc. 2nd Bio-NETICS 2007*, Budapest, Hungary, Dec. 2007, pp. 135–138. (cited on page 9)

[37] Y. Moritani, S. Hiyama, and T. Suda, "Molecular communication among nanomachines using vesicles," in *Proc. NSTI-Nanotech 2006*, vol. 2, 2006, pp. 705–708. (cited on page 9)

[38] A. Enomoto, M. Moore, T. Nakano, R. Egashira, T. Suda, A. Kayasuga, H. Kojima, H. Sakakibara, and K. Oiwa, "A molecular communication system using a network of cytoskeletal filaments," in *Proc. NSTI-Nanotech 2006*, 2006. (cited on page 9)

[39] T. Nakano, T. Suda, M. Moore, R. Egashira, A. Enomoto, and K. Arima, "Molecular communication for nanomachines using intercellular calcium signaling," in *IEEE Nano 2005*, Nagoya, Japan, Jul. 2005, pp. 478–481. (cited on page 9)

[40] A. W. Eckford, "Nanoscale communication with brownian motion," in *CISS 2007*, Baltimore, MD, USA, Mar. 2007, pp. 160–165. (cited on page 10)

[41] ——, "Achievable information rates for molecular communication with distinct molecules," in *BIONETICS 2007*, Budapest, Hungary, Dec. 2007, pp. 313–315. (cited on page 10)

[42] B. Atakan and O. B. Akan, "An information theoretical approach for molecular communication," in *BIONETICS 2007*, Budapest, Hungary, Dec. 2007, pp. 33–40. (cited on page 10)

[43] M. J. Moore, T. Suda, and K. Oiwa, "Molecular communication: Modeling noise effects on information rate," *IEEE Trans. Nanobiosci.*, vol. 8, no. 2, pp. 169–180, Jun. 2009. (cited on page 10)

[44] N. Farsad, H. B. Yilmaz, A. Eckford, C.-B. Chae, and W. Guo, "A comprehensive survey of recent advancements in molecular communication," *IEEE Commun. Surveys Tuts.*, vol. 18, no. 3, pp. 1887–1919, 3rd Quart. 2016. (cited on page 11)

[45] V. Jamali, A. Ahmadzadeh, W. Wicke, A. Noel, and R. Schober, "Channel modeling for diffusive molecular communication–a tutorial review," *Proc. IEEE*, Jun. 2019. (cited on pages 11, 24, 51, 74, and 90)

[46] A. Noel, D. Makrakis, and A. Hafid, "Channel impulse responses in diffusive molecular communication with spherical transmitters," in *Proc. Biennial Symp. Commun.*, 2016. (cited on page 11)

[47] H. B. Yilmaz, G.-Y. Suk, and C.-B. Chae, "Chemical propagation pattern for molecular communications," *IEEE Wireless Commun. Lett.*, vol. 6, no. 2, pp. 226–229, Apr. 2017. (cited on pages 11 and 27)

[48] H. Arjmandi, A. Ahmadzadeh, R. Schober, and M. N. Kenari, "Ion channel based biosynthetic modulator for diffusive molecular communication," *IEEE Trans. Nanobiosci.*, vol. 15, no. 5, pp. 418–432, Jul. 2016. (cited on pages 11, 12, and 20)

[49] M. F. Bellemare and C. J. Wichman, "Elasticities and the inverse hyperbolic sine transformation," *Oxf. Bull. Econ. Stat.*, vol. 82, no. 1, pp. 50–61, Jul. 2029. (cited on page 12)

[50] M. Schäfer, W. Wicke, W. Haselmayr, R. Rabenstein, and R. Schober, "Spherical diffusion model with semi-permeable boundary: A transfer function approach," in *Proc. IEEE ICC 2020*, Dublin, Ireland, Jun. 2020. (cited on pages 12, 20, and 27)

[51] L.-S. Meng, P.-C. Yeh, K.-C. Chen, and I. F. Akyildiz, "On receiver design for diffusion-based molecular communication," *IEEE Trans. Signal Process.*, vol. 62, no. 22, pp. 6032–6044, Nov. 2014. (cited on pages 12, 17, and 48)

[52] A. Noel, K. C. Cheung, and R. Schober, "Using dimensional analysis to assess scalability and accuracy in molecular communication," in *Proc. IEEE ICC Workshops*, Budapest, Hungary, June 2013, pp. 818–823. (cited on pages 12, 13, and 101)

[53] M. U. Mahfuz, D. Makrakis, and H. T. Mouftah, "A comprehensive study of sampling-based optimum signal detection in concentration-encoded molecular communication," *IEEE Trans. Nanobiosci.*, vol. 13, no. 3, pp. 208–222, Sep. 2014. (cited on page 12)

[54] B. Alberts, D. Bray, K. Hopkin, A. D. Johnson, J. Lewis, M. Raff, K. Roberts, and P. Walter, *Essential Cell Biology*, 4th ed. New York: Garland Science, 2015. (cited on pages 12 and 18)

[55] H. Unterweger, J. Kirchner, W. Wicke, A. Ahmadzadeh, D. Ahmed, V. Jamali, C. Alexiou, G. Fischer, and R. Schober, "Experimental molecular communication testbed based on magnetic nanoparticles in duct flow," in *IEEE SPAWC 2018*, Kalamata, Greece, June 2018, pp. 1–5. (cited on page 12)

[56] A. Noel, K. C. Cheung, and R. Schober, "Improving receiver performance of diffusive molecular communication with enzymes," *IEEE Trans. NanoBiosci.*, vol. 13, no. 1, pp. 31–43, Mar. 2014. (cited on page 13)

[57] L. C. Andrews, *Special Functions of Mathematics for Engineers*, 2nd ed. New York, NY, USA: Oxford Univ. Press, 1998. (cited on pages 13, 31, and 57)

[58] P. Cuatrecasas, "Membrane receptors," *Annu. Rev. Biochem.*, vol. 43, no. 1, pp. 169–214, Jul. 1974. (cited on page 13)

[59] A. C. Heren, H. B. Yilmaz, C.-B. Chae, and T. Tugcu, "Effect of degradation in molecular communication: Impairment or enhancement?" *IEEE Trans. Mol. Biol. Multi-Scale Commun.*, vol. 1, no. 2, pp. 217–229, Jun. 2015. (cited on pages 13, 14, 30, 56, 66, 73, 74, and 80)

[60] H. B. Yilmaz, A. C. Heren, T. Tugcu, and C.-B. Chae, "Three-dimensional channel characteristics for molecular communications with an absorbing receiver," *IEEE. Commun. Lett.*, vol. 18, no. 6, pp. 929–932, Jun. 2014. (cited on pages 13, 66, and 87)

[61] A. Akkaya, H. B. Yilmaz, C.-B. Chae, and T. Tugcu, "Effect of receptor density and size on signal reception in molecular communication via diffusion with an absorbing receiver," *IEEE Commun. Lett.*, vol. 19, no. 2, pp. 155–158, Feb. 2015. (cited on pages 13, 14, 20, and 53)

[62] S. Kadloor, R. S. Adve, and A. W. Eckford, "Molecular communication using brownian motion with drift," *IEEE Trans. NanoBiosci.*, vol. 11, no. 2, pp. 89–99, Jun. 2012. (cited on page 14)

[63] M. Pierobon and I. F. Akyildiz, "Noise analysis in ligand-binding reception for molecular communication in nanonetworks," *IEEE Trans. Signal Process.*, vol. 59, no. 9, pp. 4168–4182, Sep. 2011. (cited on page 14)

[64] H. ShahMohammadian, G. G. Messier, and S. Magierowski, "Modelling the reception process in diffusion-based molecular communication channels," in *Proc. IEEE ICC Workshops 2013*, Budapest, Hungary, Jun. 2013, pp. 782–786. (cited on page 14)

[65] A. Ahmadzadeh, H. Arjmandi, A. Burkovski, and R. Schober, "Comprehensive reactive receiver modeling for diffusive molecular communication systems: Reversible binding, molecule degradation, and finite number of receptors," *IEEE Trans. Nanobiosci.*, vol. 15, no. 7, pp. 713–727, Oct. 2016. (cited on pages 14, 20, 26, 58, 60, and 66)

[66] J. Sun and H. Li, "Expected received signal in diffusive molecular communication with finite binding receptors," *IEEE Commun. Lett.*, vol. 24, no. 12, pp. 2829–2833, Dec. 2020. (cited on page 14)

[67] Y. Deng, A. Noel, M. Elkashlan, A. Nallanathan, and K. C. Cheung, "Modeling and simulation of molecular communication systems with a reversible adsorption receiver," *IEEE Trans. Mol. Biol. Multi-Scale Commun.*, vol. 1, no. 4, pp. 347–362, Dec. 2015. (cited on pages 14, 41, 42, 43, 66, and 87)

[68] S. Lotter, M. Schäfer, J. Zeitler, and R. Schober, "Saturating receiver and receptor competition in synaptic DMC: Deterministic and statistical signal models," *IEEE Trans. NanoBiosci.*, vol. 20, no. 4, pp. 464–479, Oct. 2021. (cited on page 14)

[69] B. Atakan and O. B. Akan, "On molecular multiple-access, broadcast, and relay channels in nanonetworks," in *Proc. Bionetics 2008*, Hyogo, Japan, Nov. 2008, pp. 1–8. (cited on page 15)

[70] Y. Fang, A. Noel, N. Yang, A. W. Eckford, and R. A. Kennedy, "Convex optimization of distributed cooperative detection in multi-receiver molecular communication," *IEEE Trans. Mol. Biol. Multi-Scale Commun.*, vol. 3, no. 3, pp. 166–182, Sep. 2017. (cited on pages 15 and 79)

[71] Y. Lu, M. D. Higgins, A. Noel, M. S. Leeson, and Y. Chen, "The effect of two receivers on broadcast molecular communication systems," *IEEE Trans. Nanobiosci.*, vol. 15, no. 8, pp. 891–900, Dec. 2016. (cited on pages 15, 16, 20, and 36)

[72] D. Arifler and D. Arifler, "Monte carlo analysis of molecule absorption probabilities in diffusion-based nanoscale communication systems with multiple receivers," *IEEE Trans. Nanobiosci.*, vol. 16, no. 3, pp. 157–165, Apr. 2017. (cited on pages 15, 16, and 20)

[73] M. Damrath, H. B. Yilmaz, C.-B. Chae, and P. A. Hoeher, "Array gain analysis in molecular mimo communications," *IEEE Access*, vol. 6, pp. 61 091–61 102, Oct. 2018. (cited on pages 16 and 20)

[74] W. Guo, Y. Deng, B. Li, C. Zhao, and A. Nallanathan, "Eavesdropper localization in random walk channels," *IEEE Commun. Lett.*, vol. 20, no. 9, pp. 1776–1779, Sep. 2016. (cited on pages 16, 20, and 80)

[75] S. Redner, *A Guide to First-Passage Processes*. New York, USA: Cambridge Univ. Press, 2001. (cited on pages 16 and 20)

[76] J. W. Kwak, H. Birkan Yilmaz, N. Farsad, C.-B. Chae, and A. Goldsmith, "Two-way molecular communications," pp. 1–11, Mar. 2019. [Online]. Available: arXiv:1903.07865v2 (cited on pages 16, 20, 81, 88, and 89)

[77] U. A. Chude-Okonkwo, R. Malekian, B. T. Maharaj, and A. V. Vasilakos, "Molecular communication and nanonetwork for targeted drug delivery: A survey," *IEEE Commun. Surv. Tutor.*, vol. 19, no. 4, pp. 3046–3096, Fourthquarter 2017. (cited on page 16)

[78] A. Ahmadzadeh, V. Jamali, and R. Schober, "Stochastic channel modeling for diffusive mobile molecular communication systems," *IEEE Trans. Commun.*, vol. 66, no. 12, pp. 6205–6220, Dec. 2018. (cited on pages 16, 33, 35, and 43)

[79] T. N. Cao, A. Ahmadzadeh, V. Jamali, W. Wicke, P. L. Yeoh, J. Evans, and R. Schober, "Diffusive mobile MC with absorbing receivers: Stochastic analysis and applications," *IEEE Trans. Mol. Biol. Multi-Scale Commun.*, vol. 5, no. 2, pp. 84–99, Nov. 2019. (cited on pages 16, 28, 33, and 48)

[80] S. Huang, L. Lin, H. Yan, J. Xu, and F. Liu, "Statistical analysis of received signal and error performance for mobile molecular communication," *IEEE Trans. Nanobiosci.*, vol. 18, no. 3, pp. 415–427, Jul. 2019. (cited on page 16)

[81] F. Tostevin, P. R. Ten Wolde, and M. Howard, "Fundamental limits to position determination by concentration gradients," *PLoS Comput. Biol.*, vol. 3, no. 4, p. e78, Apr. 2007. (cited on page 17)

[82] M. J. Moore, T. Nakano, A. Enomoto, and T. Suda, "Measuring distance from single spike feedback signals in molecular communication," *IEEE Trans. Signal Process.*, vol. 60, no. 7, pp. 3576–3587, Jul. 2012. (cited on page 17)

[83] J.-T. Huang, H.-Y. Lai, Y.-C. Lee, C.-H. Lee, and P.-C. Yeh, "Distance estimation in concentration-based molecular communications," in *Proc. IEEE GLOBECOM 2013*, Atlanta, GA, USA, Dec. 2013, pp. 2587–2591. (cited on page 17)

[84] A. Noel, K. C. Cheung, and R. Schober, "Bounds on distance estimation via diffusive molecular communication," in *Proc. IEEE GLOBECOM 2014*, Austin, TX, USA, Dec. 2014, pp. 2813–2819. (cited on page 17)

[85] C.-H. Ho, "White blood cell and platelet counts could affect whole blood viscosity," *J. Chin. Med. Assoc.*, vol. 67, no. 8, pp. 394–397, Aug. 2004. (cited on page 17)

[86] A. Noel, K. C. Cheung, and R. Schober, "Joint channel parameter estimation via diffusive molecular communication," *IEEE Trans. Mol. Biol. Multi-Scale Commun.*, vol. 1, no. 1, pp. 4–17, Mar. 2015. (cited on page 17)

[87] A. Sadeghi, S. Ghavami, and G. B. Giannakis, "Performance bounds of estimators in molecular communications under structural constraints," in *Proc. ACM NANOCOM 2017*, Washington, DC, USA, Sep. 2017, pp. 1–6. (cited on page 17)

[88] S. Qiu, W. Haselmayr, B. Li, C. Zhao, and W. Guo, "Bacterial relay for energy-efficient molecular communications," *IEEE Trans. Nanobiosci.*, vol. 16, no. 7, pp. 555–562, Oct. 2017. (cited on page 18)

[89] Y. Deng, W. Guo, A. Noel, A. Nallanathan, and M. Elkashlan, "Enabling energy efficient molecular communication via molecule energy transfer," *IEEE Commun. Lett.*, vol. 21, no. 2, pp. 254–257, Feb. 2016. (cited on page 18)

[90] W. Guo, Y. Deng, H. B. Yilmaz, N. Farsad, M. Elkashlan, A. Eckford, A. Nallanathan, and C.-B. Chae, "Smiet: Simultaneous molecular information and energy transfer," *IEEE Trans. Wirel. Commun.*, vol. 25, no. 1, pp. 106–113, Feb. 2017. (cited on page 18)

[91] A. Ahmadzadeh, V. Jamali, and R. Schober, "Molecule harvesting transmitter model for molecular communication systems," *IEEE Open J. Commun. Soc.*, vol. 3, pp. 391–410, Mar. 2022. (cited on pages 18, 21, and 95)

[92] M. Falk, J. Hüsler, and R.-D. Reiss, *Laws of Small Numbers: Extremes and Rare Events*. Springer, 2010. (cited on page 18)

[93] P.-J. Shih, C.-h. Lee, and P.-C. Yeh, "Channel codes for mitigating intersymbol interference in diffusion-based molecular communications," in *Proc. IEEE GLOBECOM 2012*, Anaheim, CA, USA, Dec. 2012, pp. 4228–4232. (cited on page 18)

[94] Q. Liu, P. He, K. Yang, and S. Leng, "Inter-symbol interference analysis of synaptic channel in molecular communications," in *Proc. IEEE ICC 2014*, Sydney, NSW, Australia, June 2014, pp. 4424–4429. (cited on page 18)

[95] M. B. Dissanayake, Y. Deng, A. Nallanathan, M. Elkashlan, and U. Mitra, "Interference mitigation in large-scale multiuser molecular communication," *IEEE Trans. Commun.*, vol. 67, no. 6, pp. 4088–4103, June 2019. (cited on page 18)

[96] K. Aghababaiyan, H. Kebriaei, V. Shah-Mansouri, B. Maham, and D. Niyato, "Enhanced modulation for multiuser molecular communication in internet of nano things,"

IEEE Internet Things J., vol. 9, no. 20, pp. 19 787–19 802, Oct. 2022. (cited on page 18)

[97] I. F. Akyildiz, M. Pierobon, and S. Balasubramaniam, "Moving forward with molecular communication: From theory to human health applications [point of view]," *Proc. IEEE*, vol. 107, no. 5, pp. 858–865, May 2019. (cited on page 19)

[98] M. Pierobon, "A molecular communication system model based on biological circuits," in *Proc. ACM NANOCOM 2014*, Atlanta, GA, USA, May 2014, pp. 1–8. (cited on pages 19 and 21)

[99] A. Marcone, M. Pierobon, and M. Magarini, "The Gaussian approximation in soft detection for molecular communication via biological circuits," in *Proc. IEEE SPAWC 2017*, Sapporo, Japan, Jul. 2017, pp. 1–6. (cited on pages 19 and 21)

[100] M. Pierobon, Z. Sakkaff, J. L. Catlett, and N. R. Buan, "Mutual information upper bound of molecular communication based on cell metabolism," in *Proc. IEEE SPAWC 2016*, Edinburgh, UK, Jul. 2016, pp. 1–6. (cited on page 19)

[101] N. Farsad, W. Guo, and A. W. Eckford, "Tabletop molecular communication: Text messages through chemical signals," *PLoS One*, vol. 8, no. 12, p. e82935, Dec. 2013. (cited on page 19)

[102] B.-H. Koo, C. Lee, H. B. Yilmaz, N. Farsad, A. Eckford, and C.-B. Chae, "Molecular MIMO: From theory to prototype," *IEEE J. Sel. Areas Commun.*, vol. 34, no. 3, pp. 600–614, Mar. 2016. (cited on page 19)

[103] D. T. Mcguiness, S. Giannoukos, S. Taylor, and A. Marshall, "Experimental and analytical analysis of macro-scale molecular communications within closed boundaries," *IEEE Trans. Mol. Biol. Multi-Scale Commun.*, vol. 5, no. 1, pp. 44–55, Oct. 2019. (cited on page 19)

[104] L. Grebenstein, J. Kirchner, W. Wicke, A. Ahmadzadeh, V. Jamali, G. Fischer, R. Weigel, A. Burkovski, and R. Schober, "A molecular communication testbed based on proton pumping bacteria: Methods and data," *IEEE Trans. Mol. Biol. Multi-Scale Commun.*, vol. 5, no. 1, pp. 56–62, Oct. 2019. (cited on page 19)

[105] T. Duke and I. Graham, "Equilibrium mechanisms of receptor clustering," *Prog. Biophys. Mol. Biol.*, vol. 100, no. 1-3, pp. 18–24, Sep. 2009. (cited on pages 20 and 95)

[106] L. Formaggia, D. Lamponi, and A. Quarteroni, "One-dimensional models for blood flow in arteries," *J. Eng. Math.*, vol. 47, no. 3-4, pp. 251–276, Dec. 2003. (cited on pages 20 and 77)

[107] P. Manocha, G. Chandwani, and S. Das, "Dielectrophoretic relay assisted molecular communication for in-sequence molecule delivery," *IEEE Trans. Nanobiosci.*, vol. 15, no. 7, pp. 781–791, Oct. 2016. (cited on pages 20 and 77)

[108] R. Jahn and T. C. Südhof, "Membrane fusion and exocytosis," *Annual review of biochemistry*, vol. 68, no. 1, pp. 863–911, Jul. 1999. (cited on page 23)

[109] A. Morgan, "Exocytosis," *Essays BioChem.*, vol. 30, pp. 77–95, 1995. (cited on page 23)

[110] J. S. Bonifacino and B. S. Glick, "The mechanisms of vesicle budding and fusion," *Cell*, vol. 116, no. 2, pp. 153–166, Jan. 2004. (cited on pages 23 and 26)

[111] L.-G. Wu, E. Hamid, W. Shin, and H.-C. Chiang, "Exocytosis and endocytosis: Modes, functions, and coupling mechanisms," *Annu. Rev. Physiol.*, vol. 76, p. 301, Nov. 2014. (cited on page 23)

[112] O. G. de Jong, S. A. Kooijmans, D. E. Murphy, L. Jiang, M. J. Evers, J. P. Sluijter, P. Vader, and R. M. Schiffelers, "Drug delivery with extracellular vesicles: From imagination to innovation," *Acc. Chem. Res.*, vol. 52, no. 7, pp. 1761–1770, Jun. 2019. (cited on page 23)

[113] R. Chang, *Physical Chemistry for the Biosciences*. University Science Books, 2005. (cited on pages 25, 53, 79, and 98)

[114] M. Kyoung and E. D. Sheets, "Vesicle diffusion close to a membrane: Intermembrane interactions measured with fluorescence correlation spectroscopy," *Biophys. J.*, vol. 95, no. 12, pp. 5789–5797, Dec. 2008. (cited on pages 26, 43, and 66)

[115] M. P. Sheetz, R. Vale, B. Schnapp, T. Schroer, and T. Reese, "Movements of vesicles on microtubules." *Ann. N. Y. Acad. Sci.*, vol. 493, pp. 409–416, Apr. 1987. (cited on page 26)

[116] D. Milovanovic and P. De Camilli, "Synaptic vesicle clusters at synapses: A distinct liquid phase?" *Neuron*, vol. 93, no. 5, pp. 995–1002, Mar. 2017. (cited on page 26)

[117] A. W. Henkel, L. Simpson, R. A. Ridge, and W. J. Betz, "Synaptic vesicle movements monitored by fluorescence recovery after photobleaching in nerve terminals stained with FM1-43," *J. Neurosci.*, vol. 16, no. 12, pp. 3960–3967, Jun. 1996. (cited on page 26)

[118] P. Cosson, M. Amherdt, J. E. Rothman, and L. Orci, "A resident Golgi protein is excluded from peri-Golgi vesicles in NRK cells," *Proc. Natl. Acad. Sci.*, vol. 99, no. 20, pp. 12 831–12 834, Oct. 2002. (cited on page 26)

[119] W. Hong, "SNAREs and traffic," *Biochim. Biophys. Acta Mol. Cell Res.*, vol. 1744, no. 2, pp. 120–144, Apr. 2005. (cited on page 26)

[120] Y. Hua and R. H. Scheller, "Three SNARE complexes cooperate to mediate membrane fusion," *PNAS*, vol. 98, no. 14, pp. 8065–8070, Jul. 2001. (cited on page 26)

[121] G. Madelaine, E. Tonello, C. Lhoussaine, and J. Niehren, "Simplification of reaction networks, confluence and elementary modes," *Computation*, vol. 5, no. 1, p. 14, Mar. 2017. (cited on page 26)

[122] H. Arjmandi, M. Zoofaghari, and A. Noel, "Diffusive molecular communication in a biological spherical environment with partially absorbing boundary," *IEEE Trans. Commun.*, vol. 67, no. 10, pp. 6858–6867, Jul. 2019. (cited on pages 26 and 43)

[123] S. S. Andrews and D. Bray, "Stochastic simulation of chemical reactions with spatial resolution and single molecule detail," *Phys. Biol.*, vol. 1, no. 3, p. 137, Aug. 2004. (cited on pages 27 and 87)

[124] S. S. Andrews, "Accurate particle-based simulation of adsorption, desorption and partial transmission," *Phys. Biol.*, vol. 6, no. 4, p. 046015, Nov. 2009. (cited on pages 27 and 97)

[125] C. K. Haluska, K. A. Riske, V. Marchi-Artzner, J.-M. Lehn, R. Lipowsky, and R. Dimova, "Time scales of membrane fusion revealed by direct imaging of vesicle fusion with high temporal resolution," *PNAS*, vol. 103, no. 43, pp. 15 841–15 846, Oct. 2006. (cited on page 27)

[126] V. Jamali, A. Ahmadzadeh, and R. Schober, "Symbol synchronization for diffusion-based molecular communications," *IEEE Trans. Nanobiosci.*, vol. 16, no. 8, pp. 873–887, Dec. 2017. (cited on page 28)

[127] M. Ş. Kuran, H. B. Yilmaz, I. Demirkol, N. Farsad, and A. Goldsmith, "A survey on modulation techniques in molecular communication via diffusion," *IEEE Commun. Surv. Tutor.*, vol. 23, no. 1, pp. 7–28, Firstquarter 2020. (cited on page 28)

[128] F. Dinç, B. C. Akdeniz, A. E. Pusane, and T. Tugcu, "Impulse response of the molecular diffusion channel with a spherical absorbing receiver and a spherical reflective boundary," *IEEE Trans. Mol. Biol. Multi-Scale Commun.*, vol. 4, no. 2, pp. 118–122, Jun. 2018. (cited on page 29)

[129] H. C. Berg, *Random Walks in Biology*. Princeton, NJ, USA: Princeton Univ. Press, 1993. (cited on pages 29, 55, 57, and 58)

[130] K. Schulten and I. Kosztin, *Lectures in Theoretical Biophysics*. Univ. Illinois, Champaign, IL, USA, 2000, vol. 117. (cited on pages 29, 33, 55, 56, 60, and 114)

[131] F. W. Olver and L. C. Maximon, *Bessel Functions*. New York, NY: Cambridge Univ. Press, 1960. (cited on page 29)

[132] K. S. Miller, R. I. Bernstein, and L. E. Blumenson, "Generalized Rayleigh processes," *Quart. Appl. Math.*, vol. 16, no. 2, pp. 137–145, Jul. 1958. (cited on page 33)

[133] A. Ahmadzadeh, V. Jamali, A. Noel, and R. Schober, "Diffusive mobile molecular communications over time-variant channels," *IEEE Commun. Lett.*, vol. 21, no. 6, pp. 1265–1268, Jun. 2017. (cited on page 33)

[134] L. Le Cam, "An approximation theorem for the Poisson binomial distribution." *Pac. J. Math*, vol. 10, no. 4, pp. 1181–1197, Nov. 1960. (cited on pages 35, 64, and 85)

[135] S. Huang, L. Lin, W. Guo, H. Yan, J. Xu, and F. Liu, "Initial distance estimation and signal detection for diffusive mobile molecular communication," *IEEE Trans. NanoBiosci.*, Jul. 2020. (cited on page 39)

[136] B. C. Akdeniz, M. Egan, and B. Tang, "Equilibrium signaling: Molecular communication robust to geometry uncertainties," *IEEE Trans. Commun.*, pp. 1–1, Oct. 2020. (cited on page 39)

[137] V. V. Petrov, *Sums of Independent Random Variables*. New York, NY, USA: Springer-Verlag, 1975. (cited on page 40)

[138] T. Nakano, Y. Okaie, S. Kobayashi, T. Hara, Y. Hiraoka, and T. Haraguchi, "Methods and applications of mobile molecular communication," *Proc. IEEE*, vol. 107, no. 7, pp. 1442–1456, Jun. 2019. (cited on page 43)

[139] M. S. Kuran, H. B. Yilmaz, T. Tugcu, and I. F. Akyildiz, "Modulation techniques for communication via diffusion in nanonetworks," in *Proc. IEEE ICC 2011*, Kyoto, Japan, Jun. 2011, pp. 1–5. (cited on page 43)

[140] W. W. Ahmed and T. A. Saif, "Active transport of vesicles in neurons is modulated by mechanical tension," *Sci. Rep.*, vol. 4, no. 1, pp. 1–7, Mar. 2014. (cited on page 48)

[141] A. D. Lander, "How cells know where they are," *Science*, vol. 339, no. 6122, pp. 923–927, Feb. 2013. (cited on page 54)

[142] L. Dagdug, M.-V. Vázquez, A. M. Berezhkovskii, and V. Y. Zitserman, "Boundary homogenization for a sphere with an absorbing cap of arbitrary size," *J. Chem. Phys.*, vol. 145, no. 21, p. 214101, Dec. 2016. (cited on page 54)

[143] H. C. Berg and E. M. Purcell, "Physics of chemoreception," *Biophys. J.*, vol. 20, no. 2, pp. 193–219, 1977. (cited on pages 57 and 58)

[144] A. E. Lindsay, A. J. Bernoff, and M. J. Ward, "First passage statistics for the capture of a Brownian particle by a structured spherical target with multiple surface traps," *Multiscale Model. Simul.*, vol. 15, no. 1, pp. 74–109, Jan. 2017. (cited on pages 58, 59, 66, and 99)

[145] K. Chung, A. Sabo, and A. Pica, "Electrical permittivity and conductivity of carbon black-polyvinyl chloride composites," *J. Appl. Phys.*, vol. 53, no. 10, pp. 6867–6879, Jun. 1998. (cited on page 58)

[146] J. M. Crowley, "Simple expressions for force and capacitance for a conductive sphere near a conductive wall," in *Proc. ESA Ann. Meeting on Electrostat.*, 2008, pp. 17–19. (cited on page 58)

[147] A. F. Cheviakov, M. J. Ward, and R. Straube, "An asymptotic analysis of the mean first passage time for narrow escape problems: Part II: The sphere," *Multiscale Model. Simul.*, vol. 8, no. 3, pp. 836–870, Mar. 2010. (cited on page 59)

[148] A. Ahmadzadeh, A. Noel, and R. Schober, "Analysis and design of multi-hop diffusion-based molecular communication networks," *IEEE Trans. Mol. Biol. Multi-Scale Commun.*, vol. 1, no. 2, pp. 144–157, Nov. 2015. (cited on page 65)

[149] A. Isgur, V. Kuznetsov, and S. M. Tanny, "Nested recursions with ceiling function solutions," *J. Differ. Equ. Appl.*, vol. 18, no. 6, pp. 1015–1026, Jul. 2012. (cited on page 65)

[150] M. Li and G. L. Hazelbauer, "Cellular stoichiometry of the components of the chemotaxis signaling complex," *J. Bacteriol.*, vol. 186, no. 12, pp. 3687–3694, Dec. 2004. (cited on page 66)

[151] B. Hat, B. Kazmierczak, and T. Lipniacki, "B cell activation triggered by the formation of the small receptor cluster: A computational study," *PLoS Comput. Biol.*, vol. 7, no. 10, p. e1002197, Oct. 2011. (cited on pages 66 and 103)

[152] D. A. Lauffenburger and J. J. Linderman, *Receptors: Models for Binding, Trafficking, and Signaling*. Oxford Univ. Press, 1996. (cited on page 67)

[153] K. Parang, J. H. Till, A. J. Ablooglu, R. A. Kohanski, S. R. Hubbard, and P. A. Cole, "Mechanism-based design of a protein kinase inhibitor," *Nat. Struc. Biol.*, vol. 8, no. 1, pp. 37–41, Jan. 2001. (cited on page 67)

[154] Á. González, "Measurement of areas on a sphere using Fibonacci and latitude–longitude lattices," *Math. Geosci.*, vol. 42, no. 1, pp. 49–64, Nov. 2010. (cited on pages 70 and 103)

[155] M. Schäfer, A. Ruderer, and R. Rabenstein, "An eigenfunction approach to parameter estimation for 1D diffusion problems," in *Proc. ECC*, Jun. 2019, pp. 3784–3789. (cited on page 77)

[156] N. Varshney, W. Haselmayr, and W. Guo, "On flow-induced diffusive mobile molecular communication: First hitting time and performance analysis," *IEEE Trans. Mol. Biol. Multi-Scale Commun.*, vol. 4, no. 4, pp. 195–207, Dec. 2018. (cited on page 77)

[157] L. Chouhan, P. K. Sharma, and N. Varshney, "Optimal transmitted molecules and decision threshold for drift-induced diffusive molecular channel with mobile nanomachines," *IEEE Trans. Nanobiosci.*, vol. 18, no. 4, pp. 651–660, Aug. 2019. (cited on page 77)

[158] Y. Fang, A. Noel, A. W. Eckford, and N. Yang, "Expected density of cooperative bacteria in a 2D quorum sensing based molecular communication system," in *Proc. IEEE. GLOBECOM*, Dec. 2019, pp. 1–6. (cited on page 80)

[159] S. M. Kay, *Fundamentals of Statistical Signal Processing: EstimationTheory*. Upper Saddle River, NJ, USA: Prentice-Hall, 1993. (cited on pages 84, 85, 86, and 123)

[160] A. Noel, K. C. Cheung, and R. Schober, "Optimal receiver design for diffusive molecular communication with flow and additive noise," *IEEE Trans. Nanobiosci.*, vol. 13, no. 3, pp. 350–362, Jul. 2014. (cited on page 85)

[161] D. Karlis and I. Ntzoufras, "Analysis of sports data by using bivariate Poisson models," *J.R. Stat. Soc.: Ser. D*, vol. 52, no. 3, pp. 381–393, 2003. (cited on page 85)

[162] I. S. Gradshteyn and I. M. Ryzhik, *Table of Integrals, Series, and Products*, 7th ed. San Diego, CA: Academic, 2014. (cited on page 85)

[163] G. Rudnick and J. Clark, "From synapse to vesicle: The reuptake and storage of biogenic amine neurotransmitters," *Biochim. Biophys. Acta Bioenerg.*, vol. 1144, no. 3, pp. 249–263, Oct. 1993. (cited on page 95)

[164] A. D. Barbour, "Stein's method and Poisson process convergence," *J. Appl. Probab.*, vol. 25, no. A, pp. 175–184, 1988. (cited on page 97)

[165] H. P. Keeler, "Notes on the Poisson point process," *Tech. Rep.*, 2016. (cited on page 97)

[166] A. Etemadi, P. Azmi, H. Arjmandi, and N. Mokari, "Compound Poisson noise sources in diffusion-based molecular communication," *IEEE Trans. Commun.*, vol. 67, no. 6, pp. 4104–4116, Jan. 2019. (cited on page 97)

[167] Y. Fang, A. Noel, A. W. Eckford, N. Yang, and J. Guo, "Characterization of cooperators in quorum sensing with 2D molecular signal analysis," *IEEE Trans. Commun.*, vol. 69, no. 2, pp. 799–816, Feb. 2020. (cited on page 97)

[168] B. C. Buddingh' and J. C. van Hest, "Artificial cells: Synthetic compartments with life-like functionality and adaptivity," *Acc. Chem. Res.*, vol. 50, no. 4, pp. 769–777, Jan. 2017. (cited on page 108)

[169] B. Alberts, A. Johnson, J. Lewis, D. Morgan, M. Raff, K. Roberts, and P. Walter, *Molecular Biology of the Cell*, 4th ed. New York: Garland Science, 2002. (cited on page 109)

[170] P. Saffman and M. Delbrück, "Brownian motion in biological membranes." *Proc. Natl. Acad. Sci. USA*, vol. 72, no. 8, pp. 3111–3113, Aug. 1975. (cited on pages 110 and 111)

[171] H. Y. Meltzer, "Relevance of dopamine autoreceptors for psychiatry: Preclinical and clinical studies," *Schizophr. Bull.*, vol. 6, no. 3, pp. 456–475, Jan. 1980. (cited on page 111)

[172] T. Carlsson, T. Ekholm, and C. Elvingson, "Algorithm for generating a brownian motion on a sphere," *J. Pgys. A Math. Theor.*, vol. 43, no. 50, p. 505001, Nov. 2010. (cited on page 111)

[173] K. Cole, J. Beck, A. Haji-Sheikh, and B. Litkouhi, *Heat Conduction Using Greens Functions*. Boca Raton, FL, USA: CRC Press, 2010. (cited on page 113)

[174] P. M. Morse and H. Feshbach, *Methods of Theoretical Physics, Part I*. New York: McGraw-Hill Book Co., 1953. (cited on page 113)

[175] J. D. Pryce, *Numerical Solution of Sturm-Liouville Problems*, Oxford, U.K., 1993. (cited on page 114)

[176] J. Chen, K. H. Lundberg, D. E. Davison, and D. S. Bernstein, "The final value theorem revisited-infinite limits and irrational functions," *IEEE Control Syst. Mag.*, vol. 27, no. 3, pp. 97–99, May 2007. (cited on pages 115 and 118)

[177] F. Oberhettinger and L. Badii, *Tables of Laplace Transforms*. Springer Science & Business Media, 1973. (cited on pages 118 and 120)

[178] D. J. Struik, "The origin of L'Hôpital's rule," *The Math. Teach.*, vol. 56, no. 4, pp. 257–260, Apr. 1963. (cited on page 121)

[179] K. V. Srinivas, A. W. Eckford, and R. S. Adve, "Molecular communication in fluid media: The additive inverse gaussian noise channel," *IEEE Trans. Inf. Theory*, vol. 58, no. 7, pp. 4678–4692, Apr. 2012. (cited on page 121)